Ammonia borane composites for solid state hydrogen storage and calcium-ammonia solutions in graphite

Atahl Nathanson

This thesis is in accordance with the requirements of the University College London for the degree of Engineering Doctorate

February 2014

Ammonia borane composites for solid state hydrogen storage and calcium-ammonia solutions in graphite

Submitted for the degree of Doctor of Engineering

February 2014

Abstract

The dual problems of worlds growing population, increasing energy demand and global warming, necessitate an alternative to fossil fuels. Hydrogen is plentiful and has a high energy density but storage in high pressure tanks is complex and presents safety concerns. Ammonia borane (AB) is one of the most promising solid state hydrogen storage materials due to its high releasable hydrogen content (13.1 wt%), stability in air, and low toxicity. On heating, however, pure AB releases hydrogen only after long nucleation times and is accompanied by the liberation of gaseous impurities including borazine and ammonia; additionally, extensive material expansion and foaming occurs. AB composites with polyethylene oxide, polystyrene and imogolite have been synthesized. It is concluded that the decomposition of AB is best ameliorated by providing access to functional groups that catalyse alternative dehydrogenation routes. Lowering the onset of hydrogen loss to below the melting temperature limits the overall foam and expansion.

The two dimensional confined motion of liquid ammonia in a multi staged ternary calcium ammonia graphite intercalation compound was studied with respect to temperature. Hopping diffusion at 300K gives way to rotation below 100K. The dynamics of this confined calcium ammonia solution are observed as similar to the three dimensional counterpart.

I, Atahl Nathanson confirm that the work presented in this thesis is my own. Where information has been derived from other sources, I confirm that this has been indicated in the thesis

Acknowledgements

Firstly, a thank you to my supervisors Stephen Bennington and Neal Skipper for their guidance, support and the enthusiasm expressed for my scientific endeavours. Both provided distinct and valuable roles in allowing me to experience both academia and industry.

The team at Cella Energy, Arthur (Thank you for being an invaluable mentor and friend.), Zeynep (Thanks for all the great food, help with experiments and political awareness.), Stephen (All that wardrobe advice and unfortunately I still wear shorts with tights.), Tom (We didn't get shot!), Dave, Joe, Lucile, Marie, Lindsey (Tango till dawn with me?), Gemma (I've still got that duck!), Anna and Matt (Many thanks, soon we will all be published authors!) and Kevin (Thank you for starting for my ill car – it's now in mechanical heaven.).

Now all those at Isis: Tati (where would we be without your bus? Thank you for all those hours spent waiting for me at the side of the road), Aziz (keep up the music), Jordi (Who will throw things at me now?), Rowen, Bruno, Konstantin, Davide, Rob, Giovanni, Sev, Roberto (Thank you, I will come to Milan…soon…very soon!), Vicky (Thank you for all your help and patience.), Ruth (Thanks for Robbie and all the fabulous gossip.), Ivan (Thanks for all those great coffees and cakes.) and Joe (Keep peddling.).

Thank you to the F10 crew for support during my write up. Emily, so handy with the hanky and the prep talks, thank you. Christian, Dave, Paddy, Radhika and Stephen, thanks for the help, lunches and letting me play my atrocious football. I'm building a team over in Chemistry so prepare yourselves! Hello and thanks also to the EngD group Nic, Nuru, Will, Szymon, Clyde, Marcus, Isaac, Liz, Jay and Kathrine, unfortunately dl-poly didn't make the final cut this time.

Thank you Chris for making the calcium and lithium graphite samples. Spencer and Jaqueline, without your guidance through Modes the neutron data would still be very raw. Derek, many thanks for all the science advices! Arthur, gracias for the Sketchup electrospinning picture.

My three keen work experience students Bouyan, Ben and Hannah. Thank you for coming and being, well, so keen!

Jaqueline (Thank you for your help, you're always in my heart.), Jake (Thanks for tolerating my general madness.) and Eloise (your good wishes are always so well timed).

Thank you to all my proof readers; Steve, Neal, Mum, Christian, Joe, Tim and Rhiain.

So to my family, Mum, Dad, Phil, Rhiain, Brighid and Lucien. Thank you for believing in me and making me feel intelligent. Sarah, Gemma, Jade, Parry, Isaac and Suki, you rock my world,

thanks for letting me live in your home. And last but not least thanks to Robbie my feline bed warmer.

Contents

1 An introduction to hydrogen storage and graphite intercalation compounds 1

1.1 Hydrogen 1

1.1.1 Fossil fuels and global warming 1

1.1.2 A hydrogen economy 1

1.2 Hydrogen storage targets for vehicles 4

1.3 Current hydrogen storage methods for vehicles 4

1.3.1 Storing hydrogen as a gas or liquid 7

1.3.2 Clathrates 7

1.3.3 Physisorbed hydrogen storage 8

1.3.4 Chemisorbed hydrogen storage 9

1.4 Alkali metal ammonia graphite intercalation compounds 12

2 Materials introduction 15

2.1 Ammonia borane 15

2.1.1 Structure 15

2.1.2 Ammonia borane synthesis and regeneration 17

2.1.3 The reaction pathway of the dehydrogenation of ammonia borane 17

2.2 Modifying the dehydration properties of ammonia borane – literature study 20

2.2.1 Ammonia borane in water 20

2.2.2 Ammonia borane in alternative solvents 20

2.2.3 Ammonia borane in ionic liquids 21

2.2.4 Ammonia borane in acidic conditions 22

2.2.5 Zeolites and metal organic frameworks 23

2.2.6 Carbon 23

2.2.7 Metal catalysts and ammonia borane 24

2.2.8 Ammonia borane in the presence of polymers 24

2.3 Materials used and project aims 25

2.3.1 Polymers 25

2.3.2 Clays 27
2.4 Graphite intercalation compounds 30
3 Experimental methods 32
3.1 Making samples 32
3.1.1 Electrospinning 32
3.1.2 Spinning parameters 39
3.1.3 Freeze drying 41
3.1.4 Dry mixing 41
3.2 A vapour transport method for intercalation into graphite 42
3.3 Analysing samples 42
3.3.1 Scanning electron microscopy 42
3.3.2 Fourier transform infrared spectroscopy 44
3.3.3 Foam tests 45
3.3.4 Thermogravimetric analysis and differential scanning calorimetry 45
3.3.5 Mass spectrometry 47
3.3.6 X-ray diffraction 53
3.3.7 Nuclear magnetic resonance spectroscopy 54
3.4 Introduction to neutron scattering 55
3.4.1 IRIS 59
3.4.2 Modes 62
4 Ammonia borane and polyethylene oxide composites 63
4.1 Electrospinning polyethylene oxide 63
4.2 Electectrospinning polyethylene oxide with ammonia borane 66
4.2.1 Uncertainty 67
4.3 Freeze drying and dry mixing polyethylene oxide and ammonia borane 68
4.4 X-ray diffraction of the electrospun and freeze dried polyethylene oxide and ammonia borane composites 68
4.5 Foam tests 70

4.6 Ramp heating of the ammonia borane-polyethylene oxide composites and pristine ammonia borane 74

4.6.1 Hydrogen release, thermogravimetric analysis and differential scanning calorimetry 74

4.6.2 Impurities 76

4.6.3 Conclusions 77

4.7 Isothermal heating 77

4.7.1 Hydrogen release under isothermal heating runs 77

4.7.2 Non-hydrogen species released form AB under step heating 79

4.7.3 Conclusions 80

4.8 Fourier transform infrared spectroscopy 85

4.8.1 FTIR of ammonia borane and polyethylene oxide 85

4.8.2 FTIR of the AB-PEO fibres 86

4.8.3 Isothermal heating of 50AB-50PEO studied by FTIR 87

4.8.4 Conclusions 89

4.9 Nuclear magnetic resonance spectroscopy 91

4.9.1 ^{11}B NMR of ammonia borane heated *in situ* at 85°C 91

4.9.2 ^{11}B NMR of the 50AB-50PEO fibres heated *in situ* at 85°C 93

4.9.3 Conclusions 94

4.9.4 ^{15}N NMR 95

4.10 *Ex situ* heating 96

4.10.1 Heating XRD 99

4.11 Discussion and conclusions 100

4.11.1 Structure of the ammonia borane-polyethylene oxide composites 100

4.11.2 Foaming of ammonia borane and of the ammonia borane-polyethylene oxide composites 100

4.11.3 Hydrogen release 101

4.11.4 Reaction mechanism in the gas stream 102

4.12 Further work 103

4.12.1 Structure 103

4.12.2 Foaming 104
4.12.3 Impurities 104
4.12.4 Reaction Mechanism 104
5 Polystyrene and ammonia borane 105
5.1 Electrospinning polystyrene and ammonia borane 105
5.2 Foam tests on the ammonia borane-polystyrene fibres 107
5.3 Ramp heating of ammonia borane-polystyrene fibres 108
5.4 Conclusions and discussion 111
5.5 Further work 112
6 Ammonia borane and clay 113
6.1 Scanning electron microscopy 113
6.2 Foam tests of AB-clay composites 115
6.3 Ammonia borane-imogolite: varying the proportion of AB 118
6.4 X-ray diffraction of AB-IMOG composites 119
6.5 Thermogravimetric analysis and differential scanning calorimetry of the ammonia borane-imogolite composites 122
6.6 Hydrogen gas stream content 124
6.7 Discussion and conclusions 126
6.7.1 Structure 126
6.7.2 Foaming 126
6.7.3 Dehydrogenation 127
6.8 Further work 128
6.8.1 Structure 128
6.8.2 Foaming 128
6.8.3 Reaction 128
6.8.4 Alternative materials 129
7 Neutron spectroscopy studies of calcium-ammonia solutions confined by graphene sheets. 130
7.1 Synthesis 130

7.2 Diffraction 130
7.3 Diffusional dynamics 133
7.4 Conclusions and discussion 137
7.5 Future work 138
8 Final conclusions 139
8.1 Structure and foaming of the ammonia borane composites 139
8.2 Hydrogen release from the ammonia borane composites 139
8.3 Solid state hydrogen storage 140
8.4 Calcium graphite intercalates 140
9 Bibliography 141

List of Figures

Figure 1: Ragone plot of the energy storage verses power for various electrochemical energy conversion systems. The high specific energy of fuel cells can provide a viable alternative to the internal combustion engine for vehicles [8]. 2

Figure 2: Proton exchange membrane fuel cells enable the controlled burn of hydrogen to produce electricity [9]. 3

Figure 3: The gravimetric and volumetric hydrogen densities of various potential hydrogen storage materials [3] 5

Figure 4: Spider plots for several hydrogen storage systems, reversible (top), chemical hydrides (middle), and sorbent (bottom) with respect to the 2010 DOE targets. The yellow areas show where improvements in technology and understading are required [13]. 6

Figure 5: Van't Hoff desorption lines for single metal and alloyed metal hydrides from Sandrocks metal hydride review paper [23]. The box area represents the desired temperature and pressure range of operation for vehicular applications. The alloys are highly versatile and tuneable. 10

Figure 6: The AA, AB and ABC stacking arrangements of graphite layers. 13

Figure 7: Possible staging arrangements for graphite intercalation compounds. 14

Figure 8: The possible dihydrogen bonding arrangement in AB determined by Bowden *et al.* [44]. A single layer on the ab plane is displayed. Nitrogen atoms are shown in pink and boron atoms are purple. a) is the orthorhombic phase observed at 200K and b) is the tetragonal phase observed at 300K. 16

Figure 9: AB regeneration with hydrazine and ammonia [52]. 17

Figure 10: Thermolysis of ammonia borane determined experimentally by Frueh *et al.*; both cyclic and polymeric amido and imido boranes are produced [57] . Slow heating rates (<1°C min^{-1}) do not produce borazine, medium heating rates (3-10 °C min^{-1}) show borazine during the release of the second hydrogen equivalent and aggressive heating regimes (>10°C min^{-1}) produce even more cyclic by-products [59]. 18

Figure 11: The themolysis reaction mechanism of AB (polymeric) proposed by Stowe *et al.* showing the induction, nucleation and growth phases [67]. 19

Figure 12: A) Decomposition pathway for AB in glyme suggested by Shaw *et al.* based on boron NMR experiments [79]. AB follows that cyclic reaction route. B) From Kim *et al.* showing how hydrogen bonding between AB and ether promotes formation of DADB [81]. 21

Figure 13: The mechanism of acid dehydrogenation of AB proposed Stephens *et al*. [37]. The acid abstracts a hydride (a) activating the boron to interact with a neighbouring AB molecule (b) forming an intermediate. Hydrogen loss follows and an intermediate with a bridging hydrogen is formed. If the acid to AB ratio is low dehydropolymerization ensues (c). However, if the ratio is high, a second reaction takes place (d) which catalyses the reaction further (e). 22

Figure 14: Schematic of the PEO monomer unit. 25

Figure 15: Schematic of the PS monomer unit. 27

Figure 16: Single phase electrospinning rig. 33

Figure 17: Schematic of a scanning electron microscope. 43

Figure 18: AB containing pellets prepared for foam testing. 45

Figure 19: Schematic of a combined DSC/TGA instrument. 46

Figure 20: Schematic of a residual gas analyser (mass spec). 47

Figure 21: Savitsky-Golay smoothing, of ammonia (m/z = 17) signal where N = 500. 49

Figure 22: Cumulative integrals of the heating ramps of two pristine AB samples (AB1 and AB2) tested several months apart. The data were normalised to the hydrogen (m/z = 2) level at 190ºC and errors in the data are shown as the lighter background. The increase in impurities observed in AB2 is likely due to the time separation between the two tests. This graph has been plotted to show care must be taken when comparing impurity levels from different samples. 51

Figure 23: The mass loss (top) of the 75AB-25PEO electrospun fibres when subjected to heat steps of 150°C, 120°C and 100°C in the combined TGA/DSC (bottom). In the 150°C and 120°C steps the majority of the hydrogen has been lost before the maximum temperature was reached. Additionally the samples never reach the set temperature. Therefore this loss data are inappropriate for analysing the activation energy of AB. 52

Figure 24: The momentum and energy changes associated with elastic and inelastic scattering. ki and kf are the initial and final wavevector of the neutron respectively. 56

Figure 25: Geometry of a scattering experiment [165] 57

Figure 26: Schematic of IRIS indirect time of flight neutron spectrometer 59

Figure 27: Schematic of the neutron scattering energy spectrum. 60

Figure 28: 3% PEO (2M) in a variety of solvents. 64

Figure 29: PEO electrospun fibres with solvents H_2O, ACN and an equal mix of the two. 65

Figure 30: The viscosity of the AB-PEO in ACN solutions with respect to shear speed. The viscosity at the high shear limit quoted in Table 14. The addition of AB successively reduces the viscosity. 66

Figure 31: Images of the AB-PEO fibre samples, 24AB-75PEO, 50AB-50PEO and 75AB-25PEO. As the ratio of AB to PEO increases the fibres become rougher. 67

Figure 32: The fluffy fibres produced from the PEO-AB-ACN solution. 68

Figure 33: X-ray diffraction pattern of PEO as received granules and electrospun fibres. 69

Figure 34: X-ray diffraction pattern of AB, PEO granules and the electrospun fibres collected on a Phillips X'pert, above, and the Rigaku SmartLab, below. 70

Figure 35: Foaming response of a compressed pellet of AB when subjected to 120°C isothermal heating..... 71

Figure 36: Foam tests with pellets made from electrospun fibres, freeze dried material, and hand milled powder with AB contents, 25, 50 and 75wt% 72

Figure 37: Unfurled pellet..... 73

Figure 38: Representative examples of the relation between initial pellet density and foaming. 73

Figure 39: Combined TGA, DSC and RGA hydrogen signal (m/z=2) for pristine AB and the AB-PEO electrospun fibres. As the fraction of PEO in the sample increases, the hydrogen release is activated at earlier temperatures. Mass loss occurs earlier in the AB-PEO composites than in the pristine AB but the final wt% loss is similar (~50%) in both. In the DSC curves, successive addition of PEO reduces the depth of the AB melting endotherm. The lower temperature release of hydrogen is accompanied by an exotherm which reduces the apparent size of the melting endotherm. 75

Figure 40: Cumulative integrals of the heating ramps of pristine AB and the AB-PEO composite fibres. It is noted that raising the amount of PEO in the mix aids the hydrogen release but produces more borazine. The data were normalised to the hydrogen (m/z = 2) level at 190ºC and errors in the data are shown as the lighter background. 78

Figure 41: Hydrogen (m/z=2) trace of the isothermal heating runs of pure AB and the composite materials. At all temperatures, the dehydrogenation of AB begins earlier and is accelerated as the PEO fraction of the composite increases. 81

Figure 42: The borazine signal, m/z=81, from pristine AB and the AB-PEO fibres under isothermal heating at 80°C, 100°C, 120°C and 150°C. The pristine AB does not release any borazine at any of the temperatures. This is consistent with literature and the heat ramp data (Figure 40) where borazine is first observed at 150°C. (The sample is actually several degrees

cooler than the written value, see experimental chapter 3). None of the AB-PEO fibres release borazine at 80°C but all give off borazine at 120°C and 150°C. At 100°C the 25AB-75PEO is the only sample that releases significant borazine. This is consistent with the ramp heating tests where it is first observed around 100°C in this sample. This suggests the PEO is encouraging borazine to be released..... 82

Figure 43: The diborane signal, m/z = 27, released by pure AB and the AB-PEO fibres under isothermal heating of 80°C, 100°C, 120°C and 150°C. No diborane was detected at 80°C and 100°C. At 120°C both the pristine AB and the AB-PEO fibres show borazine. At 150°C the diborane level are higher in the AB-PEO fibres than in the AB. This suggests PEO encourages the formation of diborane at high temperatures. 83

Figure 44: The ammonia signal, m/z= 17, released by pristine AB and the AB-PEO fibres under isothermal heating of 80°C, 100°C, 120°C and 150°C. The ammonia levels are similar in the pure AB and the fibres, but ammonia is released sooner in the fibres. At 80°C AB does not release any ammonia, but then it doesn't release any hydrogen either. This suggests PEO does have a significant effect on the ammonia release. 84

Figure 45: The FTIR spectrum of as received AB, electrospun PEO fibres and 50AB-50PEO fibres. Stretches are identified from literature. [179]–[183]. 86

Figure 47: The FTIR spectra of AB, PEO and the three electrospun fibres. As the PEO content in the fibres increases there is a change in intensity (grey highlights), a shift to higher wave number. Additionally there is splitting of the PEO C-O and C-H stretching peaks (dashed line). This supports the previous suggestion that the dihydrogen bonding of AB is being replaced by hydrogen bonding between AB and PEO. 88

Figure 48: FTIR of the heated samples. New peaks that appear during the heating are labelled. 90

Figure 49: ^{11}B NMR of pure AB at 85°C..... 91

Figure 50: ^{11}B NMR of 50AB-50PEO material heated at 85°C for several hours..... 93

Figure 51: The ^{11}B NMR studies of AB dehydrogenation at 85°C. The pristine AB superimposed on the 50AB-50PEO fibre sample. The AB in the fibres reacts faster, the BH_4 group has a broader peak and B-O bonds occur. 95

Figure 52: ^{15}N NMR of pure AB and 50AB-50PEO electrospun sample before and after 6 hours heating 85°C when PAB is observed. 96

Figure 53: The changing surface of the 50AB-50PEO electrospun fibres at 85°C..... 98

Figure 54: Higher resolution image of pockmarked 99

Figure 55: X-ray diffraction pattern of the 50AB-50PEO electrospun fibres heated *ex situ* over 3 hours. The peaks associated with AB and PEO disappear and are replaced with an amorphous hump. A hump at 22° has previously been associated to PAB. 99

Figure 56: SEM image of PS and 50AB:50PS electrospun fibres. 107

Figure 57: Foam testing AB-PS pellets made from the electrospun fibres. Foaming and residue on the test tube wall is inversely related to the PS content. Images of the final pellets once removed from the test tube have also been inserted. 108

Figure 58: TGA trace of the mass loss of the AB-PS fibres when subject to a 2°C/min temperature ramp between room temperature to 200°C. 109

Figure 59: DSC traces of the AB-PS electrospun fibres under ramp heating rate of 2°C/min. 109

Figure 60: The hydrogen and impurity trances for the AB-PS fibres. When combined with PS, AB releases hydrogen at lower temperatures than when in its pristine state. The PS does not appear to have a significant effect on the impurity levels. 110

Figure 61: SEM images of the four AB-clay composites. In the case of IMOG and LAP, the significant morphology change between the as received clay and the AB-clay composite, suggests intimate mixing of the clay and AB has been achieved. 114

Figure 62: AB:clay 1:1 ratio pellets post foam testing. 115

Figure 63: The LAP and IMOG AB-clay pellets post foam testing. The AB-LAP pellet instantly crumbles while the AB-IMOG remains whole. 116

Figure 64: The change in mass, density and volume of the AB-clay pellets as a percentage of the initial dimensions post foam testing..... 116

Figure 65: Volume expansion against initial density of the AB-clay composites. The AB-IMOG is the only sample that suggests a positive correlation. 117

Figure 66: AB-IMOG pellets after foam testing. 118

Figure 67: SEM image of the 1AB-3IMOG, 2AB-2IMOG and 3AB-1IMOG freeze dried composites. As the proportion of AB increases the visible free volume decreases. 119

Figure 68: The two main AB tetragonal peaks for pristine AB and IMOG. The relative displacement is likely due to the difference of the height of the sample as shown in the displacement of the sample holder peak. 119

Figure 69: The AB peaks in the composites are observed at the same 2 theta position..... 120

Figure 70: XRD pattern of the AB IMOG freeze dried composites. 121

Figure 71: The freeze drying process used to prepare the AB-IMOG composite leaves the IMOG tubes dispersed within the AB. 121

Figure 72: Hydrogen release profile of the AB-IMOG composites compared to pure AB under a standard ramp heating. As the IMOG content increases the pre-peak increase and the release of the 1st and 2nd hydrogen equivalent (H_2 equiv.) 122

Figure 73: TGA and DCS traces for the 1AB-3IMOG, 2AB-2IMOG and 3AB-1IMOG freeze dried composites under standard ramp heating. 123

Figure 74: Cumulative integrals of the mass spec traces of hydrogen and impurities detected under the heating ramp. The data are normalised to the hydrogen (m/z = 2) level at 190ºC and errors in the data are shown as the lighter background. As the IMOG content is raised more ammonia is released but borazine and diborane are decreased. 125

Figure 75: Hypothetical reaction scheme for the initiation (prepeak) of hydrogen release from AB by the hydroxyl groups on the IMOG surface. 127

Figure 76: The neutron diffraction pattern pre ammoniation (purple line) shows both Ca GIC and graphite. After ammoniation (long red trace) a new multistaged ternary phase Ca-NH_3 GIC was created. The final Ca-NH_3 GIC sample includes stages 2, 3 and 4 labelled GIC2, GIC3 and GIC4 respectively. During the NH_3 intercalation unidentified high stages (marked *) form before the low stages. 131

Figure 77: The layers of the Ca-NH_3 GIC contract when the temperature decreases from 300K to 2K 132

Figure 78: In graph A the total neutron scattering spectrum of the Ca-NH_3 GIC is plotted as a function of Q for a range of representative temperatures. The fit to the data are good as demonstrated by a small residual. The spectra broaden and the peak height drops as the temperature increases. In graph B the elastic incoherent structure factor, EISF, ratio of the elastic scattering over the total scattering for all Q, against temperature is depicted. With increasing temperature the shift from elastic to inelastic scattering is due to the protons becoming more active and indicates that greater motion is available to the ammonia. Considering the sharp drops in the trace of the right-hand graph, we can preliminarily define the motional modes occurring. 133

Figure 79: The FWHM of the Lorentzian fits to the data at 300 and 250K, previously divided into 17 groups to depict the changes as a function of Q^2. The Singwi-Sjölander jump model provides the best fit to the data describing an exponential distribution of jump lengths and frequency around the mean values. At 300K this corresponds to a jump distance of 3.2±0.1Å with a frequency of 19ps and at 250K, this corresponds to a jump distance of 2.88±0.2Å with a frequency of 28 ps. 134

Figure 80: Molecular graphics snap-shot of a single layer of composition $CaC_{24}(NH_3)_2$ showing the jump lengths expected (Unpublished work from Neal Skipper). 135

Figure 81: In graph A the FWHM are shown with respect to Q^2 at 200K, 150K and 100K. The linear nature of the fit suggests rotational modes with higher energy at higher temperatures. In graph B an Arrhenius plot of the FWHM obtained yields the activation energy off the rotation as 696 $Jmol^{-1}$. 135

Figure 82: The QENS spectrum before ammoniation, during the experiment and after the ammonia was pumped off, the change in intensity demonstrates the partial reversibility of ammonia intercalation. 136

List of Tables

Table 1: The revised US DOE hydrogen storage targets for automobile applications [11]..... 4

Table 2: The specific and volumetric hydrogen capacities of liquid and gaseous hydrogen..... 7

Table 3: Selected metal hydrides, hydrogen content and decomposition temperatures..... 12

Table 4: The hydrogen content of ammonia borane [37]..... 15

Table 5: Electron distribution in the AB molecule. 15

Table 6: Bond distances in ammonia borane, theoretical and experimental sources..... 16

Table 7: Solvents used in practical work, boiling point and vapour pressure..... 37

Table 8. The mass number assignment of the ionised species observed in the mass spec..... 47

Table 9: Neutrons according to temperature [164] 57

Table 10: Scattering lengths and cross sections of the nuclei observed in experiments in this thesis. 58

Table 11: Jump diffusion models, *l* is the jump length and $\boldsymbol{\tau}$ is the average translational residence time of the diffusing particle..... 61

Table 12: An illustration of the electrospinning parameters tested, to determine the ideal conditions to produce well defined PEO fibres from PEO in water solutions..... 63

Table 13: Electrospinning parameters of PEO (2M) solutions in H_2O, in ACN and in a 50:50 mix 65

Table 14: Processing parameters used for the electrospinning the AB-PEO in ACN solutions. 67

Table 15: The stretching frequencies observed in the FTIR that correspond to B-O bonds..... 89

Table 16: NMR peak assignments. 92

Table 17: The spinning conditions tested for the PS in a 1:1 ratio of THF:DMF to determine the ideal system parameters before adding AB..... 105

Table 18: The spinning conditions tested for the AB-PS single phase solution to determine the ideal system parameters to produce stable spinning conditions and dry fibres. 106

Table 19: The neutron diffraction pattern shows the Ca-NH_3 GIC to have multiple stacking arrangements. Stage 2, 3 and 4 are present but no stage 1 is observed. This is due to the low NH_3 pressure of 3bar which limits the amount of NH_3 in the galleries..... 131

Table 20: The FWHM, rotational dynamic correlation times, τrot, and rotational diffusion constant, D_{rot}, calculated at temperatures of 100K, 150K and 200K. 136

1 An introduction to hydrogen storage and graphite intercalation compounds

1.1 Hydrogen

Hydrogen is the smallest and most abundant (more than 90%) element in the universe [1]. It has a high energy density of 39.1kWh kg^{-1} about three times that of diesel making it an ideal energy carrier [2]. It is colourless, odourless, and nontoxic. Hydrogen is highly flammable and highly versatile, it can be burnt in a fuel cell, a normal combustion engine or as a component of the natural gas on a kitchen hob. The only product from this combustion is water. This makes hydrogen an ideal energy carrier.

1.1.1 Fossil fuels and global warming

Each year, human activities cause 3×10^{12} kg of carbon to be released into the atmosphere in the form of CO_2. This raises the CO_2 concentration by roughly 0.4% annually [3]. The atmospheric CO_2 level is tied closely to the global temperature and warming of the Earth's surface over the last 100 years is already causing changes in climate incompatible with sustaining human life.

Fossil fuels are essentially chemical energy carriers, where the sun's energy has been stored away by the compression of organic matter over millennia. The time scales required for the creation of coal and oil mean that as well as being polluting, fossil fuels are a quickly diminishing finite resource.

It has been shown that energy, from fossil fuels, has enabled the dramatic rise in living standards we are now enjoying in so many parts of the world [4]. Ending the worldwide use of fossil fuels is vital for sustainability but society relies heavily on cheap energy and 'pulling the plug' is not viable option. Sustainable development requires renewable energy sources with versatile energy storage and energy carriers.

1.1.2 A hydrogen economy

It has long been suggested that our current fossil fuel economy could be replaced with a hydrogen economy [5]. Such a scenario would require efficient production, storage, transportation and usage of hydrogen. Hydrogen is CO_2 neutral. The chemical energy in the hydrogen covalent bond can be accessed through its cycle with oxygen [6].

$$H_2 + \frac{1}{2}O_2 \leftrightarrow H_2O \quad \Delta H = 121\ kJ\ g^{-1} \qquad (1)$$

Currently, most of the world's hydrogen is produced through steam reforming of hydrocarbons, a costly and environmentally dirty method that releases CO_2 [6].

$$CH_4 + 2H_2O \rightarrow 4H_2 + CO_2 \qquad (2)$$

The most ideal hydrogen production method is from renewable energy produced by hydro, wind or solar cell power. The electricity produced can be used to electrolyse water to hydrogen and oxygen, see equation 1. The efficiency of water splitting can reach 83% but practically is in the range of 70 to 75%. An important consideration is the purity of the water that can be supplied to the electrolysis cell; impure water can severely impact the lifetime of the cell.

The recent developments of fuel cells over a range of size scales (1 to 100kW) through which hydrogen can be controllably burnt, facilitate the use for hydrogen to power a range of objects from mobile phones to vehicles. As 30% of global energy use is for transport [7] hydrogen, battery or hybrid energy storage systems would go a long way to reducing the global carbon output.

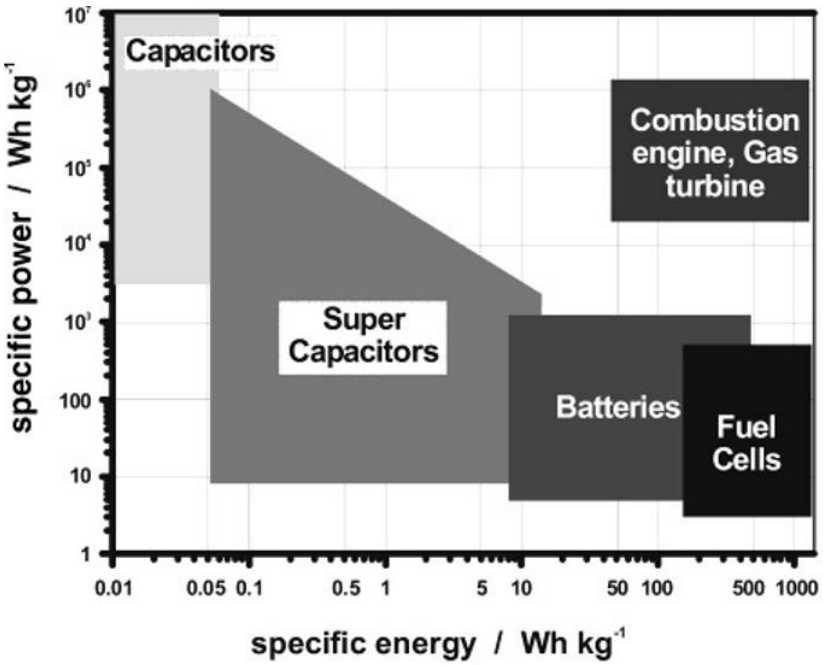

Figure 1: Ragone plot of the energy storage verses power for various electrochemical energy conversion systems. The high specific energy of fuel cells can provide a viable alternative to the internal combustion engine for vehicles [8].

The specific energy of a fuel cell comparable to that of an internal combustion engine, and it outperforms capacitors and batteries [8]. This means that a vehicle with a fuel cell engine systems can be lighter than a vehicle powered by a battery system. Capacitors can provide more power

per unit mass then fuel cells but lack the necessary specific energy to be useful. In this way fuel cells provide a very viable alternative to the internal combustion engine for powering vehicles.

A fuel cell can convert hydrogen to electrical current with an efficiency of 60%. Oxygen dissociates at the cathode, while hydrogen is split at the anode and they combine to form water and electrons see Figure 2. The electrons are used to run an electronic motor and power the vehicle.

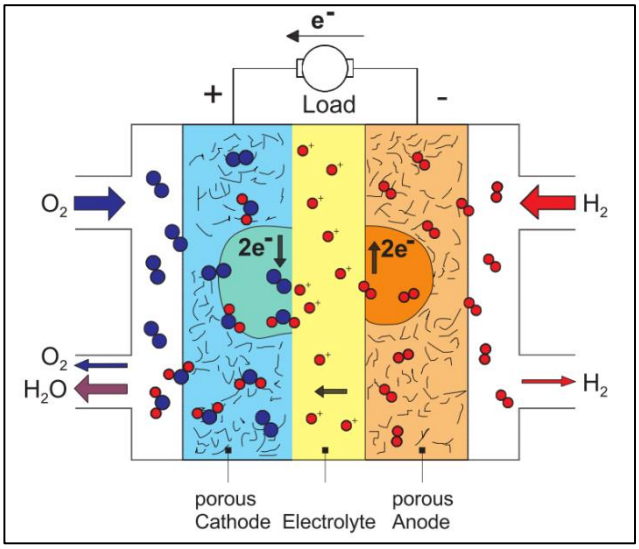

Figure 2: Proton exchange membrane fuel cells enable the controlled burn of hydrogen to produce electricity [9].

Hydrogen distribution faces many challenges. Piping hydrogen requires 4.5 times more energy than natural gas and over long distances becomes expensive [10]. However, the boil off that would occur when shipping liquid hydrogen makes piping the most suitable option available.

Because hydrogen occupies a large volume under ambient conditions, containing it in concentrated volumes is problematic. Additionally, being a tiny molecule, many materials are hydrogen permeable; particularly hydrogen can diffuse into steel causing embrittlement and cracks. Much effort and many solutions have been proposed as to the best ways to store hydrogen until it can be used and some of these are discussed in the following hydrogen storage section.

A word of warning; there are suggestions that hydrogen economy could have unforeseen effects on the environment [6]. Increasing usage of hydrogen would lead to large amounts of hydrogen being released into the atmosphere primarily from leaks. Hydrogen could dissociate and react with oxygen increasing the water levels in the stratosphere that could disrupt the polar region ozone chemistry. Leaking hydrogen could also result in high levels of greenhouse gasses in the atmosphere as in the troposphere hydrogen radicals are an essential ingredient in methane forming. There is still much debate on how much hydrogen ultimately would be released and

how exactly this would impact the globe, indeed as fossil fuels use diminishes the current release of hydrogen from incomplete combustion would also reduce.

1.2 Hydrogen storage targets for vehicles

The main challenge with hydrogen storage in a vehicle is achieving a sufficient volumetric density in the fuel tank to realise a 500km (300 mile) driving range [11] see Table 1. Meanwhile the storage system cost, weight, and refuelling time must be kept low. Also the efficiency and performance over many refuelling cycles of the system must remain high.

An ideal system would work at ambient temperature and pressure to minimise cost. Also it should be environmentally friendly (be a closed cycle that does not release by-products that negatively impact the environment). It is also important to supply a clean hydrogen stream to the fuel cell to maintain its capacity and lifetime. The tank and/or material that fills it, should be cheap to produce and easy to recycle. Additionally the system must be safe and convenient to use.

Table 1: The revised US DOE hydrogen storage targets for automobile applications [11].

Year		2010	2015	Ultimate
Gravimetric capacity	wt %	4.5	5.5	7.5
	Wh g^{-1}	1.5	1.8	2.5
Volumetric capacity	g l^{-1}	28	40	70
	kWh l^{-1}	0.9	1.3	2.3
Fill time	min	4.2	3.3	2.5

1.3 Current hydrogen storage methods for vehicles

There are many distinct methods for storing hydrogen. In Figure 3 hydrogen content by mass and volume of various potential hydrogen storage materials are plotted with respect to the DOE 2010 and 2015 targets [3]. These targets have now been revised to the less ambitious values in Table 1.

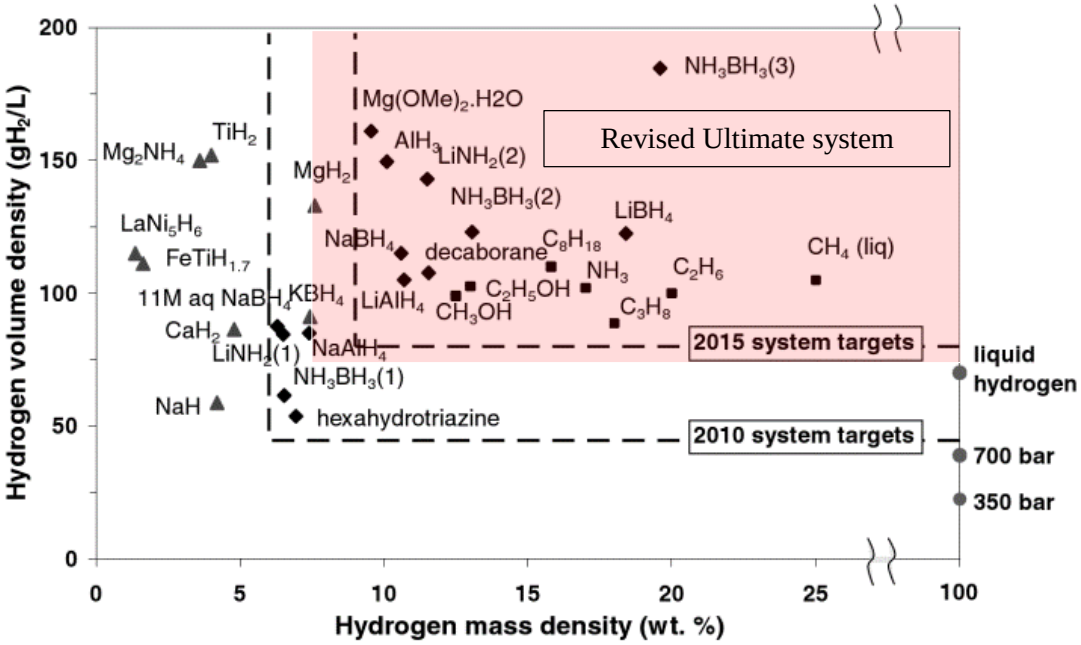

Figure 3: The gravimetric and volumetric hydrogen densities of various potential hydrogen storage materials [3]

Conceptually, the simplest hydrogen storage method is as a pressurised gas. High pressure tanks are well developed and used to power various vehicles such as cars, mopeds and buses [3], [12]. To raise the volumetric hydrogen content, the gas can be liquefied by cooling to below 20K. Maintaining such low temperatures is at best technologically challenging and limits the usefulness of liquid hydrogen storage. To reduce the necessity of high pressures and cryogenic temperatures, highly porous materials with active sites can be used to adsorb and store hydrogen, like bats hanging in interconnecting tunnels. Promising physisorbed systems include carbon, zeolites and metal organic frameworks, however, they cannot meet the DOE requirements at RTP. In the case of chemical and metal hydrides the hydrogen molecule is dissociated and the hydrogen atoms bonded into a new material. Chemical hydrides have high hydrogen contents, however, they tend to be either too stable – where the hydrogen is difficult to extract - or conversely, too unstable - where the hydrogen is difficult to incorporate. Operating under high temperatures and with catalysts is necessary to render them useful. Here it becomes clear that in addition to volume and mass hydrogen content, hydrogen storage materials can also be characterised by their operation temperature and pressure. Additional requirements such as the fill time, dehydration time, hydrogen purity and cost must also be considered to determine if a material could be an appropriate hydrogen storage system. Spider plots, where the characteristics of a hydrogen storage material are rated between 0 and 100 depending on how closely they match the DOE requirements demonstrate, at a glance, how ‘good’ a particular material is. In Figure 4 the adsorbent systems are shown as more desirable then the chemical and metal hydrides. A deeper discussion of the various methods of hydrogen storage follows.

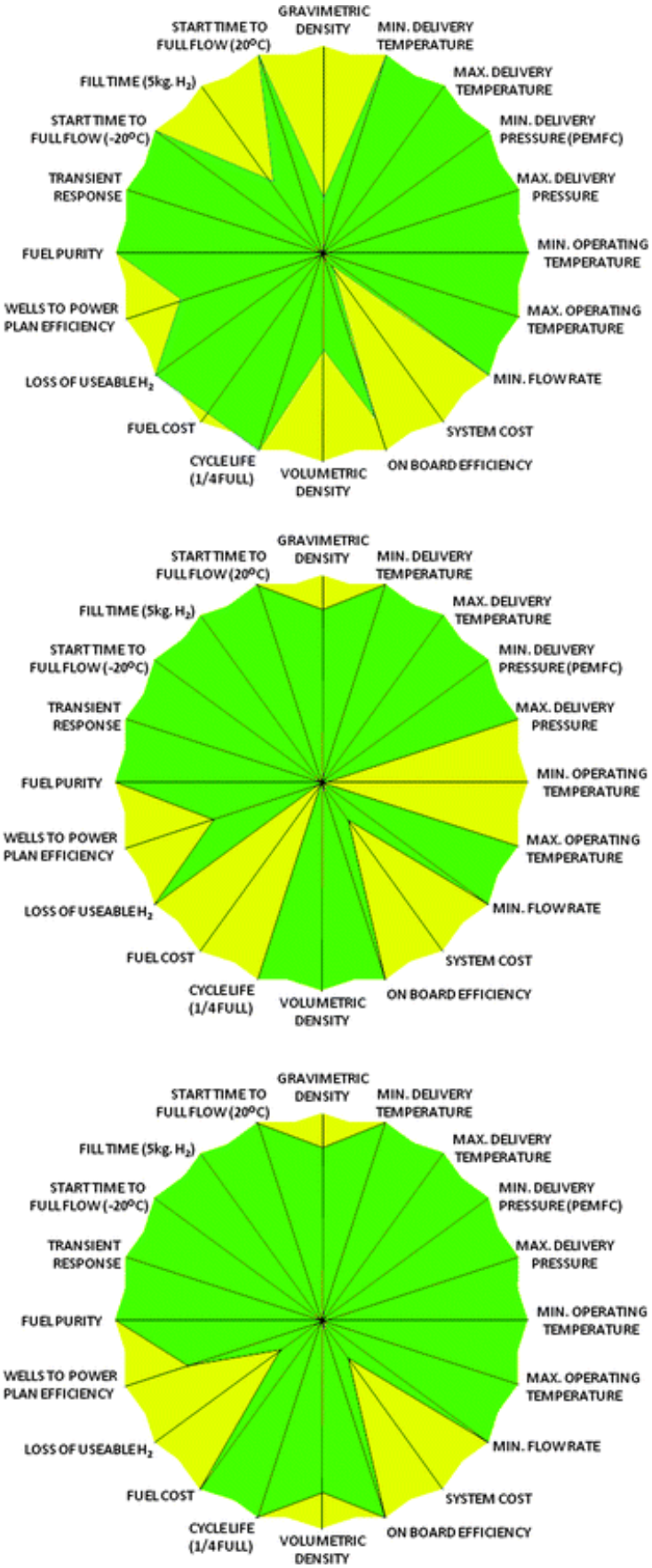

Figure 4: Spider plots for several hydrogen storage systems, reversible (top), chemical hydrides (middle), and sorbent (bottom) with respect to the 2010 DOE targets. The yellow areas show where improvements in technology and understading are required [13].

1.3.1 Storing hydrogen as a gas or liquid

At ambient conditions hydrogen is a gas with a very low density 0.09kg m^{-1}. To achieve a significant energy density, suitable for powering a vehicle, the hydrogen has to be compressed. Containing hydrogen is difficult, high pressures are required and being small it can diffuse into most materials. Also at high pressure the compression has an energy penalty (~15% for a 700bar tank). Tanks are lined with barrier material to limit the hydrogen diffusion such as aluminium oxide or austenitic steel [4], [14]. An outer layer of tightly wound carbon fibre allows high internal pressures. There are two types of gas cylinder for on board hydrogen storage currently available on the market; the low pressure, 350bar and the high pressure system at 700bar. Even at high pressures 5kg of hydrogen can require around 220l of space, in a car the space is usually scavenged from the passenger seats and boot. Even though the high pressure storage cannot meet the DOE targets, hydrogen tank systems are currently the best method for on board hydrogen storage. The refuelling times are fast (5min), the systems are already well developed in a range of vehicles. Gas tanks are particularly ideal in busses where storage space is plentiful, high speeds are not typical and the driving range can be short.

Storing hydrogen in its liquid form increases the energy density by around a third while avoiding the high pressures associated with gas storage see Table 2. Hydrogen boils at 20K so a liquid system has to be heavily insulated from the surroundings. Liquefying is also expensive costing 30% of the total energy of the hydrogen. In all existing systems boil off (0.3 - 3% per day) is a significant problem and tanks are designed currently to withstand pressure as well as the cryogenic temperatures. A release valve is also a must. Toyota have recently developed a system with 6.1wt%, and 800km range but currently it has too many boil off issues.

Table 2: The specific and volumetric hydrogen capacities of liquid and gaseous hydrogen

State	Temperature, K	Pressure, bar	Hydrogen content, wt%	Density, kg m^{-3}	Energy density, kWh kg^{-1}
Gas	298	350	3	23.3	0.9
Gas	298	700	4.5	39.3	1.8
Liquid	20	2	6.1	67.67	2.3

1.3.2 Clathrates

Clathrates are frameworks of water molecules stabilised by a guest non polar molecule such as gases or small organic molecules [15]. They generally resemble ice, and like ice no new bonds are formed between the molecules rather, a phase change has occurred. Hydrogen was initially thought too small to support a clathrate however, in 1999 hydrogen was observed to form clathrates at high pressure (1.5GPa). More recently up 5.3mass% hydrogen has been encased in

a type II clathrate (136 water molecules) [14]. However, further studies showed that added actual number of guest hydrogen molecules varies with pressure and temperature. Tetrahydrofuran can be used to stabilised the framework to allow the hydrogen to remain in the cages at conditions closer to ambient however further work is required before such a system could be employed.

1.3.3 Physisorbed hydrogen storage

In physisorbed systems, the hydrogen maintains its molecular form and associates weakly to the surface of the support material [14]. A high surface area is necessary to increase the number of binding sites per unit mass. The enthalpy of adsorption is weakly exothermic of 1-10kJ mol^{-1}. Physisorbed systems have an advantage over chemically bound hydrogen as far less heat is evolved on hydrogenation. Additionally, physisorbed materials have a long life time as the material structure is unaffected by the hydrogen cycling through. There are several candidates for hydrogen storage including, carbon, polymers zeolites and metal organic frameworks (MOFs)

While diamond and graphite are solid, carbon allotypes can have very high surface area [1], [14]. These allotypes include activated carbon, templated carbon and nanotubes. The binding energy of hydrogen to carbon (<10 kJ/mol) is too weak for ambient temperatures; 0.6wt% was achieved for activated carbon at ambient conditions. However, on cooling (to 77K) and raising the pressure (to 20bar) up to 5wt% was recorded [16]. One of the problems with activated carbon is that it is disordered and the porosity was difficult to control, regular porous carbon materials can however be achieved by templating. Chemical vapour deposition of carbon on to an ordered zeolite produced a material with small even pores capable of storing up to 6.9wt% hydrogen at 77K and 20bar [17]. This study also demonstrated that if the pores around 1nm in diameter were the most effective at holding hydrogen as more hydrogen to carbon interactions occurred. Nanotubes while attractive could only reach a capacity of around 2wt% because of the inaccessibility of binding sites [18].

Metal-Organic Frameworks (MOFs) are 3 dimensional networks formed of metal centres coordinated by organic ligands [1]. MOFs have very low densities due to their high porosity. The metal centres and ligand types can be exchanged so a vast variety of different MOFs can be created. Hydrogen storage is highly reversible with fast kinetics; however, a high hydrogen capacity can only be achieved at low temperature and high pressure. MOFs are also difficult to manufacture; in MOF-5, ~5wt% storage was achieved at 50 bar and 77K [19] but other groups with a different production method only achieved 1.6wt% [20]. One of the highest capacity hydrogen containing MOFs is MOF-177 which achieved 7wt% at 77K [21]. Of the many types of MOFs studied, the key to high adsorption was linked to high internal surface area. Again small pores were helpful especially at low pressures.

Zeolites are three dimensional silicate structures, of the general formula $M_{x/z}\left[(AlO_2)_x(SiO_2)_y\right] \cdot mH_2O$ where M is an exchangeable cation [1]. Every tetragonal silicate that is substituted by an alumina, requires also an additionally metal to balance the charge. Zeolites are very flexible and diverse due to the multiple shapes that can be produced and metals that can be included in the framework. Zeolites are highly porous with interconnected channels. The hydrogen can easily penetrate and clings with the charged metals. At low hydrogen loading pressures the number of metal centres determines the loading that can be achieved. These however fill up quickly and at high pressure the hydrogen interacts with the zeolite wall, where the pore size determines the amount of hydrogen that can be supported. Low temperatures are also helpful. Zeolite X can hold 0.1wt% hydrogen at RTP but increases to 2.2wt% on cooling to 77K.

Polymers of intrinsic porosity (PIMS) made of light atoms, are highly porous and have a high specific area [22]. PIMs are easy to manufacture and have hydrogen adsorption capacities comparable to zeolites and MOFs; 1.7wt% was absorbed below 10bar in a cyclotricatechylene PIM. Again hydrogen has a preference for small pores.

1.3.4 Chemisorbed hydrogen storage

1.3.4.1 Metal hydrides

Most metals will react with hydrogen to form hydrides. There are many varieties but all have with a general formula MH_n where n=1, 2, 3 etc. depending on the valance of the metal. Hydrides can be heavy but have a high energy content per unit volume. They can be formed by supplying hydrogen at a constant pressure to the metal; the hydrogen will penetrate into the surface and diffuse through until the metal has fully reacted. Hydrides are reversible, but the exothermic nature of most metal hydrides makes on-board filling a difficult challenge.

$$M + \frac{n}{2}H_2 \leftrightarrow MH_n + Q, \qquad (3)$$

where M is the metal and Q is the heat. In addition to the heat produced, the metal crystal has to expand to accept the hydrogen and the expansion is hard to control as there are hysteresis effects. After repeat cycles of hydrogenation and dehydrogenation the metal can become pulverized and begins to loose capacity.

Most single metal hydrides are either too stable or too unstable to be used for on board hydrogen storage. In fact, vanadium hydride it the only material that can operate in the range between 1–10atm and 0–100°C see figure X. This has led to the synthesis and analysis of hundreds of alloys of different ratio of stable and unstable metal hydrides to tune the dissociation energy to a level suitable for hydrogen storage applications.

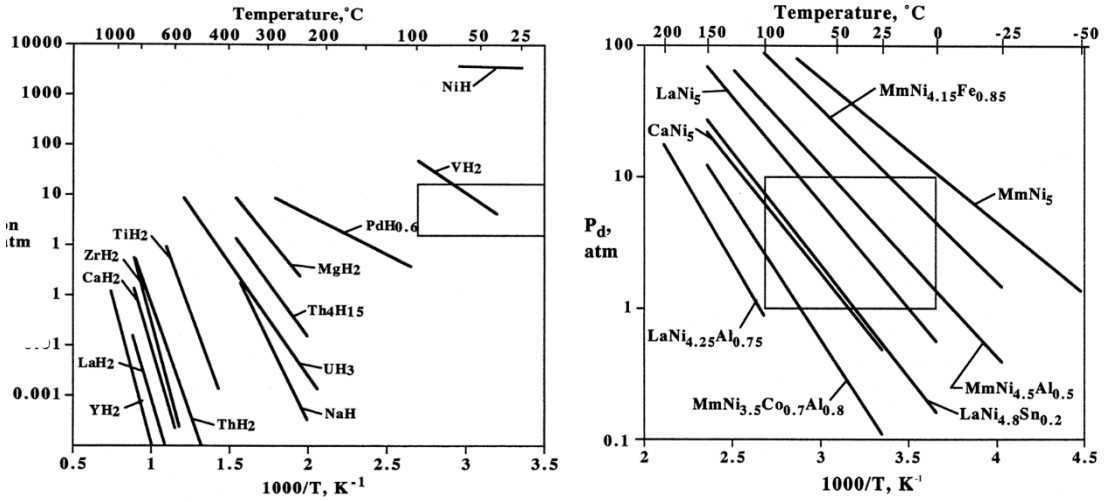

Figure 5: Van't Hoff desorption lines for single metal and alloyed metal hydrides from Sandrocks metal hydride review paper [23]. The box area represents the desired temperature and pressure range of operation for vehicular applications. The alloys are highly versatile and tuneable.

While the alloys represent highly versatile and tunable hydrogen storage material their applicability is limited by the volume expansion and heat evolved during hydration. Further most of the solids have a reversible hydrogen content of maximum 3wt%. Further work is required i.e. more different alloys need to be tested, more synthesis methods need to be explored and more systems engineering to cope with the heat expounded during the reaction.

1.3.4.2 Complex hydrides:

Complex hydrides are materials where hydrogen containing group is attached to a metal. There are three main types; the alanates (metal with AlH_4), borohydrides, (metal with BH_4) and imides and amides (metal with NH or NH_2 groups). In the borohydrides and alanates the hydrogen is hydridic (H^-) while in the amides it is protic (H^+). Complex hydrides decompose in steps, the first at low temperatures and the second and or third at higher temperatures.

Alanates have many promising characteristics they are light, cheap and have low toxicity. Also, their hydrogen content is high. However, alanates also have a very high kinetic barrier to dehydrogenation see Table 3. $NaAlH_4$ is the most promising; it is the complex hydride that is closest to fulfilling the DOE's requirements for on bored hydrogen storage. Dehydrogenation is slow but at just over 200°C three of the four hydrogen molecules can be released. The addition of catalysts can improve this such as Ce can improve this. Now high temperature (200°C) PEM fuels cells are available and systems involving doped $NaAlH_4$ these use approximately 3kg of material that releases 3.6wt% of stored hydrogen.

Borohydrides have very high wt% hydrogen contents compared to alanates because of the small size of the boron compared to the aluminium. Most are extremely stable and only decompose at high temperatures, in fact the temperature required to release hydrogen increases with metal size,

see Table 3. $LiBH_4$ is has therefore the best characteristics. Borohydrides also suffer from slow kinetics, poor reversibility and sometimes release diborane in the hydrogen stream.

Imides and amides are very interesting as they contain both metallic and non-metallic entities. Initially seen as a breakthrough, soon it became apparent that they suffer from the poor reversibility, slow kinetics and high operating temperatures. An excellent review has been written by Ichikawa and can be found in the Handbook of Hydrogen Storage [1]

1.3.4.3 Complex transition metal hydrides

Complex transition metal hydrides (CTMHs) are complex metal hydrides that contain transition metals [6]. Unfortunately the presence of the transition metal makes the complex very heavy and the hydrogen storage capacities become uncomfortably low. Additionally CTMHs require complex and expensive high pressure synthesis methods (500 MPa). This is compounded by the high temperatures required for hydrogen desorption (Table 3) makes them unsuitable as on-board hydrogen storage materials.

Table 3: Selected metal hydrides, hydrogen content and decomposition temperatures.

Borohydrides	Hydrogen content, wt%	Start of decomposition
$LiBH_4$	18.5	380
$NaBH_4$	10.8	400
KBH_4	7.4	500
$Mg(BH_4)_2$	13.7	260-280
$Ca(BH_4)_2$	9.6	350
$Al(BH_4)_2$	16.8	20
$Be(BH_4)_2$	20.7	--
Alanates		
$LiAlH_4$	7.9	170
$NaAlH_4$	5.6	230
$KAlH_4$	5.7	>300
$MgAlH_4$	9.3	110-130
$Ca(AlH_4)_2$	5.9	80
$LiMg(AlH_4)_2$	9.4	170
Complex transition metal hydrides		
Mg_3MnH_7	5.2	280
Mg_2FeH_6	5.5	320
Mg_2CoH_5	4.5	280

1.4 Alkali metal ammonia graphite intercalation compounds

The electron configuration of carbon is $1s^2\ 2s^2\ 2p^2$. This initially suggests that carbon can only form two covalent bonds, however, these orbitals can hybridise. In graphite the hybridisation leads to a $1s^2\ 2sp^3\ 2p^1$ configuration. The 2sp orbitals are arranged in a plane at 120° to each other and the 2p orbital is vertical. This enables the carbon atoms to covalently bond into a planar hexagonal array called graphene [24]. These graphene sheets interact with each other by combining of the vertical p orbitals into a π bond.

The electrons can move between π bonds and enables graphite to conduct electricity. As the π bonds are delocalised the graphene sheets can slide over each other giving graphite lubricating properties. Additionally, a fibre can be formed from graphite that can be woven into a cloth and this, when impregnated with resin, has been used in applications as diverse as boat hulls and bullet proof vests. Graphite fibre has also been used in replacement tendons and ligaments because of its high strength. The layers of graphite are only weakly bonded to each other and as such secondary species, such as lithium, can be intercalated; this is the property that allows graphite to be used as battery electrodes [25]. Graphite is the softest and most stable of all the polymorphs of carbon [24], [26]. It resembles a black opaque rock with a silvery sheen that flakes at the edges.

The carbon atoms are covalently bonded together in a hexagonal planar arrangement with a carbon-carbon bond length of 1.42Å. These graphene sheets are then stacked one above the other and each sheet is shifted slightly with respect to the one below to a more energy favourable configuration. There are two main stacking arrangements; the ABAB, where every second layer has a basal shift of 1.42Å and the ABCABC, where the second and third layers are shifted respectively by 1.42Å and 2.84 Å with respect to the first layer (figure 1) [27], [28]. Natural pristine graphite generally follows an ABAB pattern. In either case the spacing between the layers is controlled by van der Waals interactions which set the graphene layers 3.35Å apart [28].

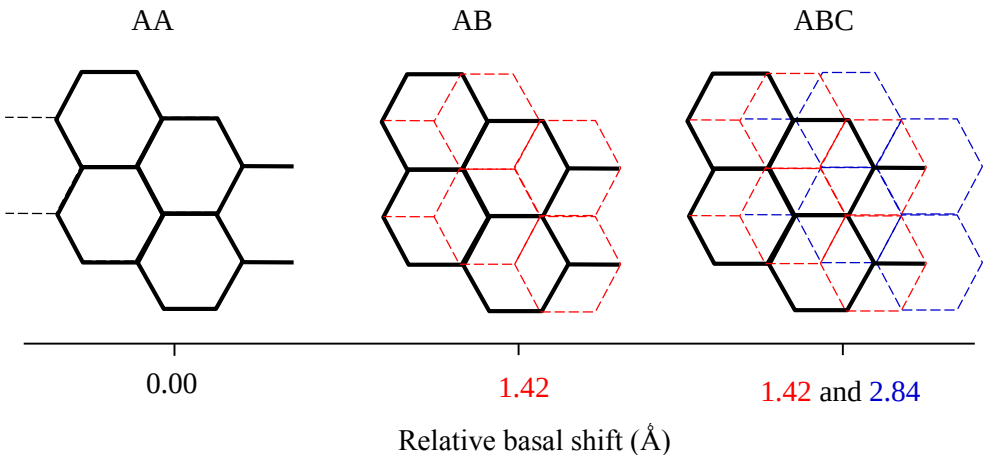

Figure 6: The AA, AB and ABC stacking arrangements of graphite layers.

The interlayer spacing in graphite provides an ideal hosting environment for group I and II alkali metals, the graphene layers move apart to admit the metal and accept the charge from the valance electrons [24], [26]**.** Many varieties of metal binary graphite intercalation compounds (GICs) are possible with a range of interesting structural and electronic properties. GICs are unique in that they undergo staging to minimise the strain on the structure due to the expansion; instead of a random distribution, the intercalates are placed between specific, equidistant graphene layers [26], [29], [30]. The stage is the number of graphene layers present between an intercalate layer. The first GIC was made in 1841 [31] and the first metal-ammonia GIC was made in 1951 by Rüdorff and Schulze [32].

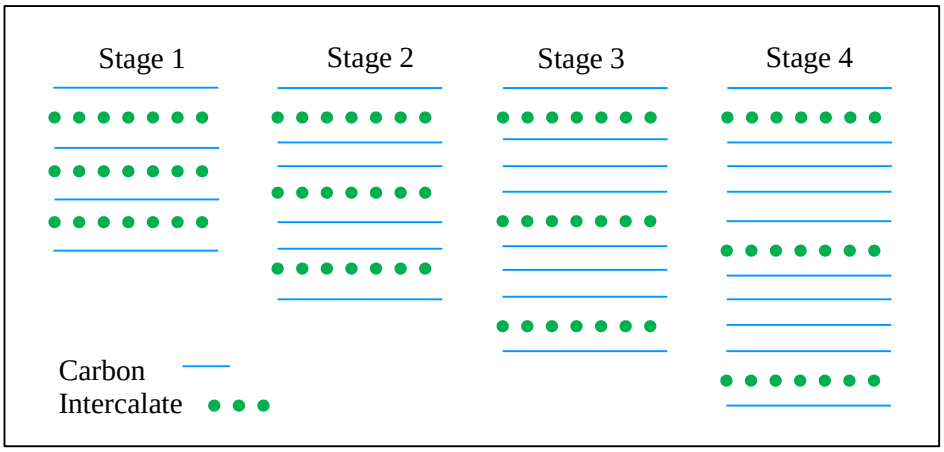

Figure 7: Possible staging arrangements for graphite intercalation compounds.

Ternary GICs, where a second complementary intercalate species is admitted in addition to the alkali metal are also possible, common entities include H_2, N_2, CH_4, and NH_3 [33]. Ternary metal GICs can only be made if a portion of virgin graphite is present as the secondary molecule typically displaces a portion of the metal in creating space for itself. Secondary species intercalation is swift, under 20 hours. This indicates a very high mobility in a two dimensional environment particularly interesting to study as it is coupled with the structural reorganization of the graphite planes [26]. While the intercalation of the primary metal is reversible, it has been shown the secondary species cannot always be fully extracted; when deintercalating NH_3 intercalated K-GIC around two NH_3 per K remain trapped in the structure [34]. It is suggested that the residual ammonia is attached to metal ions in defect sites [35] or ensnared in islands [26].

2 Materials introduction

2.1 Ammonia borane

Ammonia borane (AB) is one of the most promising complex hydrides for hydrogen storage: it contains 19.6 wt% hydrogen, two thirds of which can be released below 200°C [2], [36], [37]. It is a white solid that is relatively stable in air and moisture and, recently, successful recycling of dehydrogenated AB has also been demonstrated [38]. Its hydrogen content by volume and mass are well within the ultimate system targets as set by the DOE. With these properties, AB has the potential to meet the DoE targets for an on-board hydrogen storage material [11], [37]. It does, however, possess some critical disadvantages: its hydrogen release is preceded by a long nucleation time, and the decomposition produces foam and generates poisonous volatile by-products including ammonia and borazine [2].

Table 4: The hydrogen content of ammonia borane [37].

Hydrogen Content	wt%	Gravimetric g/kg	Volumetric g/L
Ammonia borane	19.6	190	100-140
	13.1	130	65-80

2.1.1 Structure

AB is formed from a borane and ammonia group connected by a B-N dative covalent bond; the lone pair of electrons on the nitrogen is donated into the vacant p-orbital on the boron [39].

$$^{\delta+}_{3}H - N: \rightarrow B - H_3^{\delta-} \quad (4)$$

The Pauling electronegativity values for hydrogen, boron and nitrogen are 2.2, 2.04 and 3.04 respectively, so the electrons are unevenly distributed towards the nitrogen side of the molecule. This induces a dipole moment across AB of 5.22D [40], [41] where the $B–H^{\delta-}$ and the $N–H^{\delta+}$ (Table 5).

Table 5: Electron distribution in the AB molecule.

Atom	Mulliken charge, e- [39]	Bader charge analysis, e- [42]
N	−0.91	--
B	−0.29	--
H_B	−0.04/-0.06	-0.44
H_N	0.45	0.62

The partial charges on the boron and nitrogen side of AB pull the molecules close together. The hydrogen atoms on alternate AB molecules are found to be 2.02 Å apart, less than the van der

Waals radius of 2.4 Å and close enough for dihydrogen bonds to form [37]. It is these hydrogen bonds that give AB its high melting temperature and allow it to remain a solid at RTP unlike its isoelectronic partner ethane. AB has a tetragonal unit cell at 300K, with cell parameters, a = b = 5.2630 Å and c =5.0505 Å [43], [44]. At 225K this shifts to an orthorhombic arrangement with cell parameters a = 5.541, b = 4.705 and c = 5.0237Å [45].

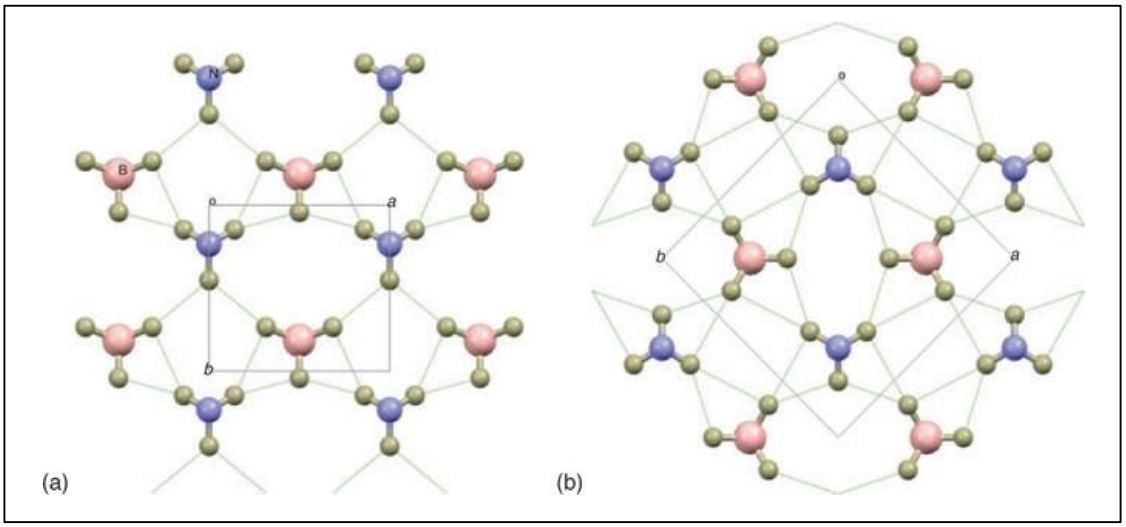

Figure 8: The possible dihydrogen bonding arrangement in AB determined by Bowden *et al.* [44]. A single layer on the ab plane is displayed. Nitrogen atoms are shown in pink and boron atoms are purple. a) is the orthorhombic phase observed at 200K and b) is the tetragonal phase observed at 300K.

The bond distances in AB from various literature sources are collated in Table 6. These values are gained from experiment and vary somewhat depending on the calculation method used [39].

Table 6: Bond distances in ammonia borane, theoretical and experimental sources.

Bond	Bulk Material, Å				Molecule, Å	
	Theoretical			Neutron Diffraction	Theoretical	Microwave spectrometry
	[42]	[46]	[47]	[43]	[42]	[41]
N-B	1.59	1.59	1.58	1.58	1.65	1.67
B-H_B	1.22, 1.23	1.22	—	1.15, 1.18	1.22	1.21
N-H_N	1.03	1.03	—	1.07, 0.96	1.02	1.01
H_N- H_B short	1.89	—	1.91	2.02	—	—
H_N- H_B median	2.19	2.20	2.17	2.21	—	—
H_N- H_B long	2.22	—	2.27	2.23	—	—

2.1.2 Ammonia borane synthesis and regeneration

Ammonia borane can be synthesised in a variety of ways. The first published account by Shore and Parry, which gives yields of 45%, is an exchange reaction with lithium borohydride [48],

$$LiBH_4 + NH_4Cl\ (or (NH_4)_2SO_4) \xrightarrow{diethyl\ ether} NH_3BH_3 + LiCl\ (or\ Li_2SO_4) + H_2 \quad (5)$$

There is also a reaction involving base displacement: an adduct, $H_3B \cdot THF$, is formed by dispersing diborane in tetrahydrofuran, THF; ammonia is added and the reaction takes place in diethyl ether [49]

$$H_3B \cdot THF + NH_3 \xrightarrow{diethyl\ ether} NH_3BH_3 \quad (6)$$

Higher yields of over 90% can be obtained with sodium borohydride and ammonium salts; an example from Ramachandran and Gagare follows [50].

$$NaBH_4 + (NH_4)_2CO_3 \xrightarrow{THF} NH_3BH_3 + H_2 + NaCO_3(NH_4) \quad (7)$$

The AB used in these experiments was sourced from Sigma Aldrich, 97% purity.

The hydrogen release from AB is an exothermic reaction process which leads to the formation of many strong covalent bonds, making it difficult to dehydrogenate. However, regeneration routes have recently been developed that remove this obstacle. Several methods exist [50], [51]; the one detailed here enables regeneration from polyborazylene (NBH), the product when more than two equivalents of hydrogen have been extracted using hydrazine [52].

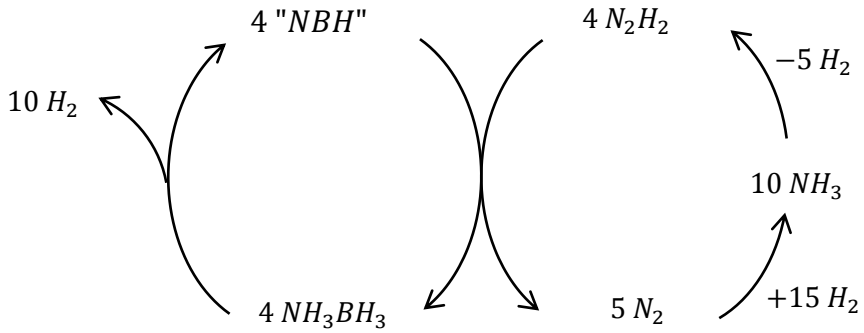

Figure 9: AB regeneration with hydrazine and ammonia [52].

2.1.3 The reaction pathway of the dehydrogenation of ammonia borane

The hydrogen release from AB occurs in discrete steps, activated by temperature, during which the 1st, 2nd and 3rd dihydrogen equivalents from each AB molecule are lost. The reaction is initiated

in the material and propagates outwards from the nucleation site as a chain reaction. These steps are sequential but overlapping; before the entire 1st equivalent of hydrogen has evolved, the second step will have begun [53], [54]. Hydrogen evolution follows a sigmoidal form, indicative of nucleation and then growth. The reaction equations for the release of the 1st, 2nd and 3rd hydrogen equivalents are written below.

$$nBH_3NH_3 \rightarrow [H_2BNH_2]_n + nH_2, \quad \text{<150°C [55] , <100°C [56], 110-130°C [57]} \qquad (8)$$

$$[H_2BNH_2]_n \rightarrow [HBNH]_n + nH_2 , \quad \text{150-200°C [55], >100°C [56]} \qquad (9)$$

$$[HBNH]_n \rightarrow nBN + nH_{2(g)} , \quad \text{> 200°C [55], >150°C [56]} \qquad (10)$$

This general reaction scheme hides much complexity as the species can polymerise to form chains or become terminated in rings [46], [58]. Chains are preferred if the temperature is kept low, while rings are more probable under aggressive heating regimes [57].

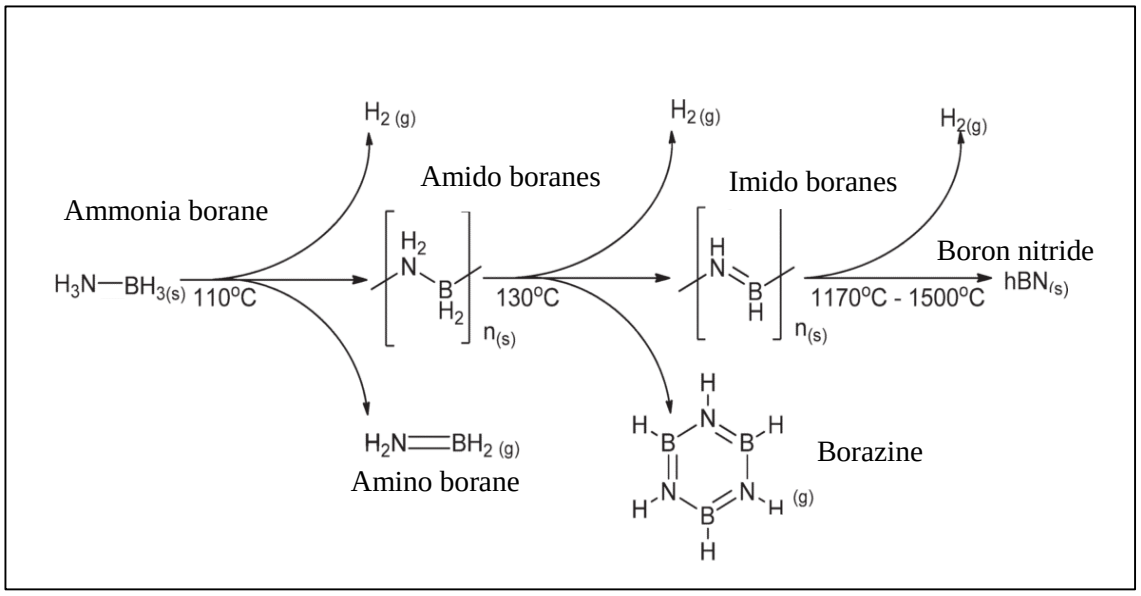

Figure 10: Thermolysis of ammonia borane determined experimentally by Frueh *et al.*; both cyclic and polymeric amido and imido boranes are produced [57] . Slow heating rates (<1°C min^{-1}) do not produce borazine, medium heating rates (3-10 °C min^{-1}) show borazine during the release of the second hydrogen equivalent and aggressive heating regimes (>10°C min^{-1}) produce even more cyclic by-products [59].

The melting point of ammonia borane ranges in the literature from 104.5°C [60] 105°C [61], through 110-112°C [62] and 112-114°C [36] to 112-117°C [55] and 121-124°C [63]. Most sources agree that the melting peak is somewhat broad and begins at around 90°C, a few degrees before the quoted value [60]. The melting is accompanied by the hydrogen release in step 1 which starts simultaneously [55], [57], [62]. As soon as the AB molecules gain some conformational freedom, the barrier to hydrogen release is significantly reduced and the reaction accelerates.

The activation energy to hydrogen release from AB is high owing to the dihydrogen bonding between molecules [54]. As with the melting temperature, a wide range of values for the strength of these bonds are reported: 125kJ/mol [54] 150 kJ/mol [64] and 47.02kJ/mol [65].

It has been proposed that the first step can be broken down into three substeps: nucleation, where AB softens and becomes mobile $BH_3NH_3{}^*$; induction, where the diammoniate of diborane, DADB, $[NH_2BH_2NH_2]^-[BH_4]^+$, forms; and growth, where AB and DADB react together releasing hydrogen [66].

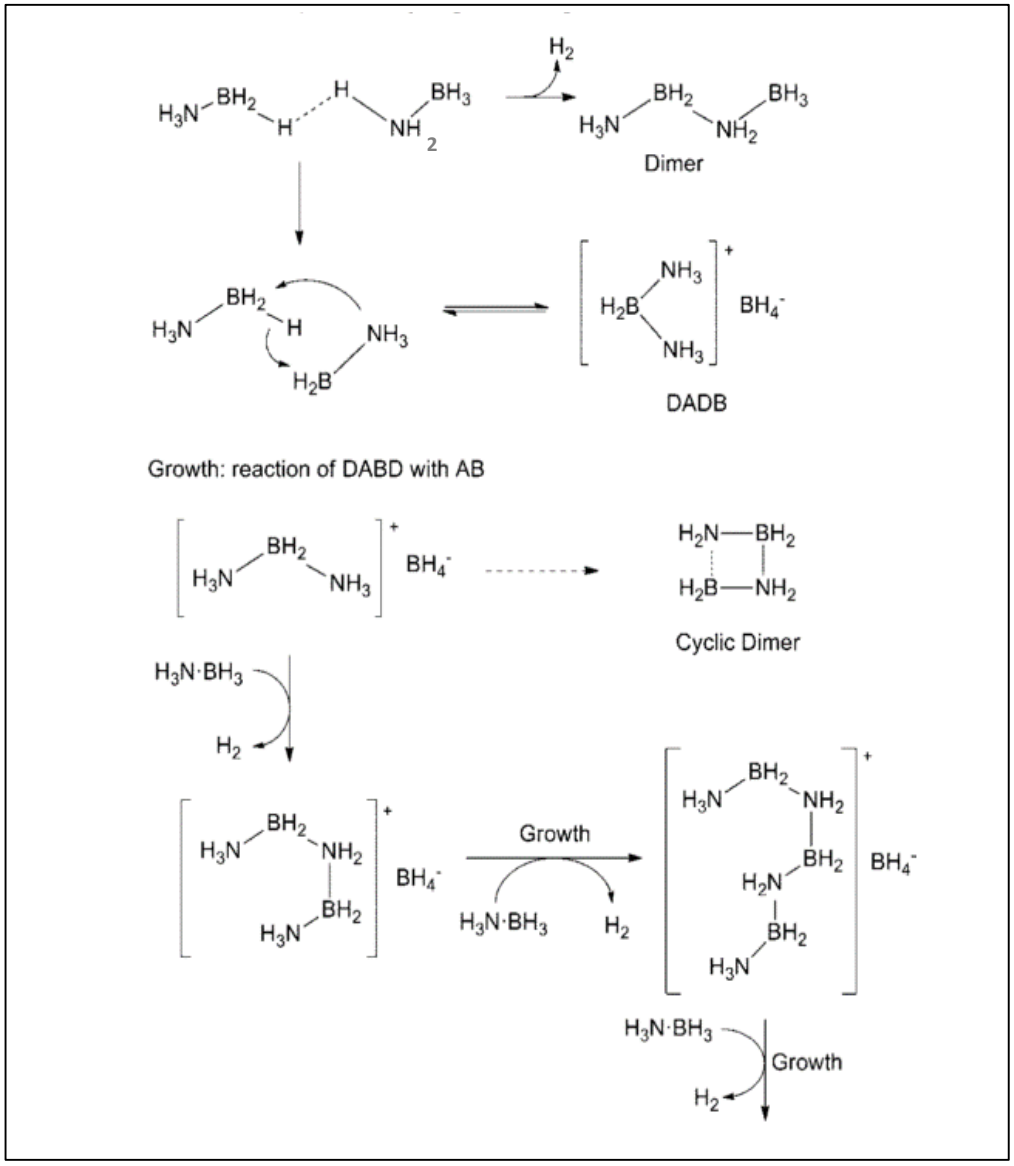

Figure 11: The themolysis reaction mechanism of AB (polymeric) proposed by Stowe *et al.* showing the induction, nucleation and growth phases [66].

One equivalent of hydrogen can also be released from AB while in the solid state – over several hours – by maintaining the temperature between 70-90°C [53], [54]. However, at these

temperatures the barrier to the formation of DADB is high and so an induction period of several hours precedes the hydrogen loss [56], [65], [67].

One of the more serious impediments to commercialising AB is the foaming that occurs during dehydrogenation [65], [68], [69]. As the hydrogen release occurs after melting, large stable bubbles form in the molten AB. The ensuing volume expansion can be in the range of several thousand percent, see Chapter 4.

2.2 Modifying the dehydration properties of ammonia borane – literature study

2.2.1 Ammonia borane in water

AB dissolves in water (pH=9.1) [70] to about 25wt% [55]. AB at 25wt% can decompose in water and release 9wt% H_2 via this reaction pathway.

$$BH_3NH_3 + 2H_2O \xrightarrow{catalyst} NH_4{}^+ + BO_2{}^- + 3H_2 \quad (11)$$

The AB-water solution is stable in an inert atmosphere but begins to release H_2 if left in air. In air the water becomes acidified by absorbing CO_2 (to form carbonic acid) which catalyses the hydrogen release [71]. Hydrolysis of AB is energetically favourable due to the formation of strong B-O bonds and occurs at roughly 100 times the rate of AB thermolysis [55]. The rate of hydrogen release only reaches acceptable levels if catalysts such as acids or transition metals are used [72]–[76].

The hydrolysis of AB has several advantages over the thermolysis of AB. Once dissolved in water the AB can be flowed making the material easier to handle and the dehydrogenation easier to control. Additionally the AB reaction products are insoluble in water and therefore can be separated from the still unreacted AB. However, due to the weight of water, hydrolysis of AB is unlikely to meet the DOE system weight requirements for on-board hydrogen storage.

2.2.2 Ammonia borane in alternative solvents

AB is soluble in various other polar solvents, many of which are shown to improve the AB reaction kinetics and thermodynamics. Ethers such as glyme, diglyme, tetraglyme, THF and 2-methyl THF have been particularly well studied [77]–[80]. In ethereal solvents AB decomposes via the two-step mechanism. However, instead of producing polymeric PAB type species the hydrogen release leads to cyclic products such as cyclotriborazane and borazine [67], [79]. In fact, AB in diglyme (at 130°C) and tetraglyme is considered a suitable method for producing borazine with hydrogen as a side product [77].

$$3BH_3NH_3 \xrightarrow{\text{tetraglyme,150°C,3hours}} N_3B_3H_6 + 6H_2 \quad (12)$$

AB reacting in the presence of these solvents releases hydrogen at accelerated rates at lower temperatures. The lack of induction period has been linked to the early appearance of DADB, observed in NMR studies [78], [80]. Colquhoun *et al.* showed that hydrogen bonds formed between the $H_N^{\delta+}$ on the AB and the electron-donating oxygen on the ether [80], [81]. AB has been observed to react in acetonitrile to produce hydrogen and ethylamine-borane, C_2H_5-NH_2BH_3. [79].

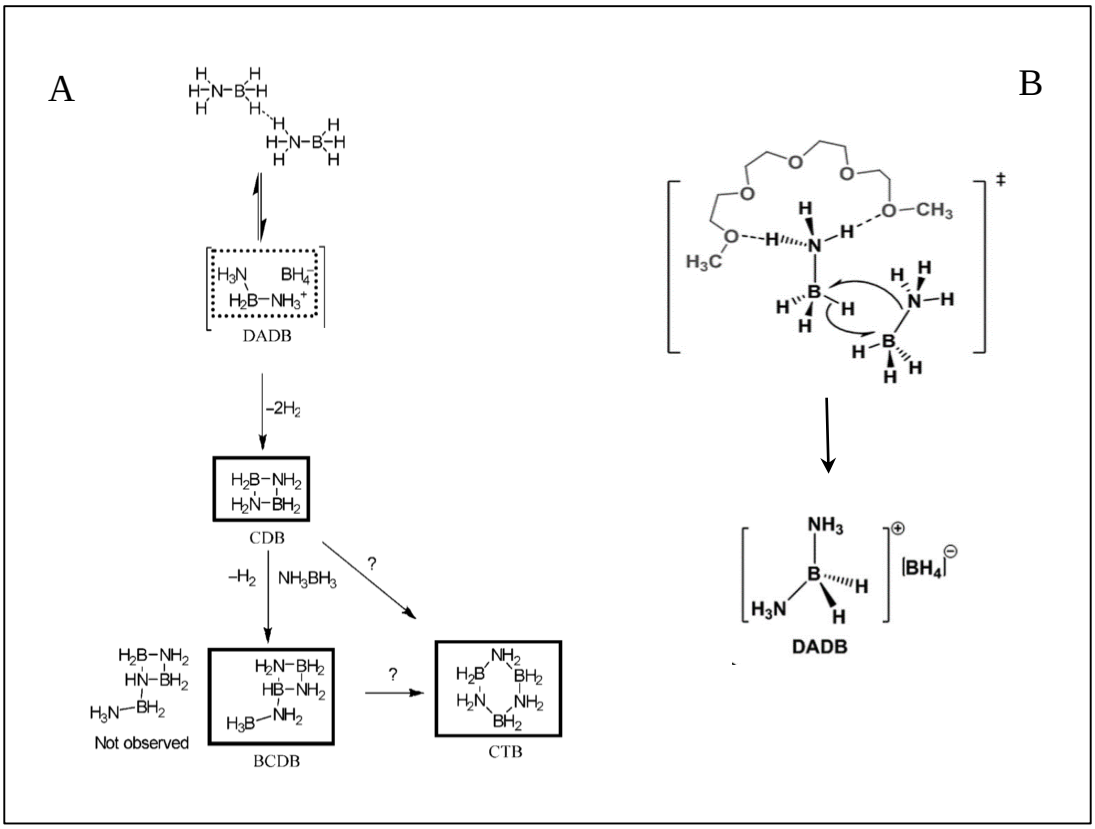

Figure 12: A) Decomposition pathway for AB in glyme suggested by Shaw *et al.* based on boron NMR experiments [78]. AB follows that cyclic reaction route. B) From Kim *et al.* showing how hydrogen bonding between AB and ether promotes formation of DADB [80].

2.2.3 Ammonia borane in ionic liquids

Ionic liquids have also been shown to have an accelerating effect on AB dehydrogenation while limiting the production of borazine [67], [82]. Wright *et al.* have written an excellent review on metal catalysed AB dehydrogenation in ionic liquids. Yields of greater than 2.2 equivalents of hydrogen can be achieved at increased rates compared to pristine AB [83]. The AB follows the polymeric reaction route and so the release of borazine is limited.

2.2.4 Ammonia borane in acidic conditions

Acidic conditions cause rapid hydrogen release from AB [48], [62]. The rate determining step in the reaction is the B-N bond cleavage [37], [84]. This is achieved by attack with the electrophilic H^+ which leads to NH_4^+.

Brønsted and Lewis acids were shown to encourage the breaking of the B-N bond [37]. Hydrogen release was enhanced but cyclic products were also generated.

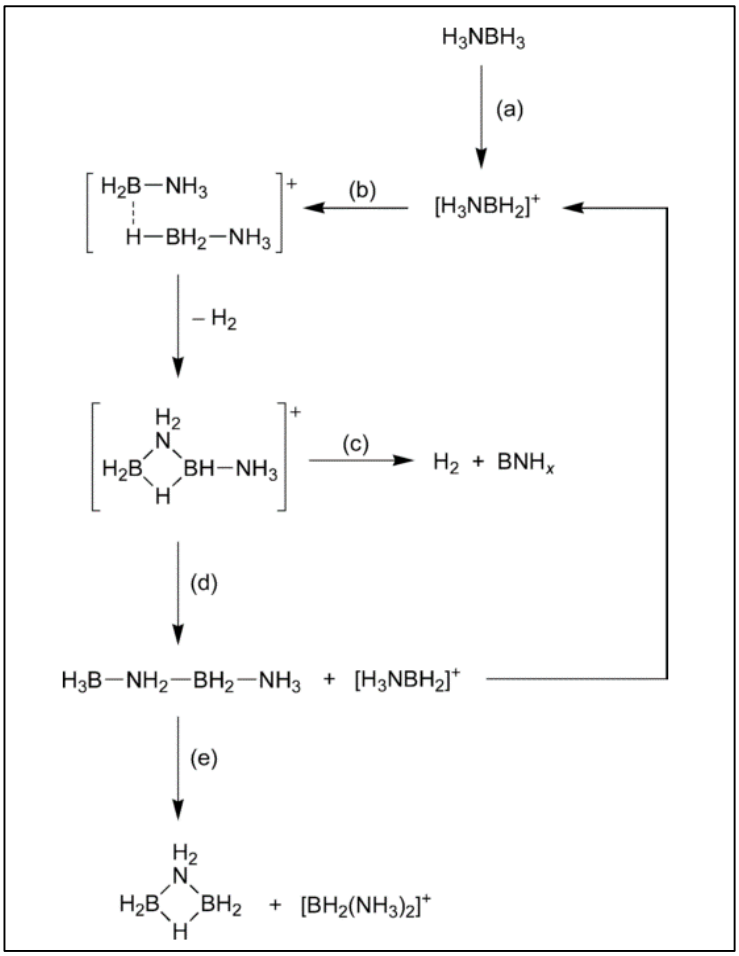

Figure 13: The mechanism of acid dehydrogenation of AB proposed Stephens *et al*. [37]. The acid abstracts a hydride (a) activating the boron to interact with a neighbouring AB molecule (b) forming an intermediate. Hydrogen loss follows and an intermediate with a bridging hydrogen is formed. If the acid to AB ratio is low dehydropolymerization ensues (c). However, if the ratio is high, a second reaction takes place (d) which catalyses the reaction further (e).

An interesting study that combined both catalysis and nanostructuring was conducted by Zhang *et al*. AB (20wt% only) was combined with silica nanospheres (coated with acidic hydroxyl groups) [85]. Earlier hydrogen release with supressed borazine and ammonia was observed. A similar effect was observed by Stephens *et al.* with their study on AB in hydroxyl-coated carbon cryogel [84]. Acid additives have a good tradition of encouraging improved dehydrogenation characteristics in AB.

2.2.5 Zeolites and metal organic frameworks

Zeolites are highly porous, low density, crystalline aluminosilicates, cheaply available and simple to synthesise. Zeolites provide an ideal hosting environment for various metal nanoclusters that can be used to catalyse AB. Examples include Pd, Rh, Ni and Co [65], [74]. While zeolites favourably improve the AB hydrolysis, often the overall the system weight is too high to meet the DOE targets [11].

Zeolite-X (containing caesium active sites) and Chabazite (casium substituted potassium) were ball-milled with AB, (ratio AB:zeolite 10:1) [86]. At low heating the zeolites reduced the induction period significantly and at high temperature they increased the amount of hydrogen released. Borazine levels were reduced but not eliminated.

2.2.6 Carbon

Carbon by itself is not active in the catalysis of ammonia borane. However activated or functionalised carbon can provide a combined nanoscaffold and catalysis environment [64], [84], [87].

AB loaded on a carbon cryogel (CC) released hydrogen faster than pristine AB at 85°C [87]. The increased dehydrogenation rate was attributed to defect sites, destabilisation of the AB hydrogen bonding network and the AB reacting with the hydroxyl coated surface (B-O bonds were formed). Borazine release was suppressed. The pore size of these AB-CC composites was found to be directly correlated to the temperature of the hydrogen release [64], [84]. The greater the surface area to volume ratio the faster the dehydrogenation.

Theoretical DFT studies have suggested the internal spacing of a carbon nanotube could provide the ideal environment to ameliorate the dehydrogenation of AB [88].

AB (30wt%) loaded on the graphene oxide released hydrogen at lower temperatures than pristine AB; additionally the complete suppression of impurities including borazine, ammonia and diborane was observed up to 200°C [89]. This material is particularly interesting as the AB could be regenerated in situ with hydrazine and ammonia, 75% and 61% of the original AB was recovered in the first and second cycles.

Nanostructured AB (50wt%) was incorporated into a mesoporous carbon framework studded with Li crystallites (5wt%) [90]. Hydrogen release was accelerated such that significant amounts could be achieved at 60 due to the confinement and catalysis due to Li. The gaseous impurities where also controlled.

2.2.7 Metal catalysts and ammonia borane

AB was combined with $CoCl_2$, $NiCl_2$ and $CuCl_2$ by mechanical mixing (metal content 15wt%). The Cu^{2+} ion was the most effective catalyst causing 2 equivalents of hydrogen to be released at 60°C without incubation time [91], [92]. Decomposition was shown to proceed via an alternative reaction route which includes the intermediate$[NH_4]^+[BCl_4]^-$:

$$NH_3BH_3 + 2CuCl_2 \longrightarrow [NH_4]^+[BCl_4]^- + H_2 + 2Cu(0) \quad (13)$$

This route does not include DADB and this is part of the reason no borazine is released.

$CoCl_2$ or $NiCl_2$ (2mol %) were coprecipitated with AB. The hydrogen release from this material was observed as low as 59°C. No borazine was released and there was no perceptible foaming [92].

Alkali metal hydrides have also been used to destabilise AB and improve its reaction kinetics. LiH and NaH were ball milled with AB to produce $LiNH_2BH_3$ and $NaNH_2BH_3$ [93], [94]. The complexes demonstrated improved reaction kinetics at low temperatures (<100°C), reduced foaming and limited borazine release. In other another study, AB was combined with $NaMgH_3$ by ball-milling in a ratio of 3 AB to 1 $NaMgH_3$. 10wt% H_2 was released from the mix in 2 minutes at 80°C, and the borazine presence in the released gas was reduced [95]. Recently, $Mg(NH_2BH_3)_2$ has been synthesised by ball-milling Mg and AB together. The resulting material could release ~10 wt% high purity hydrogen below 300°C [96].

Clearly metals are a highly efficient way of catalysing AB.

2.2.8 Ammonia borane in the presence of polymers

Poly(vinyl pyrrolidone) (PVP) was combined with AB via single phase electrospinning [97]. With a 20wt% AB content the hydrogen was released at lower temperatures as compared to pristine AB but the ammonia levels were increased. This necessitated the addition of $MgCl_2$ to mop up the released ammonia.

Polyacrylamide (PAM) with AB in a 1:1 ratio demonstrated a significant improvement in hydrogen release kinetics and thermodynamics. However, $ZnCl_2$ was required, as excess ammonia was evolved [98]. It was suggested that AB was interacting with the carbonyl group on the PAM at the AB-PAM interface to release hydrogen contaminated with ammonia, but that also bulk AB was releasing hydrogen in the traditional manner.

A similar effect was observed for AB confined with poly(methyl acrylate) (PMA) with AB:PMA ratios 8:10 and 2:10 [99]. In both cases hydrogen was released earlier than in the case of pristine

AB. The borazine level in the gas stream was reduced but the ammonia level increased. Boron to oxygen bonds were observed and found to be linked to the increased ammonia level.

Ammonia borane was successfully combined in polystyrene (PS) nanocavities by co-axial electrospinning. The dehydrogenation temperature of the AB was significantly reduced compared to pristine AB and some impurities were filtered out by the PS [100]. However, the foaming could not be controlled and the AB mass content was only around 30wt%.

2.3 Materials used and project aims

2.3.1 Polymers

2.3.1.1 Polyethylene oxide

The hydrogen release of AB is preceded by melting and conversion to DADB. The melting increases the conformational freedom of the molecule, reducing the energy barrier to dehydrogenation. The melting point of AB is 112-114°C [55], [58], but melting typically begins a few degrees lower. While AB can release hydrogen at low temperatures (<100°C) while in the solid phase [53], the process is slow and several hours are required to release 1 equiv. of H_2. If the melting point of AB could be lowered, rapid hydrogen release could occur at lower temperatures.

Polyethylene oxide (PEO) is a polymer with a low melting point (66-75°C) available in a large range of molecular weights, 10 - 10,000,000 (Figure 14: Schematic of the PEO monomer unit.Figure 14). PEO is cheap and non-toxic and is often used as a binder for medicines. The shorter chains are termed polyethylene glycol (PEG) and can occur in a liquid state as the melting point decreases with decreasing chain length [101]; the monomer, ethylene glycol $C_2H_4(OH)_2$, is a liquid under standard conditions. PEO is soluble in mostly polar solvents including water, acetonitrile, benzene, alcohols, chloroform, esters, cyclohexanone and N,N-dimethylacetamide [101].

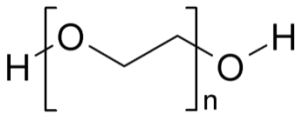

Figure 14: Schematic of the PEO monomer unit.

The PEO chains twist into helixes which can be arranged in a variety of crystal arrangements, the most thermodynamically stable of which is monoclinic with a=8.05, b=13.04, c=19.48Å and β= 125.4°.

A composite can defined as a homogenous material, composed of two or more heterogeneous substances where the final mix demonstrates superior properties to either of the constituent parts [102]. For example, the combination of calcium carbonate and collagen in bone provide both strength and flexibility and adding glass fibres to polystyrene gives it more load-bearing capability. The properties of polymer composites are often hard to predict; the polymer types and their interactions, the proportions, the mixing process and the level of crystallinity are some of the many parameters to consider. However, it is still possible to tailor the resulting properties of the blend to provide the flexibility, radiation resistance, transparency, melting point etc. that is required. PEO has a melting point of 66-75°C [103]. If correctly mixed with AB it could bring the melting point of AB down and activate the hydrogen release at lower temperatures.

Nanostructuring AB has been shown to aid dehydrogenation; graphite [89], silicone glass [87] and polystyrene [100] scaffolds have all proved helpful. Electrospinning could be an ideal method to blend PEO and AB at the nano level making not only a composite with low melting point but an AB nanostructure as well.

The thermodynamic properties and structure of AB are defined by its ability to form dihydrogen and hydrogen bonds. The repeat unit of PEO is depicted in Figure 14; the lone pair of electrons on the oxygen is capable of forming hydrogen bonds. The polar nature of both AB and PEO will facilitate their intimate mixing via electrospinning. We expect also to form hydrogen bonds between the AB and PEO.

2.3.1.2 Polystyrene

The dehydrogenation kinetics and thermodynamics of AB can be favourably modified not only by chemical catalysis [104] but by nanostructuring [84], [100], [105]. As particles get smaller, the diffusion distances shorten and this can lead to faster reaction kinetics. Also, surface energy changes can arise which alter the thermodynamic stability of the material enabling the hydrogen release to follow a different, lower energy, reaction route [106].

In particular, nanostructuring AB in coaxially electrospun polystyrene (PS) fibres has reduced the reaction temperature 15-20ºC [100]. Kurban *et al.* tuned the miscibility, conductivity and viscosity of the core (internal, containing AB) and shell (external, containing PS) solutions to allow mixing during spinning to produce highly porous fibres. The encapsulated AB demonstrated properties suggesting a nanostructured state. However, the maximum AB content achieved in the fibres that showed a significant reduction in the hydrogen release temperature was only 30wt%. Furthermore, the mass loss during reaction indicated that AB sublimed and foamed.

In chapter 4, the reaction kinetics and thermodynamics of AB are improved by combining with PEO. Additionally it suppresses foaming, but it encourages impurities such as borazine. An

improvement on this system should further limit foaming and also cut down the impurities. Being unable to accurately determine the particle size of AB in the AB-PEO composites, it is possible that the diminished activation energy is at least partly due to nanostructuring in the AB. It would therefore be useful and interesting to isolate and investigate the behaviour of nanosize particles of AB in a polymer.

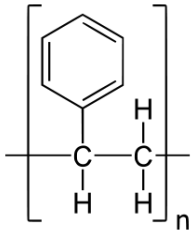

Figure 15: Schematic of the PS monomer unit.

PS is ideal polymer to use as a nanoscaffold. It has a high glass transition temperature, 100 ºC, and melting point, 240 ºC, so will remain solid as the AB reacts. There are no active functional groups so the effect should be purely physical. PS is a very well-understood material and has been electrospun extensively in the past [107]. In order to build on the previous work of Kurban *et al.* I will use single phase electrospinning. Single phase electrospinning is simpler then coaxial as there are fewer parameters to regulate and should allow a higher amount of AB to be incorporated in the fibres. To this end I will require a solvent that can dissolve both polar (AB) and nonpolar (PS). I wish to employ the repulsion between the polar and nonpolar entities to divide the AB and PS into discrete, hopefully nanostructured, areas.

This part of my thesis considers the unusual practice of electrospinning polar and nonpolar materials in a single phase. The spinning parameters necessary to produce AB-PS fibres will be explored and the material properties − hydrogen release temperature, impurity content in the gas stream, and foaming − can be studied and compared to pure AB.

2.3.2 Clays

The hydrogen release of AB has been promoted by being combined with PEO. The temperature of the onset of hydrogen liberation has been reduced and the foaming and expansion limited by the PEO. However, the proportion of the impurity borazine has increased in the gas stream. These effects are due in part to the physical behaviour of the polymer and in part to the nature of the functional group, the ethyl group.

Previous work has shown that an alternative functional group, the hydroxyl, can positively influence the dehydrogenation of AB. Materials tested include mannitol [108], hydroxyl-coated graphene oxide [89], carbon cryogel [87] and silica nanospheres [85]. In all cases the temperature

for the onset of hydrogen release was reduced and borazine was eradicated from the gas stream. These studies were particularly successful as in all cases the AB was also nanoconfined, something that was not achieved in the PEO-AB.

Clays are layered hydrous aluminosilicates covered with hydroxyls [109]. Sheets of tetragonally-coordinated silicon are layered with octahedrally-coordinated aluminium terminated with hydrogens that give the surface its acidic nature. The layers are separated by adsorbed water and the layers can slide over each other giving clay its plastic, malleable character. Variety is achieved as the aluminium can be substituted by iron and magnesium. Alkali and alkaline-earth metal cations are also found in the interlayer space. Clays are cheap, abundantly available, non-toxic and environmentally benign.

If AB was confined in the interlayer space, nano-structured AB could be attained in close proximity to catalytic hydroxyl groups.

2.3.2.1 Smectite clays, laponite and montmorillonite

Smectite clays are layered and each layer consists of two sheets of octahedrally-coordinated aluminium oxide on either side of a tetragonal silicate sheet [109]. Substitutions in the Al and Si sites create charge imbalances which are stabilised by Na and Ca counterions between the layers. Smectites are swelling clays and the layers are expandable by water, which is pulled in to hydrate the counterions. The interlayer separation means that the layer stacking is fairly disordered. Heating dehydrates the interlayer space, but the process is reversible and the clay can be rehydrated. Other polar liquids and salts can be intercalated into the layers.

Two smectites were tested: montmorillonite, a natural clay found in sedimentary rocks, and laponite [110], a synthetic smectite clay where the octahedrally-coordinated silicon has been completely replaced by magnesium. The counterion in the montmorillonite used was sodium and, in laponite, sodium and a small amount of lithium are present. In laponite the layers huddle together to form nanometre-sized disks, about 25 times wider than they are high. When hydrated, the counter ions are liberated which results in negatively-charged OH^- groups on the disk surface, while at the rim positive charges congregate. Laponite dissolves readily in water and forms gels at low concentration with a pH level of 10.

The empirical formula of montmorillonite is $Na_{0.3}Al_2Si_4O_{10}(OH)_2(H_2O)_{10}$ and for laponite it is $Na^{+0.7}[(Si_8Mg_{5.5}Li_{0.3})O_8(OH)_4]^{-0.7}$.

Smectites could improve the dehydrogenation properties of AB. AB in the interlayer spacing would be nano-confined and within reach of catalytically active hydroxyl groups.

Sodium montmorillonite SWy-1 from Wyoming, Crook County, USA and laponite RD sourced from Rockwood Additives Limited were both used as received.

2.3.2.2 Tubular clays, imogolite and halloysite

Imogolite is a tubular clay of the general formula $(OH)_3Al_2O_3SiOH$ [111] found in volcanic ash [111], [112]. It is formed of a gibbsite $Al(OH)_3$ sheet coupled on one side to a tetrahedrally-coordinated silicon oxide layer [113]. The Si−O bonds are shorter than Al−O bonds, the sheet curls into a tube displaying the gibbsite (AlOH) on the external surface and the siloxane (SiOH) on the inside. Both surfaces are positively charged, the intra-wall oxygen carries the balancing negative charge [113]. The hydroxyl groups are both acidic but as the Si-OH bonds are more ionic then the corresponding Al-OH bonds and should therefore be more active.

The imogolite used is synthetic, sourced industrially from Kodak. The tubes are approximately 100nm in length with an external diameter of around 20Å and an internal diameter of 10Å [114]. The tubes collect into bundles, with a repeat centre to centre separation distance of 23Å for natural imogolite [114] or 28Å in the synthetic case [111].

Hydrophilic behaviour occurs on both internal and external surfaces [113]. Water uptake occurs inside the tubes and in the vacant spaces between tubes [113]. As the water level increases the individual tubes become solvated and the bundles separate. The tubes gain motional freedom and can loss their circular diameter becoming elliptical [111]. Imogolite water mixes have a gel phase at low imogolite concentration.

Imogolite is both biocompatible and environmentally benign [115]. The small size of the tubes provides a very high surface area per unit mass. Through freeze drying with AB it should be possible to exploit the imogolite active external surface to catalyse hydrogen release from AB. The hydrated ammonia borane will likely be too large to enter the tubes with the water molecules, so the AB will only be exposed to the gibbsite external surface. It would be interesting to study also the effect of the siloxane surface on AB and to make a comparison to the gibbsite. For this halloysite clay nanotubes would be ideal.

Halloysite is a naturally occurring kaolinite clay found around the world in various soils but particularly in volcanic areas [109]. A layer of SiO_4 tetrahedra is bonded to a gibbsite like layer, out of every three sites, only two are filled by Al to give a final composition of $Al_2Si_2O_5(OH)_4$. The layers are separated by a single disordered layer of water to a distance of 10Å. While it can take many shapes, the Al vacancies cause the layers to curl up into spiral tubes to form the most common morphology, multi-walled tubes. Contrary to the imogolite, the halloysite tubes keep the siloxanes on the external surface leaving the gibbsite layer on the interior of the tube.

The internal layer spacing in halloysite is suitable for the intercalation of salts and organic compounds. Complexes can be achieved if the intercalant is polar [116]. Aqueous soluble salts can be intercalated into hydrated halloysite to form monolayers between the layers. If the water has been dried off, the interlayer spacing will not be amenable to rehydration or other liquids. At pH 6-7, the halloysite SiO_2 surface has a negative charge while the Al_2O_3 interior surface is positive [117].

It should be possible to load AB into and around the halloysite nanotubes using water as a carrier. Freeze drying the mixture will create an AB halloysite composite. The halloysite might improve the dehydrogenation properties of AB either as a nanoscaffold or through the catalytic nature of the hydroxyl groups.

Halloysite nanoclay was obtained from Sigma Aldrich and used as received.

2.4 Graphite intercalation compounds

Here a study of the motion of ammonia inside a calcium ammonia (Ca-NH_3) graphite intercalation compound (GIC) is presented. Calcium and ammonia are highly compatible; calcium readily dissolves in ammonia to make a highly-structured octahedrally-coordinated 3-dimensional liquid, $Ca(NH_3)_6$. In a GIC, however, the confinement in graphite restricts the vertical dimension and only allows a maximum of four ammonia to approach each metal centre [26], [34], [118], [119]. In this way the 3-dimensional solution is constrained into a 2-dimensional analogue. Here the motions of the ammonia in a Ca GIC will be studied. The motions of confined ammonia can then be compared to previous studies of the unhindered liquid $Ca(NH_3)_6$ and other metal ammonia GICs [120].

Previous studies on ammonia in similar materials have shown rotational modes at low temperatures which develop into diffusion on heating. In $Ca(NH_3)_6$ [120] and in $KC_{24}(NH_3)_{4.3}$, the potassium analogue of the material here studied, [121]–[123] the onset of movement at ~50K is the rotation of the hydrogen atoms about the fixed metal to nitrogen axis. Above between 100 and 200K a second rotational mode occurs in both complexes: in $Ca(NH_3)_6$ the whole group is slowly reoriented about the centre of mass [120], while in $KC_{24}(NH_3)_{4.3}$ the ammonia molecules wheel around the potassium centre [121]–[123]. High temperature studies of $Ca(NH_3)_6$ have not been published but for $KC_{24}(NH_3)_{4.3}$ raising the temperature to 300K increases the energy of the rotation and translational diffusion at $10^{-5}cm^2s^{-1}$ becomes apparent.

The final chapter of this thesis reports on studies of the translational and rotational motions of Ca-NH_3-GIC; a temperature dependent study has not at the time of writing been performed on this material. Time of flight neutron spectroscopy was used to follow the changes in the behaviour of

the ammonia at 50K intervals between 300K and 2K. The large incoherent scattering cross section of the proton was employed to follow the movement of the ammonia as it dominates the measured signal. We show that the diffusion at the higher temperature switches to a rotational mode at 200K which fades below 150K. Further we show that NH_3 cannot be completely deintercalated.

3 Experimental methods

3.1 Making samples

3.1.1 Electrospinning

Electrospinning is a powerful technique for the production of micro and nano sized material structures, usually long filaments, beads or beaded fibres [107]. The method is a highly versatile and controllable; the composition, shape and architecture are down to the inventiveness and skill of the technician. A one-step process, electrospinning is practically scalable for high volume production of fibres with a wide range of industrial uses. Nonwoven fibrous meshes suitable for wound dressing, air filtration or composite reinforcement have all been produced. More complex arrangements have encapsulated drugs, anti-cancer and antibiotics, into the fibres for controlled release [124], or carbon nanoparticles for battery anodes [125], and also hollow microspheres for containing proteins [126].

The base component of the solution used in electrospinning is polymeric; the polymers provide the necessary viscosity and entanglement to produce long continuous fibres [107]. In a traditional electrospinning setup, the solution is passed at a constant rate of flow, say 1 $mlhr^{-1}$, through a suspended hollow needle attached to a voltage supply. A droplet appears at the nozzle and becomes infused with charge; this potential can eventually overcome the surface tension and provoke a jet that moves towards to an earthed, or oppositely charged collection plate. As the jet extends, instabilities cause it to bend and whip around in a spiral motion, this serves to stretch and lengthen the polymer chains within the strand as it descends. The fibres or beads pile up and stick together to form a mat. The solution composition defines the integrity of the jet, and the morphology, beaded or fibrous, of the final product.

Non polymeric compounds can also be processed via electrospinning either solely or incorporated with polymers. This is useful for developing composites with unique properties and functionality such as fluorescence, conductivity or increased heat resistance. The simplest method is to make and electrospin a single solution containing all the necessary ingredients, however the final fibre will be limited to a single mixed state and a co-solvent for all the additives may not be available. To create more interesting architectures concentric needles for distinct solutions can be used. Coaxial electrospinning [107][100] allows two initially separate solutions to interact during the descent and produce a variety of structures. Electrospinning was found to be a most suitable technique to make closely mixed AB polymer composites.

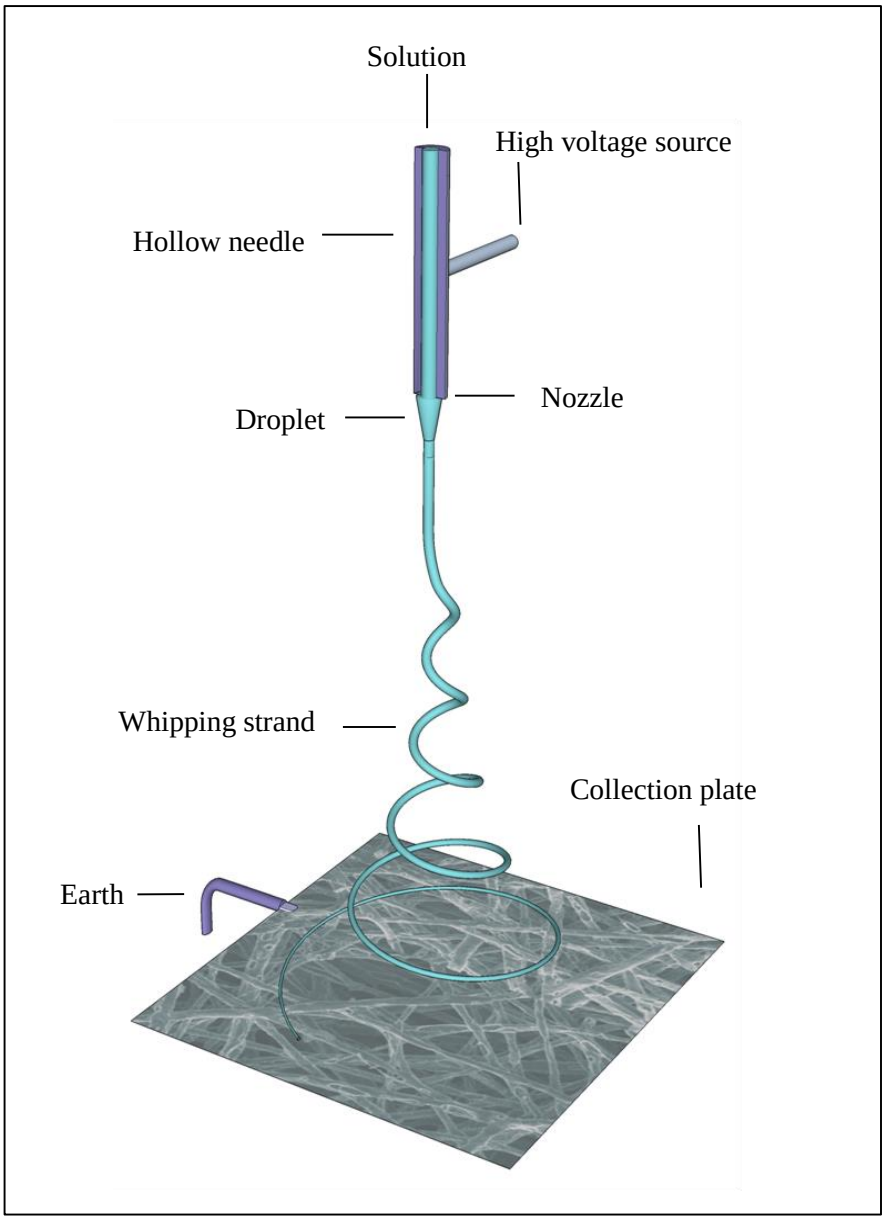

Figure 16: Single phase electrospinning rig.

There are both solution and apparatus parameters that need to be optimised to achieve the desired product. The first step is to choose the polymer and to dissolve it in a suitable solvent. The solution must be viscous and conducting. The flow rate must be set and the voltage and needle to collector distance adjusted to ensure the fibres have time to dry before they are laid down on the collector.

3.1.1.1 Solution parameters

A polymer is a chain of covalently linked, repeating monomer units, it is characterised by the monomer chemistry and the chain length, M_i. As the chain length increases the polymer glass transition and melting point will rise and it will become harder to dissolve [103], [127]. In a polymer sample there will always be a distribution of molecular weights; so usually an average

value is quoted, either the number average molecular weight, M_n, or the weight average molecular weight, M_w.

$$M_n = \frac{\sum N_i M_i}{\sum N_i} \text{ and } M_w = \frac{\sum N_i {M_i}^2}{\sum N_i M_i} \quad (14)$$

where N_i is the number of chains of molecular weight M_i. The polydispersity of a polymer sample, $P = M_n/M_w$, is influenced by the polymerisation method; free radical polymerisation will give a large P while condensation polymerisation gives a small P [128]. For electrospinning fibres, long polymer chains are desired to maintain the integrity of the jet on the other hand, making beads requires short chain polymers that allow the jet to segment [129]–[131]. Low polydispersity is preferred in both cases as it increases the quality and homogeneousness of the fibres or beads [132].

3.1.1.2 Solvent

A polymer dissolves in stages; the solid mass softens and swells before the chains peel off into the solution [127]. Areas of crystallinity are tough to dissolve as the tight packing of the polymer chains makes it difficult for the solvent to permeate. Dissolving is energetically favourable because the entropy or disorder, ΔS, of the system increases. Raising the temperature will make dissolving more energy favourable as quantified via the Gibbs equation for free energy,

$$\Delta G = \Delta H - T\Delta S \quad (15)$$

where, ΔG is the Gibbs free energy and ΔH is the enthalpy of the mixing. The chance of forming a mixed solution increases as ΔG becomes more negative i.e. the smaller the change in ΔH the more likely the polymer is to dissolve. ΔH is determined from the solubility parameters, δ, and partial volume fractions, ν, of the constituent polymer and solvent, respectively subscripts S and P.

$$\Delta H = v_S v_P (\delta_S - \delta_P)^2 \quad (16)$$

The smallest ΔH is obtained when the solubility parameters of the polymer and solvent are most similar, in other words, like dissolves like [127].

The solubility parameters are actually a description of the disruption of the cohesive energy; molecules in a material are tied together by dint of their cohesive energy, E_{coh}. The cohesive energy itself can be broken down to its contributions of the polar, dispersive and hydrogen bonding energies in the material, E_p , E_d and E_h respectively

$$\delta = \sqrt{\frac{E_{coh}}{v_m}} = \sqrt{\frac{E_p + E_d + E_h}{v_m}} \quad (17)$$

where, v_m, is the volume of the material. The solubility parameter can also be deconvoluted into its polar, δ_p, dispersive, δ_d, and hydrogen bonding, δ_h, parts.

$$\delta^2 = {\delta_d}^2 + {\delta_p}^2 + {\delta_h}^2 \quad (18)$$

Like dissolves like can now be practically exploited; for example high polarity solvents are suitable for high polarity polymers while non-polar solvents dissolve non-polar polymers.

In addition to being a good solvent for the polymer in question, the solvent must carry the charge, vaporise rapidly to ensure the fibres are dry at the collection plate and provide surface tension.

3.1.1.3 Electrical conductivity

Conductivity, C, is a measure of the current density, J, that can be induced by an electric field, E.

$$C = \frac{J}{E} = \frac{pv_c}{E} \quad (19)$$

where p is the charge per unit volume and v is the drift velocity of the charge. Electrospinning is dependent on the conductivity in the solution which carries the charge, which overcomes the surface tension, to the extremities of the droplet. The current is carried by ions or whole molecules as the electrons in liquids are usually confined to their respective molecules.

As the conductivity or dielectric constant of the solution increases it becomes more sensitive to the electric field [133]. Electrospinning will begin at lower voltages and instabilities on the droplet leading to multiple jets are more likely to occur [134], [135]. With more effective stretching forces on the jet, the incidence of beading will decrease [135], and the fibres will become finer and more uniform [131], [136]. A minimum amount of conducting species are necessary in the mixture [107] as solutions with zero or low conductivity will pour or drop from the nozzle without spinning [135]. The dielectric response (or permittivity), ε, of the solution to the field must also be considered as static charge build up can initiate an electrospinning jet. An electric field incites a polarity, P, in the molecules, which further orientate themselves to oppose the field. The level of reaction to the field is determined,

$$E = \varepsilon_o E_l + P = \varepsilon_o \varepsilon E_l \quad (20)$$

where the field, ε_o, the permittivity of free space, and the resulting field within the liquid, E.

Of the solvents used in electrospinning, most have very low conductivity (10^{-3} to 10^{-9} ohm m^{-1}) as there are very few ions available to carry charge [107]. Additives can be used to increase the conductivity of the solution and these include solvents such as DMF or water [137], or non-interacting species such as mineral salts, mineral acids, carboxylic acids or tetraalkylammoniaum salts [107]. The conductivity of the solution is directly proportional to the amount of salt added [135]. The type (size) of the charge carries affects how easily the charge can be distributed in the electrospinning process and this affects the produced fibre, smaller diameters resulting from the addition of higher density charge carriers [138]. The affect is also noted in coaxial spinning set-ups [136].

Significantly, the applied charge can be positive, negative or alternating [107]. A negative charge has been shown to give a lower diameter distribution in the fibres as it is easier to dissipate negative electrons then positive ions.

3.1.1.4 Volatility

It is important to control and balance the evaporation of the solvent during electrospinning [107]. The evaporation should be fast to prevent the deposition of wet fibres, but excessive drying should be avoided as this can lead to solidification at the nozzle and tube blockage. The fibre diameter can be controlled by the volatility of the solvent; the longer the whipping jet remains fluid, the further it can stretch and the thinner the resultant fibres will be. The rate of vaporisation from the jet is down to the vapour pressure of the solvent. The vapour pressure, P_{vap}, can be determined from the Clausius-Clapeyron equation and is related directly boiling point, T_B, and heat of vaporisation, ΔH_{vap}, of the solvent.

$$P_{vap} = exp\left[-\frac{\Delta H_{vap}}{R}\left(\frac{1}{T_B} - \frac{1}{T_o}\right)\right] P_{atm} \quad (21)$$

The vapour pressure increases with the actual temperature, T_o, and decreases with a lower atmospheric pressure, P_{atm}.

Table 7: Solvents used in practical work, boiling point and vapour pressure.

Solvent	Boiling point, °C	Vapour pressure mmHg at 20 °C
Water	100	17.5
Ethanol	78.37	44.6
Acetonitrile	81-82	72.8
Dimethyl sulphoxide	189	0.42
Tetrahydrofuran	65-67	143
Dimethyl formamide	153	2.7

If moist fibres are being produced, raising the temperature around the jet can accelerate drying. Conversely, if excess drying of the droplet is occurring, a gas jacket containing the spinning solvent, can be used around the nozzle to suppress the rate of evaporation [139], [140]. Another feature of a using a highly volatile solvent in electrospinning is the fabrication of flat fibres; when the solvent near the surface evaporates and a hard crust forms. This later collapses into the space vacated as the interior liquid evaporates.

3.1.1.5 Viscosity

The viscosity, η, of a solution is the strain rate, $\dot{\gamma}$, under a particular stress, τ; $\eta = \tau/\dot{\gamma}$ [141], [142]. Polymer solutions are naturally viscous as the entangled chains are difficult to displace. A viscous polymer solution is best achieved with a high concentration of long, branched, well solvated and unfurled polymer chains.

The polymer concentration affects the viscosity according to this power law,

$$\eta \propto {C_\eta}^{\beta} \quad (22)$$

where C_η is the polymer concentration and β is a constant dependent on the solvent polymer mix [143] and the molecular weight, M_w, and the effective volume of the polymer chain, $(r^2)^{3/2}$ influence the viscosity.

$$\eta = \frac{K(r^2)^{3/2}}{M_w} \quad (23)$$

where K is the proportionality constant from the Flory equation for hydrodynamic volume and r is the polymer end to end distance [129].

Smooth unbroken fibres can only be achieved if the polymers in the solution can entangle during the spinning process [131], a minimum concentration C_e is defined as the minimum polymer concentration necessary to move away from a bead regime [144] and form connected fibres. Upper and lower limits on the allowed polymer concentration are determined by the chain length

and the interactions between the specific polymer and solvent chosen. As the chain length of the polymer and the level of branching increases, C_e may be achieved at lower concentrations.

The fibre diameter, d, is related to viscosity, $d \propto \eta^{\alpha}$ where α is a scaling component different for every solution. A thicker solution will create larger diameter fibres, but this is also limited as if the viscosity is raised too high the solution will become too thick to pass easily through the nozzle [107]. The higher the viscosity the higher the voltage needed to produce a jet at the nozzle and the smaller the deposition will become as the viscosity can counteract the bending instability forces on the jet. This will lead to fatter fibres.

Temperature affects viscosity by increasing the solubility of the polymer,

$$[\eta] = Be^{E_a/RT} \quad (24)$$

where, B is a constant, E_a is the activation energy for viscous flow, R is the gas constant and T the temperature. Usually increasing the temperature will reduce the viscosity by allowing the chains to reptate, but if the solvent is poor than at higher temperatures the polymer chain will unfurl and increase the intrinsic viscosity [107].

Polymer solutions undergo viscosity changes due to shear thinning. Shear thinning is significant in highly concentrated solutions such as those used in electrospinning. In the natural state the polymer chains are entangled. The viscosity changes under elongation depend on the rate of change of the solution stretch. At small strain rates the polymers can reptate (wiggle) under thermal fluctuations of the polymer chain and the system remains close to equilibrium. At high strain rates, the tubes (free volume the polymer migrates in) are aligned in the direction of the strain and the viscosity is reduced. At high strain rates the polymer chains inside the tubes are forced to stretch as the tubes become thinner and the viscosity increases again [142].

3.1.1.6 Surface tension

Surface tension arises due to an imbalance of forces on the molecules at the liquid vapour barrier on a liquid surface [129], [145]. The surface tension of the solution works to reduce the unit area per unit mass, in practice it causes water droplets to pull into a ball. If we want to alter the shape of a droplet away from its preferred spherical form we will be increasing the surface area and hence the energy of the liquid.

$$\xi = 0.3\frac{L}{N_A}\left(\frac{N_A\rho}{M_w}\right)^{2/3} \quad (25)$$

where the surface tension, ξ is related to the latent heat of vaporisation, L per mole, N_A , the molecular weight, M_w and the density, ρ.

In a polymer solution the surface tension is affected by the solvent type [137], [146], the polymer concentration, chain length, conformation and polymer solvent interactions [130], [147]. The stronger the intermolecular forces in the solvent the higher the surface tension; water with its hydrogen bonding has a higher surface tension than hexane that is governed only by dispersive forces [145]. The polymer end to end length, not only controls the viscosity but the surface tension as well; an elongated polymer with good solvent-to-polymer interactions will vastly increase the surface tension.

During electrospinning surface tension works to reduce the surface area while the stretching forces work to increase the surface area of the spinning jet [129]. The surface tension of the solution is closely related to the critical voltage of electrospinning, the minimum voltage that can force a jet from the droplet [137]. A high surface tension is useful when fabricating beads as it promotes faster jet division and moulds the fragments into spheres [126].

When electrospinning, it may often be desired to change the surface tension of the solution to ameliorate the fibre morphology. Utilising a different solvent or a solvent mix has been shown to affect the surface tension by more than 10% [137]. Varying the polymer concentration up or down will modify surface tension; switching the polymer type is also an option. Surfactants, alcohols and organic molecules with a polar end, may be added to a water-type liquid to reduce the surface tension while inorganic salts can strengthen the intermolecular forces [145].

3.1.2 Spinning parameters

3.1.2.1 Voltage

The voltage provides the surface charge on the jet and the electric field between the needle tip and the collector plate. Charge builds up in the droplet until it can overcome the surface tension at which point a jet shoots out and heads towards the grounded collector. The higher the voltage the faster the solution will be whipped away from the needle, accordingly to maintain a stable electrospinning system the voltage must be matched to the federate. If the voltage used is too high, multiple jets can be produced at the nozzle and if the voltage is too low, the excess solution will build up and drip on the collector. For each solution a minimum voltage is needed to distort the droplet into a Taylor cone, usually around 6kV. In flight, increasing the voltage has the effect first of extending the fibres to make them longer and thinner and then of decreasing the flight time to produce thicker fibres. The higher the voltage the thinner the fibres will be as they will have more stretching force. An AC voltage can be used to give more aligned fibres.

3.1.2.2 Distance

The greater the distance between the tip and collector, the longer the jet will spend in flight and the smaller the electric field strength will be. Potentially, thinner and thicker fibres can be produced on increasing the tip to collector distance depending on the solution properties. While the reduced electric field means far less stretching force i.e. thicker fibres, the jet elongation can be sustained for a greater time period i.e. thinner fibres. As the solvent must evaporate before the jet reaches the collector, a minimum distance is needed for successful electrospinning of each solution.

3.1.2.3 Flow rate

As the flow rate is increased, fatter fibres and then beaded fibres, can be produced. High flow rates are useful to raise productivity but must be supported by high voltage, solvent vapour pressure and sometimes large tip to collector distances to ensure the fibres are laid down dry.

3.1.2.4 Nozzle area

The small orifice allows a smaller droplet with a corresponding higher surface tension which necessitates using a higher voltage. This results in smoother thinner fibres. It has been observed that a smaller nozzle area results in less clogging.

3.1.2.5 Humidity

Electrospinning in a humid environment causes pores to form on the fibre surface. As the solvent vaporises, it cools the jet and water droplets can condense onto the surface. The pores grow in depth and size with humidity until a saturation point is reached. Also, rate of evaporation of the solvent is influenced by the humidity, the higher the humidity the slower the evaporation.

3.1.2.6 Temperature

Changes in temperature can affect the viscosity of the solution. If the polymer is dissolved in a poor solvent, the chains are usually tightly curled up; heating can boost the solvating power and unravel the chains allowing more overlap and entanglement that increases the viscosity. If however the solvent is good and the polymer is well dissolved, on warming, the resistance between chains will decrease, reducing the viscosity of the solution. The solvent vapour pressure increases with temperature, reducing the fibre drying time. At higher temperatures, spinning can be achieved with a higher voltage or shorter tip-to-collector distance.

3.1.2.7 Pressure

If the pressure is lowered below atmospheric level, the solution will be pulled out of the needle faster and faster and bubbling will begin to occur until it is impossible to electrospin.

3.1.2.8 Atmosphere

The effect on the jet will usually be the dependent on the behaviour of the atmosphere under electric field.

3.1.3 Freeze drying

Electrospinning is an effective way to combine AB and PEO in a well-mixed microstructure, but it is slow, 1ml/hr flow rate of a solution with 6wt% solid content will produce 0.06g/hr sample, and highly involved. Multi-nozzle electrospinning goes some way to increase the sample production rate but is more technologically challenging and expensive. In order to produce large amounts of sample quickly and cheaply while keeping the PEO and AB in the well mixed state they enjoy in solution, freeze-drying was investigated. Freeze-drying [148] is a method where the abundance of solvent can be evaporated while maintaining the solution structure and keeping the AB stable.

In a freeze dryer [148] the material or solution mix is frozen and the solvent sublimed off with a low vacuum. The freezing rate affects the water crystal size and the resultant particle size also, the slower the freezing rate the large the water crystallites can grow. The effective freezing time is influenced by the sample volume and the dish shape; the greater the radius from the sample core to surface, the slower the freezing will be. While heat can be extracted from all directions, water will only evaporate from the top of the sample and the further the water has to travel through the sample the slower the evaporation.

The solutions were produced as normal, dissolving the PEO before the AB, and then poured into a wide dish; a bigger surface area aids evaporation, and placed in a standard freezer at -5°C. Once frozen, for a minimum of 12 hours at -5°C, the sample was transferred to the freeze dryer. Each sample remained under vacuum for 48 hours.

Freeze drying is an ideal method to combine species soluble in water. Clay and AB composites were also formed in this way. 5wt% clay was added to an AB-water solution and frozen before the water was sublimed off. The clay content was kept constant and the amount of AB changed to achieve the various fractions desired.

3.1.4 Dry mixing

AB was ground in a pestle and mortar for 15 minutes. PEO as-produced powder was used without modification. The powdered AB and PEO were combined at the required ratio and mixed together with a spatula.

3.2 A vapour transport method for intercalation into graphite

A two zone vapour transport method for intercalating metals into graphite is well known [26]. The graphite is outgassed under vacuum to remove impurities before being connected to a second chamber in which the intercalant metal is liquefied. The metal vaporises, filling both chambers and because of the overpressure, intercalates into the graphite. The stage number n produced is related to the temperature difference between the graphite and metal containing chambers, the smaller the difference the smaller the stage obtained.

A development on this where the staging is not controlled is to submerse the graphite in the molten metal of the desired intercalant; a single zone transport method [33], [149]. The graphite, Madagascan flake, was outgassed to remove impurities before being transferred, while inside an argon glove box, to a stainless steel tube. The calcium was added, the tube sealed and the entire ensemble put into a furnace. The tube was held under vacuum (~1.0×10^{-7} mbar) at 465°C for 10 days during this time the calcium vaporises and intercalates into the galleries.

3.3 Analysing samples

3.3.1 Scanning electron microscopy

Scanning electron microscopy (SEM) was used analyse the microstructure of the samples [150], a Hitachi Tabletop Microscope TM-1000 enabled a quick first pass view of the sample and later, high resolution images were obtained with a FE-SEM Hitachi S4000 and Jeol JSM-6480LV. The samples were mounted on carbon tabs and platinum coated to prevent charge build up (note: no coating was required for the TM 1000). To observe the fibre cross-section, the fibres were sealed in adhesive tape that was then cut along the normal to the fibre length, while submerged in a liquid nitrogen bath to keep the fibres brittle.

Compared to traditional light microscope an SEM can create clearer images of greater magnification due to the smaller wavelength of the electrons.

Electrons are generated by thermionic emission from a filament, usually tungsten and the accelerated with a positive electrical field to 1-30keV. The electron beam is focussed with magnetic condenser lenses to a spot size of 1-10nm at the sample. A picture of the entire surface is obtained by the raster motion of the beam, across the sample, controlled by scanning coils responsible for the forward and back and the side to side movement.

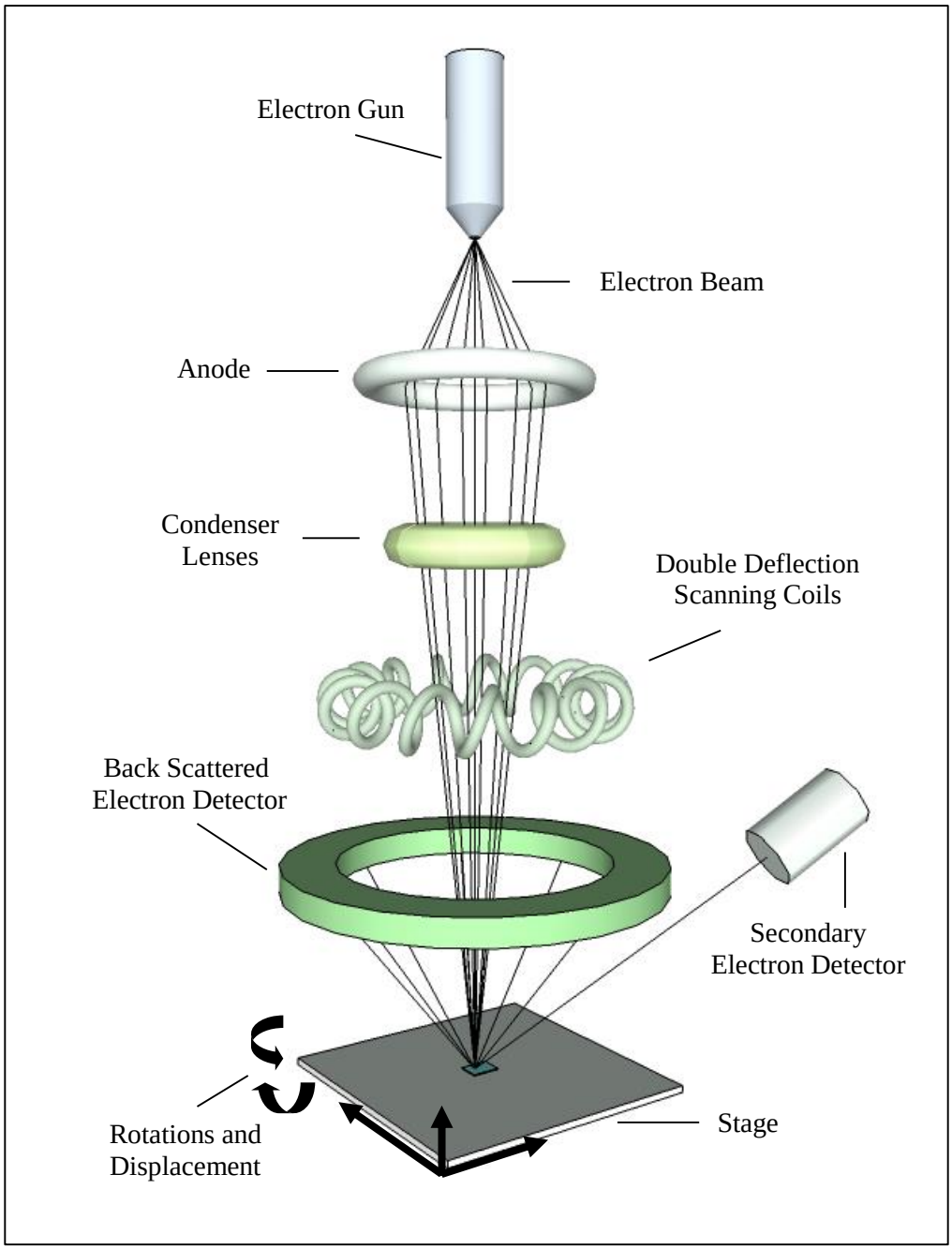

Figure 17: Schematic of a scanning electron microscope.

The electrons interact with a surface over an interaction volume; some rebound because of their high angle of incidence on the sample, others exchange energy leading to the release of secondary electrons and x-rays. Secondary and backscattered electrons are used to create an image of the surface, scan verses detection time make the picture three dimensional, while the x-rays can be studied to determine the elemental composition. A photomultiplier is used to enhance the electron signal.

3.3.2 Fourier transform infrared spectroscopy

Fourier transform infrared (FTIR) spectroscopy was performed on some of the samples to analyse the vibration states of the bonds [151]–[153]. A specific bond vibrational state, stretching, bending, twisting etc. can be excited to its excited state by absorbing IR radiation of the correct frequency. The frequency must match the energy difference between the ground and excited states. A sample is subjected to a spectrum of IR radiation and the position of the absorptions bands will indicate the energy of the motions inside the material. This allows bonds to be identified and helps elucidate the structure of the material.

An IR spectrum is usually collected over a wavenumber from 4000 to 400 cm^{-1}. Bond stretches (functional groups) are observed at the high wavenumber end of the spectrum. The low wavenumber section of the spectrum, from 1450cm^{-1} to 400 cm^{-1}, is known as the fingerprint region (every molecule has a distinct finger-print region pattern) and bending and twisting vibrations are found here.

A bond is infrared active if the vibration results in a net change in dipole moment and, as dipoles are vector additive, not all bonds give an IR signal. Carbon dioxide for example has IR active and inactive stretches; $\overrightarrow{C} = O = \overrightarrow{C}$ gives a signal but $\overleftarrow{C} = O = \overrightarrow{C}$ and $\overrightarrow{C} = O = \overleftarrow{C}$, where the dipole sum is zero, do not.

The position on the IR spectrum, $\bar{\nu}$, of a particular vibration can be defined by Hooke's law,

$$\bar{\nu} = \frac{1}{2\pi c}\sqrt{\frac{k}{\mu_r}} \qquad (26)$$

where, k is the force constant of the vibration and μ_r is the reduced mass of the of the atoms on either end of the bond. The reduced mas can be defined,

$$\mu_r = \frac{m_1 m_2}{m_1 + m_2} \qquad (27)$$

where, m_1 and m_2, are the masses of the atoms at either side of the bond. From this it is clear that the adsorption band moves to higher wavelength as the masses of the atoms increase and/or as the bond length decreases. The intensity of a particular vibrational band is principally due to the magnitude of the change in dipole that occurs.

Attenuated total reflection Fourier transform infrared (ATR-FTIR) data were collected in absorption mode from the post-heated materials at room temperature on a Bruker Optics Vertex 70 spectrometer with a 633 nm laser with 1cm^{-1} resolution. The peak positions were determined by fitting Gaussian curves to the spectrum.

3.3.3 Foam tests

The materials were heated in an oil bath at 120°C to determine the foaming characteristic. All foam tests were performed on pellets made in a small pellet press (see Figure 37). The initial mass, height and diameter of the pellets were measured with callipers and the volume and density calculated. After heating the pellets' mass and size were measured again. The volume and mass change due to the foaming could then be calculated for a particular pellet. If the pellet could not be removed intact, the diameter was taken as the internal diameter of the test tube. Residue on the inside of the tube wall was included in the final mass calculation and weight gain from the oil on the test tube was also taken into account. No correction was made for the rounded profile of the bottom of the test tube. The final height of the expanded pellet as measured with the callipers was subject to several mm of error so it was not worth correcting for the rounded bottom of the test tube.

Figure 18: AB containing pellets prepared for foam testing.

3.3.4 Thermogravimetric analysis and differential scanning calorimetry

Differential scanning calorimetry (DSC) is a thermoanalysis technique to study the phase changes in materials with respect to temperature [154]. The sample temperature is raised at a constant rate in a contained environment alongside a reference material and the difference in heat input, required to keep the sample and reference at the same temperature is recorded. This is an extremely useful technique for studying AB as melting events (endotherms) hydrogen release, (exotherms) and phase transitions can all be readily identified.

Thermogravimetric analysis (TGA) measures the mass changes that occur in a material during heating. It is an extremely useful accompaniment to DSC for understating changes that occurring during a reaction and is often part of the same instrument.

A combined DSC/TGA produced by Mettler Toledo (TGA/DSC 1) was used for analysing AB and the AB composites produced in this study (see Figure 19).

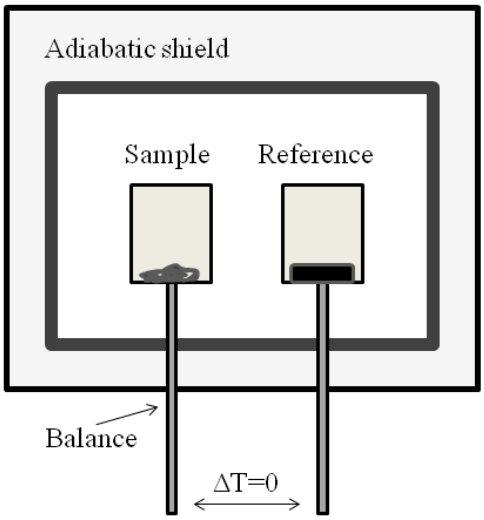

Figure 19: Schematic of a combined DSC/TGA instrument.

The effect of temperature on the samples was studied with both heat ramps (2°C min^{-1} between room temperature and 200°C) and isothermal heating steps (80°C, 100°C, 120°C and 150°C). Each sample was run three times to ensure the features observed are characteristic of the material in general and the trace that best represented each sample is displayed in the graphs.

3.3.4.1 Validity

The differential temperature measurement, the output form the DSC, is sensitive to the heating rate, sample size and shape and the gas flow rate [155]. Under ramp heating, a faster ramp rate will lower the peak resolution and push up the peak temperature. AB undergoes several heat induced changes (both exothermic and endothermic) below 200°C, therefore the ramp heating rate was set low (2°C min^{-1}) to ensure the peak features would be distinct. A larger sample will take longer to react and this will lower the peak resolution. This means that under a ramp heating, a larger sample will push the peak to higher temperatures while on an isothermal run, it will push the peak to later times. As far as possible the sample masses were kept constant, however due to the excessive foaming of AB and the small size of sample pans available, the mass of pristine AB was limited to 1mg. As the composites had reduced foaming and AB content, higher masses could be tested. For this reason caution should be taken when comparing the pristine AB and the composites. Unreliability also comes from are the sample packing in the crucible, if the sample is whole it will heat at a more consistent rate then if it is powdered. All the samples were squashed to the base of the pan to ensure good contact. However, variation in the initial compression and expansion during the test could change the sample connection to the crucible and still have an appreciable effect. The argon flow through the chamber affects the heat control and the buoyancy. As the DSC chamber heats so too does the gas inside i.e. argon. This means the argon density decreases and reduces the buoyancy making the sample appear to gain mass. Convection currents and the gas flow velocity can also impact the recorded mass and the heating of the sample.

The DSC and TGA signal from the pristine AB and the AB-PS material were both affected by a ramping baseline shift. The TGA data slopes upwards and displays a slight increase before mass loss begins significantly. The DAC data also slopes upwards and to enable clear interpretation of the graph features a background quadratic curve was subtracted.

3.3.5 Mass spectrometry

To understand the dehydrogenation process of the AB composites, a mass spectrometer (mass spec) was used to analyse the residual gases released during the decomposition of pristine AB and the AB composites (see Figure 20). A quadruple residual gas analyser (RGA) (MKS Cirrus 2 Atmospheric pressure RGA) was connected to the out flow of the combined TGA/DSC.

A quadrupole mass analyser (QMS) works like a standard mass spec but instead of separating the ions with a bending magnetic field the ions are filtered through a changing magnetic environment [156]. Four conducting rods are arranged in parallel and a varying current applied to allow specified mass/charge (m/z) particles to pass through to the detectors.

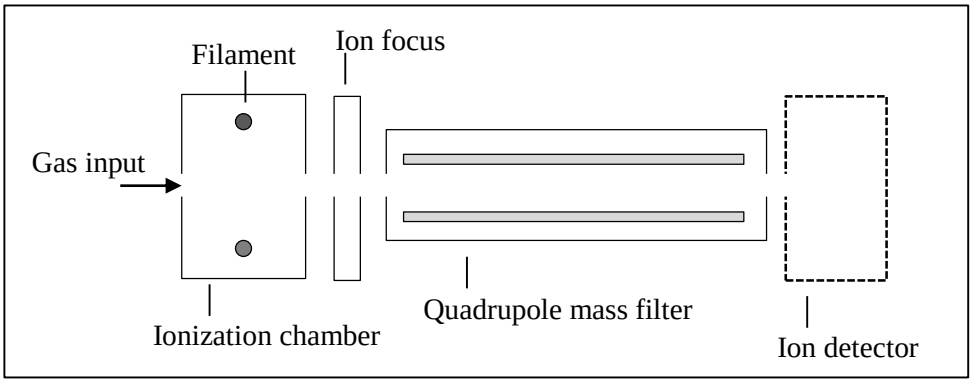

Figure 20: Schematic of a residual gas analyser (mass spec).

A vacuum is established in the mass spec. As the sample is heated in the DSC a steady stream of argon is introduced to the sample chamber to transport the gaseous products into the mass spec. Once inside a filament ionises the gas cloud by stripping away electrons, creating a plasma of charged particles. Often molecules will be destroyed in the process and it is common also to observe the fragments. The cloud is funnelled via the QMS into the ion detectors.

Table 8. The mass number assignment of the ionised species observed in the mass spec.

Mass Number m/z	2	17	18	27	32	36	81
Assignment	H_2^+	OH^+, NH_3^+	H_2O^+	$B_2H_6^+$, BNH_x^+	$NH_3BH_3^+$	Ar^+	$B_3N_3H_6^+$

The mass spec analysers can detect species of mass to charge ratio from 1 to over 100. I have chosen to consider the classic gaseous products and impurities released on heating AB, hydrogen (m/z = 2), ammonia (m/z = 17), diborane (m/z = 27) and borazine (m/z = 81). And to ensure no unreached AB is thrown off the material the AB (m/z = 32) has been observed. As water is also a known fuel cell contaminant and AB is known to be hydroscopic, the water signal water (m/z = 18) has also been monitored. In addition the argon (m/z = 36) carrier gas flow level has been followed as it will affect the partial pressure of the ionised reaction products and therefore the intensity of the data readings. Finally, the list here is far from conclusive as only a few mass numbers from the whole possible range have been observed; furthermore each detected mass number can represent a variety of different ions, for example m/z = 17 can represent ammonia or a hydroxyl [53]

The data presented has been processed from its initial raw form to clarify the important features and give fair consideration to the errors. Each composite has been put through the same heating test three times on the same day to ensure consistency. The data sets have been normalised to the mass of AB in the sample and the argon gas flow so what begins as a reading of current is transformed into arbitrary units (a.u.) per gram (g^{-1}). The argon gas flow rate is taken from the average value of the m/z = 36 trace from 5 to 9 minutes, the interval before heating commences.

Because the data are noisy mathematical smoothing via the Savitsky-Golay method has been employed [157]. Savitsky-Golay smoothing uses a least squares fitting and sustains peak features better than adjacent averaging methods. It calculates a polynomial regression, $p(n_f)$, around the central point, n_f, of a moving envelope of points, $N = n_0, n_1 \dots n_n$ and outputs a new smoothed value for that point, n_g.

$$p(n_g) = \sum_{k=2}^{N} n_g {n_f}^k \quad (28)$$

A second order polynomial, $k = 2$, gave a suitable fit in all cases. However, the value of N (= 2M+1) was varied between 50 and 500 depending on the trace, typically the data for hydrogen (m/z = 2) used n=50 and borazine (m/z = 81) used n=5000. The fit is decided by minimising the least squares error, E, of the new points to the original values,

$$E = \sum_{n=-M}^{M} \left(p(n_g) - n_n\right)^2 \quad (29)$$

In all cases, the goodness of smoothing was assessed by eye to ensure no obvious features had been erased, an example of a particularly noisy ammonia (m/z = 17) signal is below in Figure 21.

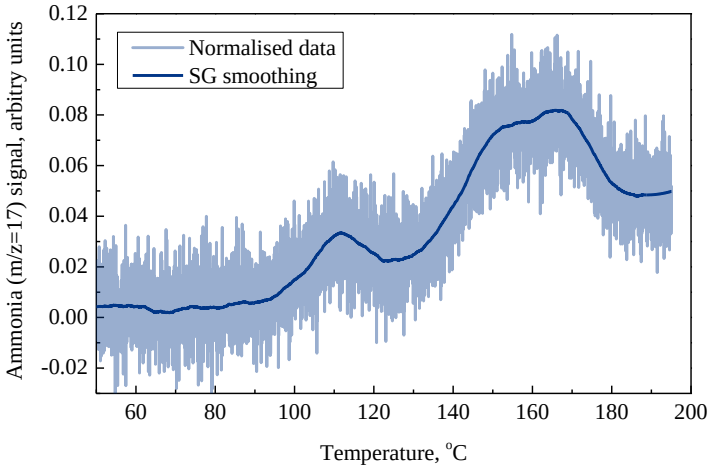

Figure 21: Savitsky-Golay smoothing, of ammonia (m/z = 17) signal where N = 500.

From the three normalised curves of each mass number detected, a mean curve and error (standard deviation) was calculated. These graphs are used to show the changes in the reaction over time. Further, the peaks are integrated and normalised to the hydrogen signal level at maximum times. This is used to show the relative levels of impurities to hydrogen in the various materials.

3.3.5.1 Validity

Finally, it is important to discuss the validity of the mass spec data. To ensure precision three data traces form each sample have been combined to give a mean trace (the values) and standard deviations (the errors). In Figure 22 the data form two separate AB samples is shown, AB1 and AB2. Both AB samples have been sourced form Sigma Aldrich, are 97% pure and were tested in their as-received state. The two samples were tested on the same equipment several months apart. The small error bars in the hydrogen trace (light background) show that data from the three traces of each sample are well correlated; AB2 is more similar to itself than AB1.

Looking below to the impurity graphs in Figure 22, AB2 seems to release far more ammonia, diborane, borazine and water than AB1. Both sets of data have been processed in the same ways, normalising to the AB mass, the argon flow and have undergone the same smoothing technique. By normalising to the nominal mass of AB in the samples it has been assumed that the output signal from the detectors varies linearly with the gas output from the samples. This has not actually been verified, indeed the mass spec manufacture suggested that the ratio between gas input and signal output could vary. The data are normalised to the carrier gas stream (argon) because logically a higher, faster throughput will result in a higher signal. However, there is no actual information to suggest that this is the case. Perhaps a lower, slower gas flow would actually result in a higher signal as the gas would not be rushed past the detectors as quickly. Secondly, it has been assumed that all mass fragments here are detected equally. It is possible that there is

some variable sensitivity to the different mass fragments; some may be more equal than others [158]. Also some mass fragments may ionise more easily than others.

The differences between the impurity levels in Figure 22 are probably due the samples being run several months apart. Tests performed on the same day show greater similarity then those taken a year apart, due to changes in the environment, equipment and materials.

Normalising to the mass of AB is valid as the detection level can be approximated as linear when the samples are of a similar mass. Sequences of samples are well correlated so this is a credible theory. (Consider the ammonia traces form the 25wt%, 50wt% and 75wt% AB in clay (imogolite) in Figure X in chapter 6.) However, when the mass difference between the samples is large (comparing AB in clay to pristine AB in chapter 6) the intensities of the integral plots should not be trusted. In many cases the pristine AB has been plotted alongside the composites as comparing the graph profiles can be useful.

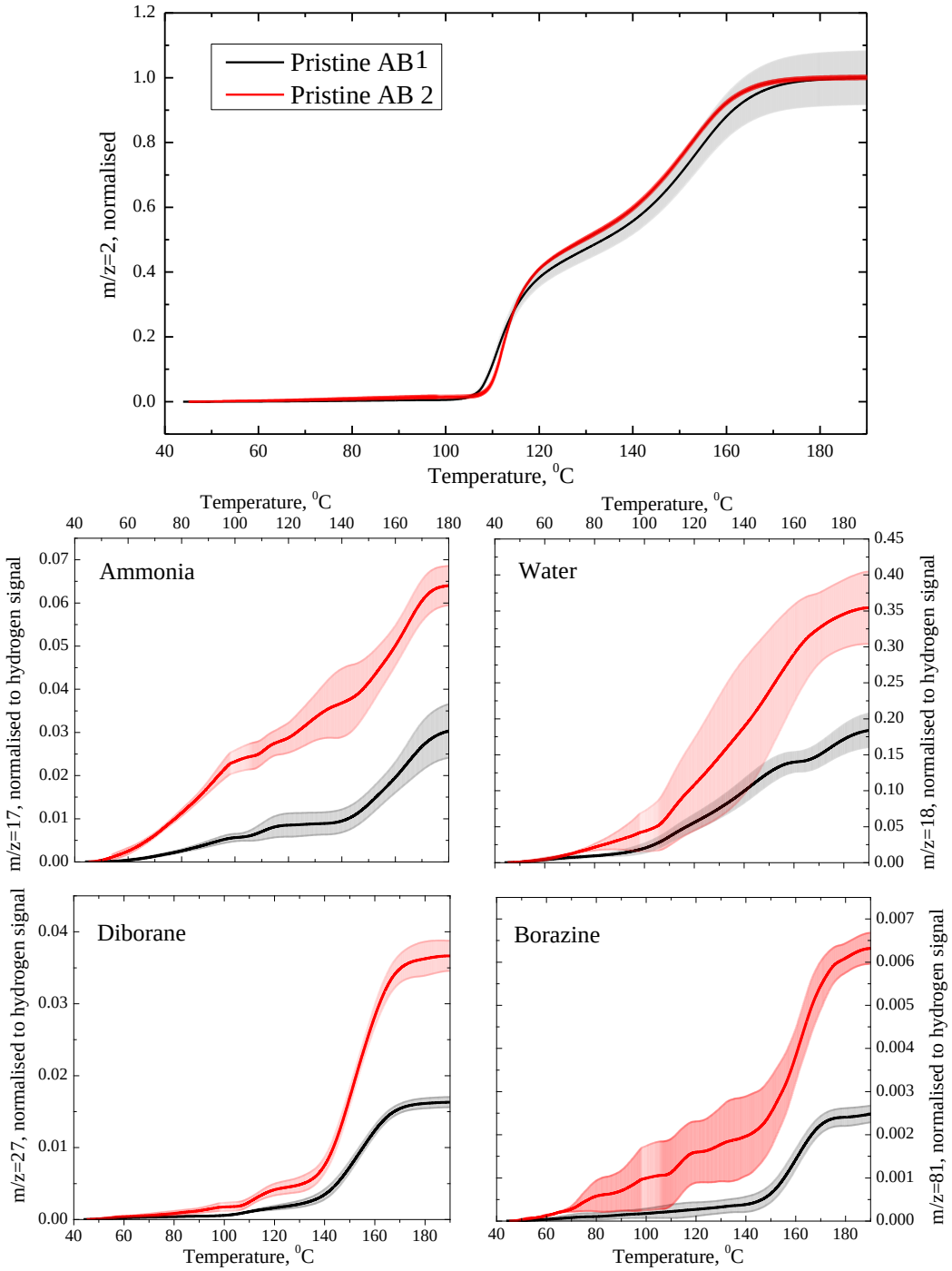

Figure 22: Cumulative integrals of the heating ramps of two pristine AB samples (AB1 and AB2) tested several months apart. The data were normalised to the hydrogen (m/z = 2) level at 190ºC and errors in the data are shown as the lighter background. The increase in impurities observed in AB2 is likely due to the time separation between the two tests. This graph has been plotted to show care must be taken when comparing impurity levels from different samples.

3.3.5.2 Activation Energy

The activation energy of the dehydrogenation of the AB can be determined using the Avramie-Erofeyev model [159]. The isothermal hydrogen release is sigmoidal as shown in Figure 22 and specifies a nucleation, growth and saturation process [160]. The growth phase of the reaction, moves outward in all directions from the nucleation point [54]. The Avrami-Erofeyev equation is reserved for solid phase reactions. While AB melts during the dehydrogenation the actual molecules maintain their approximate position and so the reaction can be modelled as a solid.

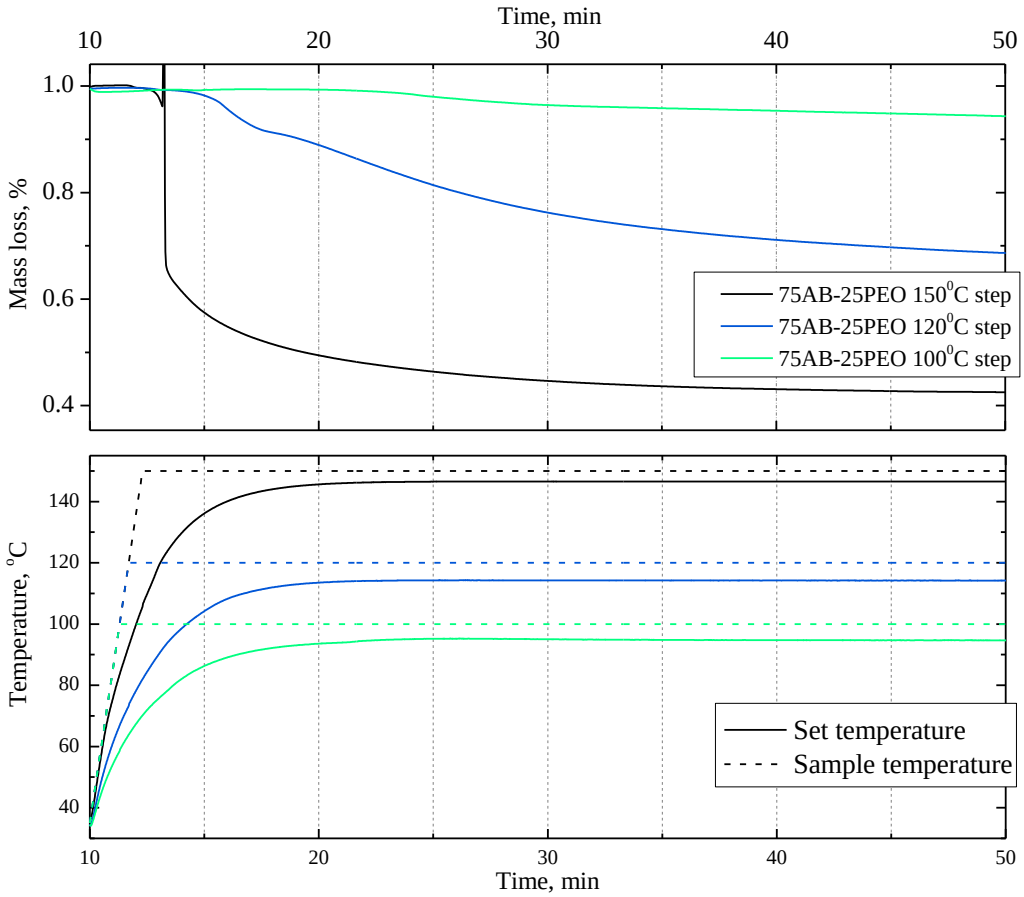

Figure 23: The mass loss (top) of the 75AB-25PEO electrospun fibres when subjected to heat steps of 150°C, 120°C and 100°C in the combined TGA/DSC (bottom). In the 150°C and 120°C steps the majority of the hydrogen has been lost before the maximum temperature was reached. Additionally the samples never reach the set temperature. Therefore this loss data are inappropriate for analysing the activation energy of AB.

Close examination of the TGA and mass spec data revealed several issues that meant it could not be used for this type of analysis. The step heats are not really step heats as the actual sample temperature lags so far behind the set temperature. The instrument reaches the target temperature in ~2 minutes (a rate of 75°C/min) but the sample temperature lags behind by approximately 20 minutes (see Figure 23). Also, the final temperature attained is several degrees below the target. In the 150°C and 120°C runs the majority of the hydrogen release occurred before the maximum temperature was reached. This means that most of the hydrogen released during the step heats is

actually released on a fast 20 minute ramp heating. For this reason it was not possible to calculate the activation energy of the hydrogen release from AB in the composites.

3.3.6 X-ray diffraction

A diffraction pattern can be describes as the interference pattern that occurs if a wave encounters the regular lattice of a crystal [161], [162]. The recurring dimensions of the lattice, d, can be obtained by relating the angle of the incident beam, θ, via the Bragg approximation,

$$n\lambda = 2dsin\theta \quad (30)$$

where n is an integer representing the scattering order and λ is the wavelength. Sharp peaks occur with constructive interference and these diminish as the lattice becomes disordered. A diffraction pattern of a material gives access to the repeat distances inside and is therefore ideal for determining the crystal structure. X-rays are ideal for exploring materials as the wavelength is comparable to interatomic spacings.

Traditional methods of obtaining a crystal diffraction pattern with x-rays require a single crystal that must be correctly aligned to the beam to expose the plane of interest. Diffraction from other repeat distances in the crystal can be only be accessed by turning the crystal to reveal a new plane to the beam. Making and aligning a single crystal is challenging at best and a second method designed for powders is more appropriate. The Debye-Scherrer method uses the distribution of the random crystallite orientations in a powder sample to present multiple planes to the beam at the simultaneously. The sample is fixed to the sample holder and revolves to achieve an average distribution of the scattered intensity.

Electrons are produced by thermionic emission off a cathode and accelerated towards a cooled metal target, often copper as it has a high thermal conductivity. On collision the electrons are decelerated in the material which results in the emission of Bremsstrahlung photons – a continuous spectrum of x-rays. During this process the inner shell electrons in the atoms are knock out and when an outer shell electron drops down to replace the displaced one, an x-ray is emitted. If the electron drops into a K shell this is called K-radiation, Cu K_α X-rays are particularly intense peaks in the spectrum and are ideal to be used in a diffraction experiment. Once produced the X-rays of the required wavelength are selected by diffracting off a graphite lattice. The x-rays are detected by a NaI scintillator with a combined photomultiplier to strengthen the signal.

Diffraction patterns were collected to study the structure and composition of the materials. A Rigaku SmartLab diffractometer with Cu K_α radiation of wavelength 1.54Å between 10 and 110° with a scan rate of 1.50 deg/min and resolution of 0.0002° was used. Lower resolution patterns

were also collected with a high and a Phillips X'pert Xray diffractometer with Cu K_α radiation of wavelength 1.54Å between 5 and 75° with a scan rate of 1deg/min and resolution of 0.02°.

3.3.7 Nuclear magnetic resonance spectroscopy

Nuclear magnetic resonance (NMR) is an extremely useful technique to study the structure, dynamics, reaction states and the chemical environments of magnetic nuclei.

Isotopes with an odd number of protons and/or neutrons have a magnetic moment (μ) and angular momentum. Boron has five protons and has a magnetic moment that can be explored by NMR while ^{16}O and ^{12}C are isotopes with an even number of protons and neutrons and therefore do not have a magnetic moment. Protons and neutrons all have spin of ±1/2. The magnetic moment is related to the nuclear spin quantum number (S),

$$\mu = S \cdot \gamma_g$$

where γ_g is the gyromagnetic ratio; the ratio of the magnetic dipole to the angular momentum. There are 2S+1 angular momentum states from –S to +S in integer steps.

The nuclear magnetic moment of a nucleus will align with an external magnetic field either parallel or antiparallel. The nuclei magnetic moment will precess around the direction of the field. Aligning parallel to the field is preferred then aligning against it. The larger the magnetic field, the larger the energy difference between the two states.

In nuclear magnetic resonance (NMR) spectroscopy the nuclei are subjected to a magnetic field, up to 20tesla, to align the spins parallel and antiparallel to the field. Then radio frequency waves, energise the lower energy (parallel aligned) nuclei which flip into the higher energy (antiparallel aligned) state. When the frequency is removed the nuclei relax back to their initial states perturbing the magnetic field. This perturbation is called the resonance and is gives the measured signal.

The frequency, ν, at which a resonance can occur is related to the external magnetic field, B_0,

$$\nu = \frac{\mu B_0}{hS} \quad (31)$$

where S is the spin quantum number and h is Planks constant. Thus if a high field is used to polarise the spins a higher frequency electromagnetic radiation is required.

Electrons have a magnetic moment as well as protons and neutrons. The electron spin opposes the nuclear spin and can shield the nucleus from an external magnetic field. High shielding will

shift the resonance to lower frequency while low shielding will shift the resonance to higher frequency.

NMR spectroscopy is ideal for studying AB as AB contains three NMR active nuclei, boron, nitrogen and hydrogen. While both ^{11}B and ^{10}B are NMR active and have spins of S = 3/2 and 3 respectively, however, ^{11}B NMR was performed on AB as ^{11}B has an 80% abundance and gives a clearer signal. Time resolved studies of AB and the AB composites during the dehydrogenation could be performed at 85°C. Nitrogen has two naturally occurring isotopes ^{14}N and ^{15}N with abundance 99.6% and 0.4% respectively. While both isotopes are NMR active, ^{14}N is hampered by quadrupole interactions which broaden the peak and can render it unobservable under high resolution. Therefore, ^{15}N NMR was performed on the AB samples. As the natural abundance of ^{15}N is very low, the spectra must be left to accumulate for several hours.

In situ solid-state ^{11}B NMR was performed on the pristine AB and the 50AB-50PEO electrospun material while being heated at 85°C. NMR magic-angle spinning (MAS) spectra were recorded at 128.3 MHz using a Varian VNMRS 400 spectrometer and a 4mm (o.d.) rotor. Spectra were obtained using cross-polarisation with a 1.0s recycle delay, 40ms contact time and at a sample spin-rate of 10kHz. Between 20 and 100 repetitions were accumulated. Spectral referencing was performed with respect to an external sample of $F_3B\text{-}OEt_2$. Additionally, ^{15}N NMR was performed on the initial and final products (after heating in oven at 85 °C for 6 hours) at ambient temperature. The spectra were recorded at 40.527 MHz using cross-polarisation with a 5.0s recycle delay, 40ms contact time and at a sample spin-rate of 6.8 kHz. The data were referenced to neat nitromethane.

3.4 Introduction to neutron scattering

Neutron scattering is a valuable tool for exploring condensed matter systems. Both structure and motions can be studied as the neutron wavelength, λ, is akin to interatomic spacings. Being uncharged, neutrons can penetrate far into matter where they interfere directly with the nucleus. Neutrons have mass and accordingly, can scatter inelastically; the direct nuclear interaction ensures intensity is maintained at high scattering angle. Interactions are irregular with respect to nuclear size and isotope allowing isotope substitution to gather more information.

The energy of a neutron E_n, is described

$$E_n = \frac{p^2}{2m_n} = \frac{m_n v^2}{2} = \frac{m_n}{2}\left(\frac{L}{t}\right)^2 \quad (32)$$

where p is the momentum, m_n is the neutron mass equal to $1.675 \cdot 10^{-27}$ kg, v is the velocity, t is the time and L is the distance travelled. Using the de Broglie relationship

$$p = \hbar\vec{k} \tag{33}$$

where $\vec{k}$ is the wavevector of the neutron propagation and $\hbar$ is the reduced Planks constant equal to 6.582×10^{-16} eV·s. We also note that

$$\vec{k} = \frac{2\pi}{\lambda} \tag{34}$$

where λ is the neutron wavelength.

When a neutron, with a propagation vector, collides with a nucleus it will undergo a momentum change, $\Delta p = \vec{Q} = \vec{k}_i - \vec{k}_f$, where $\vec{k}_i$ and $\vec{k}_f$ are the initial and final wavevector of the neutron respectively. The neutron can also gain or lose energy to the sample, $\Delta E = \hbar\omega = E_i - E_f = \frac{\hbar^2}{2m}(k_i - k_f)$, where E_i and E_f are the initial and final energies of the neutron (see Figure 24). The scattering process is described as elastic when the neutron energy remains constant and inelastic when there is a change. Analysing these changes allows us to understand the structure and motions inside materials.

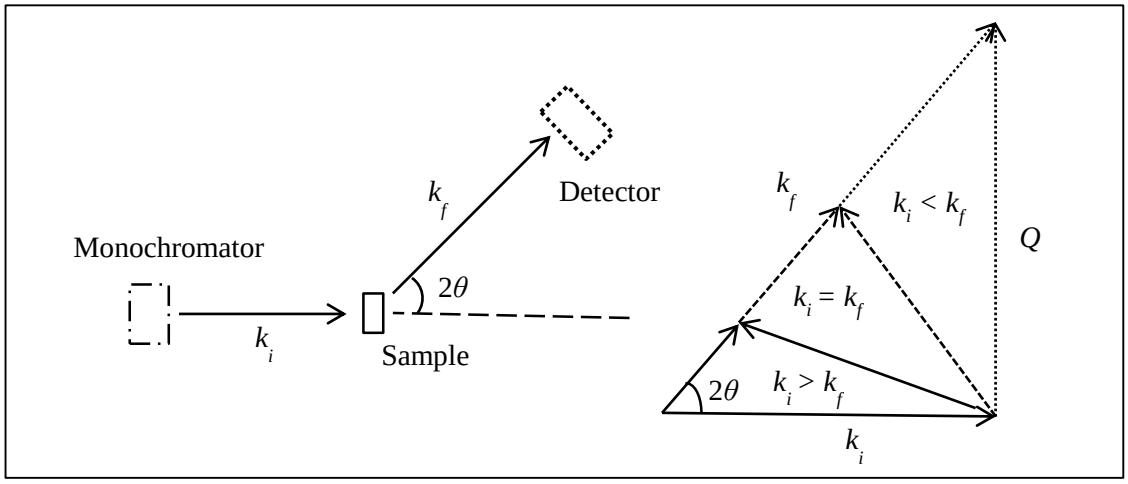

$$k_i = k_f \; Neutron\ energy\ constant \} \; Elastic\ scattering \rightarrow \; Q = \frac{4\pi sin\theta}{\lambda} \tag{35}$$

$$\left.\begin{array}{l} k_i > k_f \; Neutron\ energy\ loss \\ k_i < k_f \; Neutron\ energy\ gain \end{array}\right\} \; Inestastic\ scattering \rightarrow \; Q = \sqrt{\frac{2m}{\hbar^2}\left[2E_i - \hbar\omega - 2\sqrt{E_i(2E_i - \hbar\omega)}\cdot cos2\theta\right.} \tag{36}$$

Figure 24: The momentum and energy changes associated with elastic and inelastic scattering. k_i and k_f are the initial and final wavevector of the neutron respectively.

A neutron beam at a facility will combine a distribution of neutron energies these can are generally described according to their temperature (see Table 9).

Table 9: Neutrons according to temperature [163]

Neutron	Energy (meV)	T (K)	λ (Å)
Hot	100-500	1000-6000	0.4-1
Thermal	5-100	60-1000	1-4
Cold	0.1-10	1-120	4- 30

The neutrons that have been used in the experiment were thermal neutrons. The data were collected on the Iris beam line at Isis, Rutherford Appleton Laboratory, UK.

In a scattering experiment we measure the partial differential cross-section. This is the fraction of neutrons of incident energy E scattered into a solid angle element, dΩ with an energy transfer element, dω. Here, $\sigma = 4\pi b^2$ is the total scattering cross section of the atoms in the sample and b represents the scattering interaction of the particular nucleus (see Figure 25). $S(\vec{Q}, \omega)$ is the dynamic structure factor, the total scattering with respect to Q and ω.

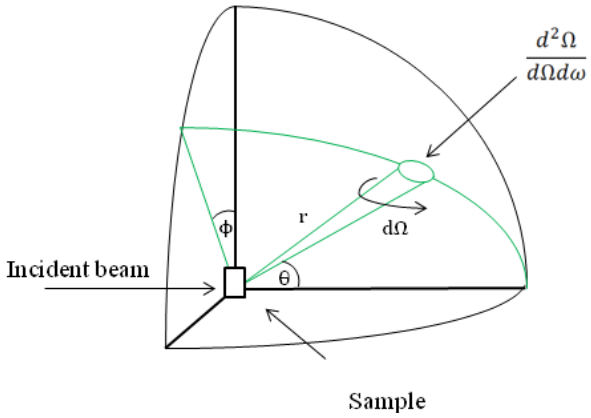

Figure 25: Geometry of a scattering experiment [164]

$$\frac{d^2\Omega}{d\Omega d\omega} = \frac{\sigma}{4\pi} \cdot \frac{|\vec{k_f}|}{|\vec{k_i}|} S(\vec{Q}, \omega) \quad (37)$$

As well as elastic and inelastic, a scattering interaction is also described as coherent or incoherent. Coherency, $S_{coh}(Q, \omega)$, arises from interference scattering off a regular lattice within the material. Elastic coherent scattering can be used to pinpoint the locations of atoms while inelastic coherent scattering is ideal for studying excited states such as phonons. Incoherent scattering, $S_{inc}(Q, \omega)$, is the result of neutrons scattering independently off atoms. Whereas elastic incoherent scattering is usually isotropic and seen as a diffuse background, inelastic incoherent scattering gives information about uncorrelated motion of nuclei such as diffusion and vibration.

Each nuclei has a coherent scattering cross section, σ_{coh}, and an incoherent scattering cross section σ_{coh} such that,

$$\sigma_{coh} = 4\pi b_{coh}^2 \text{ and } \sigma_{inc} = 4\pi b_{inc}^2 \quad (38)$$

Below in Table 10 are the scattering cross sections of the elements used in the experiments in this thesis. Dynamics studies of hydrogen or hydrogen containing groups are facilitated by the high incoherent cross section of the proton. The variance between hydrogen and deuterium enables contrast studies to be performed between the protic and non protic areas as well as absolute scattering experiments.

Table 10: Scattering lengths and cross sections of the nuclei observed in experiments in this thesis.

Species	b_{coh}/fm	b_{inc}/fm	σ_{coh}/barn	σ_{inc}/barn
H	−3.74	25.27	1.76	80.26
D	6.671	4.04	5.592	2.05
C	6.64	0	5.55	0.00
Ca	4.90	0	2.78	0.05
N	9.36	2.0	11.01	0.5
B	6.65	-1.3	5.56	0.21
O	5.803	0	4.232	0.00
S	2.804	0	0.988	0.00

The total scattering, is the sum of the coherent and incoherent parts, $S(\vec{Q},\omega) = S_{coh}(Q,\omega) + S_{inc}(Q,\omega)$ and depending on the identity and number of atoms being irradiated, a scattering intensity will be measured. However, to determine anything useful about the system the atoms must be correlated, i.e. must relate meaningfully to each other. Correlation between atoms can be described as regularity within the sample structure, such as the repeat distance between atoms in crystal lattice sites, distribution of molecules in a liquid or the unique rotational energy of a chemical group. The time-dependent self-pair correlation function $G(\boldsymbol{r},t)$ is a theoretical description of the probability of encountering atoms at position **r** and time t with reference to the origin, **r** = 0 and t = 0. It allows $S(\vec{Q},\omega)$ to be Fourier transformed into a real space and time description of the positions, motions and energetics of the atoms.

$$S(\vec{Q},\omega) = \frac{1}{2\pi\hbar}\iint G(\boldsymbol{r},t)exp\{i(Q\cdot r-\omega t)\}\,d\boldsymbol{r}dt \quad (39)$$

The reader can extend this basic introduction of neutron scattering with this excellent book by Willis *et al* [165].

3.4.1 IRIS

Crystal diffraction patterns and spectroscopic studies of Ca-NH_3 GIC were performed on the IRIS instrument at the ISIS Neutron Scattering Facility at the Rutherford Appleton Laboratory in the UK. IRIS is an indirect geometry and is a time of flight spectrometer (see Figure 26). IRIS has cold neutrons, when these arrive they are moderated, passed along a guide and through two choppers which are used to define the wavelength distribution at the sample. As a spread of neutron energies is present the initial flight time, t_1, along the initial flight path, L_1, will be different. However, an analyser crystal ensures that only neutrons of a defined energy that satisfy Bragg's Law reach the detectors.

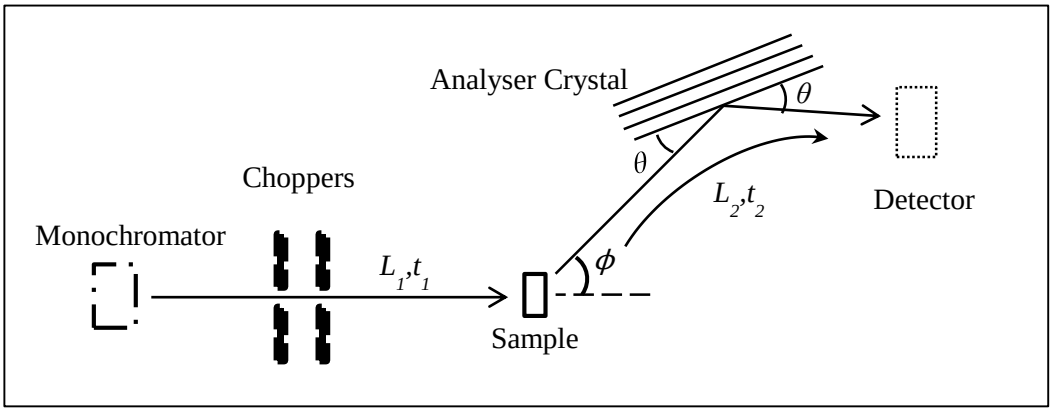

Figure 26: Schematic of IRIS indirect time of flight neutron spectrometer

The final energy, E_f, can be calculated by combining equations, x and y

$$E_f = \frac{m_n}{2}\left(\frac{L_2}{t_2}\right)^2 = \frac{m_n v^2}{2} = \frac{p^2}{2m_n} = \frac{1}{2m_n}\left(\frac{h}{\lambda}\right)^2 = \frac{1}{2m_n}\left(\frac{h}{\lambda 2d_a sin\theta}\right)^2 \quad (40)$$

Between the sample and the detector the flight length of the neutron, L_2 is accurately known therefore the time, t_2, to make the journey can be calculated.

$$t_2 = \frac{m_n L_2 d sin\theta}{h} \quad (41)$$

Should inelastic scattering occur, a spread of neutron energies and therefore arrival times at the detector will be observed. The energy change, ΔE, of the neutron can be ascertained,

$$\Delta E = E_i - E_f = \frac{1}{2}m_n\left[\left(\frac{L_1}{t - t_2}\right)^2 - \left(\frac{L_2}{t_2}\right)^2\right] \quad (42)$$

IRIS has detector coverage for a Q range of 0.4 to 3.7$Å^{-1}$ for spectrometry and crystallography, with additional detectors for purely diffraction experiments, this case the scattered neutrons

bypass the analyser crystal. Diffraction data can be collected on IRIS in in sync with a scattering experiment or the instrument can be setup for a purely diffraction experiment. During the experiment diffraction data were collected over a d-spacing range from 3.4 to 7.4Å using the IRIS settings d-range 3, 4 and 5. Data presented with a smaller d-spacing has been collected during the scattering experiments and then collated onto the graph. The scattering data were collected over an energy range of -0.3 to 1.2 meV with pyrolytic graphite crystals. The neutron energy of 1.845 meV affords an energy resolution of 17.5 μeV. The instrument resolution was defined with a vanadium annular cylinder as vanadium is an isotropic, purely elastic scatterer.

The total spectrum obtained from a neutron experiment is composed of elastic, inelastic and quasi-elastic regions as shown in Figure 27. Quasi-elastic neutron scattering (QENS), inelastic scattering close to the elastic line, can access timescales of motion of 1ps – 1ns and therefore the movements both rotation and translational.

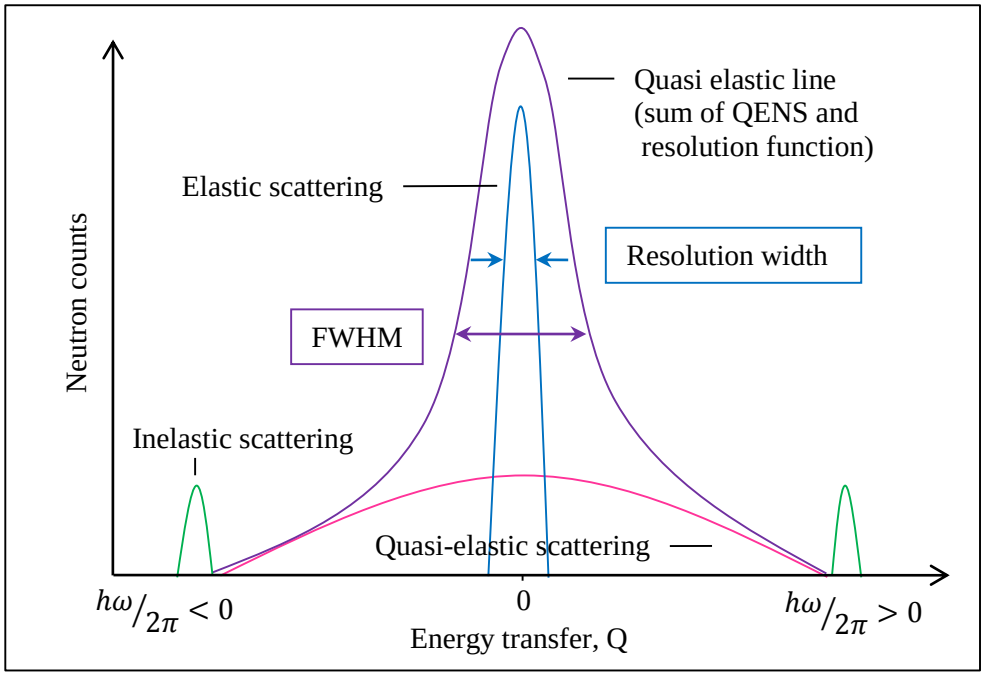

Figure 27: Schematic of the neutron scattering energy spectrum.

The incoherent dynamic structure factor, $S_{inc}(Q,\omega)$, is taken from the QENS and is a function of the translational, $S_{inc}^{trans}(Q,\omega)$ and rotational, $S_{inc}^{rot}(Q,\omega)$ incoherent structures and the mean square displacement $\langle u^2 \rangle$. The convolution of the three terms can be expressed:

$$S_{inc}(Q,\omega) = e^{-\frac{1}{3Q^2\langle u^2\rangle}} S_{inc}^{trans}(Q,\omega) S_{inc}^{rot}(Q,\omega), \quad (43)$$

where $\hbar\omega$ is the energy transfer and $\hbar Q$ the momentum transfer of the neutron. At low Q values, where, compared to the mean time between atomic collisions the times are long, the diffusion

process is ruled by the solution of Fick's Law and results in a translational incoherent scattering function of the form:

$$S_{inc}(Q,\omega) = \frac{1}{\pi}\frac{\hbar DQ^2}{(\hbar DQ^2)+(\hbar\omega)^2}, \quad (44)$$

where D is the diffusion coefficient. Thus, the translational incoherent scattering function is a single Lorentzian function, with the full width half maximum (FWHM),

$$\Lambda(Q) = \hbar DQ^2. \quad (45)$$

Further information about the diffusion process can be gained from the QENS by considering the higher Q values as deviation from the Fickian model at high Q would suggest jump diffusion. Several models have been considered for the system particularly the Singwi-Sjölander [166] and the Hall-Ross [167] and Chudley-Elliot [168] (see Table 11). While evenly distributed, the calcium in the layers do not occupy a perfect lattice, consequently a distribution of the ammonia jump lengths is probable. All the models afford good fitting and give similar values of l and τ. The Hall-Ross model has been selected in this case.

Table 11: Jump diffusion models, *l* is the jump length and $\boldsymbol{\tau}$ is the average translational residence time of the diffusing particle.

Model	Chudley-Elliot	Singwi-Sjölander	Hall-Ross
$\Lambda(Q) =$	$\frac{\hbar}{\tau}\left(1-\frac{\sin(Ql)}{Ql}\right)$	$\frac{\hbar DQ^2}{1-(\mathrm{DQ}^2\tau)}$	$\frac{\hbar}{\tau}[1-exp(-\mathrm{Q}^2\mathrm{D}\tau)]$
Jump characteristic	Finite	Exponential distribution	Gaussian distribution

The diffusing particle is characterised by the diffusion coefficient is found from:

$$D = \frac{l^2}{6\tau}. \quad (46)$$

where *l* is the jump length and τ is the average translational residence time of.

The rotational incoherent dynamic scattering function describes the rotation on the surface of a sphere of radius R;

$$S_{inc}(Q,\omega) = j_0^2(Q\cdot R)\delta(\omega) + \sum_{i=1}^{\infty}(2i+1)j_i^2\,(Q\cdot R) \times \frac{1}{\pi}\frac{D_{rot}i(i+1)}{(D_{rot}i(i+1))^2 + (\hbar\omega)^2} \quad (47)$$

Where D_{rot} is the rotational diffusion constant and $j_i(Q\cdot R)$ is the *i*th spherical Bessel function. In the context of the system under consideration only the first two terms (*i*=0,1) are required as the higher order terms only have a significant contribution at larger momentum transfers then those probed in this experiment. Within the scope of this series truncation the (Q independent) FWHM is given by:

$$\Lambda(Q) = 2D_{rot} = \frac{\hbar}{3\tau_{rot}}, \quad (48)$$

where τ_{rot} is the rotational dynamic correlation time.

Quasi-elastic neutron scattering (QENS), inelastic scattering close to the elastic line, can access timescales of motion of 1ps – 1ns and therefore the movements both rotation and translational, of the NH_3 molecules can be tracked.

3.4.2 Modes

The data has been analyzed with MODES v3 a program designed specifically to process data from the IRIS beam line [169]. MODES facilitates data binning and background subtraction, it displays diffraction data and fits inelastic peaks with a combination of Gaussian and Lorentzian curves.

4 Ammonia borane and polyethylene oxide composites

This chapter describes the study on the AB and polyethylene oxide (PEO) composites. Both making and testing the composites is explained. Here, PEO is shown to have a positive effect on the dehydrogenation of AB.

4.1 Electrospinning polyethylene oxide

PEO has previously been electrospun with a range of solvents, including water, ethanol and acetone, as part of a polymer blend or unaccompanied for a variety of applications including filters, wound dressing and microelectronics [107], [132], [170]. Many solutions of various concentrations of distinct PEO molecular weights have been processed under a range of spinning parameters. However, considering the large number of changeable electrospinning parameters, coupled with equipment and environment variables, it was deemed necessary to experiment with various solutions as opposed to copying from literature sources.

At the time of writing PEO is cheaply and abundantly available in a wide range of molecular weights. A selection of molecular weights between 400,000g/mol (4k) and 8,000,000g/mol (8M) were purchased for testing. Deionised water was chosen as the solvent; it has been used extensively for electrospinning PEO in the past, is benign and is a co-solvent for both PEO and AB. PEO in water is termed PEO-H_2O solution, and PEO in acetonitrile is termed PEO-ACN.

Table 12: An illustration of the electrospinning parameters tested, to determine the ideal conditions to produce well defined PEO fibres from PEO in water solutions.

PEO Mw g/mol	Conc. wt%	Flow rate ml/hr	p.d. keV	Observations
400k	5	1	10 - 30	Spraying not spinning, no fibres
900k	5	1	10 - 30	15-17keV Spinning.
	2	1 - 5	9 - 16	Unstable
2M	2.5	1	16	Damp fibres
	3	1	14 - 16	Shiny fibre mat
4M	1	1 - 4	13 - 46	1ml/hr, 13-17keV spinning, but wet
8M	1	0.25 - 1	12 - 15	0.25 ml/hr, 12keV stable, but wet
	2	2	10 - 30	14-16keV Spinning

The ideal system would be robust and have a high fibre production rate (flow rate multiplied by concentration). The low molecular weight PEO solutions, 400 and 900k, were unsuitable as they had a tendency to spray or to generate multiple jets from the droplet instead of spinning (see Table 12). The low viscosity and surface tension of the 400 and 900k PEO-H_2O solutions seem unable to support the charge necessary to eject a filament at a rate that prevents dripping. The high Mw

PEO solutions, using 4M and 8M, were also unsuitable, as they were extremely viscose at low concentration, so a high solid content could not be achieved. The 2M PEO solutions were most suitable as they could be stably spun with a range of concentrations and conditions; the 3wt% solution is the most appropriate having the highest polymer content and was used as a base for the AB PEO solutions.

Two issues arose. Firstly, the fibres adhered strongly to the aluminium foil collector and were problematic to remove and secondly, the fibres were still damp when they reached the collection plate. Replacing the aluminium sheet with grease proof paper, simplified the fibre collection but the fibres were still too damp. In literature, dry fibres can be achieved by increasing the jet flight time, lowering the humidity and raising the temperature of the spinning rig environment or replacing the solvent with another of a higher vapour pressure [107]. The distance between the nozzle and collector was already large (30cm) and maintaining a low humidity was problematic, as the chamber leaked. Additionally, higher spinning temperatures were not possible as AB is temperature sensitive. Therefore alternative solvents were considered.

3wt% PEO was added to a wide range of solvents (Figure 28) however, most were unsuitable. PEO did not dissolve in ethanol. When acetone was added to PEO a white solid was produced. PEO with DMA and DMSO produced a solid opaque gel. PEO in xylene, dichloroethane or toluene resulted in a clear to opaque gel. DMF was a good solvent for PEO but the tube became blocked during spinning. Acetonitrile, ACN, offered a viable alternative being a good solvent for PEO and having a high vapour pressure.

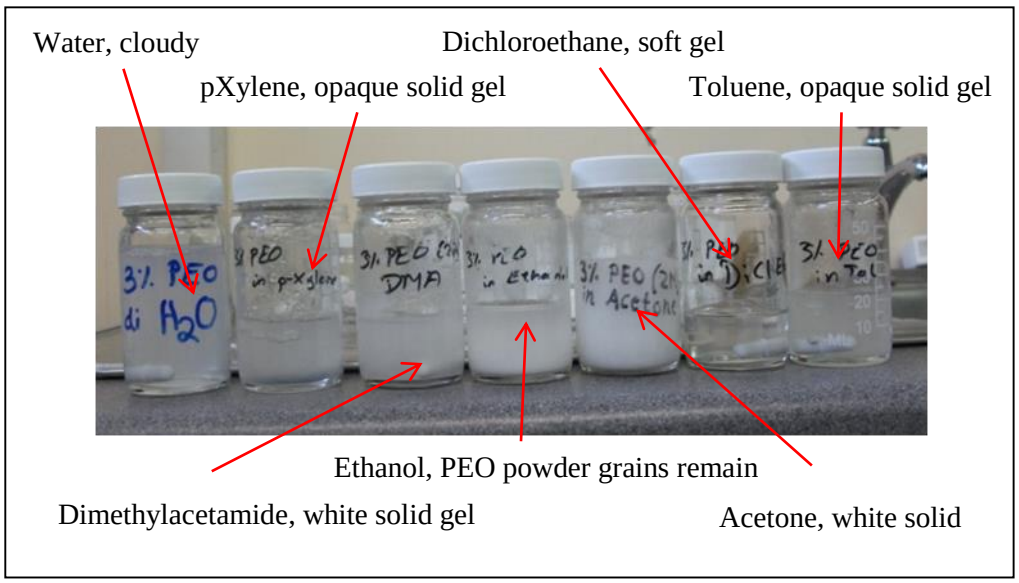

Figure 28: 3% PEO (2M) in a variety of solvents.

To determine the effect of the ACN on the PEO–H_2O solution, three solutions containing 0, 50 and 100% ACN as solvent were electrospun and compared (see Table 13). The ACN reduces the

conductivity and the viscosity of the end solution as compared to water. The change in conductivity is due to the difference in conductivity of the pure solvents, ACN being lower then H_2O. The drop in solution viscosity suggests the ACN is a better solvent. Either, the ACN is the preferred solvent to H_2O and the polymer chains are better lubricated and their reptation is enhanced, or the ACN is a poor solvent and the polymer chains, although dissolved, remain curled and the shorter end-to-end distance is responsible for the drop in viscidity.

Table 13: Electrospinning parameters of PEO (2M) solutions in H_2O, in ACN and in a 50:50 mix

Solvent	Conc. wt%	Conductivity, µSv/cm ±1	Viscosity high shear, cP ±10	Flow, ml/hr	p.d. keV	Observations
H2O	3	76	1760	1	10-20	12keV – flat shiny mat
50ACN-50H2O	3	18	1690	1	10-20	12keV – fluffy pile
ACN	3	1	785	1	10-20	Spins fine

The carrier solvent used (H_2O or ACN) dramatically affects the morphology of the electrospun PEO fibres as shown in Figure 29. The SEM images in Figure 29 show that the PEO produces thin smooth fibres while the PEO-ACN solution produced fibres which are wide and rough. The PEO-H_2O-ACN solution resulted in the most interesting morphology, reminiscent of beads on a string.

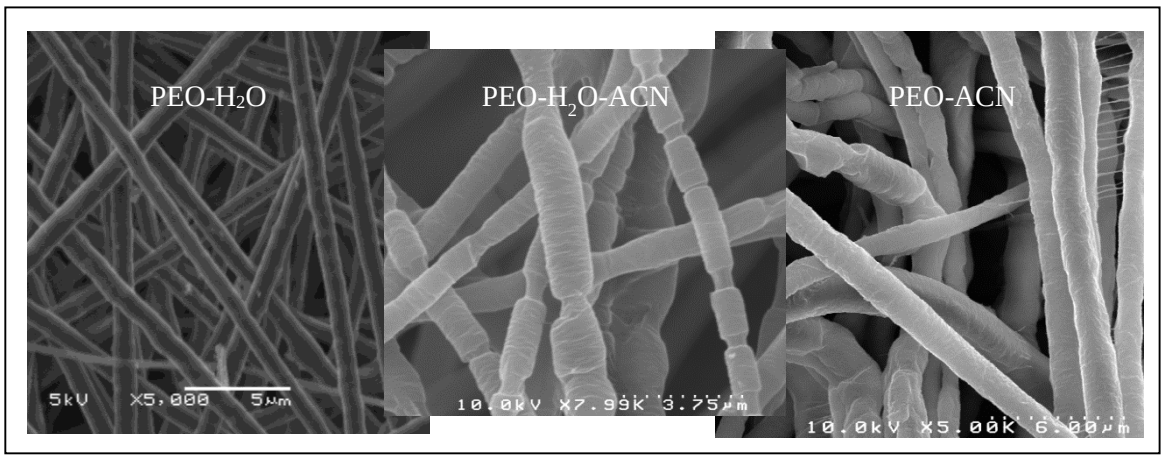

Figure 29: PEO electrospun fibres with solvents H_2O, ACN and an equal mix of the two.

The fibres were electrospun under similar conditions in the same eletrospinning rig, therefore the differences observed are likely to originate from the solutions themselves. The PEO-H_2O solution, being highly conductive, is very responsive to the electric field, and would consequently experience a high stretching force. The low vapour pressure of H_2O will keep the jet fluid allowing greater elongation to occur before drying (the fibres were damp on the collection plate) leading

to thinner, smoother fibres. The PEO-ACN solution has a high viscosity and low conductivity and the ACN has a high vapour pressure. This suggests that the jet can dry fast before the filament stretches significantly, resulting in wide fibres. The PEO-H_2O-ACN solution has intermediate conductivity, therefore intermediate stretching and evaporation. The fibre 'bead on a string' morphology suggests that surface evaporation has formed a solid surface shell while leaving a liquid core that is still able to extend. These results demonstrate the dramatic effect on the fibre morphology of the interplay of conductivity, viscosity and vapour pressure in electrospinning.

4.2 Electectrospinning polyethylene oxide with ammonia borane

It proved uncomplicated to dissolve varying amounts of AB into the 3wt% PEO (2M) in ACN solution. The amount of AB added was such that the dry mass ratio of AB:PEO in the final material would be 25:75, 50:50 and 75:25; these samples are termed the 25AB-75PEO, 50AB-50PEO and 75AB-25PEO respectively. While the PEO solutions are highly viscous, it is shown in Figure 30 that adding AB markedly reduces the viscosity.

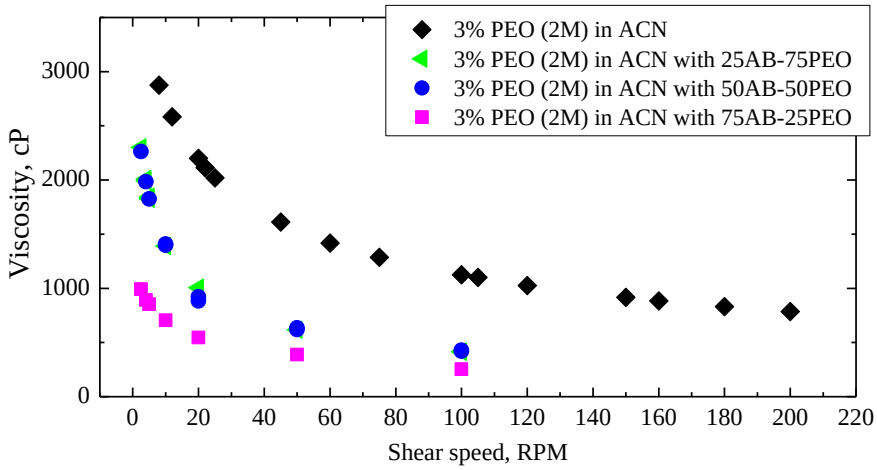

Figure 30: The viscosity of the AB-PEO in ACN solutions with respect to shear speed. The viscosity at the high shear limit quoted in Table 14. The addition of AB successively reduces the viscosity.

Table 14 lists the electrospinning parameters used when making the AB-PEO fibres. No Taylor cone was observed but nonetheless the solutions could be stably electrospun. The 75AB-25PEO solution was temperamental at times, probably due to the combination of the high conductivity and low viscosity. The jet would break periodically, sometimes multiple jets could be observed and once or twice solids built up on the nozzle. These issues would resolve themselves without interference.

Table 14: Processing parameters used for the electrospinning the AB-PEO in ACN solutions.

AB:PEO dry mass ratio	Flow rate ml/hr	p.d. keV	Conductivity µSv/cm	Viscosity at high shear, cP	Observations
25:75	1	12	2.2±0.2	360	Stable spinning
50:50	1	12	7±2	350	Stable spinning
75:25	1	12	25±5	240	Temperamental spinning

The AB-PEO fibres are integral even in the 75AB-25PEO sample where the polymer is supporting a large proportion of AB (see Figure 31). As the AB content increases, the fibres become rougher and more uneven. While the fibres appear dry when electrospun at cross points in the 50AB-50PEO and the 25AB-75PEO samples, the fibres have melded together. This suggests some solvent has been retained in the fibres. To limit this residual ACN, the fibres were left open to the air for 24 hours to dry.

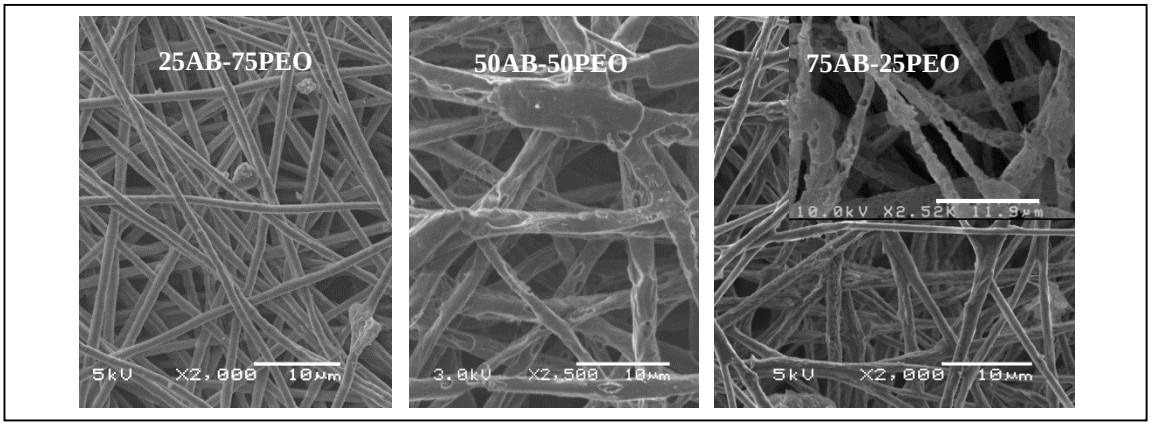

Figure 31: Images of the AB-PEO fibre samples, 24AB-75PEO, 50AB-50PEO and 75AB-25PEO. As the ratio of AB to PEO increases the fibres become rougher.

4.2.1 Uncertainty

In contrast to flat fibre mat obtained from PEO-H_2O solution, the PEO-AB-ACN solutions produced fluffy fibres (see Figure 32). To isolate the cause of this effect, PEO-AB-H_2O solutions were made and electrospun. The solution compositions and electrospinning parameters were kept identical to those in Table 14 but the ACN was substituted for H_2O. The fibres produced by the PEO-AB-H_2O solutions laid down flat. The 'fluffy' effect is probably due to an accumulation of static charge. The ACN evaporates quickly and PEO is an electrical insulator so charge caught by the AB would remain trapped.

As the pile of fibres builds up, the size of the whipping zone decreases. The initial fibres are subjected to more stretching and drying time than the final fibres. This suggests variability across the fibre sample.

Figure 32: The fluffy fibres produced from the PEO-AB-ACN solution.

During the electrospinning of the PEO-AB-ACN solutions, bubbles evolved inside the syringe. This suggests room temperature evolution of hydrogen from the AB in the solution. This is likely as AB has been shown to decompose when refluxed with ACN [79].

This implies that both the nominal amount of pristine AB and the fibre production conditions are subject to some ambiguity.

4.3 Freeze drying and dry mixing polyethylene oxide and ammonia borane

Electrospinning is an elegant but slow and labour intensive technique for producing AB-PEO integrated materials and therefore two other methods, freeze drying and dry mixing, were considered as alternatives. The freeze drying was relatively simple compared to electrospinning: the solutions were prepared by dissolving the polymer in water and then AB was added to the required dry mass ration AB:PEO of 25:75, 50:50 and 75:25. When the solids had blended with the solvent, the mixture was placed in a freezer at -5°C and a day later transferred to the freeze dryer. The dry mixing was done after grinding the solids with a pestle and mortar for ~15min.

4.4 X-ray diffraction of the electrospun and freeze dried polyethylene oxide and ammonia borane composites

The XRD pattern of the PEO as-received granules and electrospun fibres display the monoclinic (120) and (112) reflections at 19° and 23.2° respectively (Figure 33) [171], [172]. In the PEO granules, numerous higher order peaks are also present and indicate a high level of crystallinity. In the PEO fibres the peak intensity reduces and the higher order peaks disappear entirely. This suggests the PEO fibres have less long range crystallinity than the unprocessed material. In the solid state the PEO polymer backbone is twisted into a helix and these helices are laid parallel to each other [173], [174]. The stretching forces experienced during electrospinning could distort the polymer chain arrangement and limit the long range crystal ordering.

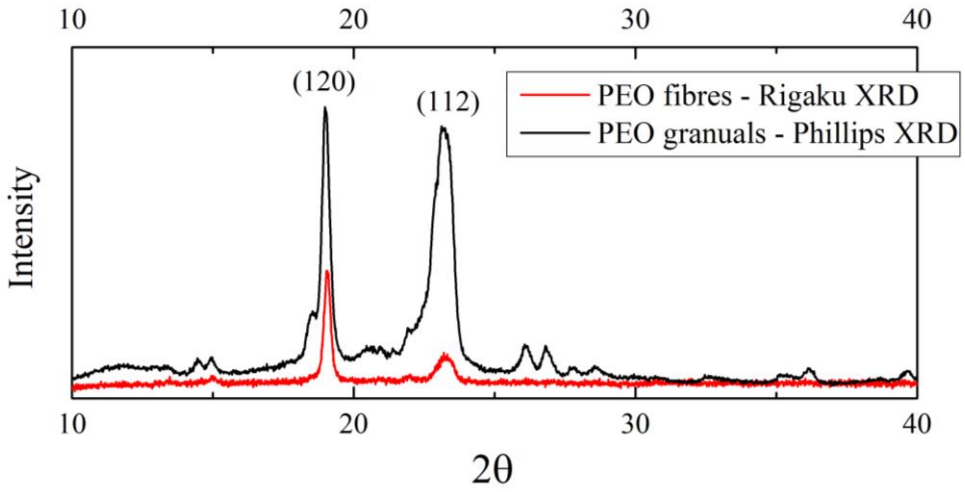

Figure 33: X-ray diffraction pattern of PEO as received granules and electrospun fibres.

In the electrospun composites, the tetragonal AB is clearly present in the 75AB-25PEO and 50AB-50PEO composite samples, as evidenced by the (110), (101), (200), (002), (121) and (112) peaks in Figure 34 [84]. In the 25AB-75PEO sample the (110) and (101) peaks are reduced to a small hump and the reflections at higher theta values are not visible either. This suggests that no tetragonal crystalline AB is present in the 25AB-75PEO sample. The viscosity of the PEO solution decreases with the addition of AB (Figure 30) indicating a high affinity between AB and PEO. The data here implies that the low concentration of AB in the 25AB-75PEO solution inhibits the formation of large AB crystallites, possibly because each AB molecule is more statistically likely to interact with a PEO molecule then with itself. This suggests that the AB is so well integrated with the PEO that the original crystal structure has been destroyed. This implies that a different AB-PEO phase has been formed.

The (120) and (112) reflections from the PEO occur in some but not all of the composite fibres. The quartet at 27° (marked +) is observed in all the composites but loses clarity when viewed with the Philips diffractometer in the 50AB-50PEO and 75AB-25PEO samples. The quartet at 27° is associated with crystalline PEO. The changes in the (120) and (112) reflections between the pure PEO and the PEO in the fibres suggests that monoclinic crystalline PEO is in some of the fibres. The changes in the quartet at 27° suggest that monoclinic crystalline PEO is present in all the fibres samples. To complicate the issue further new peaks have appeared at 10.6°, 12.1°, 13.4°, 14.9°, and 25.2° (marked *). These new peaks could be indicative of novel PEO phases or novel AB-PEO phases. The novel peaks were observed in the 50AB-50PEO and the 75AB-25PEO in the Rigaku but not in the Phillips diffractometer. Over the course of the study, fibres of the same nominal AB and PEO contents were produced several times. The fibres tested on the different instruments were from different batches. This suggests the preparation conditions can

effect the overal structure of the composites. Ultimately, it is clear that the AB and PEO have interacted and formed a new phase with a well-defined crystal structure.

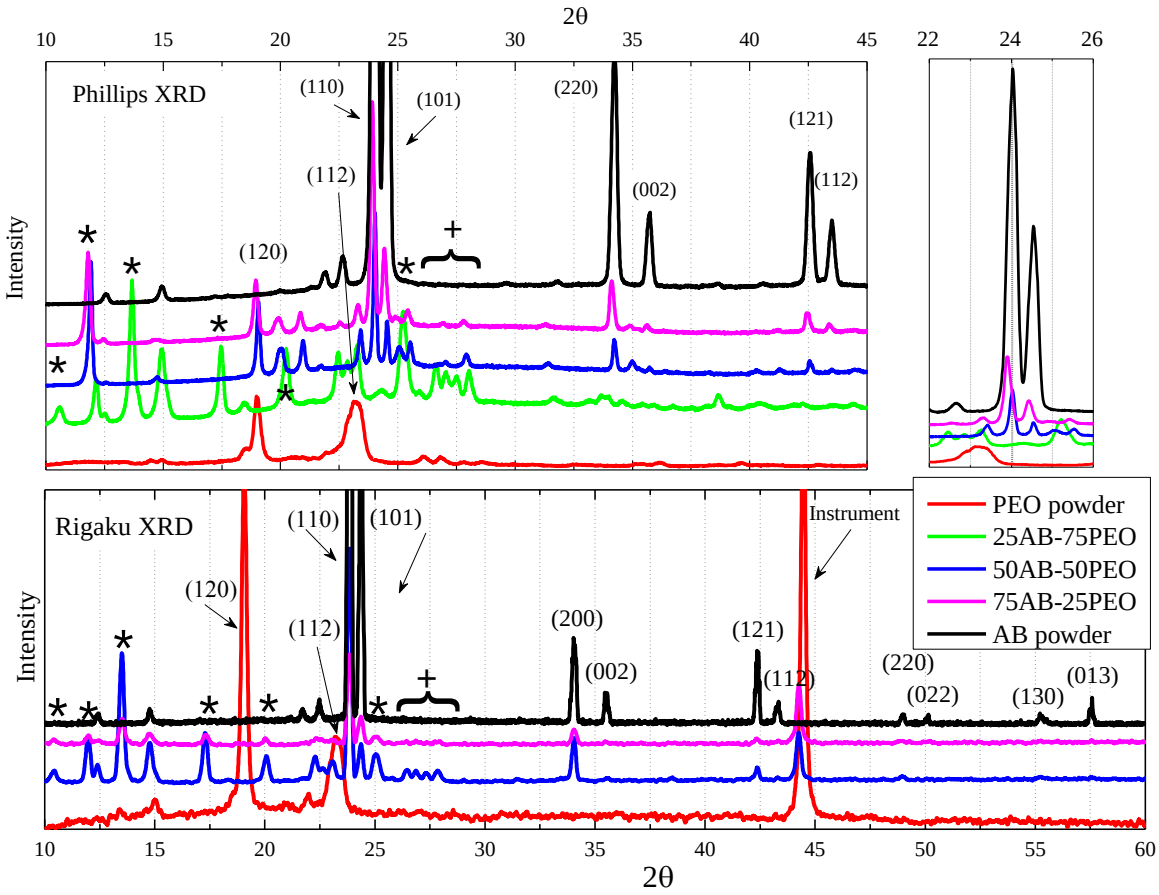

Figure 34: X-ray diffraction pattern of AB, PEO granules and the electrospun fibres collected on a Phillips X'pert, above, and the Rigaku SmartLab, below.

4.5 Foam tests

One of the main barriers to commercialising AB is the foaming that accompanies the hydrogen release. The foam occurs because the hydrogen gas is evolved inside the highly viscous liquid that AB becomes on melting at 112°C. Figure 35 shows the typical response of a compressed pellet of AB to heating; volume expansion of ~2000±140% is observed with a mass change of 15±8%. The volume change is probably greater than reported as the pellet rises up on the column of foam until it is above the surface of the oil bath where the temperature is lower and so the expansion ends.

Similar tests were performed with the electrospun fibres, freeze dried material and the hand milled powder (Figure 36). In all examples, the foaming is successively supressed as the PEO content increases. However, unlike for the case of pure AB, the composites all ejected white solids that collected on the inside of the test-tube.

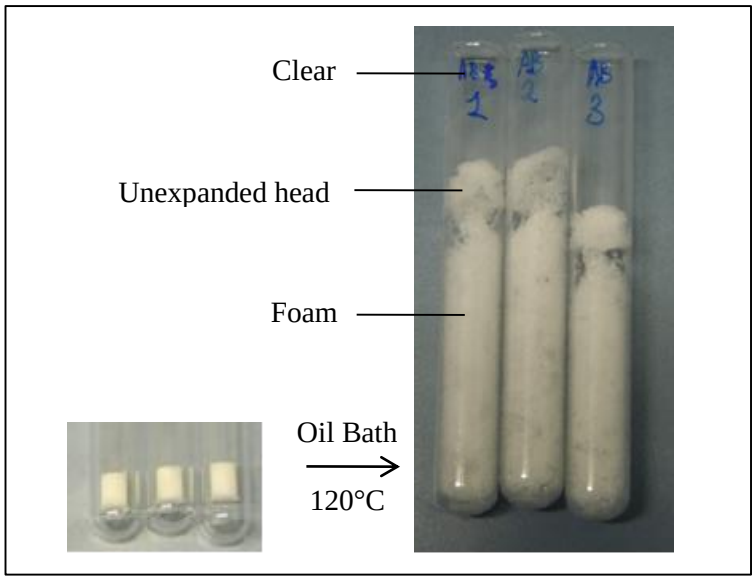

Figure 35: Foaming response of a compressed pellet of AB when subjected to 120°C isothermal heating

For the high ratio AB samples (75AB-25PEO) the electrospun fibres outperformed the freeze dried and hand milled materials. On lowering the AB content (50AB-50PEO) the hand milled material had the best antifoaming properties as the pellet shrank, but the freeze dried material ejected fewer solids. The low AB content materials (25AB-75PEO) in general expanded more than their 50AB-50PEO counterparts. The electrospun 25AB-75PEO sample expanded vertically, the freeze dried 25AB-75PEO sample unravelled and the hand milled 25AB-75PEO sample expanded equally in all directions. This suggests that for 25AB-75PEO samples have expanded along the packing axis. The freeze dried and electrospun pellets are made by folding the original sheet like material into the pellet press. Each fold is held under tension from the compression but the expanding gas seems to give it power to unfurl (Figure 37).

The large error bars in Figure 36 suggested a factor other than the AB content is affecting the foaming of the composites. When a large number of pellets from a single sample were foam tested, a positive trend was observed between the packed density of the pellet and the expansion in the foam test (Figure 36). With a higher density there will be fewer cavities and gas release pathways in the pellet. This suggests that the gas escape will be slowed and a greater pressure will be created in higher density pellets. More compressed gas will eventually form larger bubbles and the overall pellet expansion will be greater.

The 50AB-50PEO samples are unusual in that they seem to shrink as often as expand. When the pellets are closely studied, they expand in the vertical axis but the cross section shrinks, overall resulting in a final reduction in volume. At 120°C melting of the AB and PEO and foaming of the AB are occurring. It is likely, that the foaming is causing the vertical expansion while the AB and PEO are melting into the free volume in the initial pellet.

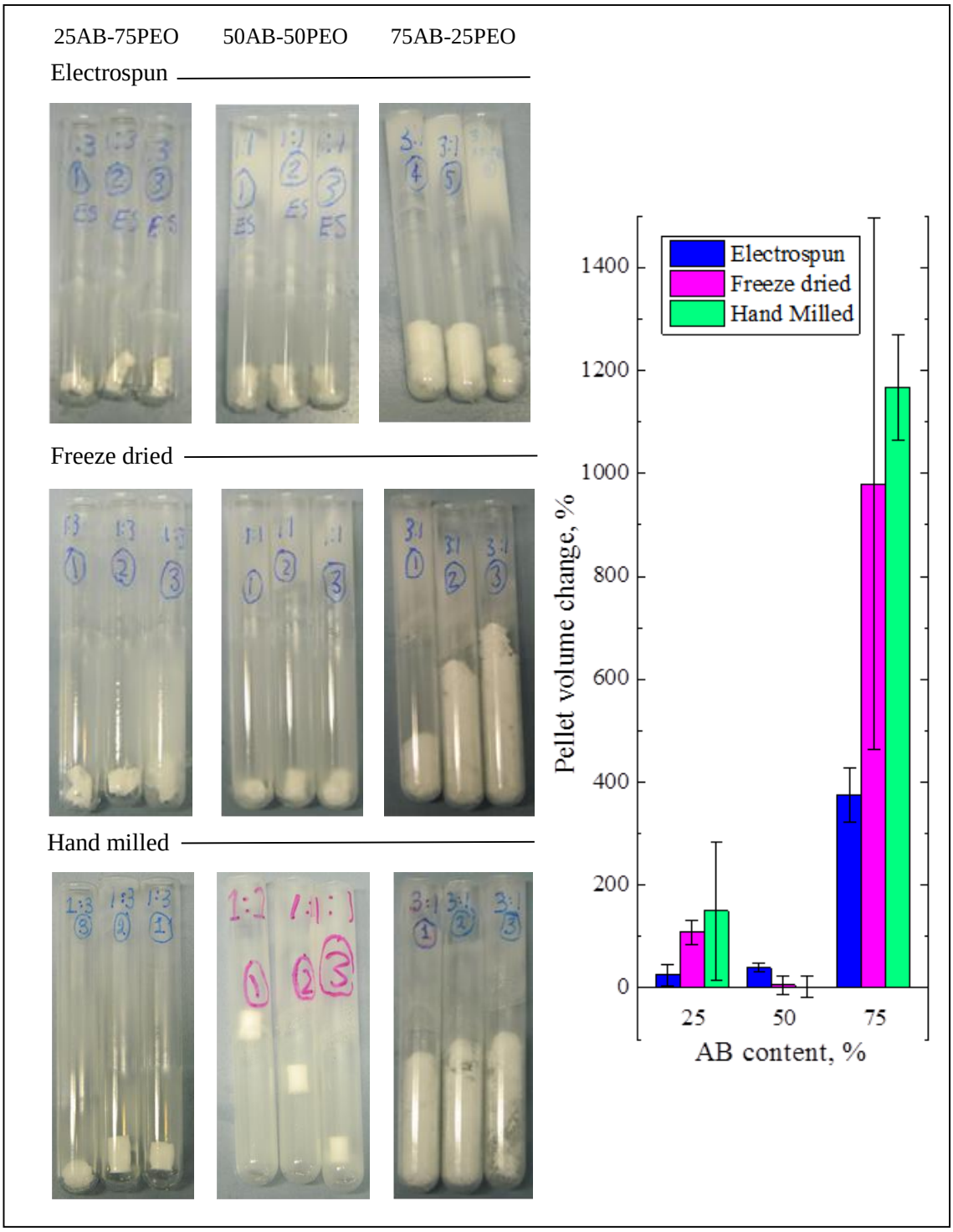

Figure 36: Foam tests with pellets made from electrospun fibres, freeze dried material, and hand milled powder with AB contents, 25, 50 and 75wt%

Pellet press

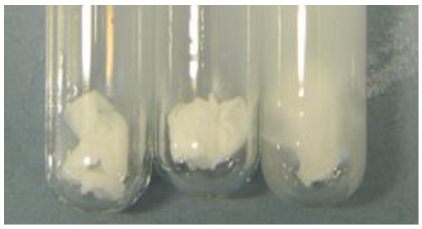

Unfurled pellet

Mat like freeze dried 25AB-75PEO material

Figure 37: Unfurled pellet

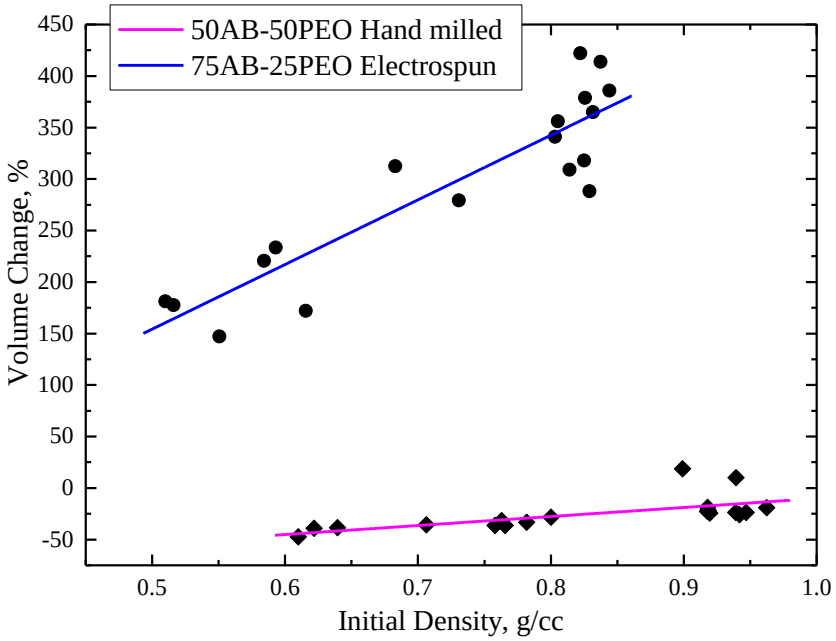

Figure 38: Representative examples of the relation between initial pellet density and foaming.

The final consideration is the white residue that appears on the inside of the test-tube ejected from the AB-PEO samples. When the pellets in the test-tube are immersed in the hot oil, a period of inactivity (about 1 minute long) precedes the foaming. The foam is accompanied by particulates some which seem to explode off the pellet and some which travel out of the test tube in the gas stream; both types collect on the inside of the glass. If an AB composite of this type is to be commercialised particulate filters would be necessary to keep solids from poisoning the fuel cell.

On the whole PEO has a beneficial effect by acting as an antifoaming agent and is a suitable additive to AB. With low AB content, 50% and less, the pellet made from the compressed hand milled material foams the least but when the AB content is raised to 75% the electrospun material has the best characteristics.

4.6 Ramp heating of the ammonia borane-polyethylene oxide composites and pristine ammonia borane

The AB-PEO composites were analysed in a combined thermogravimetric analyser (TGA) and differential scanning calorimeter (DSC) with attached residual gas analyser (RGA). The samples were subjected to ramp heating runs of 2°C/min, between room temperature and 200°C and isothermal heating runs at 80°C, 100°C, 120°C and 150°C. The RGA data are normalised to the mass of AB in the sample and to the argon flow, the TGA data are normalised to the nominal AB content and the DSC data are normalised to the total sample mass.

4.6.1 Hydrogen release, thermogravimetric analysis and differential scanning calorimetry

In Figure 39 the RGA, TGA and DSC of the pristine AB and the AB-PEO electrospun samples are plotted. The TGA hydrogen (m/z=2) trace for pure AB has a profile that is typically associated with pure AB [55], [56]. The hydrogen is released in two stages, the first peaking at 110°C and the second at 150°C. The two stages are the release of the 1st and 2nd hydrogen equivalents (H_2 equivs.). In the TGA, the AB mass loss curve is steepest when the hydrogen signal is highest, implying hydrogen liberation is responsible for the change in sample mass. However, the AB has lost approximately 50% of its mass and as the 2 H_2 equivs. account for just 13wt% of AB, other entities besides hydrogen are being released. In the DSC curve an endothermic melt dip, beginning near 95°C with a minimum at 105°C, occurs before the hydrogen is released. The main melting peak is accompanied by a small pre-dip. This is possibly a signal of eutectic impurities in the raw AB [175]. The AB used for the experiments is 97% pure and the impurities present could perhaps influence areas of the solid to have lower melting points. Or alternatively this feature is the result of the overlay of the exothermic hydrogen release and the endothermic melting. The melting of AB is the result of the dihydrogen bonding network breaking; the AB molecules become mobile and can react easily [176].

The pure PEO does not release hydrogen (not shown) and does not show any mass change over the course of the heating ramp (TGA curve). The DSC trace shows a melting endotherm which begins at 60°C and reaches the minimum at 69°C, this is comparable to the literature melting temperature of PEO (67°C) [103].

Adding PEO to AB dramatically changes the H_2 release profile (RGA), the mass loss (TGA) and the heat flow (DSC). Increasing the PEO content in the fibres (75AB-25PEO→50AB-50PEO→25AB-75PEO) successively lowers the temperature of the onset of the release of the 1st and 2nd H_2 equivs. The associated mass loss also occurs at lower temperatures and reaches a maximum of between 45% and 55% of the initial AB mass. Like with the pristine AB, the

approximately 50wt% mass loss is too high to be due only to hydrogen. In the DSC, the exothermic peaks for the 1st and 2nd H_2 equivs. also occur at lower temperatures as the PEO content increases. This implies that the PEO is actively encouraging the AB to react at lower temperatures.

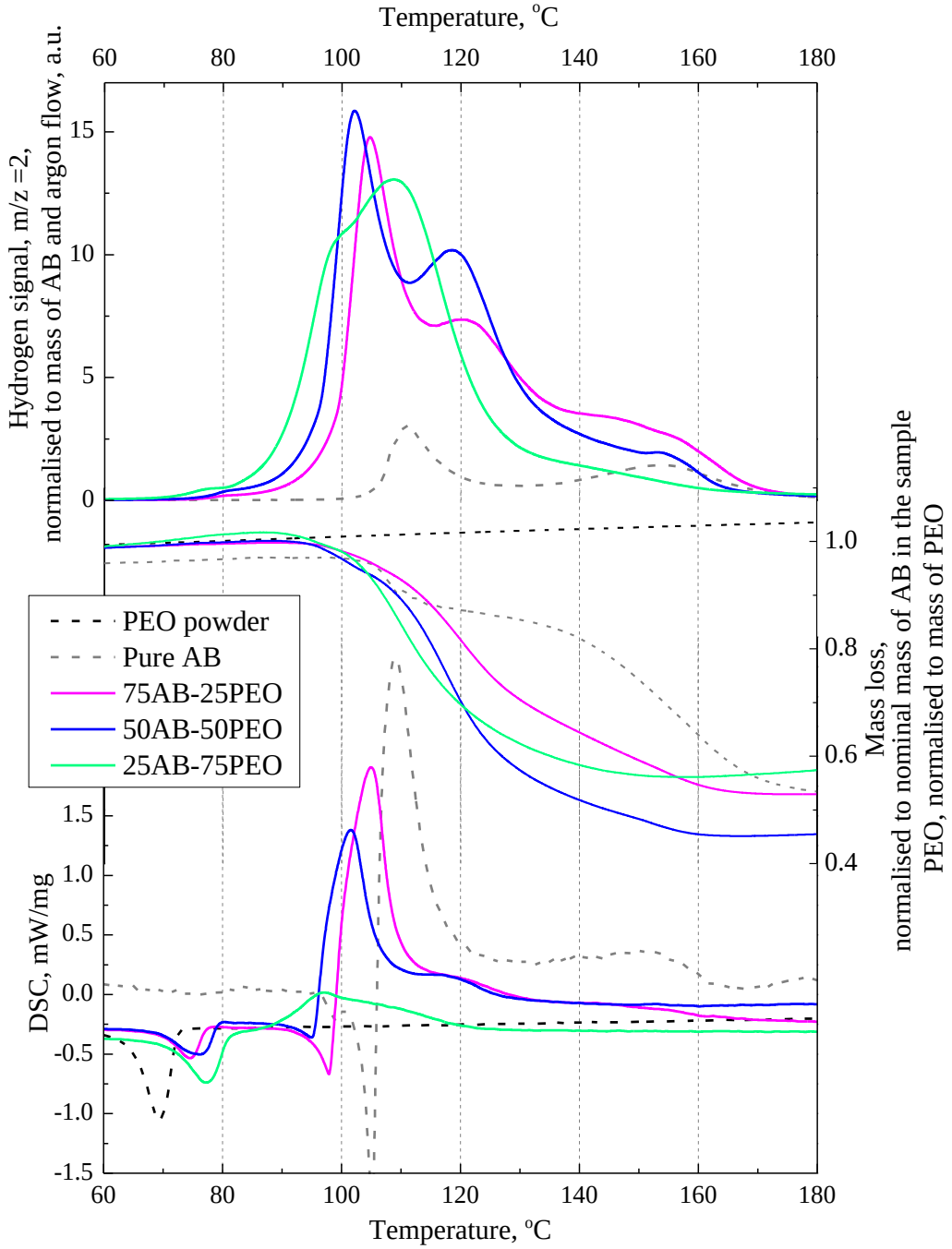

Figure 39: Combined TGA, DSC and RGA hydrogen signal (m/z=2) for pristine AB and the AB-PEO electrospun fibres. As the fraction of PEO in the sample increases, the hydrogen release is activated at earlier temperatures. Mass loss occurs earlier in the AB-PEO composites than in the pristine AB but the final wt% loss is similar (~50%) in both. In the DSC curves, successive addition of PEO reduces the depth of the AB melting endotherm. The lower temperature release of hydrogen is accompanied by an exotherm which reduces the apparent size of the melting endotherm.

There are a few interesting things to notice in the DSC trace in Figure 39. In the composites the PEO melting dip minimum moves successively upwards in temperature (74°C to 76.5°C to

78.5°C) as the AB content decreases from (75AB-25PEO→50AB-50PEO→25AB-75PEO). Also, as expected, the area of the dip reduces as the PEO content is reduced. The electrospinning process is known to align and increase the crystallinity of polymers [129]. Greater crystallinity in a polymeric material will push the melting point upwards. This could account for the rise in melting temperature. Alternatively, intermolecular hydrogen bonding between the PEO and AB could be occurring. These bonds would likely be stronger than the PEO to PEO inter-chain interactions because of the greater polarity/dielectric constant of AB, requiring more heat energy to melt them.

The AB melting curve initiates at lower temperatures as the PEO content in the fibres increases. Further, the depth of the AB melting curve, decreases as a fraction of the height of the following exothermic peak, as the PEO content increase. This suggests two things. Firstly, the PEO is lowering the melting point of AB, perhaps through the AB to PEO bonds suggested above. Secondly, the exothermic peak due to the release of the 1^{st} H_2 equiv. is also occurring at lower temperatures. It is possible that the onset temperature for the exothermic peak has reduced a greater degree than the onset temperature for the AB melting. As the melting has not completely disappeared in the samples, it is likely that some of the AB is in its bulk state. The PEO and AB melting peaks are well separated so it is unlikely that serious AB melting is occurring at the same time as the PEO.

In the X-ray diffraction pattern the 75AB-25PEO and 50AB-50PEO fibres show evidence of containing tetragonal AB by the intense (110) and (101) reflections. In the 25AB-75PEO sample these peaks have all but disappeared so the AB must exist in a different form.

It can be concluded that the AB and PEO have combined into a unique, new phase. It is this phase that initiates the reaction at lower temperatures without requiring the AB to melt.

The freeze dried materials were also tested under similar ramp heating runs. The results obtained are indistinguishable from the electrospun materials.

4.6.2 Impurities

Cumulative integrals of the heating ramps of pure AB and the AB-PEO composite materials were compared to study the impurity levels in the gas stream. For reasons explained in chapter 3, the RGA signal and the normalising technique are not adequate to provide a robust measure of the differences between the quantity of hydrogen released from pure AB and the AB-PEO composites. However, it is possible to compare between the plots for AB-PEO samples.

The hydrogen (m/z=2) release in Figure 40 shows as before, that the PEO reduces the temperature of the onset of hydrogen release. Further, with more PEO the slope of the graph steepens. In the pristine AB, the steps associated with the release of the 1st and 2nd H_2 equiv. are clearly differentiated. As the PEO fraction in the fibres is raised (75AB-25PEO→50AB-50PEO→25AB-75PEO) the release of the 2nd H_2 equiv. moves down and overlaps the peak for the release of the 1st H_2 equiv.

In the composite materials the levels of borazine (m/z = 81) and diborane/borazine fragments (m/z = 27) as a fraction of the hydrogen signal, increase as the PEO fraction increases. Additionally, borazine and diborane first appear from the composites at 105°C, a much lower temperature than the pristine AB at around 145°C. Borazine, $B_3N_3H_6$, has one hydrogen atom per base atom (B or N) and is only formed during the release of the 2nd H_2 equiv. [46], [53], [59]. The earlier release of boron-containing impurities is consistent with the drop in temperature of the release of 2nd H_2 equiv. already observed.

In Figure 40 the levels of water (m/z = 18) and ammonia (m/z = 17), remain similar in the three AB-PEO composites. Water is the principal impurity in the gas stream, and accounts for around 10% of the gas detected in the RGA. As water is nine times heavier than hydrogen this could go some way to account for the massive and unexpected mass loss in Figure 39. Water has not been used in electrospinning the composites but AB has probably absorbed moisture from the air [177]. Acetonitrile was the solvent used in the electrospinning and some residue is expected in the fibres, however it was not observed in the RGA.

4.6.3 Conclusions

From this data several things can be concluded about the effect of PEO on AB. Firstly, PEO is helpful in nucleating the dehydrogenation of AB. Additionally, it encourages all stages of the reaction to occur at lower temperatures. Borazine is observed in the AB trace, but only at high temperatures during the release of the 2nd H_2 equiv. When PEO is added, the ratio of borazine to hydrogen is increased. This could be a feature of the reaction being further along at lower temperatures, or perhaps the PEO is encouraging the formation of cyclic products. Water might be responsible for some of the excessive mass observed.

4.7 Isothermal heating

4.7.1 Hydrogen release under isothermal heating runs

In addition to the heating ramps the AB-PEO fibres and freeze dried composites were subjected to isothermal heating runs in the TGA/DSC with attached RGA. Isothermal runs at 80°C, 100°C,

120°C and 150°C were performed. The RGA data were normalised to the nominal AB content and the argon level.

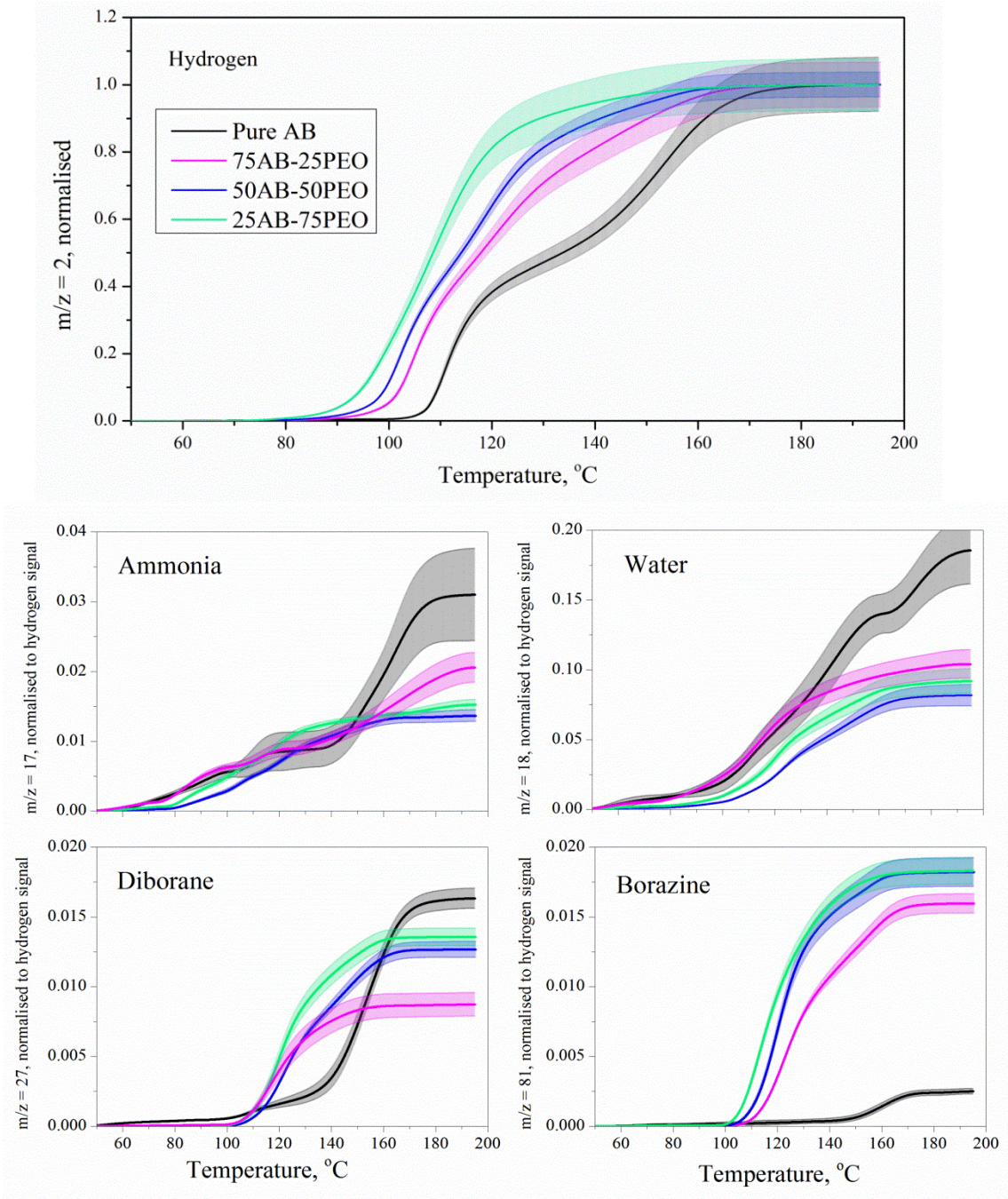

Figure 40: Cumulative integrals of the heating ramps of pristine AB and the AB-PEO composite fibres. It is noted that raising the amount of PEO in the mix aids the hydrogen release but produces more borazine. The data were normalised to the hydrogen (m/z = 2) level at 190ºC and errors in the data are shown as the lighter background.

Following the hydrogen (m/z = 2) trace in Figure 41 demonstrates some of the properties of the composites and AB. Firstly, at a constant 80ºC pristine AB evolves minimal hydrogen. When PEO is added (75AB-25PEO sample), hydrogen is produced and if the PEO content in the composite is raised (25AB-75PEO sample), hydrogen is released at earlier times. In fact, at all temperatures, as the proportion of PEO is increased the onset and the peak of the main hydrogen release will tend to earlier times.

At 80ºC and indeed the other higher temperature runs, a pre-peak (marked *) is visible before the main hydrogen release peak. This pre-peak is only observed in the composites not in the pure AB. Also, the pre-peak decreased in size (with respect to the main hydrogen release peak) as the temperature was raised. This suggests the earlier occurrence of the main hydrogen release peak is over shadowing the pre-peak at 150 ºC. This pre-peak is likely the hydrogen release from the new AB or AB-PEO phase observed in the XRD pattern (Figure 34).

The sample temperature lags behind the set temperature, only achieving its maximum temperature between minutes 10 and 20. This and the ramp heating data indicates that rapid hydrogen release occurs above 80ºC in the AB-PEO fibres without the preceding induction period observed for AB.

The shape of the traces is similar for the AB, 75AB-25PEO and 50AB-50PEO samples. The 25AB-75PEO sample is much broader. Possibly more hydrogen is being released overall (1st and 2nd H_2 equivs.) from the 25AB-75PEO sample but this has not been verified.

4.7.2 Non-hydrogen species released form AB under step heating

Fuel cells require a stream of pure hydrogen to work efficiently and contaminants in this gas stream will poison the cell and reduce its lifetime. For this reason additional species besides hydrogen that are released during the dehydrogenation of AB are undesirable and should be controlled as far as possible to minimise the use of filters in the system.

The presence of borazine in the gas stream is influenced both by temperature and the PEO fraction in the material. In Figure 42 at 80°C no borazine is observed. At 100°C, only the 25AB-75PEO sample releases borazine, the sample with the greatest PEO content. At 120°C all the AB-PEO composites release some borazine but the pristine AB does not. At 150°C, the borazine released by the AB-PEO has increased while the pristine AB appears not to release any. In the ramp heating runs, pure AB began to release borazine at about 145°C so we should expect to see it here. Closer examination of the raw data shows that while the furnace is set for a particular temperature, the sample temperature is recorded between 4°C and 6°C lower: the 150°C heating run is actually at 146.5°C (see Figure 23). Borazine is released as a by-product during in the release of the 2nd H_2

equiv., as this begins above 150°C [55], [56] we would not expect to detect borazine in the gas stream from pristine AB.

The borazine is release is coordinated with the release of the 2nd H_2 equiv. And the ramp heating runs showed that the PEO accelerated the dehydrogenation so that the release of the 2nd H_2 equiv. occurs at lower temperatures. The increased borazine detected from the AB-PEO composites could be due to the accelerated hydrogen release. Or the PEO could be actively catalysing the formation of borazine.

The diborane release, in Figure 43 is similar to that of borazine. At low temperatures, 80°C and 100°C no diborane is observed, while at high temperatures, 120°C and 150°C more borazine is observed form the AB-PEO fibres then for the PEO.

As in the heat ramps, the ammonia signal in Figure 44 in the isothermal heating steps remains fairly constant sample to sample. At 80°C the pure AB does not release ammonia, this is however unsurprising considering no hydrogen is released either. At 100°C and above the pure AB does release ammonia. The PEO-AB samples all release ammonia, and the release occurs earlier as the temperature is raised like the hydrogen.

4.7.3 Conclusions

The dehydrogenation of AB under isothermal conditions initiates at earlier times as the PEO content is raised. However, increased borazine levels are also observed.

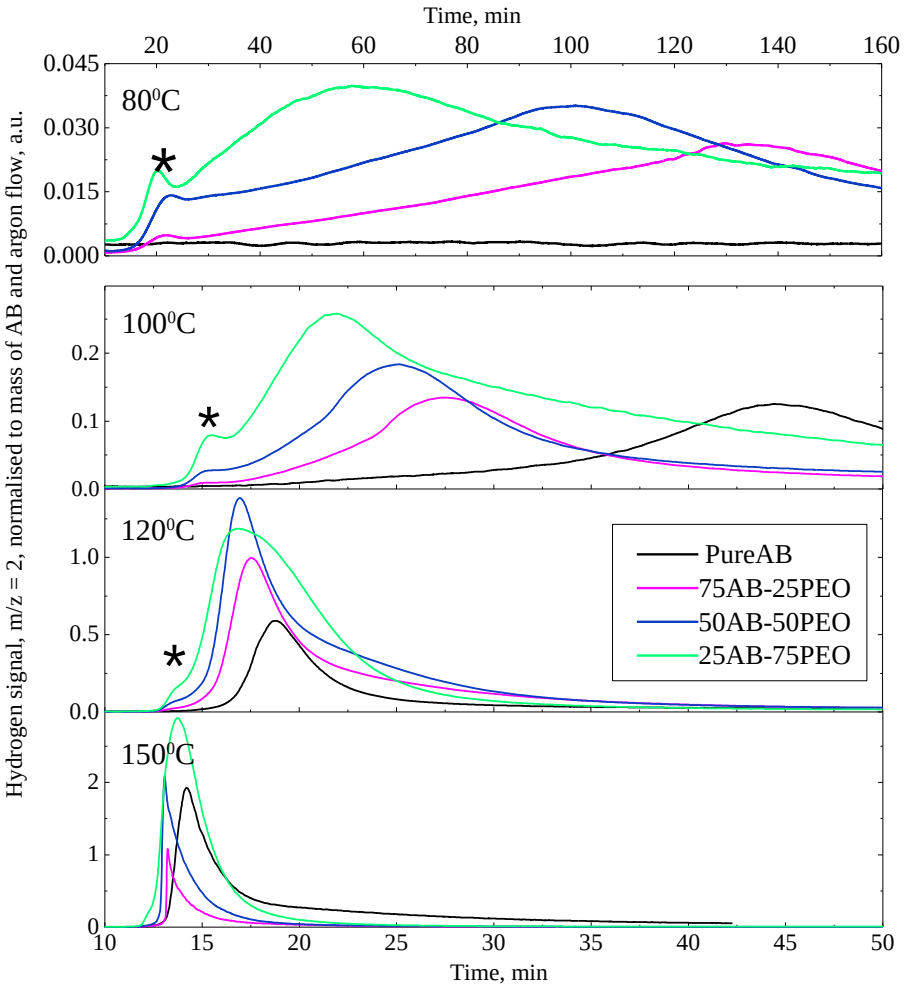

Figure 41: Hydrogen (m/z=2) trace of the isothermal heating runs of pure AB and the composite materials. At all temperatures, the dehydrogenation of AB begins earlier and is accelerated as the PEO fraction of the composite increases.

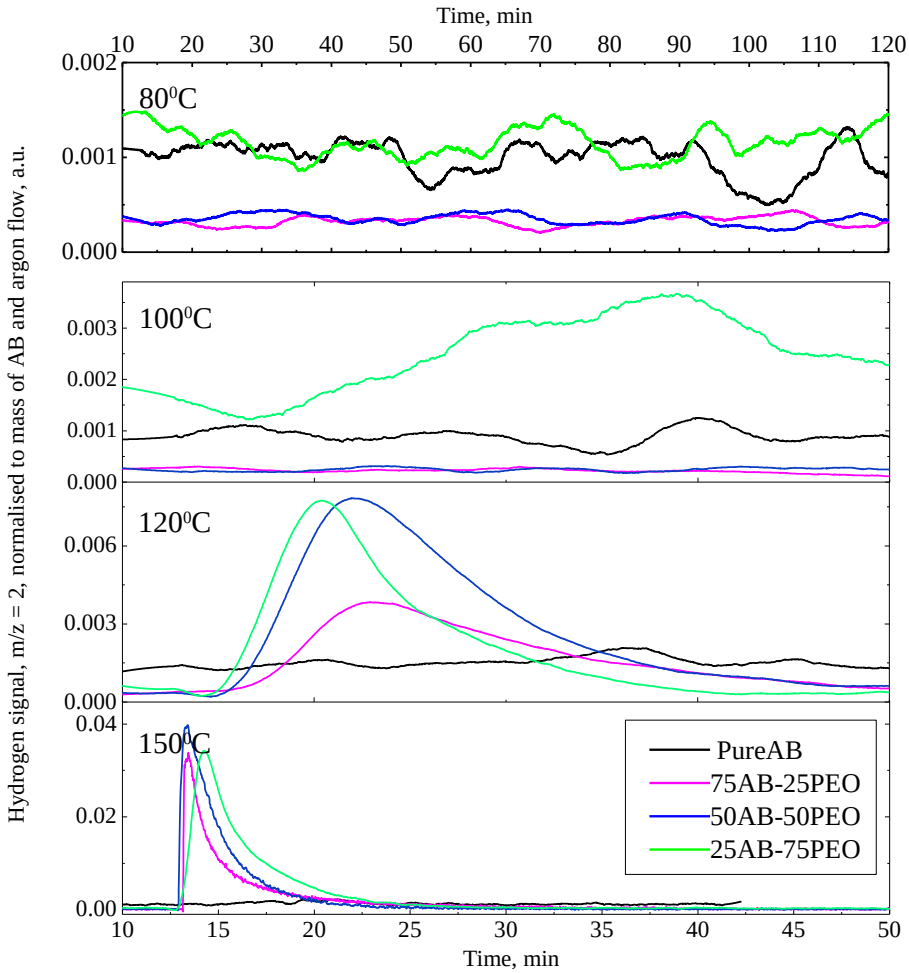

Figure 42: The borazine signal, m/z=81, from pristine AB and the AB-PEO fibres under isothermal heating at 80°C, 100°C, 120°C and 150°C. The pristine AB does not release any borazine at any of the temperatures. This is consistent with literature and the heat ramp data (Figure 40) where borazine is first observed at 150°C. (The sample is actually several degrees cooler than the written value, see experimental chapter 3). None of the AB-PEO fibres release borazine at 80°C but all give off borazine at 120°C and 150°C. At 100°C the 25AB-75PEO is the only sample that releases significant borazine. This is consistent with the ramp heating tests where it is first observed around 100°C in this sample. This suggests the PEO is encouraging borazine to be released.

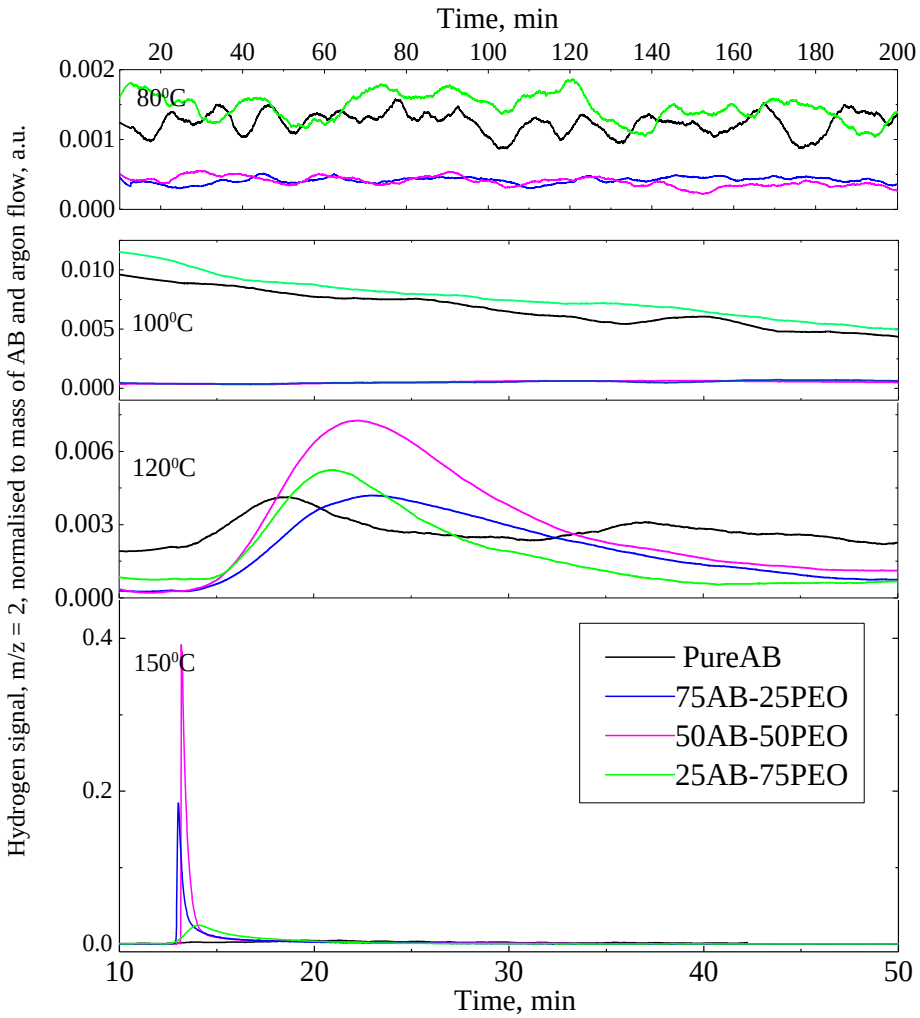

Figure 43: The diborane signal, m/z = 27, released by pure AB and the AB-PEO fibres under isothermal heating of 80°C, 100°C, 120°C and 150°C. No diborane was detected at 80°C and 100°C. At 120°C both the pristine AB and the AB-PEO fibres show borazine. At 150°C the diborane level are higher in the AB-PEO fibres than in the AB. This suggests PEO encourages the formation of diborane at high temperatures.

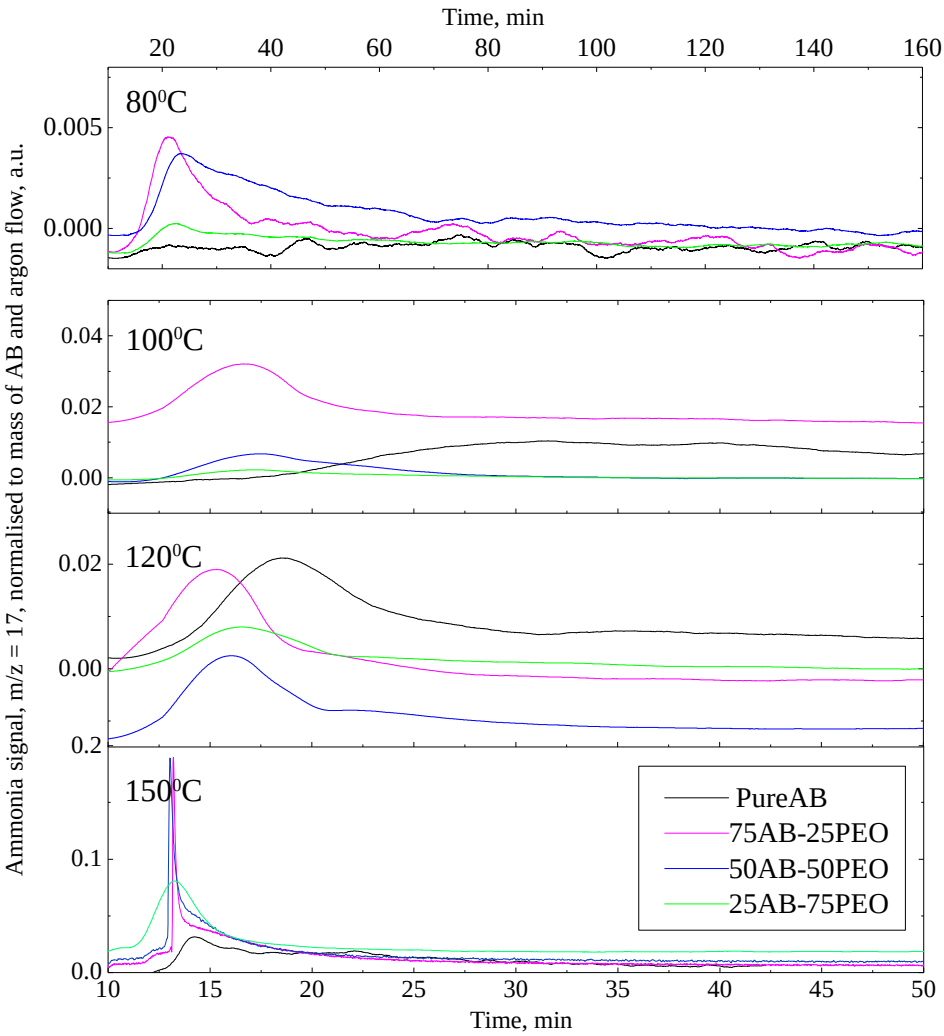

Figure 44: The ammonia signal, m/z= 17, released by pristine AB and the AB-PEO fibres under isothermal heating of 80°C, 100°C, 120°C and 150°C. The ammonia levels are similar in the pure AB and the fibres, but ammonia is released sooner in the fibres. At 80°C AB does not release any ammonia, but then it doesn't release any hydrogen either. This suggests PEO does have a significant effect on the ammonia release.

4.8 Fourier transform infrared spectroscopy

Fourier transform infrared spectroscopy was performed on the as-received AB and the as-electrospun PEO and AB-PEO fibres to study changes that may have occurred in either the AB or the PEO structure and intermolecular interactions as a result of being in a combined composite. Further, samples of the 50AB-50PEO fibres have been heated at 85°C *ex-situ* for different periods of time (up to 2 hours) to examine how the bonding is affected as the hydrogen is released. The absorption peaks of the pristine AB sample were referenced from Zhang *et al.* 2011, Demirci *et al.* 2011 and Xie *et al.* 2009 [178]–[180] and absorption peaks of the PEO have been assigned to Gondaliya *et al.* 2011 and Sundar *et al* 2006 [181], [182].

The experiment being performed on the solids *ex situ*, ammonia, diborane, borazine and other liquid or gaseous products form AB are not likely to be observed.

4.8.1 FTIR of ammonia borane and polyethylene oxide

The AB and PEO FTIR spectra in Figure 45 are typical of literature, the N-H, B-H and C-H stretching modes are well represented in the high wavenumber end of the spectrum and even the peaks in the fingerprint region are distinct and were easily assigned [178]–[182]. The N-H and B-H stretching modes are wide and diversified as they are a collective of the asymmetric and symmetric stretches and may include NH_4 and BH_4 moieties.

The intensity of a peak in the infrared spectrum is determined by the magnitude of the change in dipole moment induced by the vibration [152]. Because of this, infrared spectroscopy cannot be used as quantitative tool except when dealing with peaks of identical origin. Because of the greater difference in electronegativity the N-H bands are expected to be of higher relative intensity than either the C-H or B-H bands. However in our samples, rather surprisingly, the spectrum is dominated by the BH bands and this may be a direct reflection of the strong N->B dative interaction which affects the charge at the boron centre.

The electrospun PEO is crystalline as defined by the triplet peaks 1147cm^{-1}, 1097cm^{-1} and 1060cm^{-1} [89], [181].

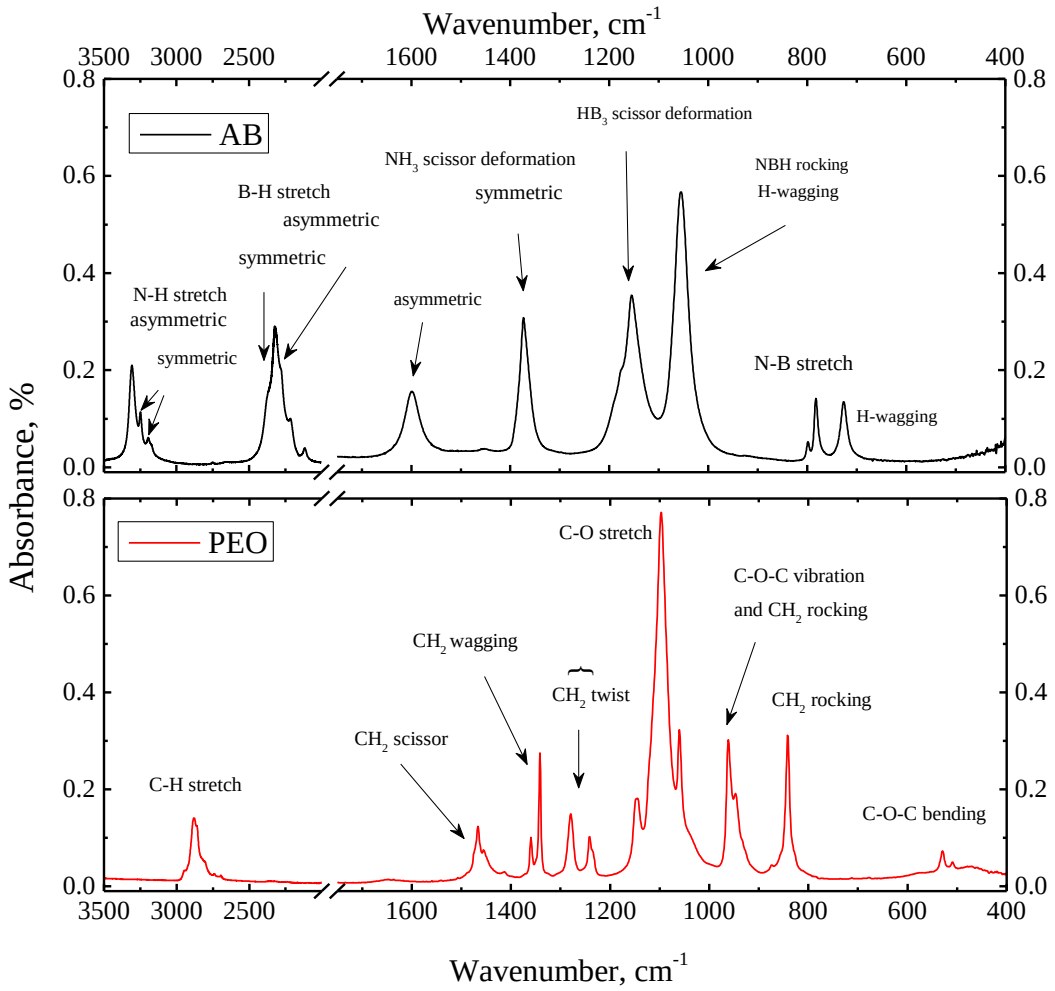

Figure 45: The FTIR spectrum of as received AB, electrospun PEO fibres and 50AB-50PEO fibres. Stretches are identified from literature. [178]–[182].

4.8.2 FTIR of the AB-PEO fibres

The AB-PEO electrospun fibres clearly display features from AB and PEO as well as some additional stretches (Figure 46). This suggests a combination of areas of bulk AB and PEO and also mixed regions where new interactions between the AB and PEO can exist.

A change in the hydrogen bonding will alter the peak position because the strength of the hydrogen bond inversely affects the length and therefore vibrational frequency of the covalent bond [151], [152], [183]. In a simple case, weakening the hydrogen bonds between the AB molecules will move the N-H and B-H stretches to a higher wavenumbers. In Figure 46 in the fingerprint region of the AB-PEO samples, peaks corresponding to the NH_3 and BH_3 have undergone blue shifting (highlighted in grey). The NH_3 symmetric and asymmetric deformations at respectively 1599cm^{-1} and 1376 cm^{-1} both produce peaks at higher wavenumber (1635 cm^{-1} and 1401 cm^{-1} respectively). The BH_3 deformation (B-H scissor) at 1154cm^{-1} and the N-B-H rocking

at 1056cm^{-1}, display a new shoulder in the AB-PEO samples at 1165cm^{-1} and 1077cm^{-1} respectively.

In addition to the differences observed in the FTIR spectra between the pristine AB and PEO and the AB-PEO samples, there is variation between the three AB-PEO samples. In Figure 46, moving from the 75AB-25PEO through to the 25AB-75PEO sample, a successive increase in peak intensity occurs in the new bands at 1635, 1402, 1187, 1165 and 1077cm^{-1} (grey highlights). In the high frequency region a similar shift is faintly observed (grey highlights). This, and the other peaks highlighted in grey shows that the blue shift of the AB peaks is enhanced with the increased availability of PEO.

Correspondingly, the PEO peaks at 1096 cm^{-1} (C-O stretch) and 1279 cm^{-1} (CH_2 twist) have both split into two overlapping peaks in the fibres at 1105 and 1093 cm^{-1} and 1285 and 1275 cm^{-1} respectively (dashed lines).

These bond vibrational changes are expected due to the crystal structure changes of the AB and PEO previously observed in the XRD pattern (**Error! Reference source not found.**). Across the fibre samples, the intensity of the new bands scale with the PEO content, yet the peak positions are constant. This shows that the new features present in the fibres represent an ideal, well-defined and preferred arrangement between AB and PEO. The increase in bond vibrational frequency observed indicates a reduction of AB intramolecular bond lengths which correspond to a lengthening and weakening of intermolecular bonds - the dihydrogen bonds.

Here it is conceivable that the self-to-self dihydrogen bonding is partially replaced by AB-to-PEO hydrogen bonding. Possibly electron donation from the oxygen lone pair to the AB has increased the electron density on the N-H and B-H bonds which shortens them [152].

4.8.3 Isothermal heating of 50AB-50PEO studied by FTIR

In Figure 47 in the high frequency part of the spectrum, 4000 to 2000cm^{-1} over two hours at 85°C the N-H and B-H stretching regions lose intensity while the C-H stretching peak remains constant. Clearly hydrogen loss is only from the AB and occurs at both the nitrogen and boron ends of the molecule. The peaks corresponding to the PEO in the fingerprint region also retain their intensity throughout the experiment, while those corresponding to N-H and B-H diminish.

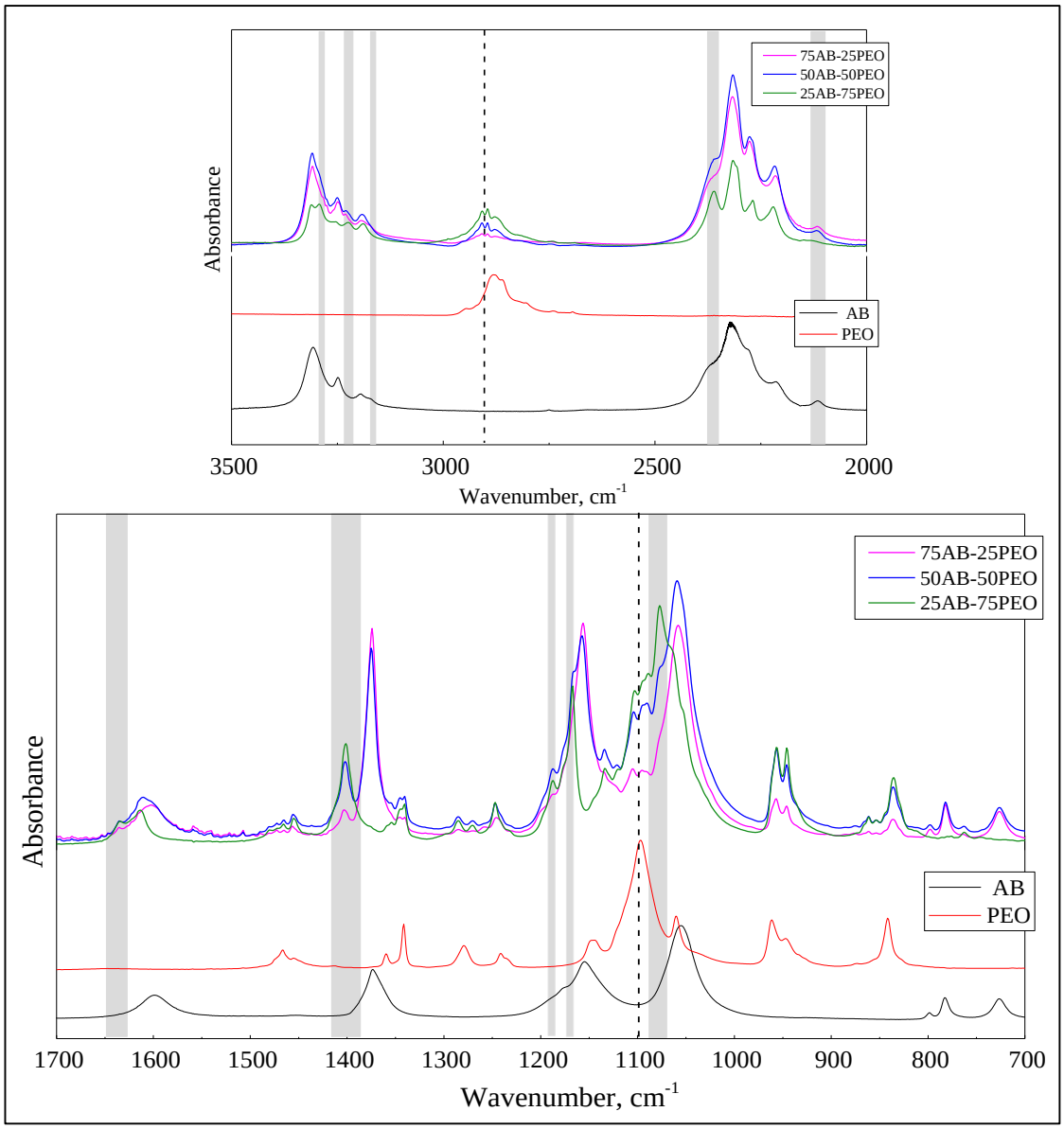

Figure 46: The FTIR spectra of AB, PEO and the three electrospun fibres. As the PEO content in the fibres increases there is a change in intensity (grey highlights), a shift to higher wave number. Additionally there is splitting of the PEO C-O and C-H stretching peaks (dashed line). This supports the previous suggestion that the dihydrogen bonding of AB is being replaced by hydrogen bonding between AB and PEO.

Over the course of the experiment several new peaks arise; they are concentrated in the fingerprint region and their positions are marked in Figure 47. Of these, a significant proportion have been identified as originating from a boron to oxygen (B-O) bond. Considering the proximity of the AB and the PEO in the electrospun fibres, an interaction between the electron donating oxygen and the electron accepting boron is highly likely and these peaks in Table 15 substantiate this hypothesis.

Table 15: The stretching frequencies observed in the FTIR that correspond to B-O bonds

Wavenumber, cm-1	Description [87], [184], [185]
1402	B-O Asymmetric stretch
1024	B-O Interaction
807 & 887-872 & 920-925	B-O Symmetric stretch
696 & 665	B-O out of plane bend

Previously, the peak at 1401cm^{-1} has been associated to an overall weakening of the hydrogen bonding of the NH_3 group and to the symmetric stretching of a newly formed B-O bond. There is third contender for the peak which is a group NH_4^+ noted by Demirci *et al* [179] who put the B-O asymmetric stretch at 1450cm^{-1} [186].

If an NH_4^+ group were present, IR bands would occur also at 3145cm^{-1} (stretching), 3040cm^{-1} (N-H stretch) and 1680cm^{-1} (N-H deformation) as well as the 1402cm^{-1} (bending) [187]. None of these additional bands were observed suggesting that no NH_4^+ was present. Thus the band at 1402cm^{-1} is either a B-O stretch or a change in the dihydrogen bonding of the AB NH_3 group. It is most likely that it is due to a B-O stretch as it was only observed in the heated sample.

The original B-N bending peaks at 726cm^{-1} and 783cm^{-1} (B-N stretch) disappear on heating and simultaneously two peaks at 753 cm^{-1} and 758 cm^{-1} appear. Taylor and Cluff observed a shift to lower wavenumber of the B-N band as the hydrogen atoms were replaced with deuterium [188]. The two new peaks are likely the result of a change in the B-N stretch, either DADB, linear dimers or PAB. This suggests they are related to B-N bonding, probably DADB, PAB, or other fragments and cyclic products associated with PAB. The two new peaks at 479 cm^{-1} or 465 cm^{-1} could not be identified.

4.8.4 Conclusions

These data suggests the PEO and AB interact via hydrogen bonding in the 50AB-50PEO electrospun fibres. On heating hydrogen, loss occurs at both the nitrogen and boron side of AB. Boron to oxygen bonds form. There is no oxygen in the pristine AB. This suggests that the boron to oxygen reaction could be part of the reason the AB in the fibres decomposes at an accelerated rate and produce borazine.

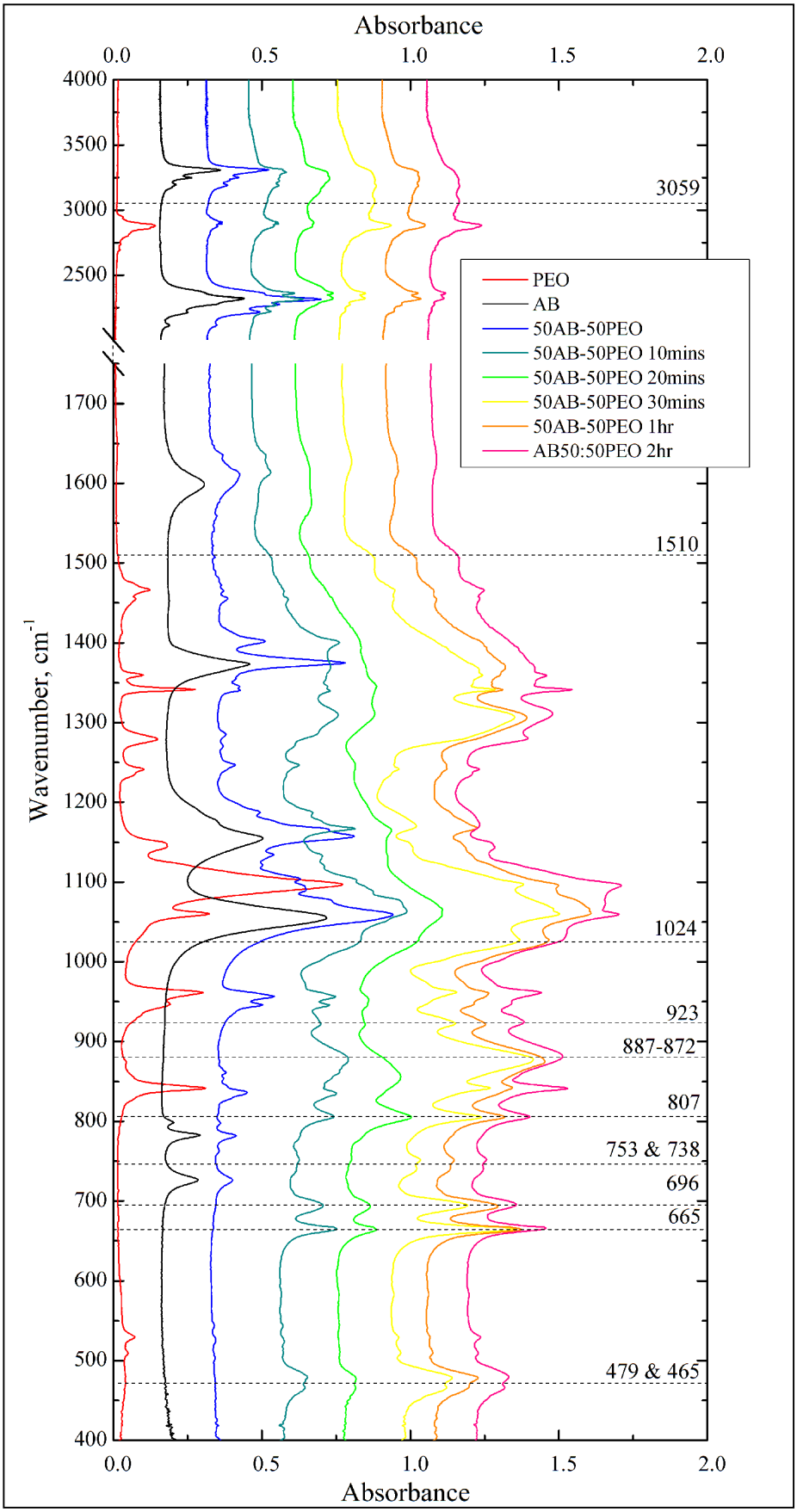

Figure 47: FTIR of the heated samples. New peaks that appear during the heating are labelled.

4.9 Nuclear magnetic resonance spectroscopy

4.9.1 ^{11}B NMR of ammonia borane heated *in situ* at 85°C

NMR spectra were initially recorded at room-temperature before the temperature was rapidly increased to 85°C, where it was kept constant for the duration of the experiment. *In situ* ^{11}B NMR spectroscopy was performed on a pristine AB sample and on the 50AB-50PEO electrospun material. Any gaseous products were able to evaporate during the experiment so we do not expect to observe any peaks associated with ammonia, borazine or diborane.

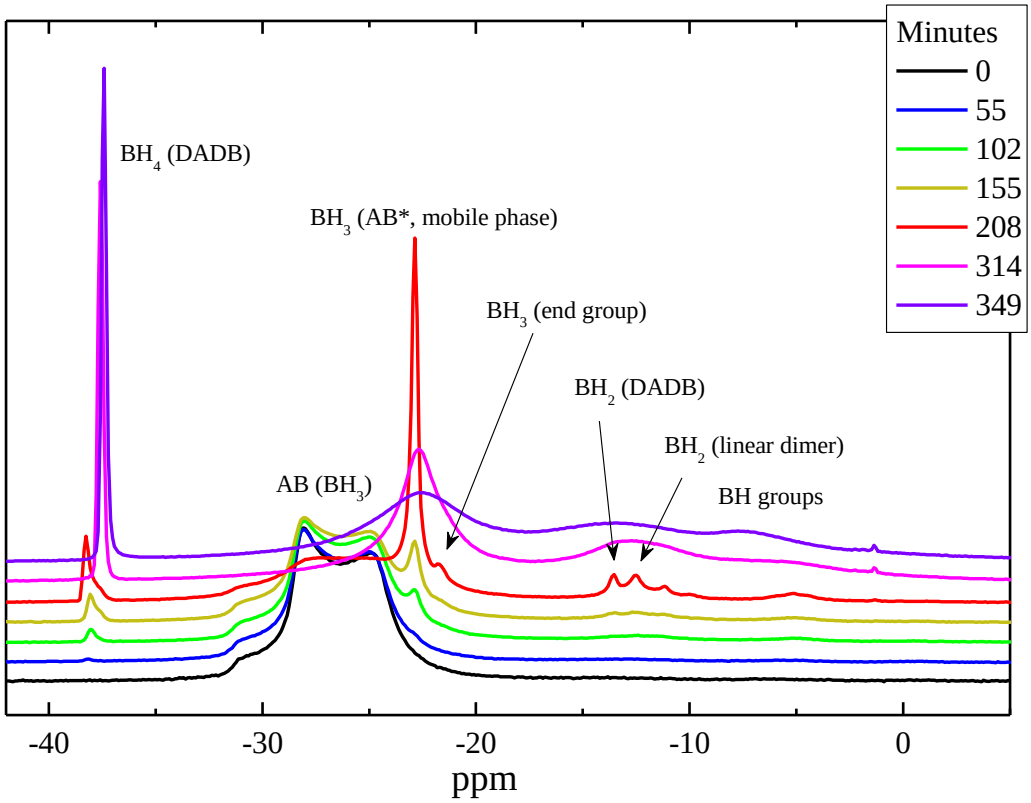

Figure 48: ^{11}B NMR of pure AB at 85°C.

Assignment of NMR spectra peaks in Table 16 was made with reference to literature including both experimental [66], [78] and theoretical studies [82] of AB and its reaction products.

Table 16: NMR peak assignments.

Signal (ppm)	Group
-38	BH4 (DADB) [66]
-25 & -28	BH3 (AB) [66]
-23	BH3 (AB*) [66] or end group [82]
-21.7	BH3 (end group, linear dimer) [66]
-13.5	BH2 (DADB) [66]
-12.5	BH2 [66] (linear dimer) [66]
-11.2	BH2 [66] (PAB) [82]
-9.9	BH2 (PAB) [82]
-7	BH (PIB or branched PAB) [82]
1.2	BO interaction [87]
-14	BO interaction [87]

In Figure 48, BH_3 peaks corresponding to AB were initially observed at -25ppm and -28ppm, these signals reduce in intensity as a signal at -23 ppm corresponding to the mobile phase of AB (AB*) increase. (AB* is not the melting of AB [66].) As the AB* peak drops, signals corresponding to the diammoniate of diborane (DADB) at -38ppm (BH_4) and -12ppm (BH_2) grow [66], [78]. Shortly after, the combined very broad signals at around -5 ppm, assigned to BH and the peaks at -12 ppm, belonging to the BH_2, suggest the presence of either a branched or cyclic PAB or PIB. The spectrum at 208 minutes has high resolution in the BH_2 region. Distinct peaks are observed at -13.5, -12.5, -11.2 and -9.9ppm that are indicative of discrete BH_2 environments. These peaks are consistent with the presence of DADB (BH_4 at -38ppm and BH_2 at -12ppm) [66], linear dimers ($NH_3BH_2NH_2BH_3$) (terminal BH_3 at -21.7ppm and BH_2 -12.5 or -11.2ppm) [66] and tentatively, PAB (BH_2 -11.2 or -9.9ppm) [82].The simultaneous presence of several species is reasonable given the long timescale of the reactions and is attributed to the reaction being at different stages in different areas of the sample.

On close observation the peak assigned to the BH_4 group appears to be the sum of two peaks (-37.5 and -38.2ppm). It is suggested that this difference is due to the existence of two distinct BH_4 environments. At -38.2ppm the BH_4 is associated with DADB, the shift to -37.5ppm indicates decreased symmetry about the boron and such as might be experienced in the vicinity of PAB moieties [189]. This is supporting of the nucleation and growth mechanism proposed by Shaw *et al* [78] where PAB chains are constantly lengthened by -BH_4 working to add other AB molecules but is never used up itself. At 314 minutes it is suggested that the dominant species switches from DADB to PAB, thus the peak assigned to BH_4 shifts from -38.2ppm to -37.5ppm. By the end of the experiment, at 349 minutes, the progress of the decomposition is indicated by the broad peak at -7 ppm, which is assigned to BH and indicates the presence of PIB. It is difficult to produce

PIB from AB at 85°C, however, as the pristine AB has been heated for 6 hours it is conceivable that in some areas of the sample more than 1 equiv. of hydrogen has been lost.

4.9.2 ^{11}B NMR of the 50AB-50PEO fibres heated *in situ* at 85°C

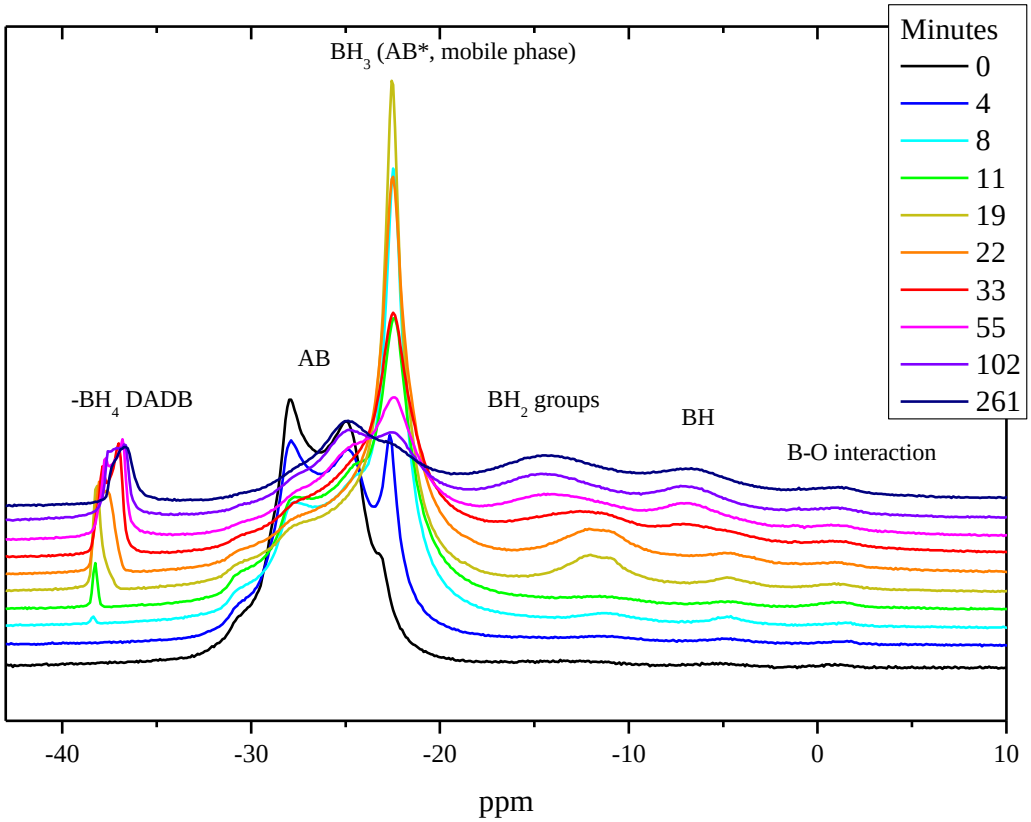

Figure 49: ^{11}B NMR of 50AB-50PEO material heated at 85°C for several hours.

In the 50AB-50PEO sample, the spectra are similar in many ways, though dehydrogenation occurs significantly faster – AB* is observed within 4 minutes and DADB within 8. Unlike the AB sample, the BH_2 area is not well resolved, nor is there any evidence for a terminal BH_3 group. This is suggestive of the formation of a profusion of cyclic products [78], precursors to the borazine observed in the RGA.

The BH_4 peak shifts from -36.7 to -38.3ppm over the course of the dehydrogenation suggesting two distinct environments for the BH_4^+ ion. These are assigned to DADB and PAB respectively, and unlike the AB sample, are observed to coexist for much of the experiment. The coexistence of these environments may be a result of the greater reaction speed. This would allow at time 33 minutes of heating, where in some regions of the sample the reaction has already progressed to the end, while in other parts, DADB is still being nucleated.

Another difference is that as the AB* peak fades (55 minutes onwards) while intensity at -25ppm (also corresponding to a BH_3) emerges. Possibly with continued heating, the pure AB will

eventually demonstrate the same peak, or this could be an artefact of different reaction products, maybe (cyclodiborazanyl) aminoborohydride (BCDB) as this would fit with the shift to lower energy of the BH_2 peaks [78],

Additional peaks were observed at 1.2 and 14ppm which suggests the presence of a B-O bond [87] Chen *et al* also observed a peak at -0.9 ppm from the interaction of BH_3 with the oxygen on THF [125]. This could form as the result of a lone pair donation from the oxygen atom (in the PEO chain) to the boron atom (in AB) or one of its decomposition intermediates.

4.9.3 Conclusions

In Figure 50 the spectra of the AB and 50AB-50PEO have been superimposed to clearly show the differences. It is proposed that during electrospinning, an intimate mix of PEO and AB is formed. The oxygen in PEO has a partial negative charge, $O^{\delta-}$, and the ability to hydrogen bond via lone pair donation. This composite should therefore contain hydrogen bonds between AB and PEO, as well as the traditional dihydrogen bonds between AB molecules. In the 50AB-50PEO sample, the AB* peak is present before any heating has occurred. The formation of AB* being a rate limiting step in the AB dehydrogenation, this could explain the increased reaction kinetics of 50AB-50PEO material. Solid AB and AB* seem to coexist for longer in the 50AB-50PEO, likely the result of the far faster reaction time in the fibres than in the case of pristine AB. In the 50AB-50PEO the B-O bonds appear at the same time as the BH_4 and BH_2 groups. This suggests that the forming of B-O bonds could be the activator for the early appearance of DADB. The width and position change of the BH_4 peak is discussed in the final conclusions.

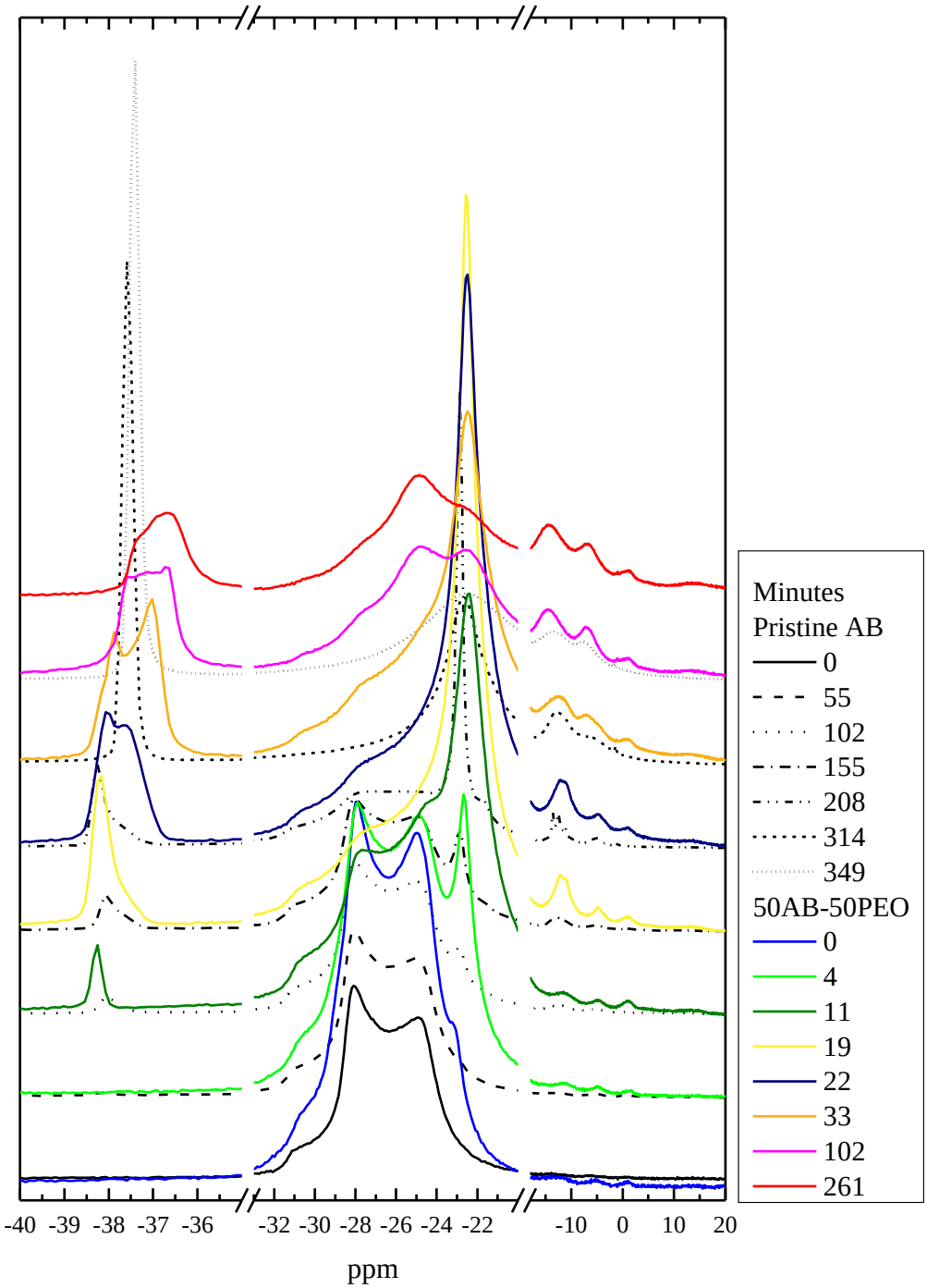

Figure 50: The ^{11}B NMR studies of AB dehydrogenation at 85°C. The pristine AB superimposed on the 50AB-50PEO fibre sample. The AB in the fibres reacts faster, the BH_4 group has a broader peak and B-O bonds occur.

4.9.4 ^{15}N NMR

The natural abundance of ^{15}N is very low, <1%, however it is still possible to collect NMR data if the cycle is run for long enough. Data were collected (at room temperature) from the pristine AB and the as-spun fibres and AB and fibres that had been heated in an oven at 85°C for 6 hours. In Figure 51 the pristine AB and the AB in the fibres both demonstrate a strong peak at -366.8ppm

indicating the presence of tertiary amines, NH_3. However, two small extra peaks (-371.3ppm and -374ppm) are observed for the AB in the 50AB-50PEO. This indicates that the nitrogen environment, for a portion of the AB molecules, changed when PEO was added to the mixture. A shift down field of the nitrogen peak can be due to increased shielding from the magnetic field due to increased electron density on the nitrogen. As suggested above, the most likely explanation is that a portion of the N-H groups are hydrogen bonding to the oxygen in preference to B-H groups.

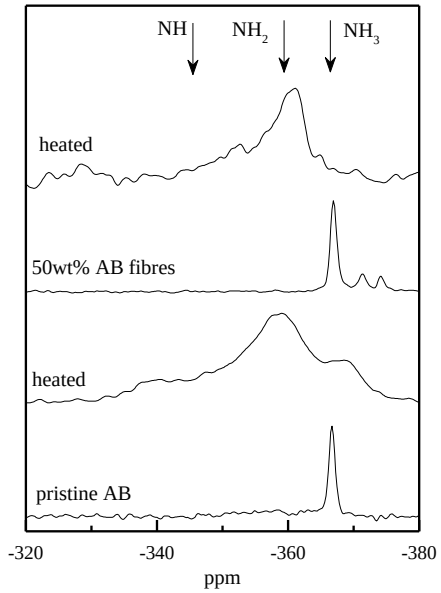

Figure 51: ^{15}N NMR of pure AB and 50AB-50PEO electrospun sample before and after 6 hours heating 85°C when PAB is observed.

The majority of the pure AB transforms to PAB [190] after 6 hours of heating at 85°C. This is expected as in six hours at 85°C AB can release one equivalent of hydrogen [53]. However, there is still some residual intensity from NH_3 groups indicating the reaction is not complete. With the 50AB-50PEO sample the NH_3 peak is totally removed by the heating and the resulting peak is representative of PAB although narrower than for the heated AB. The dehydrogenation in the 50AB-50PEO material is faster than in pristine AB at 85°C so over the same period of time (six hours) we expect to see less NH_3 in the 50AB-50PEO material than in pristine AB.

4.10 *Ex situ* heating

Samples of the electrospun 50AB-50PEO fibre mat composite where encased in baking foil, placed in small test-tubes, and then held in an oil bath at 85°C for distinct periods of time. The heating time ranged from 10 to 180 minutes. On removal, the samples were quenched by plunging the test-tube into iced water, a technique that rapidly reduced the temperature to halt the dehydrogenation.

The fibres, clearly visible in the as-spun 50AB-50PEO material, agglomerate swiftly at 85°C as after 10 minutes no fibres are in evidence. This is expected as PEO in the 50AB-50PEO fibres melts at 76.5°C. The melt has flowed together to fill the gaps between the fibres. The samples are very thin as evidenced by the holes through the material and when handling them they were observed to be very brittle. The initial three images of the fibres that have been heated for 10 20 and 30 minutes respectively, exhibit two distinct regions a rough surface and below it a smooth undulating space. It is likely that during the heating the melted material flows into the vacant space that exits between the fibres, additionally it will seek to reduce its overall surface area. When running the experiment, firstly aluminium foil was used to package the fibres as it provides an inert surface against the sample; unfortunately it adhered strongly to the melted PEO and the sample was impossible to remove. Baking paper was substituted which improved the situation; however there is still some stickiness between the paper and the PEO which is confirmed as being the cause of the rough surface. Between 1 and 2 hours the hydrogen release causes the once smooth craters to become pockmarked with tiny holes or likely gas vents.

With higher magnification the crater surface appears coarser rather than full of holes, this could be due to the AB having changed to PAB and the craters themselves are evidence of large gas bubbles.

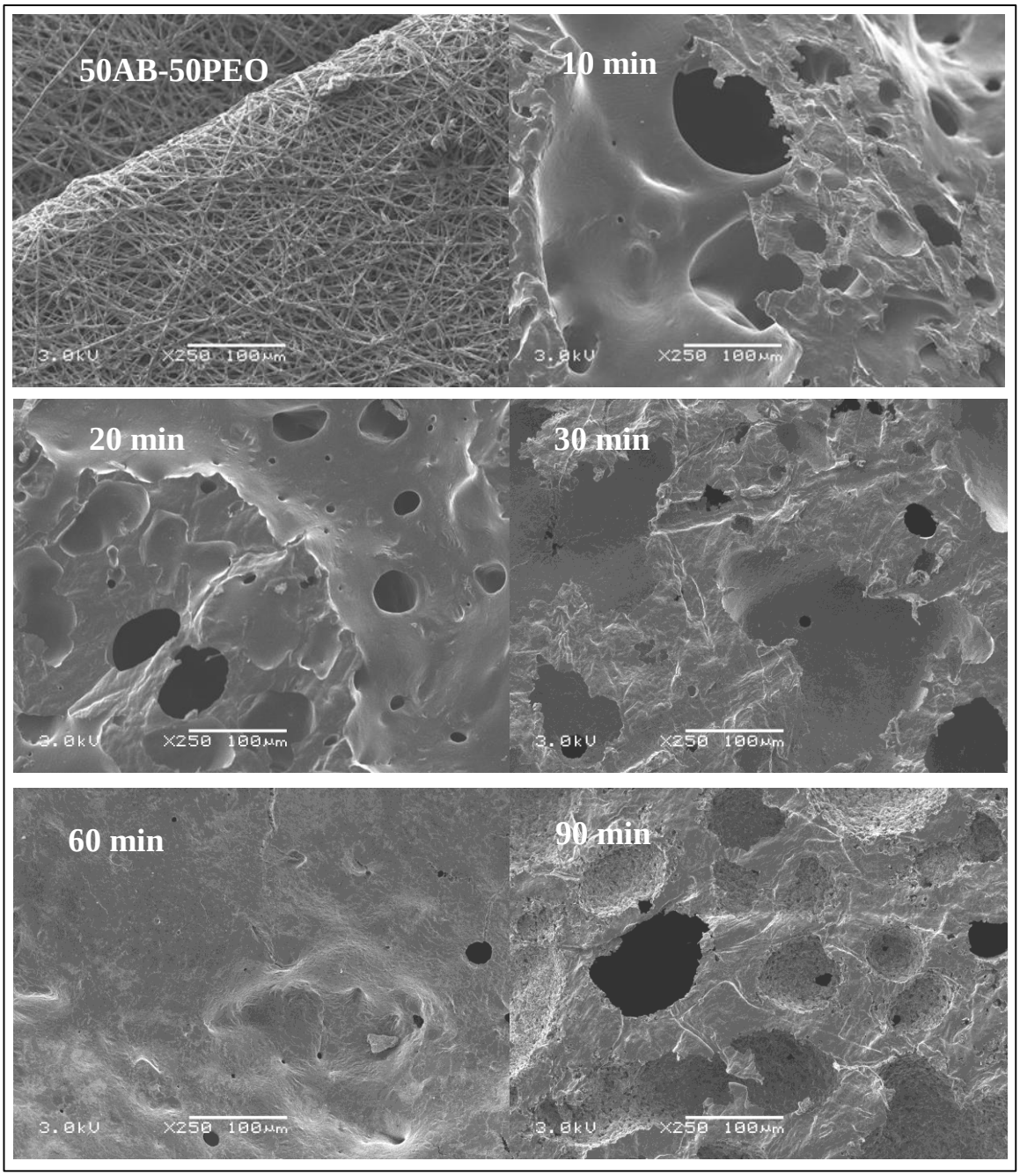

Figure 52: The changing surface of the 50AB-50PEO electrospun fibres at 85°C.

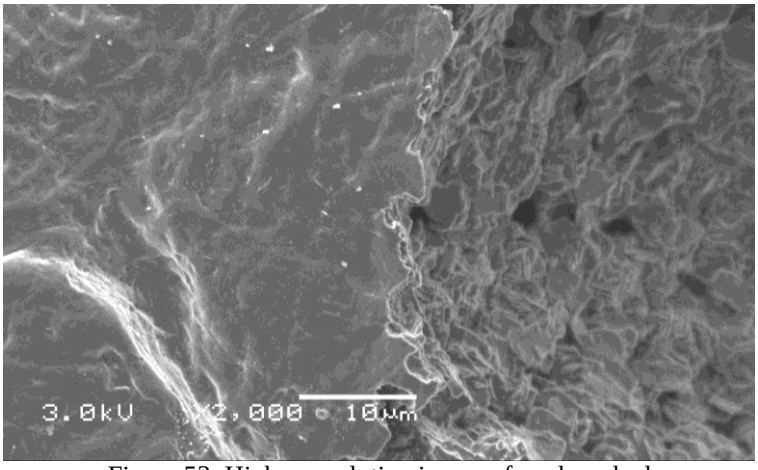

Figure 53: Higher resolution image of pockmarked

4.10.1 Heating XRD

In the XRD pattern (Figure 54) both AB and PEO are present as evidenced by the AB tetragonal crystal structure (110) and (101) peaks and the PEO triplet at 22.5° and the quartet at 27° peaks (see Figure 34). After 10 minutes under 85°C heating, a slight peak shift is observed, probably an artefact of the melted and recrystallized process. After 20 minutes under 85°C heating the sample can return to its crystal form. At 30 minutes the peak features have all but disappeared to be replaced by an amorphous hump at 22°. This amorphous peak indicates a large proportion of the AB in the 50AB-50PEO material has reacted to PAB [190]. Of course this hump must also represent all the PEO in the sample as well, as there are no distinctive peaks it can be assumed that the AB and PEO are well mixed.

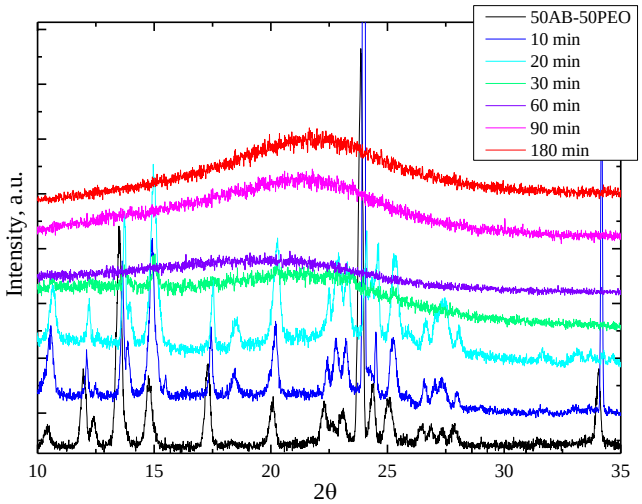

Figure 54: X-ray diffraction pattern of the 50AB-50PEO electrospun fibres heated *ex situ* over 3 hours. The peaks associated with AB and PEO disappear and are replaced with an amorphous hump. A hump at 22° has previously been associated to PAB.

4.11 Discussion and conclusions

4.11.1 Structure of the ammonia borane-polyethylene oxide composites

Electrospinning the AB-PEO solutions as described, produced piles of integral fibres. Some melding of the fibres occurred at cross points indicating that the fibres were not completely dry when they reached the collection plate. The low AB content fibres (25AB-75PEO) were smooth, similar to the pure PEO fibres. Increasing the AB content (50AB-50PEO and 75AB-25PEO) caused the fibres to become rough and porous.

The diffraction patterns of the AB-PEO electrospun fibres showed that both AB and PEO are present in the electrospun fibres. The pristine AB has a tetragonal structure which was maintained in the 75AB-25PEO and 50AB-50PEO samples but not in the 25AB-75PEO sample. The pristine PEO is monoclinic. In the electrospun materials, new peaks, as well as the traditional monoclinic ones, are observed. This suggests some, if not all, of the PEO is distorted by the presence of AB. The diffraction data imply that a new AB-PEO phase has formed.

The vibrational energies of the bonds in the pristine AB and electrospun PEO fibres were observed via FTIR and corresponded to that reported in the literature. When the AB and PEO were combined in the AB-PEO electrospun fibres, new reflections occurred. These new bands suggest a shift form AB-to-AB dihydrogen bonding to AB-to-PEO hydrogen bonding as the PEO content in the fibres increase. Additionally structural changes in the PEO backbone were also observed.

Further, the nitrogen NMR performed suggests that the new hydrogen bonding in the 50AB-50PEO sample is between the H_N on AB and the O in the PEO. The boron NMR signal of the 50AB-50PEO suggests that this new hydrogen bonding stabilises a portion of the AB in the AB* form.

4.11.2 Foaming of ammonia borane and of the ammonia borane-polyethylene oxide composites

The tendency of AB to produce foam while releasing hydrogen, limits its applicability. The hydrogen release of the pure AB in Figure 39 is preceded by an endothermic melting curve, meaning that the gas must pass through a highly viscous liquid, characterised by strong intermolecular interactions, to escape. These are ideal circumstances for bubbles. AB can release hydrogen slowly in the solid phase and more quickly in the liquid phase.

In the AB-PEO composites, the foam production is successively restricted, as the PEO content is increased. It is therefore safe to conclude that PEO is responsible for supressing the foam.

In Figure 39 it is noted that the melting of AB is curbed by the presence of PEO and that the hydrogen release occurs at lower temperatures in the solid phase. If the AB is not melting, there is no liquid to contain the released gases, and so less foaming will occur.

High density pellets expand more than low density ones. Consequently, free volume within the compressed material lessens foam development. This suggests that the interconnected space provides escape routes for the hydrogen and that more free volume minimises gas containment and the build-up of pressure in the pellet.

PEO is used as an industrial antifoaming agent as it contains both oily and polar domains. The polar domains/areas mix well with other polar materials and connect via dipole-dipole interactions. In contrast, the oily areas only exhibit weak intermolecular interactions with like species. When bubbles form, the oily domains constitute the weakest point in the bubble wall, helping it to break sooner (at lower internal pressures) and so control the build-up of foams. As the foam tests were conducted at 120°C, it is safe to assume that the AB is liquid. Also, the NMR and IR experiments show polar hydrogen bonding interactions that intimately connect the AB to the PEO. This suggests that in the composites, the PEO is an integral part of the bubble wall which causes the bubble to burst at lower internal pressures and therefore subdue the foaming.

The PEO used in the pellets has a chain length of 2 million monomer units. The integral fibres formed in the electrospinning show the PEO chains to be entangled. Once the fibre mat is compressed into a pellet, the AB is effectively tied together by an interconnected polymer framework. This framework would hold the AB together and work against the expansion caused by the foaming.

These arguments are not mutually exclusive and may explain different contributions to the antifoaming influence of the PEO on AB.

4.11.3 Hydrogen release

The pristine AB releases hydrogen under ramp heating in two steps corresponding to the 1st and 2nd hydrogen release steps observed in the literature. With successive addition of PEO to the AB, the onset temperatures for these steps are lowered. This suggests the PEO has a positive effect on AB by reducing the energy barrier to dehydrogenation.

The AB-PEO fibres were also analysed under step heats to a variety of set temperatures. At each temperature, earlier release of hydrogen, with a reduced induction period, was directly related to

the PEO content in the fibres. This suggests that PEO improves both the kinetics and thermodynamics of the hydrogen release from AB.

The dehydrogenation of the samples was accompanied by mass loss, the majority of which occurs during the release of the 2nd H_2 Equiv. Even though the mass loss profile (in all cases) corresponded to the hydrogen trace in the RGA, the total mass loss exceeded that accounted for by hydrogen by at least three times. The total mass loss from the pristine AB and the AB-PEO fibres is similar. This indicates the PEO affects the mass loss rate but is not responsible for the excess of mass loss quantity. Other gases such as water, borazine etc. or sublimed solids, could be responsible for the unexpected change. This implies a filter would be required to purify the gas stream before feeding the hydrogen into a fuel cell.

The changing DSC trace profile suggests that increasing the amount of PEO in the material enables the AB to release significant quantities of hydrogen below its melting temperature.

In the AB-PEO composites greater levels of borazine were observed in the hydrogen gas stream than compared with the pristine AB. Also, the borazine was observed at lower temperatures in the gas stream from the fibres (corresponding to the release of the 2nd H_2 equiv.). This strongly implies that PEO causes AB to release more borazine than in its pristine state.

Many studies have previously been conducted on AB dehydrogenation in the presence of liquid ether type compounds, diglyme, tetrglyme, THF etc. [78]–[80], [191]. These studies showed accelerated hydrogen releases but also large amounts of boron containing products. As well as the chemical effect of the ether group, the liquid state of AB was also assumed to be improving the hydrogen release. This work demonstrates that the hydrogens release can be accelerated whilst suppressing the melting of AB. This indicates that the catalytic effect of the group is more important than the physical state of AB at the time of hydrogen release.

4.11.4 Reaction mechanism in the gas stream

There are increased levels of borazine in the gas stream observed from the AB-PEO fibres as compared to AB. The borazine and diborane are observed at earlier times in the AB-PEO fibres (in accordance with the release of 2nd H_2 equiv.), and also the overall levels are higher. This suggests that PEO is encouraging the AB to release hydrogen via the cyclic reaction route.

The *in situ* boron NMR shows that the PEO massively increases the speed of the reaction. In both the pristine AB and the 50AB-50PEO material, the AB first becomes mobile (AB*) before forming DADB. This means that PEO lowers the activation energy to the formation of DADB. AB is stabilised by its hydrogen bonding network [176]. The IR data shows that in the 50AB-

50PEO sample, the bending modes N-H and B-H are changed in the presence of PEO. This indicates that the AB is forming hydrogen bonds to oxygen in PEO. An overall reduction in AB-AB hydrogen bonding would push the AB-DADB equilibrium towards DADB. An alternative way to think about the system is that DADB is a more polar molecule then AB and that DADB would prefer the polar environment supplied by the PEO more than AB [66].

In the 50AB-50PEO, the BH_4 reflection is broader than in AB. Also, throughout the reaction, in the 50AB-50PEO, the BH_4 reflection shifts to higher energy than in AB. In pristine AB, BH_4 reflection shift is suggested as due to the reaction of DADB (highly shielded) to PAB (reduced shielding). (A shift to higher energy in a material indicates a reduction in the shielding effect of the electron cloud around the boron, suggestive of longer B-H bonds.) There are three possibilities: one the BH_4 is in the vicinity of cyclic moieties in preference to PAB, two, the oxygen is interacting with the boron, three, the tetrahedral arrangement of the hydrogens has been disturbed, possibly by forming a bridge hydrogen with the boron end of an adjacent AB molecule. One is unlikely as a good proportion of the AB does react to PAB as seen in the XRD pattern of the heated 50AB50PEO material. Two is also unlikely as BH_4 is negatively charged overall, so the oxygen would donate its electron pair elsewhere, perhaps to the BH_2. The third possibility is the most likely.

One of the greatest differences between the 50AB-50PEO sample compared to pristine AB are the reflections due to B-O interactions. The B-N bond in AB is dative as the N donates into the vacant B orbitals; it is highly probable that the B would also accept electrons from other donating species close by, namely the O.

The FTIR of 50AB-50PEO sample shows that hydrogen is lost from both the nitrogen and the boron end of the AB molecule. Also, it confirms the presence of B to O bonds throughout the dehydrogenation.

4.12 Further work

4.12.1 Structure

This thesis has concluded that PEO and AB in the composites are well mixed, that they interact via hydrogen bonding and that a new AB-PEO phase is formed. The structure of this new phase is however unknown. Further work to determine the crystal structure could include refinement of the XRD pattern guided by molecular dynamics simulations.

4.12.2 Foaming

The reduction in foaming of the AB in the PEO composites during dehydrogenation has been linked to reduced melting of the AB, weakening of the bubble wall and structural integrity of the material. Further work could include viscosity measurements on molten pristine AB and the composites and a detailed study of AB-PEO composites with different chain length PEO polymers.

4.12.3 Impurities

The high level of boron containing impurities in the gas stream from the AB-PEO composite, does not make PEO an attractive additive for AB. Further work should include the study of polymers with different catalytic functional groups.

4.12.4 Reaction Mechanism

The AB in the composites follows both the polymeric and cyclic reaction route. The cyclic route is encouraged by the PEO but no hydrogen is lost from the polymer. The barrier to DADB formation is lowered and boron to oxygen bonds are formed. This is still very poorly understood more research will be needed. Simulation work would be extremely helpful as would selective deuteration of the B and N ends of the AB molecule before performing, IR, NMR and RGA *in situ* studies.

5 Polystyrene and ammonia borane

5.1 Electrospinning polystyrene and ammonia borane

Polystyrene (PS) has been extensively electrospun in the past in a variety of solvents including dimethylformamide (DMF), tetrahydrofuran (THF), t-butylacetate, chlorobenzene, chloroform, dichloroethane, 1,4-dioxane, MEK, and toluene to name but a few [107], [131], [137], [192]–[194]. A blend of equal parts by mass of DMF and THF was selected. AB decomposes slowly in THF [50] so diluting with DMF is prudent. DMF has a low vapour pressure, diluting with THF raises the vapour pressure sufficiently to produce dry fibres. The DMF-THF blend is ideal for single phase electrospinning as it is a co-solvent for both PS and AB [103], [195].

PS of two weight average molecular weights, 350,000g mol^{-1} (350k) and 1,000,000g mol^{-1} (1M), were tested. Various concentrations and spinning conditions were explored to isolate the ideal parameters for the system (Table 17). A suitable regime for the stable spinning of the pure PS solution was identified before AB was added. This initially limits the number of variable parameters and is an efficient way to determine the ideal spinning conditions for a new solution. Once stable spinning of a pure PS solution had been achieved AB was added to give a the required dry mass AB:PS ratios (Table 18).

Table 17: The spinning conditions tested for the PS in a 1:1 ratio of THF:DMF to determine the ideal system parameters before adding AB.

Polymer M_w g/mol	Solvent	Conc. wt%	Flow rate ml/hr	p.d. keV	Observations
PS 350K	1:1 DMF:THF	10	2	8-30	Terrible, multiple jets formed.
		15	1-5		Better at 2.5-5ml/hr with 5keV. But still excess jets observed.
		20			Stable spinning achieved at 2.5-5ml/hr with 15keV. This system is ideal.
		25			Stable spinning achieved at 2.5-5ml/hr with 15keV.
PS 1M	1:1 DMF:THF	1	0.5-10	8-30	Stable at any flow rate. 15keV ideal voltage.
		3			Fabulous at 15keV, flow rate must be <2.5ml/hr to stop multiple jets forming. Makes shiny fibre mat.
		5			Fabulous at 15keV, flow rate must be <2.5ml/hr to stop multiple jets forming. Makes shiny fibre mat.

Table 18: The spinning conditions tested for the AB-PS single phase solution to determine the ideal system parameters to produce stable spinning conditions and dry fibres.

Polymer M_w g/mol	Solvent	Conc. wt%	AB:PS ratio	Flow rate ml/hr	p.d. keV	Observations
PS 1M	1:1 DMF:THF	3	50:50	0.5-10	8-30	0.5-1ml/hr multiple jets! But flow rate between 2.5-10ml/hr much improves the system! Very fluffy fibre mat produced. 5ml/hr with 12keV gives stupendously stable spinning!
			60:40			5ml/hr under 15keV, produced dry fibres.
			70:30			5ml/hr under 15keV, produced dry fibres.
			80:90			5ml/hr under 15keV, produced dry fibres.
			90:10			5ml/hr under 15keV, produced dry fibres.

During the electrospinning of the AB-PS fibres, bubbles were formed in the syringe (approximately $2cm^3$ volume). This indicates that AB was beginning to decompose in the THF probably because the solution was not completely anhydrous. This distorted the flow rate and the reduced slightly the final amount of AB in the fibres. Minimising both the amount of AB in the solution and the time AB spends in the solvated state limited bubble formation. This was achieved with a low AB content and a high flow rate. To reach a high AB to PS ratio, the PS content in the solution must also be low. With a longer chain PS polymer (1M) far lower concentrations (i.e. 1wt%) are sufficient to afford the viscosity and chain entanglement necessary for fibre production. Finally, 3wt% PS solution spun at 5ml/hr flow rate was chosen as a compromise between fast sample production and averting bubble formation when AB was added.

Five distinct AB-PS fibre materials were produced containing nominal AB contents of 50, 40, 30, 20 and 10wt%, these are termed 50AB:50PS, 40AB:60PS, 30AB:70PS, 20AB:80PS and 10AB:90PS respectively. The 50AB:50PS fibres where the first created and tested. No particular lowering of the dehydrogenation of the AB in this sample was observed. In chapter 4, the temperature of the dehydrogenation of AB was lower as the AB content in the AB-PEO fibres was lowered. Therefore, further AB-PS fibres were electrospun, with low AB contents to determine if a similar effect would be observed here.

On the collection plate, the pure PS fibres formed a flat, dry and shiny mat below the nozzle. The fibres made from the PS and AB containing solutions did not lie down flat but instead amassed into a fluffy, cotton wool like, pile. The cotton wool effect is likely due to static charge in the fibres. As this effect was also noticed when electrospinning the PEO-AB solutions it is likely that the AB is responsible for the charge retention.

The vertical build-up of PS-AB fibres resulted in a reduction of the whipping distance over time. This meant, the initial fibres produced had more inflight drying and stretching time than those produced later. AB decomposes in THF it is prudent to assume the first fibres will have a different AB content then those produced an hour later from the same solution. This implies that there is variability across the fibre sample.

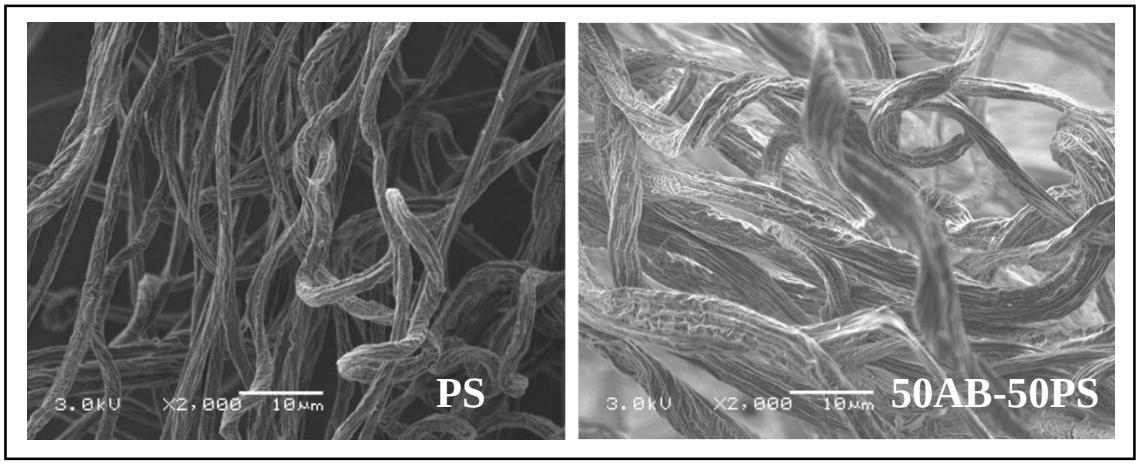

Figure 55: SEM image of PS and 50AB:50PS electrospun fibres.

The electrospun fibres have a ribbon like shape and highly crinkled surface (see Figure 55). This is somewhat unusual as PS fibres are usually rounder and smoother with surface pores caused by humidity in the environment [144], [192], [196], [197]. However, short PS chain lengths, 100-500K, and high solution concentrations, 25-35wt%, are favoured in these studies. Wrinkles can form when an outer skin, caused by fast surface evaporation, collapses slowly inward as the core dries [134], [197]. The low polymer concentration, 3wt%, afforded by the extensive polymer chain length (1M) meant a high proportion of the jet cross section was solvent. Therefore, as the large solvent volume dries out, the skin shrinks a long way inwards resulting in many creases. The PS fibres are 2-3 µm in diameter while the 50AB:50PS are larger, 5-10µm. For the PS sample, the flow rate was kept below 2.5ml/hr while for the 50AB:50PS solution, 5ml/hr was used. The potential field was 15keV in both cases. An increase in conductivity usually results in a decrease in fibre diameter [107]. The AB containing solution is more conductive then the pure PS solution, but it has been electrospun at a higher flow rate. This indicates that for the PS-AB solution the high conductivity has been counteracted by the higher flow rate to give wider fibres.

5.2 Foam tests on the ammonia borane-polystyrene fibres

From each of the five AB-PS fibre samples, three pellets were made for foam testing. (Only two pellets where made from the 30AB-70PS fibres as there was insufficient material for three.) The AB-PS pellets were heated in a standard foam test (oil bath at 120°C). The AB in the PS fibres foamed less than pristine AB. Also, as the PS content was raised a corresponding sequential drop

in the foaming was observed (see Figure 56). In addition to the foam, some solids have detached from the pellets and coated the internal top half of the test-tubes. Again, as the PS content is raised, the amount of solid residue drops.

The high AB content sample (50AB-50PS) expands and foams as a whole in all directions, reminiscent of the 75AB-25PEO pellet. The median AB content samples (40AB:60PS and 30AB:70PS) expand somewhat before the AB bubbled out of the surface of the pellet. The low AB content pellets (20AB:80PS and 10AB:90PS) elongated along the vertical axis, the direction in which the compression force was applied. This suggests that the electrospun PS has formed a flexible network that the foaming AB can swell. When the maximum distortion of the PS is reached the AB foam continues growing (if sufficient AB is in the sample) and bubbles out of the pellet surface.

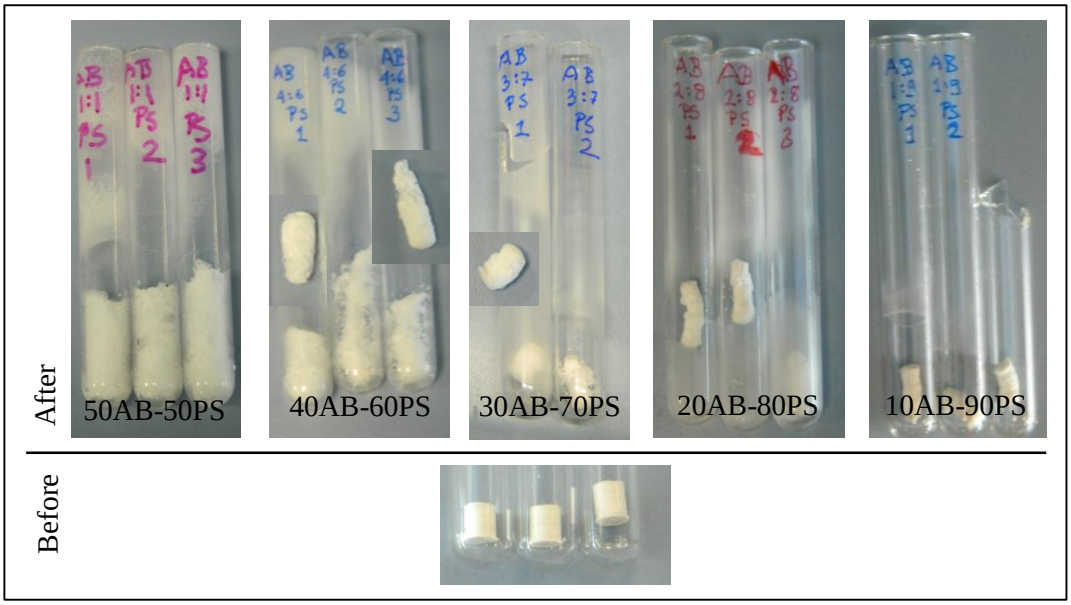

Figure 56: Foam testing AB-PS pellets made from the electrospun fibres. Foaming and residue on the test tube wall is inversely related to the PS content. Images of the final pellets once removed from the test tube have also been inserted.

This implies that PS is not actively responsible for the suppression of foaming in the samples. The high PS containing samples foam less, as the actual AB content and density in the samples, is low.

5.3 Ramp heating of ammonia borane-polystyrene fibres

The AB-PS samples were tested under a standard ramp heating run in a combined thermogravimetric analyser (TGA) and differential scanning calorimeter (DSC) with attached mass spectrometer (mass spec). The TGA and DSC data has been normalised to total sample

mass and the mass spec data has been normalised to the nominal mass of AB in the sample and the argon level (see experimental chapter for more details).

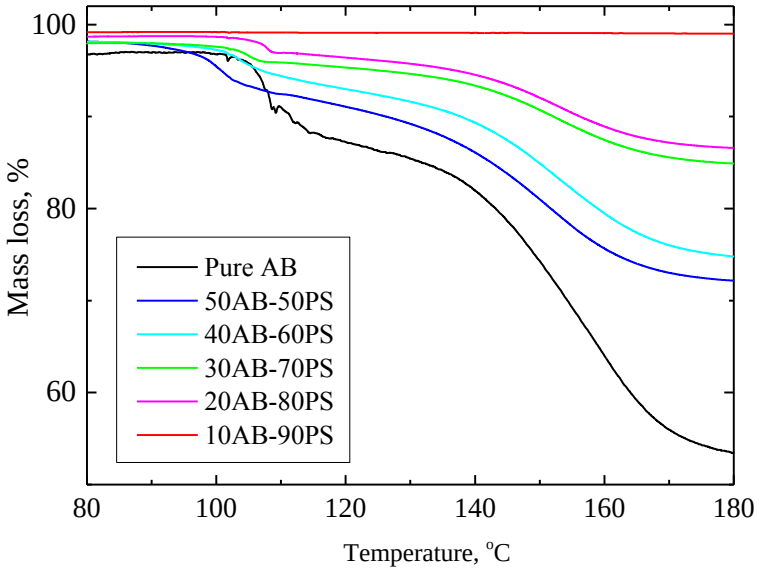

Figure 57: TGA trace of the mass loss of the AB-PS fibres when subject to a 2°C/min temperature ramp between room temperature to 200°C.

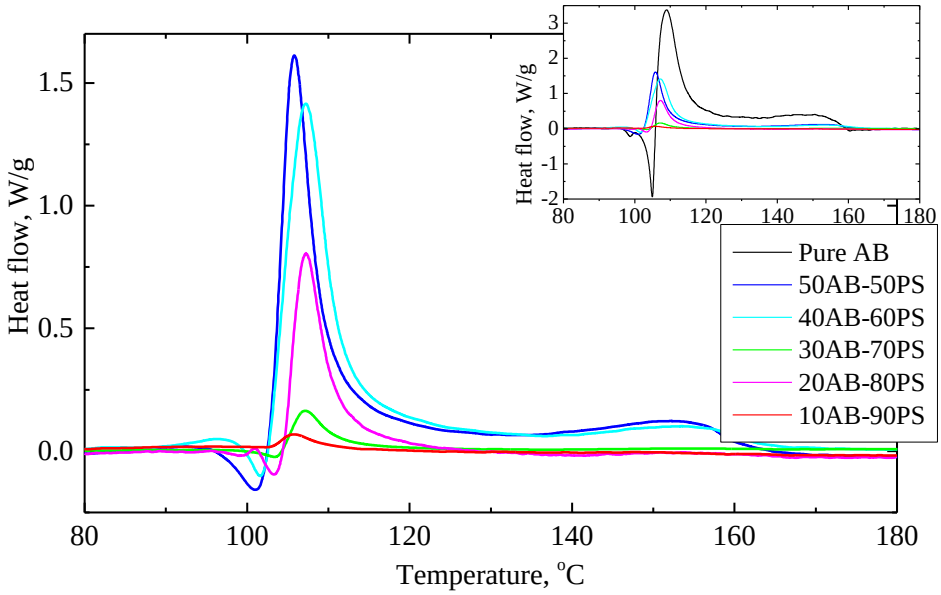

Figure 58: DSC traces of the AB-PS electrospun fibres under ramp heating rate of 2°C/min.

The total mass loss increases with the nominal AB content in the fibres in Figure 57. The mass loss profile is similar for the pristine AB and the AB-PS fibres. However, some of the AB-PS fibres, particularly the 50AB-50PS sample show mass loss to begin at a slightly lower temperature then pure AB.

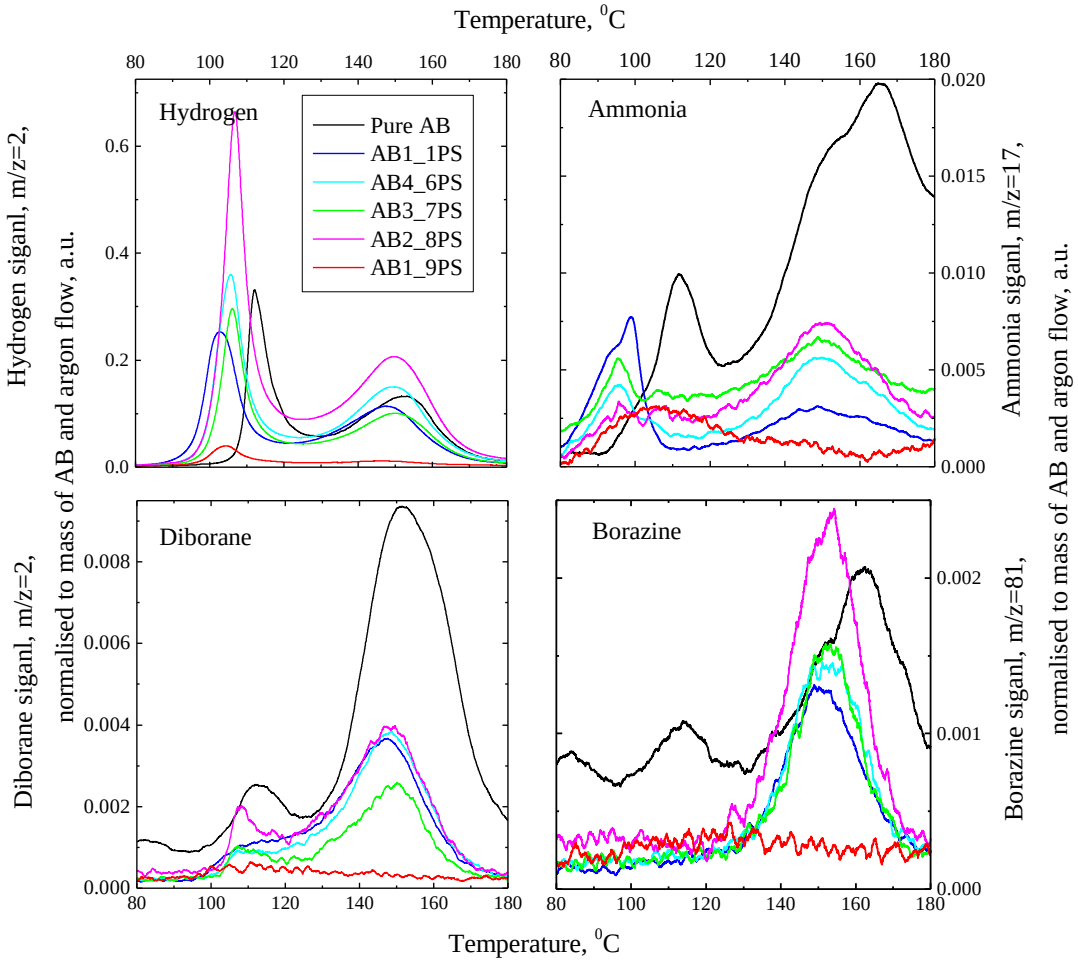

Figure 59: The hydrogen and impurity trances for the AB-PS fibres. When combined with PS, AB releases hydrogen at lower temperatures than when in its pristine state. The PS does not appear to have a significant effect on the impurity levels.

The DSC curve profiles of the AB-PS fibres in Figure 58 are similar to that of pristine AB; endothermic dip indicating melting followed by two exothermic peaks for the release of the 1st and 2nd hydrogen equivalents (H_2 equiv.). Yet, the graph shows some differences. Firstly, the peak of the first exothermic dip occurs at a slightly lower temperature in the AB-PS fibres than in the pristine AB. And secondly, the endothermic melt dip is shallower as compared to the exothermic peak in the AB-PS fibres than in the pristine AB. This suggests that hydrogen release starts earlier in the AB-PS fibres than in pristine AB, before the AB has melted.

Let us take a quick look at the impurities that accompany the hydrogen release form the AB-PS fibres. In Figure 59 the peaks, for the release of the 1st H_2 equiv. from the AB-PS samples, reached their apex around 104°C, a good 8°C before the pristine AB which peaks at 120°C. The ammonia and borazine graphs also show that the AB-PS samples react at lower temperatures than pristine AB. The actual impurity levels in the hydrogen gas stream cannot be accurately determined from this plot. However, the plot implies that while the AB in the fibres decomposes at lower

temperatures then the pristine AB the impurity levels do not vary significantly across the AB-PS samples.

Some difference between the dehydrogenation of pure AB and AB-PS fibre samples as a whole is observed. However, no meaningful trend connecting the AB-PS samples is observed. This suggests that the PS itself does not have an active effect on the dehydrogenation of AB. Rather something else in the composites is responsible.

5.4 Conclusions and discussion

Here it is shown that PS and AB can be electrospun into homogeneous fibres from a single solution. The fibres produced are flat and wrinkly likely due to the low polymer content.

The foam tests show that successively adding PS to AB via electrospinning successively supresses the foaming. However, the AB in the fibres behaves in a fashion similar to bulk AB. This indicates that the reduced foaming is in fact the result if the reduce amount of AB in the materials.

The dehydrogenation of the AB in the AB-PS fibres is initiated at slightly lower temperatures than the pristine AB. However, no trends are observed when the PS content in the AB-PS fibres is varied. This suggests that the PS itself is not responsible for lowering the AB reaction temperature.

Perhaps, some of the AB in the fibres is nanostructured. As AB is polar molecule and PS a nonpolar polymer it is likely that they would repel each other in solution and heterogeneous bulk regions would occur in the solid fibres. Yet, it is possible that some AB has become isolated in PS nano-cavities [100] and it is these nano-sized AB particles that react first and initiate hydrogen release in the bulk sections of the AB at lower temperatures. This theory seems somewhat farfetched and it is possible the AB was activated in a different way.

All the solutions had the same PS content, 3wt%, and were electrospun with the same kit under the same conditions (5ml/hr at 15keV). The amount of AB was the only changing factor. In all the cases, during the electrospinning gas was evolved inside the syringe and this was identified as the AB decomposing in the THF [79]. This means, the AB in the fibres is likely contaminated with some small amounts of partially reacted AB such as DADB or PAB. It has been shown previously that adding DADB to AB significantly reduces the induction time to hydrogen release [56]. As all the electrospun AB remained in solution for a similar period of time it is possible that a similar percentage of AB was converted to DADB in each case and distributed within the bulk AB.

The foaming and dehydrogenation behaviour of the electrospun AB-PS fibres shows that nanostructured AB was not achieved. It is suggested that the lowering of the induction temperature of the AB in the fibres is due to the processing parameters. AB in this form is not suitable as hydrogen store for a fuel cell as a 50% weight concession has been made and the hydrogen release properties have not been significantly improved.

5.5 Further work

Combining AB with PS via electrospinning does not, according to the data presented here, ameliorate the hydrogen release properties of AB. Further work on this system is therefore not recommended.

6 Ammonia borane and clay

AB was combined with several distinctive clays; montmorillonite (MONT), laponite (LAP), imogolite (IMOG) and halloysite (HAL). These composite materials were prepared via freeze drying and contain equal amounts by dry mass of AB and clay (1:1 AB:clay). Freeze drying limits the carrier solvent choice to one – water to which 5wt% clay was added. The IMOG and LAP dispersed well and formed gels but the HAL and MONT did not dissolve and sedimented on the base of the jar. The gel from the LAP and IMOG clays necessitated pre-dissolving the AB, so for consistency, all the solutions were made by mixing the clay into an AB solution.

The HAL used in the experiments was dry powder, as HAL is not amenable to rehydration this could have be the cause of its inability to dissolve. [116]. In the case of MONT, while the layers swell, the AB water mix was not suitable to totally exfoliate the layers. This is probably due to the high interlayer charge that binds the layers together [198].

6.1 Scanning electron microscopy

The microstructure of the four AB-clay composites was studied by SEM and the images are displayed in Figure 60. The AB-LAP and AB-IMOG composites exhibit dramatic structural change as compared to the pure clay while in the case of AB-MONT and AB-HAL composites, little contrast is observed.

The LAP clay is synthetic and of high purity which is reflected in the regular, square edged particles observed under the SEM. The freeze dried LAP-AB material is porous and flaky with a cracked, pitted surface. When AB is added to IMOG, the material produced is composed of thin, transparent flakes that taper to points. The HAL tube bundles are well recognised in both the pure and the composite material. The only noticeable difference is the increase in grain size when AB is added. This suggests that the AB is binding the HAL tubes together. In the case of MONT, no differences between the clay and composite are observed.

These images indicate that the IMOG and LAP have become well mixed through the freeze drying process with the AB. The HAL and MONT have not blended well with the AB, most probably as a result of the unsuccessful dissolution.

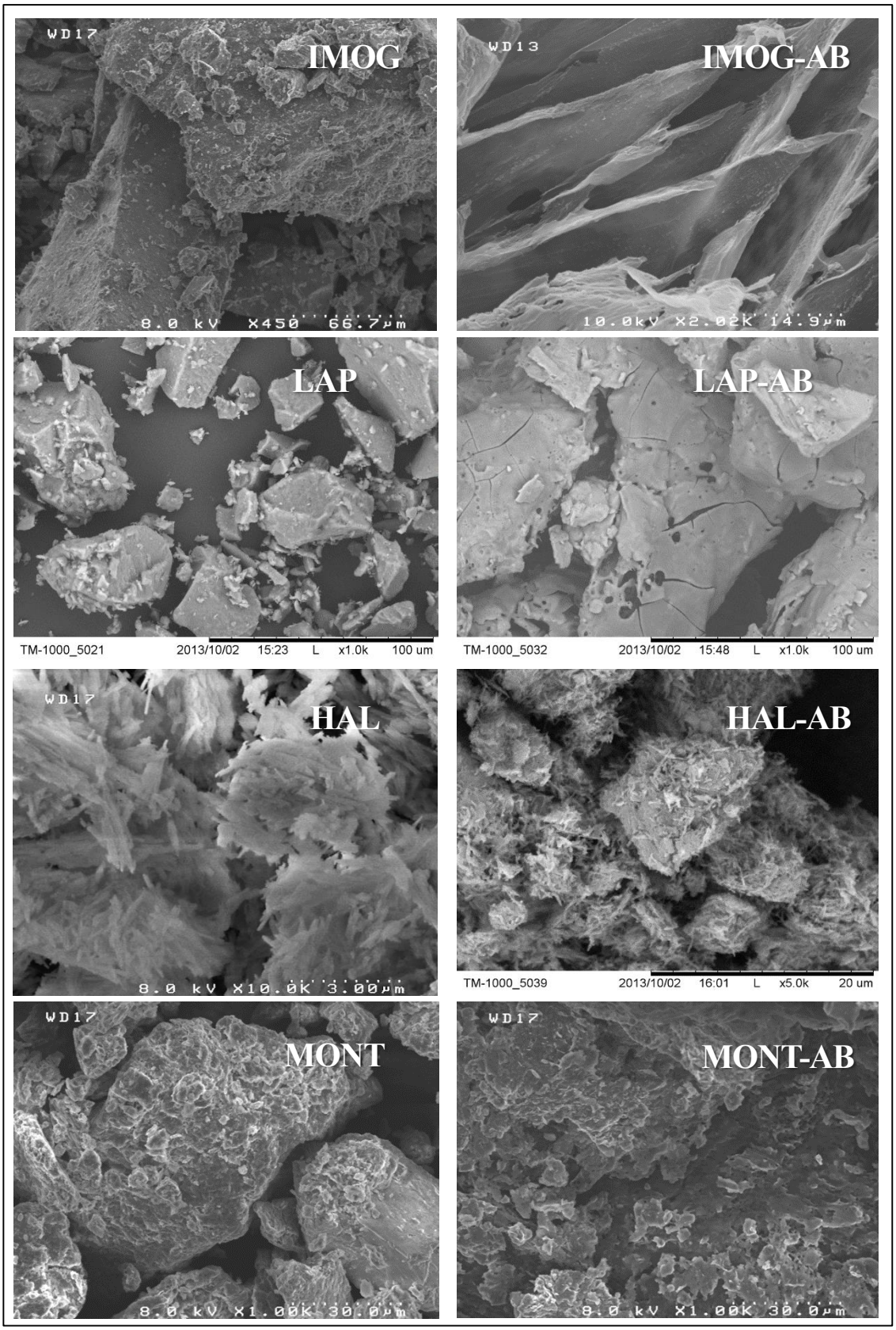

Figure 60: SEM images of the four AB-clay composites. In the case of IMOG and LAP, the significant morphology change between the as received clay and the AB-clay composite, suggests intimate mixing of the clay and AB has been achieved.

6.2 Foam tests of AB-clay composites

Elimination of the foaming and expansion associated with the H_2 release from the AB is key to its commercial prospects and so the foam test is the first test a new material must pass. Pellets where made in the usual way from the 1:1 AB-clay freeze dried materials and the foaming response on heating was tested with the standard foam test method previously described in the experimental chapter. In Figure 61 a reduction in foaming is observed for all the clay-AB composites. Two contrasting effects were noticed. Foam and expansion, with some large bubbles, are observed in the HAL and MONT composites, while a more explosive change, with a greater solid loss but fewer bubbles, is noted in the LAP and IMOG materials.

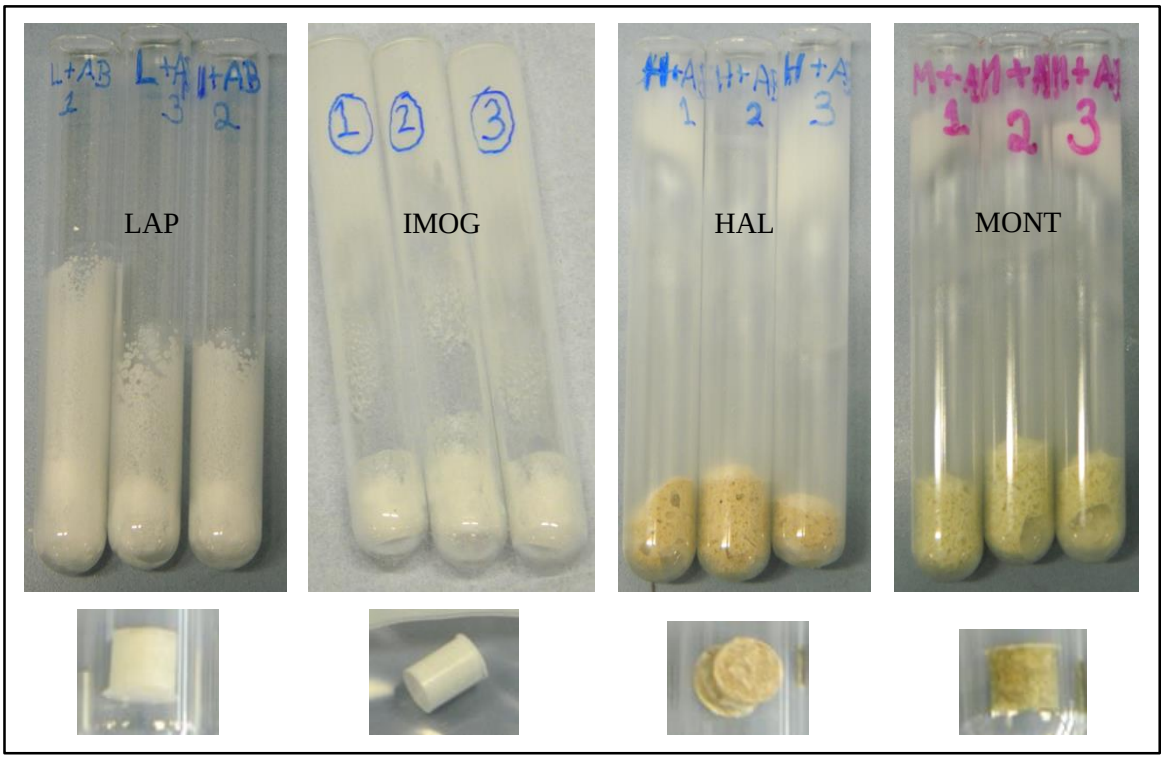

Figure 61: AB:clay 1:1 ratio pellets post foam testing.

The LAP and IMOG pellets could be removed post heating while the HAL and MONT samples adhered to the internal wall of the test-tube. The LAP pellet was extremely fragile, crumbling instantly while the IMOG version was swollen but maintained its integrity, see Figure 62. This suggests that the tubular nature of the IMOG can provide a stronger framework than the disk shapes that are LAP.

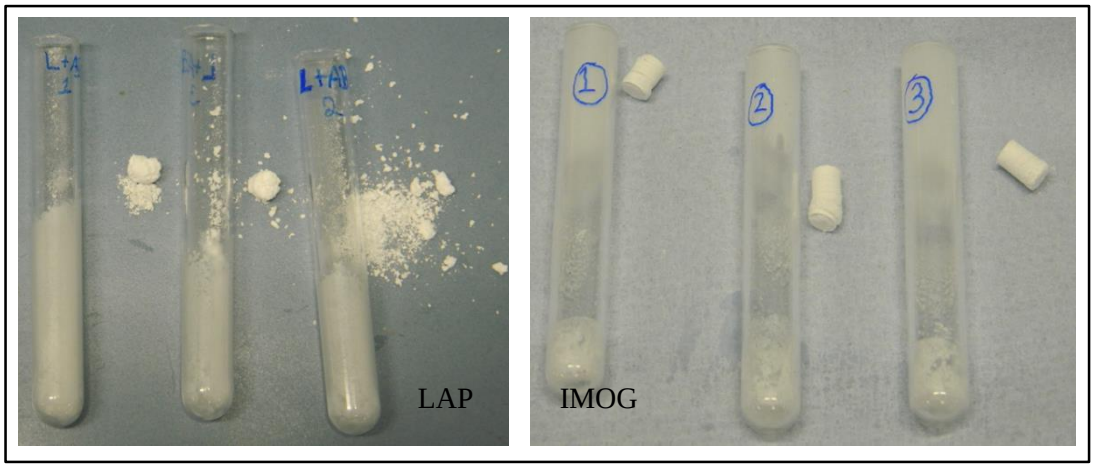

Figure 62: The LAP and IMOG AB-clay pellets post foam testing. The AB-LAP pellet instantly crumbles while the AB-IMOG remains whole.

In Figure 63 the change in pellet density, volume and mass which occurred during the foam test are displayed. The change in pellet mass (the final mass includes residue on the internal wall of the test tube) caused by the heating is high (around 25%) and fairly constant across the samples. It can be inferred that the mass loss is independent of clay type. The H_2 loss can account for a maximum of 13.1% mass loss [36] and the excess is probably due to the sublimation of solids and the discharge of heavier gaseous elements. The change in volume on the other hand varies hugely from clay to clay. The AB-MONT pellets displayed the greatest swelling (600%) and the AB-IMOG pellets outperformed the other composites with the smallest volume expansion (150%).

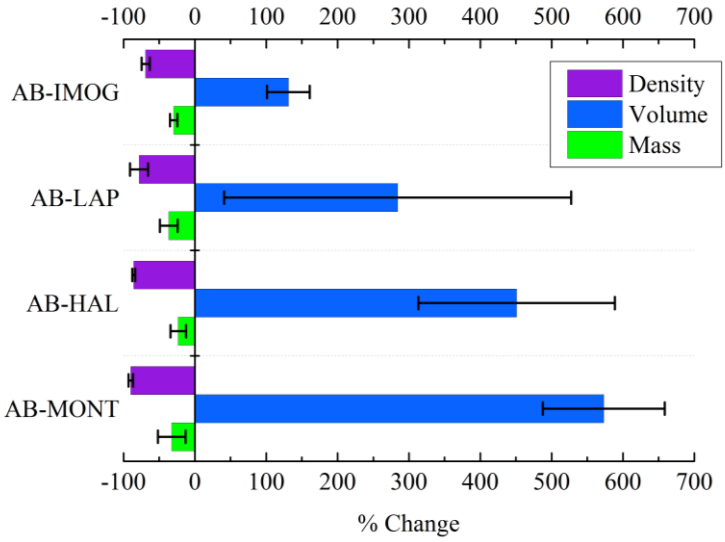

Figure 63: The change in mass, density and volume of the AB-clay pellets as a percentage of the initial dimensions post foam testing.

In Figure 38 in Chapter 4 the AB-PEO composites demonstrated a direct relationship between the initial density of the pellet and the expansion on heating. The initial densities of the AB-clay pellets are in general higher than their PEO counterparts, AB-clay>1g/cc>AB-PEO, and this is attributed to the higher density of clay, ~2g/cc [109] when compared to polymers ~1g/cc. For this reason it is to be expected that the clay composites would foam more than the AB polymer materials but this is not the case, see Figure 64. Also, in Figure 64, with the data available, no correlation between expansion and initial density that could explain the various volume changes, is evident. The points for the AB-IMOG sample hint at a positive correlation but the data are limited and no clear assertion can be made.

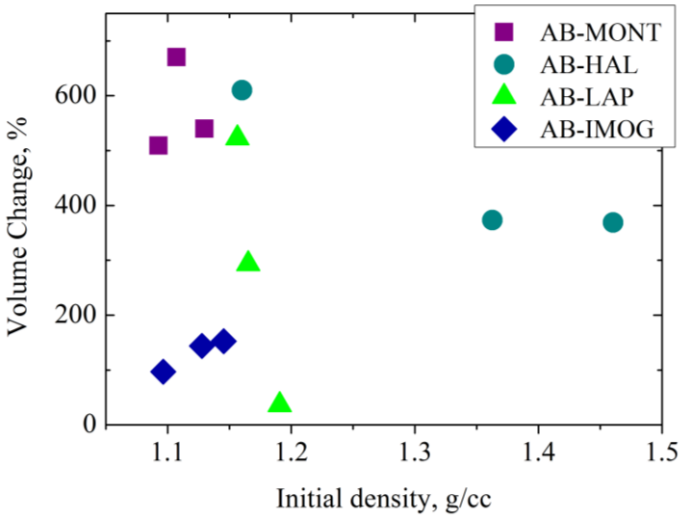

Figure 64: Volume expansion against initial density of the AB-clay composites. The AB-IMOG is the only sample that suggests a positive correlation.

The complete destruction of the pellets of the AB-MONT and AB-HAL composites suggests that AB is in the bulk state. Some abatement of foaming, as compared to pure AB is however observed. Perhaps the presence of the clay creates more escape pathways for the gas so less pressure can build in the pellet. Or, the clay separates the AB clusters and on melting, the AB cannot form large interconnected bubbles. Another possibility is that the solid state and high mass of the clay makes it harder to be displaced.

In the AB-IMOG and AB-LAP pellets expansion is limited and the initial pellet shape is maintained. However, in place of foaming, matter is ejected from the surface. This indicates that while the clay and AB are strongly bound together, the integrity of the pellet is limited due to the small particle size of the clay. This suggests that as hydrogen is liberated, pressure builds up in the pellet. Finally the hydrogen forces its way out carrying lose matter with in the gas stream.

6.3 Ammonia borane-imogolite: varying the proportion of AB

The AB-IMOG mix provides the most desirable properties in terms of foaming, and perhaps IMOG would be a suitable additive to ameliorate the hydrogen release properties of AB. To determine quantitatively the effect of IMOG on AB three new composites were made with AB:IMOG ratios 1:3, 2:2 and 3:1. The AB content in solution was varied while the IMOG ratio in the gel was kept constant. The samples were 1AB-3IMOG, 2AB-2IMOG and 3AB-1IMOG for the AB-IMOG 1:3, 2:2 and 3:1 ratios respectively.

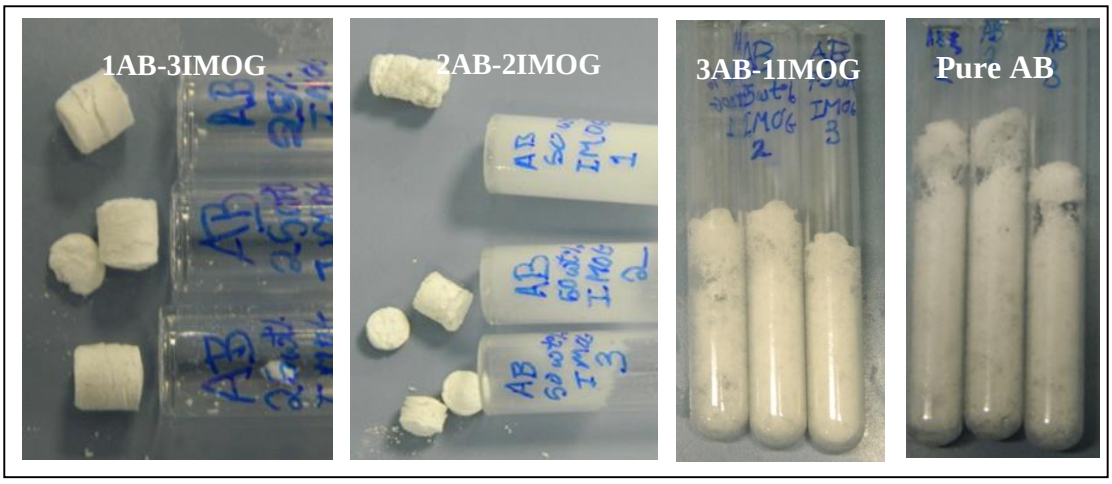

Figure 65: AB-IMOG pellets after foam testing.

In Figure 65 it is clear that the AB-IMOG pellets all foamed less than pure AB. The 3AB-1IMOG sample only demonstrated a minor decrease in foaming as compared to the pure AB. The 1AB-3IMOG and 2AB-2IMOG pellets however maintained their original shape only swelling minimally. The heated 2AB-2IMOG pellets here were more brittle than those from the first batch [XREF fig 2], perhaps due to the initial compression force, but the solid deposits on the internal test-tube surface are similar in both cases. Combining IMOG with AB has a successively positive, limiting influence on the foaming of AB.

SEM images of the three, uncompressed AB-IMOG composites were taken to determine if changes in the microstructure could be responsible for the change in foaming, see Figure 66. The flakes that give the 1AB-3IMOG a corallesque appearance disappear as the proportion of AB increases. In the 3AB-1IMOG sample, the amount of porous surface is reduced and this suggests a reduction of free volume in the composite.

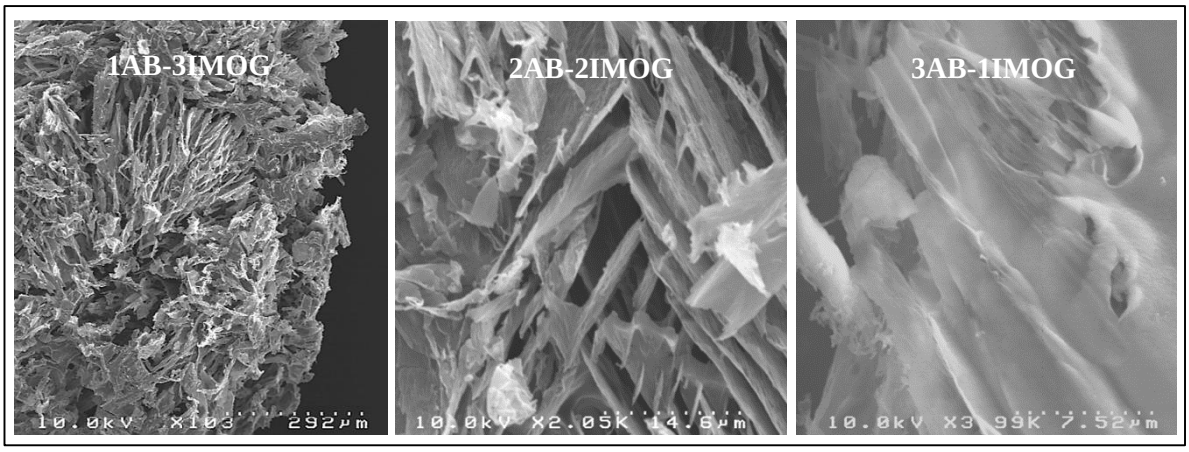

Figure 66: SEM image of the 1AB-3IMOG, 2AB-2IMOG and 3AB-1IMOG freeze dried composites. As the proportion of AB increases the visible free volume decreases.

6.4 X-ray diffraction of AB-IMOG composites

X-ray diffraction (XRD) patterns were obtained for the composites. All data were collected on the Rigaku using an automatic sample changer apart from the AB which was collected on the Phillips X'pert. Firstly, by comparing the position of the reflections from with the sample holder, the 75AB-25IMOG sample was observed to be slightly displaced to higher angles (Figure 63). The samples are coarse powder and each was glued to a different but similar sample holder. This suggests that the displacement is likely the result of varied sample height in the beam. The pristine AB peaks are also displaced but to higher angle. In this case the shift is probably due to the data being collected on the Phillips X'pert rather than the Rigaku.

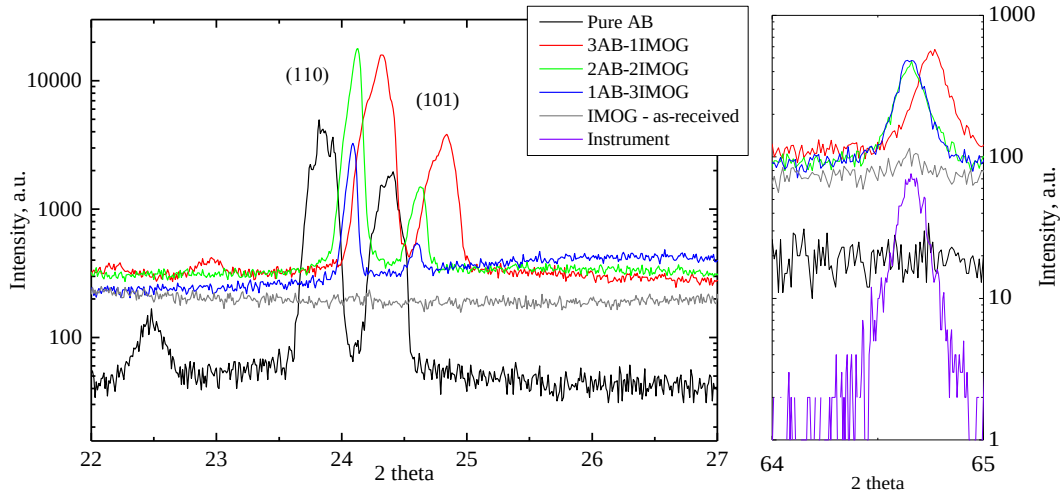

Figure 67: The two main AB tetragonal peaks for pristine AB and IMOG. The relative displacement is likely due to the difference of the height of the sample as shown in the displacement of the sample holder peak.

AB is observed in all composites and is structurally unchanged by the presence of IMOG. The peak intensity changes attest to the changing proportions of AB present in Figure 68. The slight shifts observed in the AB peak positions are due to variation in the sample height level under the beam.

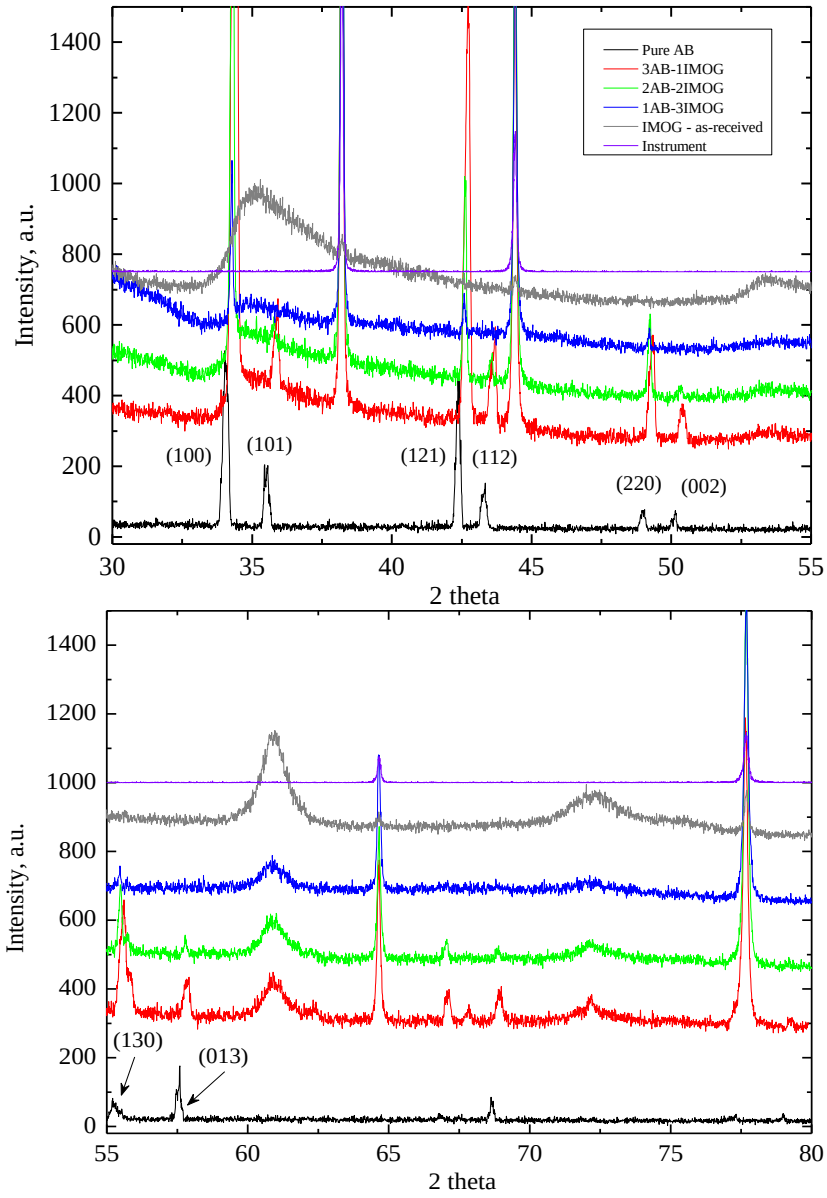

Figure 68: The AB peaks in the composites are observed at the same 2 theta position.

The diffraction pattern for the initial IMOG sample has an exceptionally broad peak at 5° (between 5 and 20Å) and sharper reflections at 19.8, 28.3, 35, 53.5, 61.0 and 72.5° (corresponding to 2.25, 1.35, 1.61, 0.95, 0.85 and 0.8Å) see Figure 69. The broad span, around 5°, encompasses the literature values for the (001) repeat distance along the IMOG tube (8.25Å) and the centre to centre distance of two adjacent tubes (~20Å) [114], [199]–[201]. The peak being broad suggests an ill-defined crystalline arrangement for the IMOG tubes, probably amorphous [202]. The peaks

between 19 and 72.5° could not be identified, but have previously been associated with IMOG [200].

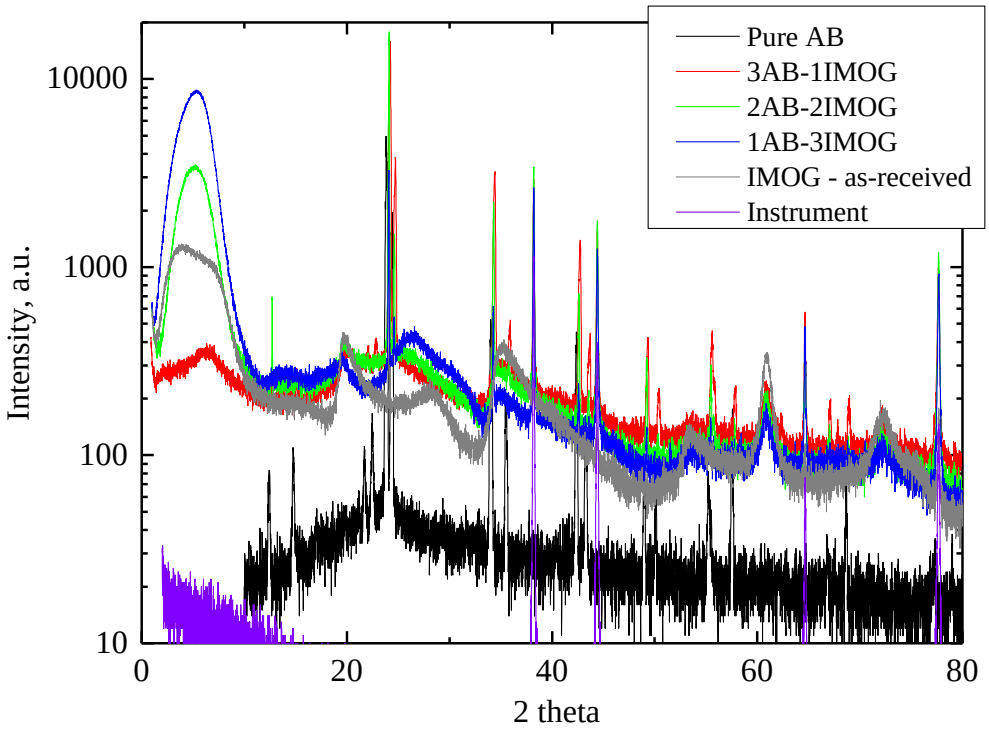

Figure 69: XRD pattern of the AB IMOG freeze dried composites.

As AB is successively added to the IMOG the broad peak around 5° (5 to 20Å) becomes sharper. A better defined peak position is observed in the 25AB-75IMOG sample at 8.5° and in the 50AB-50PEO sample at 7°. In the 75AB-25PEO the peak has almost vanished. The reduction in intensity around 8° suggests that the IMOG tubes become isolated from each other due to the presence of AB as shown in Figure 70. The AB and IMOG must be well dispersed within each other.

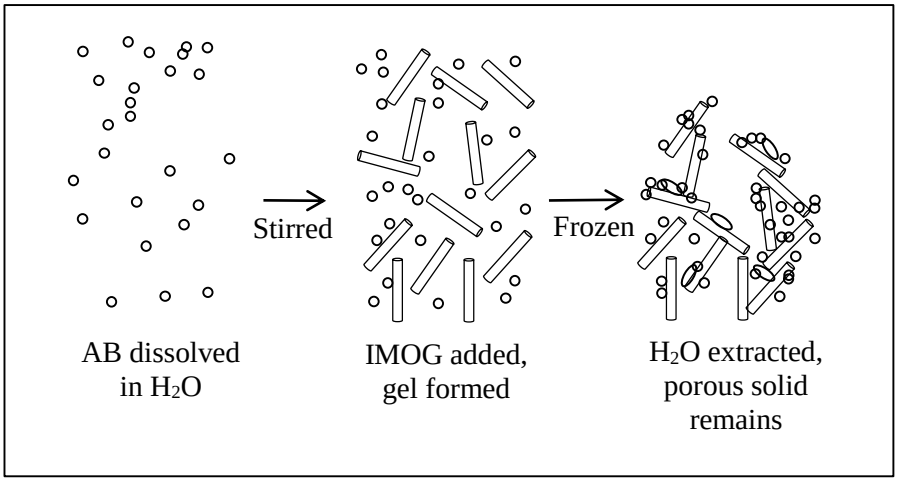

Figure 70: The freeze drying process used to prepare the AB-IMOG composite leaves the IMOG tubes dispersed within the AB.

6.5 Thermogravimetric analysis and differential scanning calorimetry of the ammonia borane-imogolite composites

The dehydrogenation characteristics of the three AB-IMOG composites was studied via standard ramp heating runs in the combined TGA and DSC with attached mass spec. The IMOG seems to have a positive effect on the hydrogen release characteristic of AB. In Figure 71 the peaks corresponding to the release of the first and second hydrogen equivalents (1st and 2nd H_2 equiv.), both move down in temperature as the proportion of IMOG increases. Concurrently, the hydrogen release 'pre-peak' at 85°C intensifies. This indicates that hydrogen is released at lower temperatures in the composites than the pristine AB.

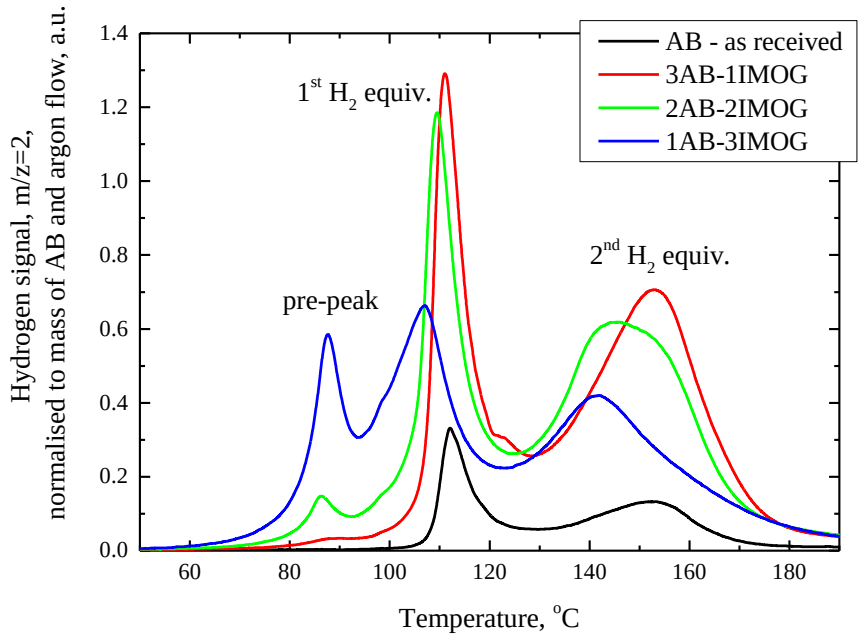

Figure 71: Hydrogen release profile of the AB-IMOG composites compared to pure AB under a standard ramp heating. As the IMOG content increases the pre-peak increase and the release of the 1st and 2nd hydrogen equivalent (H_2 equiv.)

In Figure 72 the TGA mass change curve profile switches from a two-step to a three-step process, as the fraction of IMOG in the sample increases. The gradient inflection points correspond to the DSC peak maxima, showing they are directly linked to the exothermic events in the sample. The DSC peak maxima in Figure 72 also correspond to the hydrogen release peak maxima in Figure 71. The mass loss can thus be attributed to the decomposition of the AB in the samples.

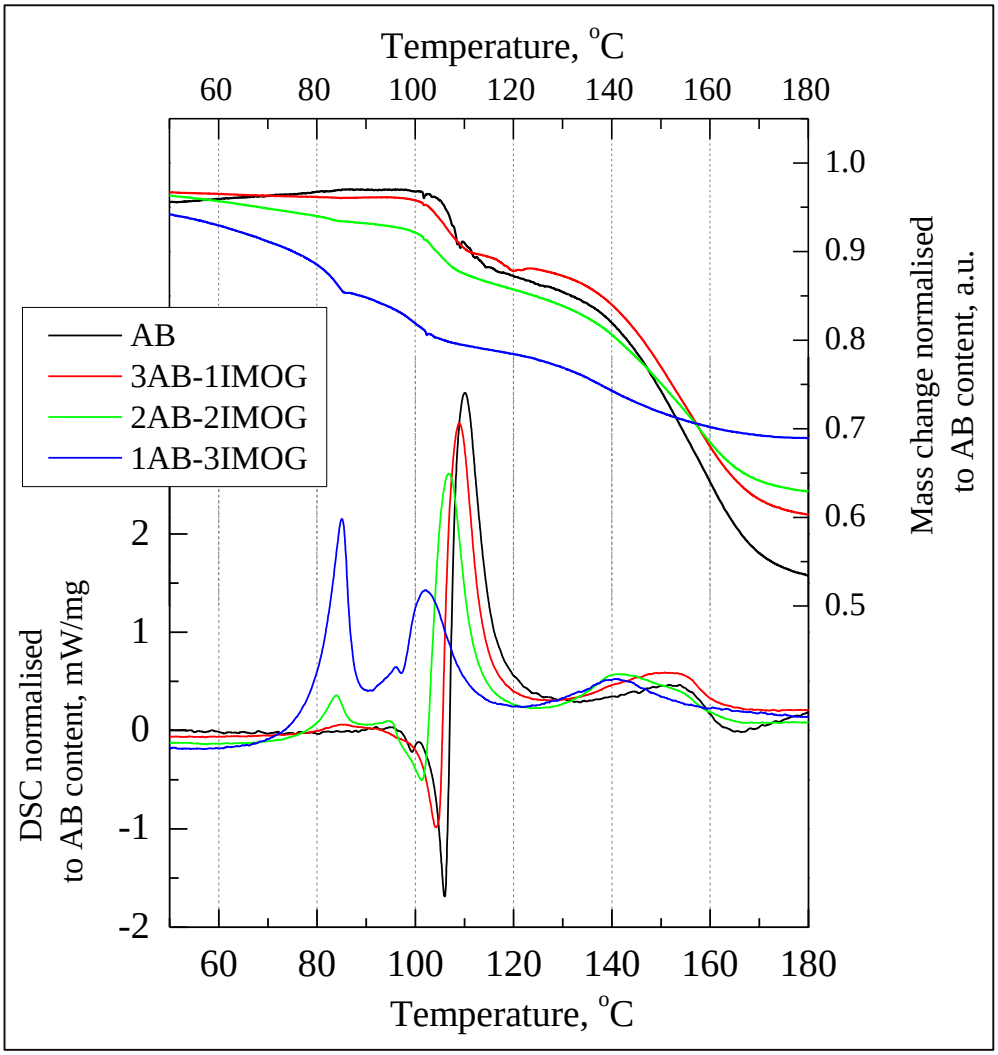

Figure 72: TGA and DCS traces for the 1AB-3IMOG, 2AB-2IMOG and 3AB-1IMOG freeze dried composites under standard ramp heating.

In Figure 72, the change in the 1st and 2nd H_2 equiv. release peaks is modest when compared to the large intensity change in the pre-peak. Looking at the DSC curve in Figure 72 we can see that this hydrogen is being released before the AB melts (melting point of AB is between 95°C and 105°C). This indicates that the IMOG enables the AB to lose hydrogen while in the solid phase. The shape of the curves suggests that two types of AB exist in the composites, one in the bulk that behaves like standard AB and a second that is closely involved with the IMOG, let's call it $AB^{\#}$. $AB^{\#}$ is probably in direct contact with the IMOG.

Hypothetically as the temperature is raised, $AB^{\#}$ will release hydrogen before the bulk AB accounting for the pre-peak. The reaction front will propagate outwards [54] and the DADB and PAB evolved at this stage, would go on and react with the adjoining bulk AB before the natural AB melting temperature is reached. This would bring down the temperature of the release of 1st and 2nd H_2 equiv. peaks. Finally, the increasing sample temperature passes 100°C and causes any remaining bulk AB to melt and react in the normal way. If the 1st H_2 equiv. peak moves down in

temperature the associated exotherm will overshadow the endotherms associated with the bulk AB melt. Thus the melting endotherm in the DSC decreases as the percentage of IMOG is increased. This model accounts for the pre-peak, the earlier appearance of the 1st and 2nd H_2 equiv. release peaks and the decrease in melting endotherm as a function of increasing IMOG.

There is one further detail, the 2nd H_2 equiv. release peak seems to be actually representing two different overlapping peaks: one at 140°C and the other at 154°C. This is most evident in the 2AB-2IMOG sample. The dehydrogenation of AB can be described as a chain reaction [53], [54]. Assuming, the composite contains bulk AB and $AB^{\#}$ and that the $AB^{\#}$ reacts at lower temperatures, two peaks for the release of the 2nd H_2 equiv. are too be expected.

6.6 Hydrogen gas stream content

Besides the hydrogen release, the impurity levels must also be considered. For this, cumulative integrals of the mass spec traces detected under the heating ramp from the pure AB and the AB IMOG composites have been plotted (Figure 73). It is difficult to compare the pure AB to the AB-IMOG composites for the reasons outlined in Chapter 3. The AB traces have been included because, while the intensity cannot be trusted, the temperatures at which gradient changes occur, is valid.

On examination of the three clay composites, some trends can be observed. Firstly, the proportion of ammonia in the hydrogen stream increases as more IMOG is added. Conversely, the levels of diborane and borazine drop with greater amounts of clay. Water levels though remain fairly constant. All samples have been dried in the same freeze dryer over the same period of time and it is expected that the water residue would be similar. Even so the 1AB-3IMOG sample releases water between 60°C and 90°C whereas the other two composites only perceptibly release water after 100°C. Perhaps this in linked to the greater clay content or this is a feature of the measuring equipment.

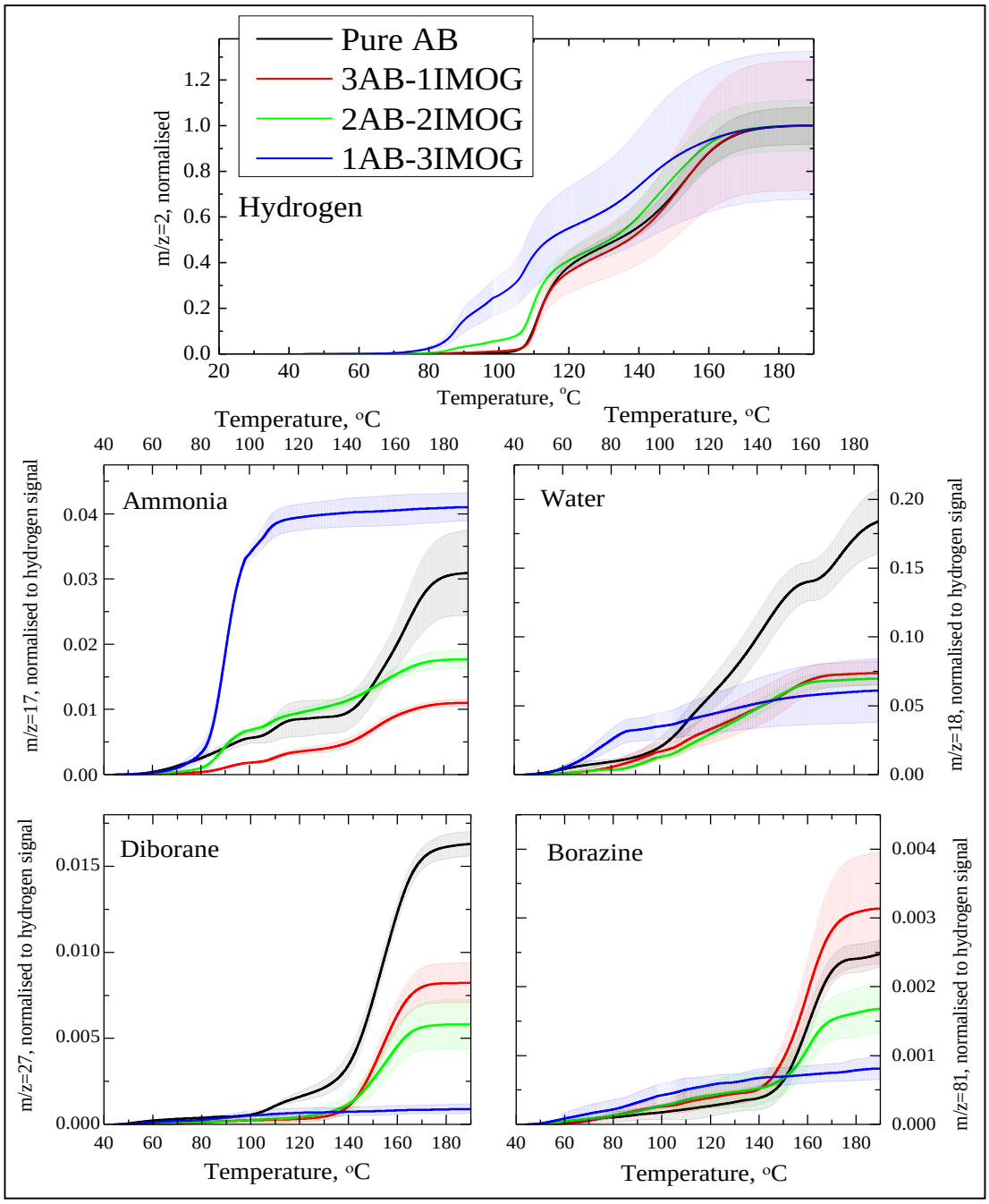

Figure 73: Cumulative integrals of the mass spec traces of hydrogen and impurities detected under the heating ramp. The data are normalised to the hydrogen (m/z = 2) level at 190°C and errors in the data are shown as the lighter background. As the IMOG content is raised more ammonia is released but borazine and diborane are decreased.

6.7 Discussion and conclusions

6.7.1 Structure

The x-ray diffraction patterns suggest that the IMOG tubes are well dispersed while the AB has managed to dry into its preferred tetragonal crystal structure, even in the 1AB-3IMOG sample. This indicates that while the AB and IMOG are not mixed and have formed well dispersed regions of homogeneous AB and IMOG. Likely these bulk clusters of AB have boundary regions of AB$^{\#}$ that are connected to the IMOG.

IMOG is a tubular clay with an internal diameter of around 10Å which water is able to penetrate [114], [200], [203], [204]. When the IMOG is immersed in the AB–water solution it is possible that as well as solvating the surface, the water entered into the tubes, dragging AB along. Theoretically, one could assume that some of the AB is within the tubes. The diffraction pattern, however, attests to a tetragonal AB crystal and there are no unexplained peaks associated with AB nor any broad humps to signify amorphous areas. This suggests that the tubes are AB free and that AB$^{\#}$ is likely connected to the external hydroxyls.

6.7.2 Foaming

When IMOG and LAP where intimately combined with AB, the foaming of AB was dramatically reduced. When HAL and MONT where mixed with AB, the foaming was not as much suppressed. This indicates that the clay morphology, layered (MONT and LAP) or tubular (HAL and IMOG) did not significantly affect the foaming of the composites. The highest foam reduction was achieved with the clays (LAP and IMOG) that formed gels with the AB-water mix. In a gel the clay particles will be interspersed with the AB molecules as shown in Figure 70. On drying this will ensure AB is integrated with the clay. This suggests that the foaming of AB is controlled by intimate mixing with clay.

AB could be facilely blended with IMOG in a variety of ratios, via freeze drying, provided the AB was dissolved before the IMOG. The fraction of IMOG in the composite was observed to be inversely related to the amount of foaming that occurs. The microstructure of the AB-IMOG materials as viewed via SEM suggests that the IMOG is responsible for adding porosity to the solids. As pores provide escape routes for the gas, with more pores, less hydrogen could be trapped in the material and less foaming would occur. Alternatively, the increasing proportion of IMOG in the sample could serve simply to increase the separation between AB clusters. If the AB clusters are dispersed, the chance of forming large stable bubbles reduces.

In the DSC the AB showed reduced melting as the IMOG content was raised. The reduced foaming could be due to AB releasing more hydrogen in the solid state. Less liquid AB reduces the likelihood of foam occurring.

6.7.3 Dehydrogenation

The IMOG content in the composites has a direct effect on the quantity of ammonia in the gas stream. The majority of the ammonia is released between 80°C and 95°C, coinciding with the 'prepeak' of the hydrogen release. To release ammonia from AB the B-N bond must be severed. The IMOG surface, Al-$O^{\delta-}$-$H^{\delta+}$ could attract the boron side of AB, $B^{\delta+}$-$H^{\delta-}$. Electron transfer to the boron could weaken the B-N bond till it breaks and liberates ammonia. This would leave space for hydrogen molecule to form, half from the IMOG and half from the boron resulting in a B-O bond such that Al-$O^{\delta-}$ $B^{\delta+}$-$H_2^{\delta+}$, please see Figure 74. H_2 release from AB has previously been shown to be initiated boron interaction with an active oxygen i.e. carbon cryogel [84], [87] [89]. Zhao *et al* showed how a B-O bond can lead to the simultaneous release of H_2 and NH_3 [60].

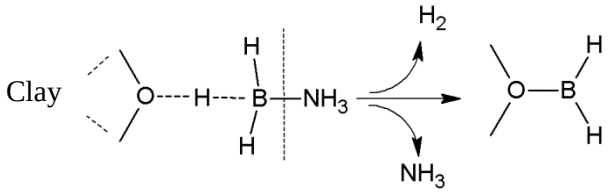

Figure 74: Hypothetical reaction scheme for the initiation (prepeak) of hydrogen release from AB by the hydroxyl groups on the IMOG surface.

The step of the release of the 1st H_2 equiv. occurs between 95°C and 120°C. Hydrogen is the main gas released from the composites over this temperature range and it is accompanied by a small amount of ammonia. A possible mechanism for this step, in Figure 74, shows how in place of DADB the dehydrogenation of AB can be catalysed by $BH_2NH_3^+$.

The release of the 2nd H_2 equiv. occurs between 130°C and 160°C. Here, the hydrogen release is accompanied by borazine and diborane. However, as the IMOG content in the composite increases the fraction of borazine and diborane in the gas stream reduces. This indicates that the AB follows the polymeric dehydrogenation route (AB→PAB→PIB) as opposed to the cyclic one (AB→CTB→borazine) [46]. PAB produced in the 1st step has reacted to PIB in the 2nd step. As the IMOG fraction increases more hydroxyl groups are available to AB (making $AB^{\#}$) which then follows the polymeric AB dehydrogenation route.

The borazine and diborane traces are limited but not eliminated by the clay. This suggests that areas of bulk AB that release hydrogen in the traditional way are present in the composites. This

assertion is supported by the diffraction pattern which shows AB tetragonal crystal reflections even in the 25AB-75IMOG composite.

IMOG improves the kinetics of hydrogen release from AB, lowers impurities (bar ammonia) and controls foaming. The hydroxyl surface is actively involved in the reaction as the hydrogen is replaced by a stronger bond to the boron. A 50% weight penalty (50AB-50PEO) is necessary to significantly control the foaming. To significantly speed the hydrogen release (25AB-75IMOG) a 75% weight penalty was required. While the IMOG does provide some hydrogen from the hydroxyls, the release of 1 hydrogen atom from a hydroxyl is accompanied by the loss of 1 ammonia molecule. Each ammonia equates to the loss of 2 useable hydrogen atoms, this in total is therefore a net loss of 1 hydrogen atom per hydroxyl group that interacts with AB.

The ammonia could be cleaned from the gas stream by adding an ammonia absorber such $MgCl_2$ [108] and could be used to feed a polymer membrane fuel cell [205]. However, this would necessitate a further weight penalty perhaps unnecessary when the material could be used to feed a combined hydrogen and ammonia solid oxide fuel cell.

6.8 Further work

6.8.1 Structure

FTIR and molecular dynamics simulations, for example of an AB molecule on an IMOG surface, could be employed to determine the nature of the suggested interaction between the AB and IMOG as suggested. The IMOG and AB crystallite sizes could be determined Scherrer analysis of the XRD peaks and energy dispersive X-ray spectroscopy.

6.8.2 Foaming

The data suggests that the foaming is reduced in the composites as the decomposition of AB is following a different reaction route that initiates before the AB melting temperature is reached. In situ microscope studies could be useful to study how and when the bubbles, if any, form. Also high resolution SEM combined with TEM could be employed to see if the study the AB particle sizes.

6.8.3 Reaction

More conclusive evidence is required to determine if the AB is actually reacting with the IMOG. This could be obtained by deuterating the AB and then observing the masses of the released hydrogen moieties with the mass spec. Selective deuteration of one side of the AB molecule

would give more in depth information. *In situ* IR, Raman, inelastic neutron scattering and NMR studies of the heated AB-IMOG composites would also be useful.

6.8.4 Alternative materials

It was shown here that in all likelihood the AB has not crystallised inside the IMOG tube. A synthetic IMOG with wider tube diameter could perhaps encourage the AB into the channel and increase the proportion of active surface available to the AB.

The AB-LAP composite was dropped from further experimentation due to the structural weaknesses, expansion and ejected solids, exhibited in the foam test. However, studying the effect of the LAP on the hydrogen release behaviour of AB, under perhaps a more moderate heating regime, is still valid. Comparisons between a layered clay (LAP) and tubular clay (IMOG) could be made.

If MONT and HAL clays could be fully solvated, an intimate blend of clay and AB could be created. Solvents that could be tested are salt water and THF [198]. As freeze drying is most suitable for water, electro spraying could be used to process the solutions or gels made with alternative solvents into a dry state.

This leads on the studies on alternative clays. Many and varied clay materials could be combined with AB and tested as to their suitability as hydrogen store. Metals, transition and alkali earth, have been shown to have a catalytic effect on AB dehydrogenation and these also could be included in the composites [91]–[94]

7 Neutron spectroscopy studies of calcium-ammonia solutions confined by graphene sheets.

7.1 Synthesis

Madagascan flake graphite was intercalated with calcium (Ca) to form a Ca graphite intercalation compound (GIC) using the single zone metal vapour technique [33], [149]. The raw materials, graphite and excess calcium were placed into a steel container and held under vacuum at 465°C for 10 days; during this time the calcium vaporised and intercalated into the galleries.

1.16g of the Ca GIC was packed in a cylindrical aluminium sample can, 50mm high by 20mm diameter and mounted in the neutron beam. A gas manifold containing a 0.5l ammonia vapor reservoir was fitted and a high vacuum pumping system attached to the sample can. The sample was evacuated to a pressure of 10^{-7} mbar and subsequently exposed to an NH_3 atmosphere. The NH_3 was loaded slowly by raising the pressure from 0.5 to 5.2 bar at 300K over approximately 14 hours. Before readings commenced the pressure was reduced to 3bar pressure to ensure only the residual material was measured this material is termed Ca-NH_3 GIC. Afterwards, the reversibility of the NH_3 intercalation was examined by holding the pressure at 10^{-5} mbar at 300K for 1hour. The high temperature and low pressure conditions were used to encourage the loosely bound NH_3 to deintercalate.

The quasi elastic neutron scattering (QENS) spectrum was recorded at 50K intervals moving from 300K to base at 2K. The analysis focused on the energy range -0.3 to 0.8 meV, beyond 0.8 meV the scattering becomes asymptotic to the baseline. Scattering was observed over the Q range from 0.42 to 1.85 $Å^{-1}$ and analysed by segregating the detectors into 17 groups. Neutron diffraction patterns were measured between d = 2.7 and 7.2Å. The IRIS wavelength bands are narrow, so to achieve the entire spectra displayed the Bragg reflections were collated from the pyrolytic graphite 002 and the mica graphite analysers. The data were analysed with MODES v3 a program designed specifically to process data from the IRIS beam line [169].

7.2 Diffraction

In the diffraction pattern of the as-intercalated Ca-NH_3 GIC in Figure 75 (purple) two peaks were observed, one at 3.355Å assigned to the graphite (002) [24], [26] and one at 4.518Å assigned to layer spacing of the Ca GIC. The d-spacing Ca GIC layer of stage 1 CaC_6 is quoted in literature as 4.6Å [164], [206], [207]. The d-spacing measured here for the Ca GIC layer is 4.518Å and a stage 1 arrangement is likely considering the gold colour of the sample [26]. The peak at 4.518 Å

is broader than the graphite (002) peak, this suggests that the Ca intercalated areas may be smaller than the graphite ones.

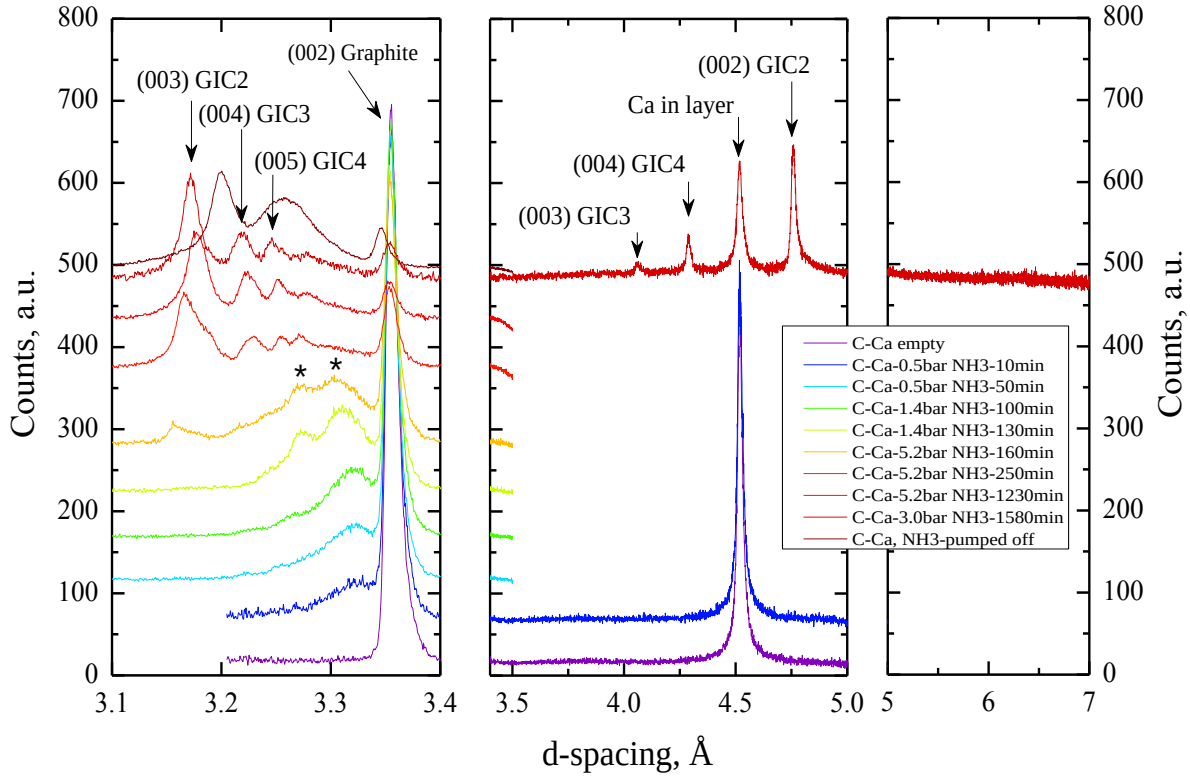

Figure 75: The neutron diffraction pattern pre ammoniation (purple line) shows both Ca GIC and graphite. After ammoniation (long red trace) a new multistaged ternary phase Ca-NH_3 GIC was created. The final Ca-NH_3 GIC sample includes stages 2, 3 and 4 labelled GIC2, GIC3 and GIC4 respectively. During the NH_3 intercalation unidentified high stages (marked *) form before the low stages.

Table 19: The neutron diffraction pattern shows the Ca-NH_3 GIC to have multiple stacking arrangements. Stage 2, 3 and 4 are present but no stage 1 is observed. This is due to the low NH_3 pressure of 3bar which limits the amount of NH_3 in the galleries.

00l reflection	Stage 1(Å)	Stage 2 (Å)	Stage 3 (Å)	Stage 4 (Å)
001	6.4 [206]	9.52 ‡	12.87‡	16.25‡
002		4.76§		
003		3.17§	4.29§	
004			3.22§	4.06§
005				3.246§

§ Observed distances and ‡ calculated distances from observed peaks.

The difference in peak intensity between the graphite (003) peak and the Ca GIC suggests more graphite layers than Ca intercalate layers. When the NH_3 is added the Ca become solvated and require more pristine graphite to expand into. At low NH_3 pressure, 0.5 bar, a broad peak (marked *) developed around 3.3Å. The peak became more pronounced at 1.4bar and when the pressure was raised to 4.0bar a second peak appeared at 3.28Å. These peaks (marked*) could not be further identified without data at higher d-space. The ammoniation is accompanied by a reduced intensity

of the graphite (003) reflection suggesting the solvated Ca is infiltrating the pristine graphite even at low NH_3 pressures.

After stabilising the sample under 3bar NH_3, additional reflections appeared at the expense of the Ca GIC and graphite peaks which diminished. With reference to Srinivas *et al* and Hönhe *et al*, the reflections were indexed to the 00*l* reflections of a ternary Ca-NH_3 GIC with various stage arrangements; stages 2, 3 and 4 are evident. Measured reflections and the associated calculated values for the d-spacing distance of the various stages are shown in Table 19. No stage 1 ternary GIC is apparent. Since the staging of the system is controlled by the applied ammonia pressure [207], [208] and stage 1 can be achieved if the pressure is raised to around 7 bar [209] we assume a low ammoniation pressure, 3bar, is insufficient to produce stage 1. Unidentified stages, defects or diffuse scattering from within the layers, may be responsible for the broad feature at 3.5Å as the majority (80%) of the coherent scattering is due to the graphite Table 10.

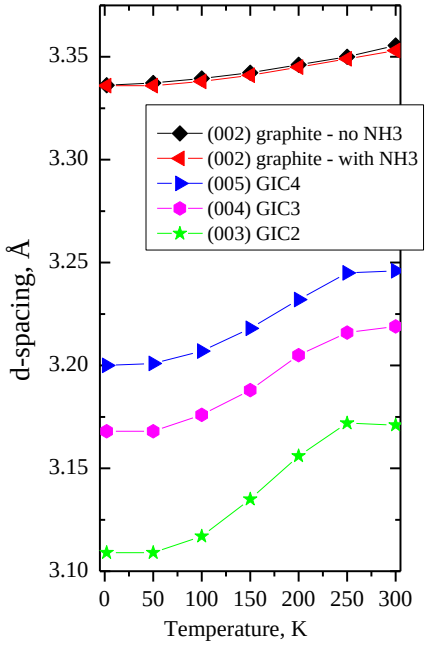

Figure 76: The layers of the Ca-NH_3 GIC contract when the temperature decreases from 300K to 2K.

The interlayer spacing of the final Ca-NH_3 GIC structure at 3bar NH_3 is sensitive to temperature. In Figure 76 all the layers contract when the temperature is reduced from 300K to 2K. This is due to the reduction in thermal motions as temperature decreases. Also, the ammoniated layers put pressure on the adjoining graphite layers forcing them together. In figure X the graphite (001) layer at 3.355Å decreases to 3.353Å when NH_3 it is added. To accept NH_3 into the galleries the graphene layers must expand which will result in strain on the graphite [26]. This data suggests that to minimise the strain the graphene layers move closer together.

7.3 Diffusional dynamics

The motion of the ammonia molecules was studied at ~50K intervals between 300K and 2K. The data were refined by removing a background (including the sample can) and fitting with an elastic line curve (Gaussian) and one or two quasi scattering curves (Lorentzian) as appropriate.

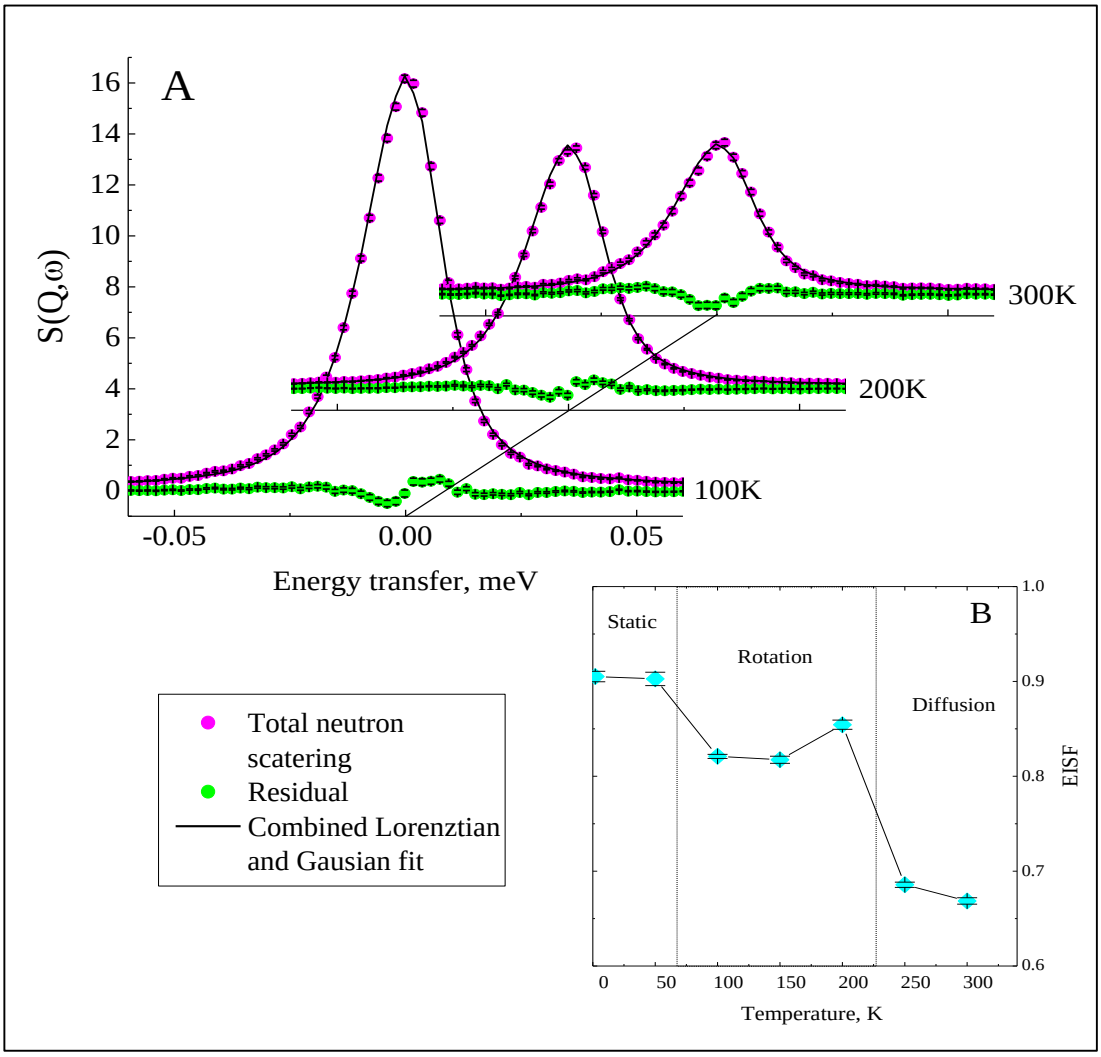

Figure 77: In graph A the total neutron scattering spectrum of the Ca-NH_3 GIC is plotted as a function of Q for a range of representative temperatures. The fit to the data are good as demonstrated by a small residual. The spectra broaden and the peak height drops as the temperature increases. In graph B the elastic incoherent structure factor, EISF, ratio of the elastic scattering over the total scattering for all Q, against temperature is depicted. With increasing temperature the shift from elastic to inelastic scattering is due to the protons becoming more active and indicates that greater motion is available to the ammonia. Considering the sharp drops in the trace of the right-hand graph, we can preliminarily define the motional modes occurring.

In Figure 77 the total scattering spectrum over a range of representative temperatures is depicted. As the temperature is raised the peak are under the peak and the width increases. This is the result of an increasing fraction of the beam being scattered by the sample and indicates that a greater range of motion possible for the ammonia at higher temperatures. Previous studies have identified a range of possible modes of motion of ammonia in similar situations beginning with rotation

about a fixed position at low temperatures, hopping from one metal site to another at medium temperatures and diffusing freely at high temperatures [121]–[123], [210]. A plot of the elastic line intensity (elastic incoherent structure factor, EISF) against temperature in Figure 77 suggests distinctive modes of motion take place at different temperatures. The large change in the amplitude between 250K and 200K and the second shift between 100K and 50K demonstrates that the type of movement of the ammonia is experiencing changes at these points.

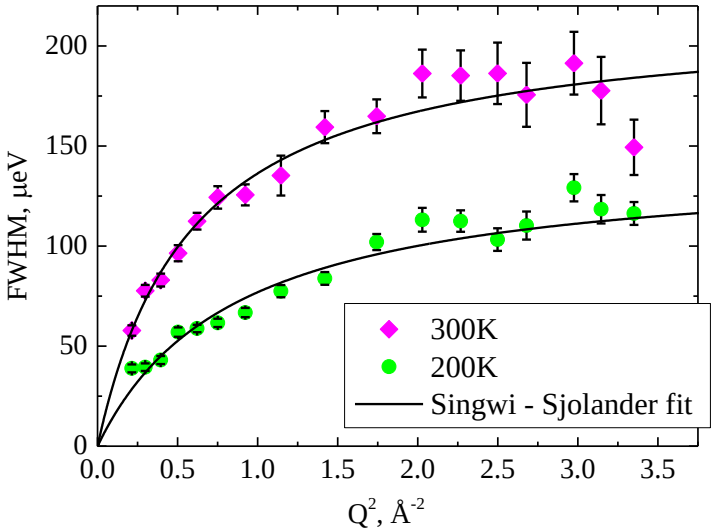

Figure 78: The FWHM of the Lorentzian fits to the data at 300 and 250K, previously divided into 17 groups to depict the changes as a function of Q^2. The Singwi-Sjölander jump model provides the best fit to the data describing an exponential distribution of jump lengths and frequency around the mean values. At 300K this corresponds to a jump distance of 3.2±0.1Å with a frequency of 19ps and at 250K, this corresponds to a jump distance of 2.88±0.2Å with a frequency of 28 ps.

At both 300K and 250K a Gaussian and single Lorentzian was found suitable to meet the statistical requirements of the fit. In Figure 78the FWHM is plotted as a function of Q^2 and in both the 300K and 250K cases exemplifies the Singwi-Sjolander jump diffusion model. At 300K ammonia is typified as jumping 3.2±0.1Å every 19ps. The motion is retarded at 250K with a shorter jump of 2.9±0.2Å that occurs less often, every 28ps. As the sample cools, less energy is available for motion accounting for the variance in the jump profile at 300K and 250K. The diffusion coefficients, at 300K and 250K, reflect this and are calculated as 8.91×10^{-5} $cm^2s^{-1}$and $4.02\times10^{-5}cm^2s^{-1}$ respectively. Considering a molecular graphics snap-shot of $CaC_{12}(NH_3)_2$ in Figure 79 the jump distances calculated with the Singwi-Sjolander model are seen to be realistic.

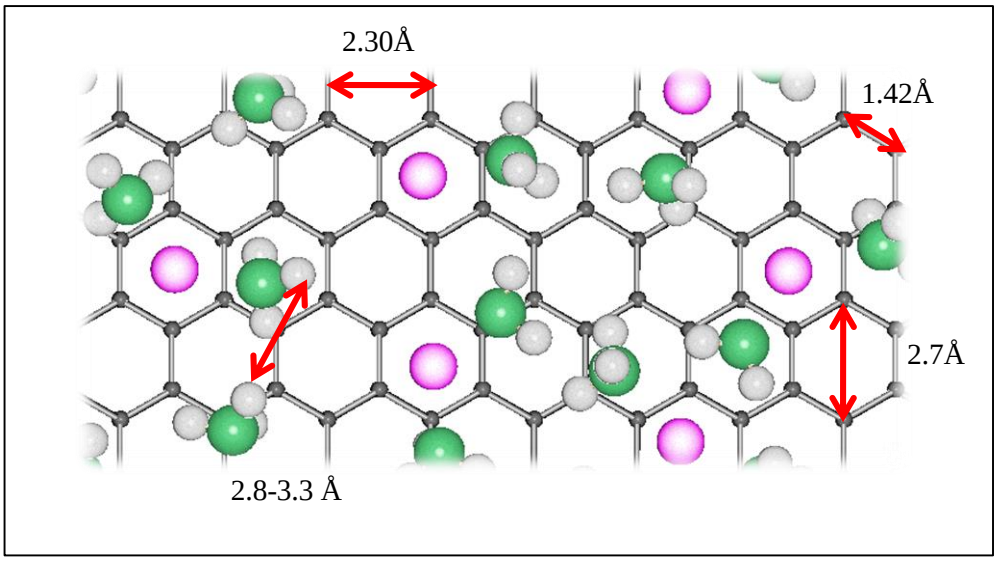

Figure 79: Molecular graphics snap-shot of a single layer of composition $CaC_{24}(NH_3)_2$ showing the jump lengths expected (Unpublished work from Neal Skipper).

A Delta and two Lorentzians where required to fit the spectra acquired at the temperatures of 200K, 150K and 100K. The fitted parameters are Q independent (Figure 80) and indicate a rotational mode. The determined values for the rotational diffusion constant and rotational dynamic correlation times are displayed in Table 20. A point has been discounted in the fit of the data at 200K at $Q^2 = 0.92Å^{-2}$ as the error bar spanned the entire energy range. A large residual accompanied the fittings at 200Kand we suggest some diffusion is also present as observed by Neumann *et al* in $KC_{24}(NH_3)_{4.3}$ [211]. The scattering is however dominated by a rotation signal.

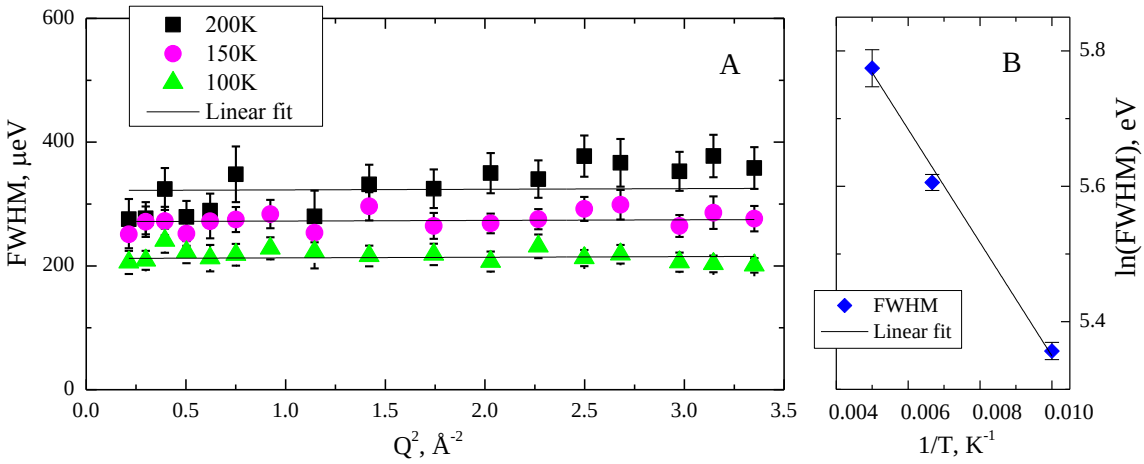

Figure 80: In graph A the FWHM are shown with respect to Q^2 at 200K, 150K and 100K. The linear nature of the fit suggests rotational modes with higher energy at higher temperatures. In graph B an Arrhenius plot of the FWHM obtained yields the activation energy off the rotation as 696 $Jmol^{-1}$.

Table 20: The FWHM, rotational dynamic correlation times, τ_{rot}, and rotational diffusion constant, D_{rot}, calculated at temperatures of 100K, 150K and 200K.

Temp. (K)	200	150	100
FWHM (μeV)	322 ±9	272 ±3	212 ±3
τ_{rot} (ps)	0.68	0.81	1.05
D_{rot}(μeV)	161	136	106

The second Lorentzian peaks for the temperatures 200K, 150K and 100K are within the resolution of the instrument and therefore cannot be analysed. A spectrometer with a higher resolution is required to discern if another higher order rotational mode is present or if this is merely a feature of the background. At 0 and 50K no spreading into the QENS was detected. While some movement may still be occurring again it is not observable without an instrument of higher resolution.

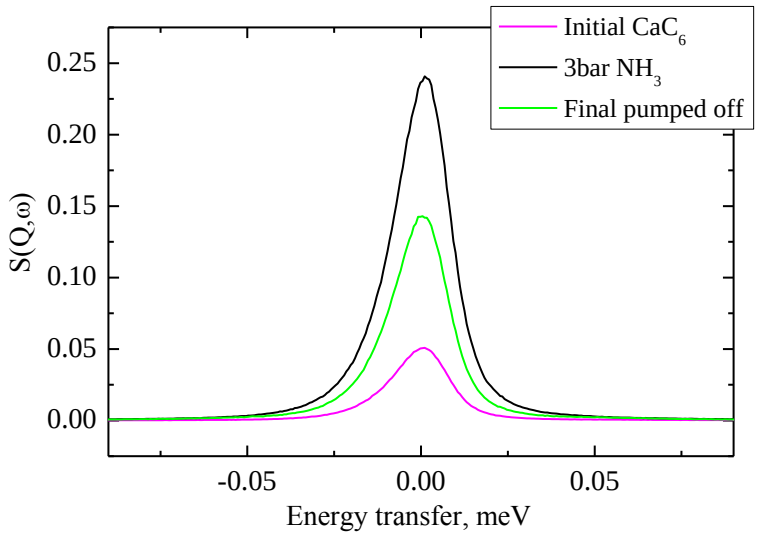

Figure 81: The QENS spectrum before ammoniation, during the experiment and after the ammonia was pumped off, the change in intensity demonstrates the partial reversibility of ammonia intercalation.

Once the readings had been taken the pressure in the sample chamber was reduced down to ~10^{-5} bar while the temperature was gently raised from 2K to 300K over approximately 15 hours in an attempt to deintercalate the ammonia. In Figure 81the intensity of the QENS spectrum is raised due to the ammonia intercalation and drops when the ammonia pressure is removed. However, the final peak does not return to the same level as the initial Ca GIC. This indicates residual ammonia is present within the structure and shows the intercalation process is only partially reversible. Possibly when the pressure is removed molecules that are near the sample edges will escape, while others remain trapped in the structure perhaps in intercalant islands or defect sites [26].

7.4 Conclusions and discussion

A binary Ca GIC (CaC_6) was generated via the vapour transport method. A ternary NH_3-Ca GIC was then made *in situ* by an over pressure of 5.2 bar NH_3 atmosphere. The ternary GIC composition was stabilised at 3bar NH_3 and found by diffraction to be multi-staged. The process of ammoniation initially created high stage ternary phases followed by lower stages as the level of ammonia was raised. While the exact composition of the ternary GIC is unknown the interlayer NH_3-Ca arrangement will be constant through the sample and each NH3-Ca complex will have a maximum of four surrounding NH3 [34], [118], [119]. The interlayer graphite space is 3.353Å, it increases with the intercalation of Ca to 4.518Å and then further on addition of NH3 to 6.16Å. All of these distances are temperature dependent however, as when the sample is taken to 2K a marked decrease in the spacing is observed. This indicates that the structure contracts as the temperature falls.

Neutron scattering was used to elucidate two modes of movement and one still state. Hopping diffusion following the Singwi-Sjolander model occurred at 300K and 250K and as the sample cooled the hopping movement disappeared to be replaced with a rotational mode at temperatures 200K, 150K, and 100K.

The diffusion coefficients at 300K and 250K have been calculated as 8.91×10^{-5} cm^2s^{-1} and 4.02×10^{-5} cm^2s^{-1} respectively for CaC12(NH3)2, it is expected that less energy is available for motion at lower temperatures. In the K analogue, KC24(NH3)4.3, at 300K, the translational diffusion of the same order of magnitude 10-5 cm2s-1 was observed, however this was accompanied by a rotational mode of 1.17meV that was not observed in CaC12(NH3)2 [211].

At 200K, 150K and 100K the rotation of NH_3, successively decreasing in energy is observed. These reorientation times (0.68 and 1.05ps) are within the same order of magnitude as those observed in the octahedral Ca-NH_3 complex (1.0ps at 120K) [120] suggesting that the interaction energy between the Ca and ammonia is unaffected by the containment in the layers.

However, compared to the K-NH_3 GIC studies by Neumann *et al* [211], the energy of rotation of the NH_3 in the Ca-NH_3 GIC is much higher (270μeV compared to 130μeV at 150K). I suggest this is the direct result of the dipole increase between the metal and the ammonia due to the change from the univalent K to the divalent Ca. At 50 and 2K no movement was observed in the Ca GIC, this is contrary to both literature sources which detect broadening indicative of rotation at 40K in $Ca(NH_3)_6$ [120] and at 78K in $KC_{24}(NH_3)_{4.3}$ [211].

The ammoniated state is only partially reversible at conditions of 300K and ~10^{-5} bar. The final trace in the diffraction graph, figure three, shows the sample after deintercalating has been

attempted. Two broad peaks, one at 3.2Å and the other at 3.26Å are present, similar to what was observed by Srinivas *et al*. [206]. The graphite (001) peak has also shifted down slightly to 3.347Å. The disappearance of intensity at 3.17Å suggests that the stage 2 GIC, the lowest in this sample, disappears first. The peak broadness suggests an irregular array of filled and empty layers. A plausible model is that NH_3 is indiscriminately pulled out of the edges of the structure leaving a haphazard arrangement of stages behind.

7.5 Future work

While this study has characterized the high temperature behaviour of the ammonia in the Ca GIC, at 50K and below the data are poor. In studies of Ca-NH_3 solution [120], [212] and a Cs-NH3 GIC [210] tunnelling rotations of the hydrogen atoms are observed below 50K. A high resolution neutron scattering spectroscopy study with longer counting times or hydrogen nuclear magnetic resonance spectroscopy are both suitable probes. Molecular dynamics simulations could provide insight into the exact rotation and hopping mechanisms involved.

8 Final conclusions

8.1 Structure and foaming of the ammonia borane composites

The tendency of AB to produce foam while releasing hydrogen limits its applicability. The hydrogen release of the pristine AB is preceded by an endothermic melting curve. This means that the gas must pass through a highly viscous liquid, characterised by strong intermolecular interactions, to escape. These are ideal circumstances for bubbles. AB can release hydrogen slowly in the solid phase and more quickly in the liquid phase.

All the composites synthesised foamed less than pristine AB. Additionally increasing the additive content in the sample successively impedes the foaming. The PEO, PS and clays are very distinct both in structure and chemical behaviour. This suggests that simply disrupting the long range connectivity of the AB to itself reduces the foaming.

Let us consider the 50AB-50additive materials first. The foaming and expansion varied depending on the additive. The PS-AB pellets showed the greatest expansion, for the AB-clay pellets the volume increase was more than 100% while the AB-PEO pellets expanded by less than 100%. The XRD pattern of the 50AB-50PEO suggests the presence of an AB-PEO mixed phase. In the 50AB-50IMOG material, the AB is observed by the XRD in its tetragonal crystalline state. Let us consider the material from a theoretical perspective. Assuming the AB indulges in hydrogen bonding with either electron donors (ether oxygen in PEO) or electron acceptors (IMOG hydroxyl) hydrogen bonds can be formed with the IMOG and PEO but not to the same extent with the PS.

The DSC traces for the 50AB-50additive (PEO, PS and IMOG) composites suggested that the foam reduction could be linked to a decrease in the melting of AB. When less liquid is available less foam can form.

In the AB-PEO pellets, expansion and foaming showed a positive correlation with initial pellet density. This suggests that the interconnected space provides escape routes for the hydrogen and that more free volume minimises gas containment and the build-up of pressure in the pellet.

8.2 Hydrogen release from the ammonia borane composites

Pristine AB releases hydrogen in two steps, corresponding to the 1st and 2nd hydrogen release, that take place around 110°C and 150°C. This is ideally high and limits the applicability of AB as a solid state hydrogen storage material in a vehicle.

With successive addition of PEO and IMOG the AB, the onset temperatures for these steps are lowered. Adding PS has no appreciable effect on the dehydrogenation temperature of AB. This implies that the PEO and IMOG have a positive effect on AB by reducing the energy barrier to dehydrogenation. In the AB-PS fibres the AB decomposed exactly like bulk AB, in the AB-PEO fibres the AB decomposed like bulk AB (two steps) but these occurred at lower temperatures and in the AB-IMOG composite a portion of the AB reacted like bulk and a portion reacted via an alternative route as suggested by the 'pre-peak'.

The impurity release was also quite illuminating. The impurities in the gas stream from the AB in the AB-PS fibres resembled that of pristine AB. In the AB-PEO fibres the AB released increased amounts of boron containing impurities. And in the AB-IMOG composite has increased levels of ammonia, but reduced boron containing products. The impurity levels in the hydrogen stream the AB-PEO and the AB-IMOG were directly related to the fraction of additive in the material. This suggests that the chemical nature of the additive environment was responsible. This implies that ether groups foster the production of boron containing by-products, a statement that is in line with the sources literature quoted in the materials introduction and that hydroxyl groups are responsible for increased ammonia levels, not commonly observed in the literature.

8.3 Solid state hydrogen storage

So now the final question, are any of these composites suitable to be used as a hydrogen storage system for a vehicle? Well the AB-PS system is clearly not suitable in any way. The 25AB-75additive composites (PEO and IMOG) are able to release hydrogen quickly at lower temperatures than pristine AB. However, the weight penalty combined with the impurity release does not fit these materials for purpose. Further work is required.

8.4 Calcium graphite intercalates

A multiphase ternary calcium ammonia GIC was made by intercalating a mix of stage 1 CaC_6 and graphite with pressurised ammonia vapour. The intercalating material moved through a vast number of phases indicating radical reordering and diffusion of the interlayer species. The calcium ammonia GIC was found to be highly sensitive to temperature. Thermal expansion of the layers was observed and the diffusion of the interlayer ammonia was affected. Hopping diffusion following the Singwi-Sjolander model occurred at 300K and 250K and as the sample cooled the hopping movement disappeared to be replaced with a rotational mode at temperatures 200K, 150K, and 100K. The mechanism by which the GIC restages is unknown.

9 Bibliography

[1] M. Hirscher, *Handbook of Hydrogen Storage: New Materials for Future Energy Storage*. Weinheim: WILEY-VCH Verlag GmbH & Co. KGaA, 2010.

[2] S. Satyapal, J. Petrovic, C. Read, G. Thomas, and G. Ordaz, "The U.S. Department of Energy's National Hydrogen Storage Project: Progress towards meeting hydrogen-powered vehicle requirements," *Catal. Today*, vol. 120, no. 3–4, pp. 246–256, Feb. 2007.

[3] R. H. Jones and J. G. Thomas, Eds., *Materails for the hydorgen economy*. Boca Raton: CRC Press Taylor & Francis Group, 2008.

[4] G. Walker, Ed., *Solid state hydorgen storage Materails and chemistry*. Cambridge England: Woodhead Publishing Limited and Maney Publishing Limited, 2008.

[5] J. O. M. Bockris, "The hydrogen economy: Its history," *Int. J. Hydrogen Energy*, vol. 38, no. 6, pp. 2579–2588, Feb. 2013.

[6] A. Zuttel, A. Borgschulte, and L. Schlapbach, *Hydrogen as a Future Energy Carrier*. Weinheim: Wiley-VCH Verlag GmbH & Co, 2008.

[7] IEA, "ENERGY," 2013.

[8] M. Mohseni, Bahram Ramezanzadeh, H. Yari, M. Moazzami, and M. M. Gudarzi, *New Advances in Vehicular Technology and Automotive Engineering*. In-Tech, 2012.

[9] L. Carrette, K. a. Friedrich, and U. Stimming, "Fuel Cells - Fundamentals and Applications," *Fuel Cells*, vol. 1, no. 1, pp. 5–39, May 2001.

[10] IEA, "Hydrogen Production & Distribution," 2007.

[11] DOE, "Targets for Onboard Hydrogen Storage Systems for Light-Duty Vehicles," pp. 1–22, 2009.

[12] "Driving the Future Today A strategy for ultra low emission vehicles in the UK," London, UK, UK, 2013.

[13] W. I. F. David, "Effective hydrogen storage: a strategic chemistry challenge," *Faraday Discuss.*, vol. 151, p. 399, 2011.

[14] A. Züttel, A. Remhof, A. Borgschulte, and O. Friedrichs, "Hydrogen: the future energy carrier.," *Philos. Trans. A. Math. Phys. Eng. Sci.*, vol. 368, no. 1923, pp. 3329–42, Jul. 2010.

[15] D. J. J. Sloan, *Clathrate hydrates of natural gases*. New York: Marcel Dekker, Inc., 1990.

[16] R. Chahine and T. K. Bose, "Low pressure adsorption storage of hydrogen," *Int. J. Hydrogen Energy*, vol. 19, no. 2, pp. 161–164, 1994.

[17] P. Ciambelli, D. Sannino, M. Sarno, a. Fonseca, and J. B. Nagy, "Selective formation of carbon nanotubes over Co-modified beta zeolite by CCVD," *Carbon N. Y.*, vol. 43, no. 3, pp. 631–640, Jan. 2005.

[18] G. Yushin, R. Dash, J. Jagiello, J. E. Fischer, and Y. Gogotsi, “Carbide-Derived Carbons: Effect of Pore Size on Hydrogen Uptake and Heat of Adsorption,” *Adv. Funct. Mater.*, vol. 16, no. 17, pp. 2288–2293, Nov. 2006.

[19] A. Dailly, J. J. Vajo, and C. C. Ahn, “Saturation of hydrogen sorption in Zn benzenedicarboxylate and Zn naphthalenedicarboxylate.,” *J. Phys. Chem. B*, vol. 110, no. 3, pp. 1099–101, Jan. 2006.

[20] B. Panella and M. Hirscher, “Hydrogen Physisorption in Metal-Organic Porous Crystals,” *Adv. Mater.*, vol. 17, no. 5, pp. 538–541, Mar. 2005.

[21] H. Chae, D. Siberio-Pérez, J. Kim, and Y. Go, “A route to high surface area, porosity and inclusion of large molecules in crystals,” *Nature*, vol. 427, no. February, pp. 523–527, 2004.

[22] N. B. McKeown and P. M. Budd, “Polymers of intrinsic microporosity (PIMs): organic materials for membrane separations, heterogeneous catalysis and hydrogen storage.,” *Chem. Soc. Rev.*, vol. 35, no. 8, pp. 675–83, Aug. 2006.

[23] G. Sandrock, “A panoramic overview of hydrogen storage alloys from a gas reaction point of view,” *J. Alloys Compd.*, vol. 293–295, pp. 877–888, Dec. 1999.

[24] D. Chung, “Review graphite,” *J. Mater. Sci.*, vol. 37, pp. 1475 – 1489, 2002.

[25] D. Aurbach, E. Zinigrad, Y. Cohen, and H. Teller, “A short review of failure mechanisms of lithium metal and lithiated graphite anodes in liquid electrolyte solutions,” *Solid State Ionics*, vol. 148, pp. 405 – 416, 2002.

[26] M. S. Dresselhaus and G. Dresselhaus, “Intercalation compounds of graphite,” *Adv. Phys.*, vol. 51, no. 1, pp. 1–186, Jan. 2002.

[27] W. Lehnert, “The diffusion of lithium through graphite: a Monte Carlo simulation based on electronic structure calculations,” *Chem. Phys.*, vol. 163, no. 3, pp. 331–337, Jul. 1992.

[28] R. C. Boehm and A. Banerjee, “Theoretical study of lithium intercalated graphite,” *J. Chem. Phys.*, vol. 96, no. 2, pp. 1150–1157, 1992.

[29] L. Reghai, J. Conard, H. Fuzellier, M. Lelaurain, and E. McRae, “Transport and 13C nuclear magnetic resonance studies on potassium–ammonia intercalated graphite,” *J. Phys. Chem. Solids*, vol. 62, no. 11, pp. 2083–2090, Nov. 2001.

[30] A. Lovell, S. M. Bennington, N. T. Skipper, C. Gejke, H. Thompson, and M. A. Adams, “Neutron scattering studies of hydrogen in potassium–graphite intercalates: Towards tunable graphite intercalates for hydrogen storage,” *Phys. B Condens. Matter*, vol. 385–386, pp. 163–165, Nov. 2006.

[31] C. Schafhaeutl, “Uber die Verbindungen des Kohlenstoffes mit Silicium, Eisen und anderen Metallen welche die verschiedenen Gattungen von Roheisen, Stahl und Schmeideeisen bilden.,” *J. Prakt. Chem.*, vol. 21, pp. 129–157, 1841.

[32] W. Rüdorff and E. Schulze, “Neue Alkali-Graphit-Verbindungen,” *Angew. Chem.*, vol. 66, p. 305, 1954.

[33] T. Enoki, M. Suzuki, and M. Endo, *Graphite Intercalation Compounds and Applications*. Oxford: Oxford University Press, 2003.

[34] S. A. Solin, "Two-dimensional metal-ammonia-solutions in graphite," *J. Phys. IV*, vol. 1, no. C5, pp. 311–324, 1991.

[35] B. R. York and S. A. Solin, "Effect of composition on charge exchange, lattice expansion, and staging in potassium-ammonia graphite intercalation compounds," *Phys. Rev. B*, vol. 31, no. 12, pp. 8206–8220, 1985.

[36] E. Mayer, "Symmetrical cleavage of diborane by ammonia in solution," *Inorg. Chem.*, vol. 11, no. 4, pp. 866–869, 1972.

[37] F. H. Stephens, V. Pons, and R. T. Baker, "Ammonia-borane: the hydrogen source par excellence?," *Dalt. Trans.*, vol. 2, no. 25, pp. 2613–26, Jul. 2007.

[38] A. D. Sutton, A. K. Burrell, D. a Dixon, E. B. Garner, J. C. Gordon, T. Nakagawa, K. C. Ott, J. P. Robinson, and M. Vasiliu, "Regeneration of ammonia borane spent fuel by direct reaction with hydrazine and liquid ammonia.," *Science*, vol. 331, no. 6023, pp. 1426–9, Mar. 2011.

[39] B. Zhong, L. Song, X. Huang, L. Xia, and G. Wen, "First-principles investigation of ammonia borane for hydrogen storage," *Phys. Scr.*, vol. 86, p. 015606, 2012.

[40] R. D. Suenram and L. R. Thorne, "Microwave spectrum and dipole moment of NH_3BH_3," *Chem. Phys. Lett.*, vol. 78, no. 1, pp. 1980–1981, 1981.

[41] L. R. Thorne, R. D. Suenram, and F. J. Lovas, "Microwave spectrum, torsional barrier, and structure of BH_3NH_3," *J. Chem. Phys.*, vol. 78, no. 1, pp. 167–171, 1983.

[42] D. West, S. Limpijumnong, and S. Zhang, "Band structures and native defects of ammonia borane," *Phys. Rev. B*, vol. 80, no. 6, pp. 1–10, Aug. 2009.

[43] W. T. Klooster, T. F. Koetzle, P. E. M. Siegbahn, T. B. Richardson, and R. H. Crabtree, "Study of the N-H•••H-B Dihydrogen Bond Including the Crystal Structure of BH_3NH_3 by Neutron Diffraction," *J. Am. Chem. Soc.*, vol. 121, no. 27, pp. 6337–6343, 1999.

[44] M. E. Bowden, G. J. Gainsford, and W. T. Robinson, "Room-Temperature Structure of Ammonia Borane," *Aust. J. Chem.*, vol. 60, no. 3, p. 149, 2007.

[45] N. J. Hess, M. E. Bowden, V. M. Parvanov, C. Mundy, S. M. Kathmann, G. K. Schenter, and T. Autrey, "Spectroscopic studies of the phase transition in ammonia borane: Raman spectroscopy of single crystal NH_3BH_3 as a function of temperature from 88 to 330 K.," *J. Chem. Phys.*, vol. 128, no. 3, p. 034508, Jan. 2008.

[46] C. R. Miranda and G. Ceder, "Ab initio investigation of ammonia-borane complexes for hydrogen storage," *J. Chem. Phys.*, vol. 126, no. 184703, pp. 1–11, 2007.

[47] C. A. Morrison and M. M. Siddick, "Dihydrogen bonds in solid BH_3NH_3," *Angew. Chem. Int. Ed. Engl.*, vol. 43, no. 36, pp. 4780–4782, Sep. 2004.

[48] S. G. Shore and R. W. Parry, "The Crystalline Compound Ammonia-Borane,[1] H_3NBH_3," *J. Am. Chem. Soc.*, vol. 77, no. 4, pp. 19–20, 1955.

[49] S. G. Shore and K. W. Boddeker, "Large scale synthesis of $H_2B(NH_3)_3^+BH_4^-$ and NH_3BH_3," *Inorg. Chem.*, vol. 3, no. 6, pp. 914–915, 1964.

[50] P. V. Ramachandran and P. D. Gagare, "Preparation of ammonia borane in high yield and purity, methanolysis, and regeneration.," *Inorg. Chem.*, vol. 46, no. 19, pp. 7810–7, Sep. 2007.

[51] C. Reller and F. O. R. L. Mertens, "A self-contained regeneration scheme for spent ammonia borane based on the catalytic hydrodechlorination of BCl3.," *Angew. Chemie Int. Ed.*, vol. 51, no. 47, pp. 11731–5, Nov. 2012.

[52] A. D. Sutton, A. K. Burrell, D. a Dixon, E. B. Garner, J. C. Gordon, T. Nakagawa, K. C. Ott, J. P. Robinson, and M. Vasiliu, "Regeneration of ammonia borane spent fuel by direct reaction with hydrazine and liquid ammonia.," *Science*, vol. 331, no. 6023, pp. 1426–9, Mar. 2011.

[53] G. Wolf, J. Baumann, F. Baitalow, and F. P. Hoffmann, "Calorimetric process monitoring of thermal decomposition of B-N-H compounds," *Thermochim. Acta*, vol. 343, pp. 19–25, 2000.

[54] M. Bowden, T. Autrey, I. Brown, and M. Ryan, "The thermal decomposition of ammonia borane : A potential hydrogen storage material," *Organometallics*, vol. 8, pp. 498–500, 2008.

[55] P. A. Storozhenko, R. A. Svitsyn, V. A. Ketsko, A. K. Buryak, and A. V. Ul'yanov, "Ammineborane: Synthesis and Physicochemical Characterization," *Russ. J. Iorganic Chem.*, vol. 50, no. 7, pp. 980–985, 2005.

[56] D. J. Heldebrant, A. Karkamkar, N. J. Hess, M. Bowden, S. Rassat, F. Zheng, K. Rappe, and T. Autrey, "The Effects of Chemical Additives on the Induction Phase in Solid-State Thermal Decomposition of Ammonia Borane," no. 1, pp. 5332–5336, 2008.

[57] S. Frueh, R. Kellett, C. Mallery, T. Molter, W. S. Willis, C. King'ondu, and S. L. Suib, "Pyrolytic decomposition of ammonia borane to boron nitride.," *Inorg. Chem.*, vol. 50, no. 3, pp. 783–92, Feb. 2011.

[58] A. Staubitz, A. P. M. Robertson, and I. Manners, "Ammonia-borane and related compounds as dihydrogen sources.," *Chem. Rev.*, vol. 110, no. 7, pp. 4079–124, Jul. 2010.

[59] F. Baitalow, J. Baumann, G. Wolf, K. Jaenicke-Rößler, and G. Leitner, "Thermal decomposition of B–N–H compounds investigated by using combined thermoanalytical methods," *Thermochim. Acta*, vol. 391, no. 1–2, pp. 159–168, Aug. 2002.

[60] J. Zhang, Y. Zhao, D. L. Akins, and J. W. Lee, "Thermal Decomposition and Spectroscopic Studies of Preheated Ammonia Borane," *J. Phys. Chem. C*, vol. 114, no. 45, pp. 19529–19534, Nov. 2010.

[61] V. P. Sorokin, B. I. Vesina, and S. N. Klimova, "Ammonia-Borane: A New Method of Preparation, and its Properties," *Russ. J. Inorg. Chem.*, vol. 8, pp. 66–68, 1963.

[62] M. Hu, J. Van Paasschen, and R. Geanangel, "New synthetic approaches to ammonia-borane and its deuterated derivatives," *J. Inorg. Nucl. Chem.*, vol. 39, pp. 2147–2150, 1977.

[63] R. M. Adams, J. Beres, A. Dodds, and A. J. Morabito, “Dimethyl sulfide-borane as a borane carrier,” *Inorg. Chem.*, vol. 10, no. 9, pp. 2072–2074, 1971.

[64] S. Sepehri, B. B. Garcia, and G. Cao, “Tuning dehydrogenation temperature of carbon–ammonia borane nanocomposites,” *J. Mater. Chem.*, vol. 18, no. 34, p. 4034, 2008.

[65] A. C. Gangal, P. Kale, R. Edla, J. Manna, and P. Sharma, “Study of kinetics and thermal decomposition of ammonia borane in presence of silicon nanoparticles,” *Int. J. Hydrogen Energy*, vol. 37, no. 8, pp. 6741–6748, Apr. 2012.

[66] A. C. Stowe, W. J. Shaw, J. C. Linehan, B. Schmid, and T. Autrey, “In situ solid state ^{11}B MAS-NMR studies of the thermal decomposition of ammonia borane: mechanistic studies of the hydrogen release pathways from a solid state hydrogen storage material.,” *Phys. Chem. Chem. Phys.*, vol. 9, no. 15, pp. 1831–6, Apr. 2007.

[67] D. W. Himmelberger, L. R. Alden, M. E. Bluhm, and L. G. Sneddon, “Ammonia borane hydrogen release in ionic liquids.,” *Inorg. Chem.*, vol. 48, no. 20, pp. 9883–9, Oct. 2009.

[68] D. W. Himmelberger, C. W. Yoon, M. E. Bluhm, P. J. Carroll, and L. G. Sneddon, “Base-Promoted Ammonia Borane Hydrogen-Release,” *ReVision*, vol. 6323, no. 1, pp. 73–82, 2009.

[69] V. Sit, R. A. Geanangel, and W. W. Wendlandt, “The thermal dissociation of NH_3BH_3,” *Thermochim. Acta*, vol. 113, pp. 379–382, 1987.

[70] M. Chandra and Q. Xu, “A high-performance hydrogen generation system: Transition metal-catalyzed dissociation and hydrolysis of ammonia–borane,” *J. Power Sources*, vol. 156, no. 2, pp. 190–194, Jun. 2006.

[71] M. Chandra and Q. Xu, “Dissociation and hydrolysis of ammonia-borane with solid acids and carbon dioxide: An efficient hydrogen generation system,” *J. Power Sources*, vol. 159, no. 2, pp. 855–860, Sep. 2006.

[72] M. Zahmakıran, F. Durap, and S. Özkar, “Zeolite confined copper(0) nanoclusters as cost-effective and reusable catalyst in hydrogen generation from the hydrolysis of ammonia-borane,” *Int. J. Hydrogen Energy*, vol. 35, no. 1, pp. 187–197, Jan. 2010.

[73] K. W. Boddeker, S. G. Shore, and R. K. Bunting, “Boron-Nitrogen Chemistry.,” *J. Am. Chem. Soc.*, vol. 2695, no. 9, pp. 4396–4401, 1966.

[74] D. W. Himmelberger, “Hydrogen release form ammonia borane,” 2010.

[75] H. C. Kelly and V. B. Mattiott, “Reexamination of the acid-catalysed amine-borane hydrolysis. The hydrolysis of $NH_3{\bullet}BH_3$,” *Inorg. Chem.*, vol. 18, no. 10, pp. 2875–2878, 1979.

[76] M. Chandra and Q. Xu, “Room temperature hydrogen generation from aqueous ammonia-borane using noble metal nano-clusters as highly active catalysts,” *J. Power Sources*, vol. 168, no. 1, pp. 135–142, May 2007.

[77] T. Wideman and L. G. Sneddon, “Convenient Procedures for the Laboratory Preparation of Borazine,” *Inorg. Chem.*, vol. 34, no. 4, pp. 1002–1003, Feb. 1995.

[78] W. J. Shaw, J. C. Linehan, N. K. Szymczak, D. J. Heldebrant, C. Yonker, D. M. Camaioni, R. T. Baker, and T. Autrey, "In situ multinuclear NMR spectroscopic studies of the thermal decomposition of ammonia borane in solution.," *Angew. Chem. Int. Ed. Engl.*, vol. 47, no. 39, pp. 7493–6, Jan. 2008.

[79] J. S. Wang and R. A. Geanangel, "^{11}B NMR Studies of the Thermal Decomposition of Ammonia-Borane in Solution," *Inorganica Chim. Acta*, vol. 148, pp. 185–190, 1988.

[80] Y. Kim, H. Baek, J. H. Lee, S. Yeo, K. Kim, S.-J. Hwang, B. Eun, S. W. Nam, T.-H. Lim, and C. W. Yoon, "Metal-free, polyether-mediated H2-release from ammonia borane: roles of hydrogen bonding interactions in promoting dehydrogenation.," *Phys. Chem. Chem. Phys.*, vol. 15, no. 45, pp. 19584–94, Dec. 2013.

[81] H. M. Colquhoun, G. Jones, J. M. Maud, J. F. Stoddart, and D. J. Williams, "Crystal and supramolecular strucutres of complexes* of BF_3NH_3 and BH_3NH_3 with 18-crown-6," *J. Chem. Soc. Dalt. Trans.*, pp. 147–149, 1984.

[82] M. E. Bluhm, M. G. Bradley, R. I. Butterick, U. Kusari, and L. G. Sneddon, "Amineborane-based chemical hydrogen storage: enhanced ammonia borane dehydrogenation in ionic liquids," *J. Am. Chem. Soc.*, vol. 3, pp. 7748–7749, 2006.

[83] W. R. H. Wright, E. R. Berkeley, L. R. Alden, R. T. Baker, and L. G. Sneddon, "Transition metal catalysed ammonia-borane dehydrogenation in ionic liquids.," *Chem. Commun.*, vol. 47, no. 11, pp. 3177–9, Mar. 2011.

[84] A. Feaver, S. Sepehri, P. Shamberger, A. Stowe, T. Autrey, and G. Cao, "Coherent carbon cryogel-ammonia borane nanocomposites for H2 storage.," *J. Phys. Chem. B*, vol. 111, no. 26, pp. 7469–72, Jul. 2007.

[85] T. Zhang, X. Yang, S. Yang, D. Li, F. Cheng, Z. Tao, and J. Chen, "Silica hollow nanospheres as new nanoscaffold materials to enhance hydrogen releasing from ammonia borane," *Phys. Chem. Chem. Phys.*, 2011.

[86] A. C. Gangal, R. Edla, K. Iyer, R. Biniwale, M. Vashistha, and P. Sharma, "Effect of zeolites on thermal decomposition of ammonia borane," *Int. J. Hydrogen Energy*, vol. 37, no. 4, pp. 3712–3718, Feb. 2012.

[87] S. Sepehri and A. Feaver, "Spectroscopic studies of dehydrogenation of ammonia borane in carbon cryogel," *J. Phys. Chem. B*, vol. 111, pp. 14285–14289, 2007.

[88] K. Chang, E. Kim, P. F. Weck, and D. Tománek, "Nanoconfinement effects on the reversibility of hydrogen storage in ammonia borane: a first-principles study.," *J. Chem. Phys.*, vol. 134, no. 21, p. 214501, Jun. 2011.

[89] Z. Tang, H. Chen, and X. Chen, "Graphene Oxide Based Recyclable Dehydrogenation of Ammonia Borane within a Hybrid Nanostructure," *J. Am. ...*, 2012.

[90] L. Li, X. Yao, C. Sun, A. Du, L. Cheng, Z. Zhu, C. Yu, J. Zou, S. C. Smith, P. Wang, H.-M. Cheng, R. L. Frost, and G. Q. (Max) Lu, "Lithium-Catalyzed Dehydrogenation of Ammonia Borane within Mesoporous Carbon Framework for Chemical Hydrogen Storage," *Adv. Funct. Mater.*, vol. 19, no. 2, pp. 265–271, Jan. 2009.

[91] S. B. Kalidindi, J. Joseph, and B. R. Jagirdar, "Cu^{2+}-induced room temperature hydrogen release from ammonia borane," *Energy Environ. Sci.*, vol. 2, no. 12, p. 1274, 2009.

[92] T. He, Z. Xiong, G. Wu, H. Chu, C. Wu, T. Zhang, and P. Chen, "Nanosized Co- and Ni-Catalyzed Ammonia Borane for Hydrogen Storage," *Chem. Mater.*, vol. 21, no. 11, pp. 2315–2318, Jun. 2009.

[93] X. Kang, Z. Fang, L. Kong, H. Cheng, X. Yao, G. Lu, and P. Wang, "Ammonia Borane Destabilized by Lithium Hydride: An Advanced On-Board Hydrogen Storage Material," *Adv. Mater.*, vol. 20, no. 14, pp. 2756–2759, Jul. 2008.

[94] Z. Xiong, C. K. Yong, G. Wu, P. Chen, W. Shaw, A. Karkamkar, T. Autrey, M. O. Jones, S. R. Johnson, P. P. Edwards, and W. I. F. David, "High-capacity hydrogen storage in lithium and sodium amidoboranes.," *Nat. Mater.*, vol. 7, no. 2, pp. 138–41, Feb. 2008.

[95] A. T. Luedtke and T. Autrey, "Hydrogen release studies of alkali metal amidoboranes.," *Inorg. Chem.*, vol. 49, no. 8, pp. 3905–10, Apr. 2010.

[96] J. Luo, X. Kang, and P. Wang, "Synthesis, formation mechanism, and dehydrogenation properties of the long-sought $Mg(NH_2BH_3)_2$compound," *Energy Environ. Sci.*, vol. 6, no. 3, p. 1018, 2013.

[97] Z. Tang, S. Li, Z. Yang, and X. Yu, "Ammonia borane nanofibers supported by poly(vinyl pyrrolidone) for dehydrogenation," *J. Mater. Chem.*, vol. 21, pp. 14616–14621, 2011.

[98] S. F. Li, Z. W. Tang, Y. B. Tan, and X. B. Yu, "Polyacrylamide Blending with Ammonia Borane: A Polymer Supported Hydrogen Storage Composite," *J. Phys. Chem. C*, vol. 116, no. 1, pp. 1544–1549, Jan. 2012.

[99] J. Zhao, J. Shi, X. Zhang, F. Cheng, J. Liang, Z. Tao, and J. Chen, "A soft hydrogen storage material: poly(methyl acrylate)-confined ammonia borane with controllable dehydrogenation.," *Adv. Mater.*, vol. 22, no. 3, pp. 394–7, Jan. 2010.

[100] Z. Kurban, A. Lovell, S. M. Bennington, D. W. K. Jenkins, K. R. Ryan, M. O. Jones, N. T. Skipper, and W. I. F. David, "A Solution Selection Model for Coaxial Electrospinning and Its Application to Nanostructured Hydrogen Storage Materials," *J. Phys. Chem. C*, no. 114, pp. 21201–21213, 2010.

[101] Yuan-Huffman, Q, W, "Poly(ethylene) oxide," in *Polymer data handbook*, 2nd ed., Oxford: Oxford University Press, 2009, pp. 690–700.

[102] C. Vasile and A. K. Kulshreshtha, *Handbook of polymer blends and composites, Volumes 1 - 4*. Shrewsbury: Rapra Technology, 2002.

[103] J. E. Mark, *Polymer Data Handbook*, 2nd ed. Oxford: Oxford University Press, 2009.

[104] R. J. Keaton, J. M. Blacquiere, and R. T. Baker, "Base Metal Catalyzed Dehydrogenation of Ammonia-Borane for Chemical Hydrogen Storage," vol. 2, pp. 1844–1845, 2006.

[105] A. Gutowska, L. Li, Y. Shin, C. M. Wang, X. S. Li, J. C. Linehan, R. S. Smith, B. D. Kay, B. Schmid, W. Shaw, M. Gutowski, and T. Autrey, "Nanoscaffold Mediates Hydrogen Release and the Reactivity of Ammonia Borane," *Angew. Chem. Int. Ed.*, pp. 3578 –3582, 2005.

[106] J. J. Vajo and G. L. Olson, “Hydrogen storage in destabilized chemical systems,” *Scr. Mater.*, vol. 56, no. 10, pp. 829–834, May 2007.

[107] S. Ramakrishna, K. Fujihara, W. Teo, T. Lim, and Z. Ma, *An Introduction to Electrospinning and Nanofibers*. Sibgapore: world scientific Publishing Co. Pte. Ltd., 2005.

[108] Y. Pan, Y. Wang, Y. Liang, Z. Tao, and J. Chen, “Promoted hydrogen release from ammonia borane with mannitol via a solid-state reaction route.,” *Dalton Trans.*, vol. 41, no. 3, pp. 871–5, Jan. 2012.

[109] W. A. Deer, R. A. Howie, and J. Zussman, *An introduction to the rock-forming minerals*, 2nd ed. Harlow, Essex: Longman Scientific and Technical, 1992.

[110] B. Ruzicka and E. Zaccarelli, “A fresh look at the Laponite phase diagram,” *Soft Matter*, vol. 7, no. 4, p. 1268, 2011.

[111] C. Zanzottera, A. Vicente, E. Celasco, C. Fernandez, E. Garrone, and B. Bonelli, “Physico-Chemical Properties of Imogolite Nanotubes Functionalized on Both External and Internal Surfaces,” *J. Phys. Chem. C*, vol. 116, no. 13, pp. 7499–7506, Apr. 2012.

[112] J. P. Gabriel and P. Davidson, “Mineral Liquid Crystals from Self-Assembly of Anisotropic Nanosystems,” 2003, pp. 119–172.

[113] B. Creton, D. Bougeard, K. S. Smirnov, J. Guilment, and O. V. Poncelet, “Molecular dynamics study of hydrated imogolite,” *Phys. Chem. Chem. Phys.*, vol. 10, no. 32, pp. 4879–4888, Aug. 2008.

[114] P. D. G. Cradwick, V. C. Farmer, and J. D. Russell, “Imogolite, a hydrated aluminium silicate of tubular structure,” *Nature*, vol. 240, pp. 187–187, 1972.

[115] W. Ma, W. O. Yah, H. Otsuka, and A. Takahara, “Application of imogolite clay nanotubes in organic–inorganic nanohybrid materials,” *J. Mater. Chem.*, vol. 22, no. 24, p. 11887, 2012.

[116] E. Joussein, S. Petit, J. Churchman, and B. Theng, “Halloysite clay minerals—a review,” *Clay Miner.*, vol. 40, pp. 383–426, 2005.

[117] R. Kamble, M. Ghag, S. Gaikawad, and B. K. Panda, “Review Article Halloysite Nanotubes and Applications : A Review,” vol. 3, no. 2, pp. 25–29, 2012.

[118] J. K. Walters, N. T. Skipper, and A. K. Soper, “The interlayer structure of a graphite–potassium–ammonia intercalation compound by neutron diffraction,” *Chem. Phys. Lett.*, vol. 300, no. February, pp. 444–450, 1999.

[119] H. Zabel, “Dynamics of molecules in graphite,” *Synth. Met.*, vol. 23, pp. 37–42, 1988.

[120] F. Leclercq, P. Damay, and P. Chieux, “Quantum and Diffusional Rotation of Ammonia in Hexaamminecalcium As Observed by Incoherent Neutron Scattering,” *J. Phys. Chem.*, vol. 88, pp. 3886–3890, 1984.

[121] H. Zabel and D. A. Neumann, “Neutron scattering studies of potassium-ammonia layers in graphite,” *Can. J. Chem.*, vol. 66, pp. 666–671, 1988.

[122] H. A. Resing, B. R. York, S. A. Solin, and R. M. Fronko, “Preferred Orientation of Ammonia in $KC_{24}(NH_3)_{4.3}$ Found by Proton NMR Spectroscopy,” in *17th Biennial Conference at University of Kentucky, Lexington, Kentucky*, 1985, vol. 24, pp. 4–5.

[123] T. Tsang, R. M. Fronko, H. A. Resing, X. W. Qain, and S. A. Solin, “^{1}H NMR Study of Ternary Ammonia-Alkali Metal-Graphite Intercalation Compounds.,” *Solid State Commun.*, vol. 63, no. 4, pp. 361–366, 1987.

[124] Q. P. Pham, U. Sharma, and A. G. Mikos, “Electrospinning of Polymeric Nanofibers for Tissue Engineering Applications : A Review,” *Tissue Eng.*, vol. 12, no. 5, 2006.

[125] Y. Chen, Z. Lu, L. Zhou, Y.-W. Mai, and H. Huang, “In situ formation of hollow graphitic carbon nanospheres in electrospun amorphous carbon nanofibers for high-performance Li-based batteries.,” *Nanoscale*, vol. 4, no. 21, pp. 6800–5, Nov. 2012.

[126] J. S. Choi, Y. Kim, J. Kang, S. Y. Jeong, and H. S. Yoo, “Electrospun chitosan microspheres for complete encapsulation of anionic proteins: controlling particle size and encapsulation efficiency.,” *AAPS PharmSciTech*, vol. 14, no. 2, pp. 794–801, Jun. 2013.

[127] B. a. Miller-Chou and J. L. Koenig, “A review of polymer dissolution,” *Prog. Polym. Sci.*, vol. 28, no. 8, pp. 1223–1270, Aug. 2003.

[128] T. L. Yu, “Polymer Molecular Weight from Loss Modulus.,” *Polym. J.*, vol. 24, no. 7, pp. 220–1328, 1992.

[129] S. Ramakrishna, K. Fujihara, W. E. Teo, T. C. Lim, and Z. Ma, *An Introduction to Electrospinning and Nanofibres*. Singapore: world scientific Publishing Co. Pte. Ltd., 2005.

[130] Y. Liu, J. He, J. Yu, and H. Zeng, “Controlling numbers and sizes of beads in electrospun nanofibers,” *Polym. Int.*, vol. 636, no. August 2007, pp. 632–636, 2008.

[131] G. Eda and S. Shivkumar, “Bead- to- fiber transition in electrospun polystyrene,” *J. Appl. Polym. Sci.*, no. May 2006, 2007.

[132] Z.-M. Huang, Y.-Z. Zhang, M. Kotaki, and S. Ramakrishna, “A review on polymer nanofibers by electrospinning and their applications in nanocomposites,” *Compos. Sci. Technol.*, vol. 63, no. 15, pp. 2223–2253, Nov. 2003.

[133] C. J. Luo, M. Nangrejo, and M. Edirisinghe, “A novel method of selecting solvents for polymer electrospinning,” *Polymer (Guildf).*, vol. 51, no. 7, pp. 1654–1662, Mar. 2010.

[134] S. Koombhongse, W. Liu, and D. H. Reneker, “Flat Polymer Ribbons and Other Shapes by Electrospinning,” *Polymer (Guildf).*, no. May, pp. 2598–2606, 2001.

[135] C. J. Angammana, S. Member, and S. H. Jayaram, “Analysis of the Effects of Solution Conductivity on Electrospinning Process and Fiber Morphology,” vol. 47, no. 3, pp. 1109–1117, 2011.

[136] G. H. Lee, J. C. Song, and K. B. Yoon, “Controlled wall thickness and porosity of polymeric hollow nanofibers by coaxial electrospinning,” *Macromol. Res.*, vol. 18, no. 6, pp. 571–576, Jun. 2010.

[137] K. H. Lee, H. Y. Kim, H. J. Bang, Y. H. Jung, and S. G. Lee, "The change of bead morphology formed on electrospun polystyrene fibers," *Polymer (Guildf).*, vol. 44, no. 14, pp. 4029–4034, Jun. 2003.

[138] X. Zong, K. Kim, D. Fang, S. Ran, B. S. Hsiao, and B. Chu, "Structure and process relationship of electrospun bioabsorbable nanofiber membranes," *Polymer (Guildf).*, vol. 43, pp. 4403–4412, 2002.

[139] C. Wang, C.-H. Hsu, and J.-H. Lin, "Scaling Laws in Electrospinning of Polystyrene Solutions," *Macromolecules*, vol. 39, no. 22, pp. 7662–7672, Oct. 2006.

[140] G. Larsen, R. Spretz, and R. Velarde-Ortiz, "Use of Coaxial Gas Jackets to Stabilize Taylor Cones of Volatile Solutions and to Induce Particle-to-Fiber Transitions," *Adv. Mater.*, vol. 16, no. 2, pp. 166–169, Jan. 2004.

[141] J. A. Nairn, "Viscosity," 2003.

[142] P. Sunthar, "Polymer Rheology," in *Rheology of Complex Fluids*, New York: Springer New York, 2010, pp. 171–191.

[143] J.-H. He, Y.-Q. Wan, and J.-Y. Yu, "Effect of concentration on electrospun polyacrylonitrile (PAN) nanofibers," *Fibers Polym.*, vol. 9, no. 2, pp. 140–142, Jul. 2008.

[144] M. M. Demir, "Investigation on glassy skin formation of porous polystyrene fibers electrospun from DMF," *eXPRESS Polym. Lett.*, vol. 4, no. 1, pp. 2–8, Dec. 2009.

[145] K. A. Dill and S. Bromberg, *Molecular Driving Forces: Statistical Thermodynamics in Chemistry and Biology*. London: Garland Science, 2003.

[146] D. H. Reneker, A. L. Yarin, E. Zussman, and H. Xu, "Electrospinning of Nanofibers from Polymer Solutions and Melts," *Adv. Appl. Mech.*, vol. 41, p. 43, 2007.

[147] E. Antoniou and P. Alexandridis, "Polymer conformation in mixed aqueous-polar organic solvents," *Eur. Polym. J.*, vol. 46, no. 2, pp. 324–335, Feb. 2010.

[148] G.-W. Oetjen, "Freeze-Drying," *Ullmann's Encyclopedia of Industrial Chemistry*. Wiley-VCH Verlag GmbH & Co, pp. 52–100, 2012.

[149] G. Srinivas, C. A. Howard, S. M. Bennington, N. T. Skipper, and M. Ellerby, "Effect of hydrogenation on structure and superconducting properties of CaC6," *J. Mater. Chem.*, vol. 19, no. 29, p. 5239, 2009.

[150] A. Kriete, H. Gundlach, S. Amelinckx, and L. Reimer, "Microscopy," *Ullmann's Encyclopedia of Industrial Chemistry*. Wiley-VCH Verlag GmbH & Co, pp. 298–308, 2012.

[151] J. Coates, "Interpretation of Infrared Spectra , A Practical Approach," *Encyclopedia of Analytical Chemistry*. John Wiley& Sons Ltd, Chichester, pp. 10815–10837, 2000.

[152] Y.-C. Ning, "Interpretation of Infrared Spectra," in *Interpretation of Organic Spectra*, Singapore: John Wiley & Sons (Asia) Pte Ltd, 2011, pp. 129–146.

[153] H.-U. Remlich, “Infrared and Raman Spectroscopy,” *Ullmann’s Encyclopedia of Industrial Chemistry*. pp. 177–220, 2012.

[154] a Cooper and C. M. Johnson, “Differential scanning calorimetry.,” *Methods Mol. Biol.*, vol. 22, pp. 125–36, Jan. 1994.

[155] S. B. Warrington and G. W. H. Hohne, “Thermal Analysis and Calorimetry,” *Ullmann’s Encyclopedia of Industrial Chemistry*. WILEY-VCH Verlag GmbH & Co. KGaA, pp. 415–439, 2012.

[156] J. H. Gross, *Mass spectrometry : a textbook*. Berlin: Springer, 2001.

[157] A. Savitzky and M. J. E. Golay, “Smoothing and differentialtion of data by simplified least squares procedures,” *J. Anal. Chem.*, vol. 36, no. 8, pp. 1627–1639, 1964.

[158] G. Orwell, *Animal Farm: A Fairy Story*, New Ed. London, UK: Penguin Classics, 2010.

[159] K. N. Ninan, “Kinetics of solid state termal decomposition reactions,” *J. Therm. Anal.*, vol. 35, pp. 1267–1278, 1989.

[160] A. C. Gangal, P. Kale, R. Edla, J. Manna, and P. Sharma, “Study of kinetics and thermal decomposition of ammonia borane in presence of silicon nanoparticles,” *Int. J. Hydrogen Energy*, vol. 37, no. 8, pp. 6741–6748, Apr. 2012.

[161] D. S. Sivia, *Elementary Scattering Theory, For X-ray and Neutron Users*. Oxford: Oxford University Press, 2011.

[162] Y. Waseda, E. Matsubara, and K. Shinoda, *X-ray diffraction crystallography: introduction, examples and solved problems*. Berlin: Springer, 2011, pp. 1–310.

[163] Fatima Gonzales Sanchez, “Water diffusion through compacted clays analyzed by neutron scattering and tracer experiments,” 2007.

[164] A. Lovell, “Tuneable graphite intercalates for hydrogen storage,” 2007.

[165] B. Willis and C. J. Carlile, *Experimental Neutron Scattering*. Oxford: Oxford University Press, 2009, pp. 295–309.

[166] K. S. Singwi and A. Sjölander, “Diffusive motions in water and cold neutron scattering,” *Phys. Rev.*, vol. 119, no. 3, pp. 863–871, 1960.

[167] P. L. Hall and D. K. Ross, “Incoherent neutron scattering functions for random jump diffusion in bounded and infinite media,” *Mol. Phys. An Int. J. Interface Between Chem. Phys.*, vol. 42, no. 3, pp. 673–682, 1981.

[168] C. T. Chudley and R. J. Elliott, “Neutron scattering from a liquid on a jump diffusion model,” *Proc. Phys. Soc.*, vol. 353, no. 77, pp. 353–361, 1961.

[169] W. S. Howells, V. García Sakai, F. Demmel, M. T. F. Telling, and F. Fernandez-Alonso, “The MODES User Guide v3,” *Analysis*, no. February. Rutherford Appleton Laboratory Technical Report, pp. 1–62, 2010.

[170] W. E. Teo and S. Ramakrishna, “A review on electrospinning design and nanofibre assemblies.,” *Nanotechnology*, vol. 17, no. 14, pp. R89–R106, Jul. 2006.

[171] J. Deitzel, “Controlled deposition of electrospun poly(ethylene oxide) fibers,” *Polymer (Guildf).*, vol. 42, no. 19, pp. 8163–8170, Sep. 2001.

[172] H. Tadokoro, Y. Chatani, T. Yoshihara, S. Tahara, and S. Murahashi, “Structural Studies on Polyethers, [-(CH2)m-O-]n. II. Molecular Structure of Polyethylene Oxide,” pp. 109–127, 1963.

[173] F. Gu, H. Bu, and Z. Zhang, “A unique morphology of freeze-dried poly(ethylene oxide) and its transformation,” *Polymer (Guildf).*, vol. 41, no. 21, pp. 7605–7609, Oct. 2000.

[174] A. C. French, A. L. Thompson, and B. G. Davis, “High-purity discrete PEG-oligomer crystals allow structural insight.,” *Angew. Chem. Int. Ed. Engl.*, vol. 48, no. 7, pp. 1248–52, Jan. 2009.

[175] Mettler Toledo, “Interpreting DSC curves Part 1: Dynamic measurements,” 2000.

[176] D. Wolstenholme and K. Traboulsee, “Thermal desorption of hydrogen from ammonia borane: unexpected role of homopolar B–H···H–B interactions,” *Chem. Commun.*, vol. 48, pp. 2597–2599, 2012.

[177] F. Merten, G. Wolf, and F. Baitalow, “Ammonia borane and related compouds as hydrogen source materials,” in *Handbook of Hydrogen Storage New Materails for Future Energy Storage*, M. Hirscher, Ed. Weinheim: Wiley-VCH Verlag GmbH & Co, 2010, pp. 215–244.

[178] J. Zhang, Y. Zhao, D. Akins, and J. Lee, “CO_2-enhanced thermolytic H_2 release from ammonia borane,” *J. Phys. …*, vol. 115, pp. 8386–8392, 2011.

[179] U. B. Demirci, S. Bernard, R. Chiriac, F. Toche, and P. Miele, “Hydrogen release by thermolysis of ammonia borane NH_3BH_3 and then hydrolysis of its by-product [BNH_x],” *J. Power Sources*, vol. 196, no. 1, pp. 279–286, Jan. 2011.

[180] S. Xie, Y. Song, and Z. Liu, “In situ high-pressure study of ammonia borane by Raman and IR spectroscopy,” *Can. J. Chem.*, vol. 87, no. 9, pp. 1235–1247, Sep. 2009.

[181] N. Gondaliya, Dinesh Kumar Kanchan, P. Sharma, and P. Joge, “Structural and Conductivity Studies of Poly(Ethylene Oxide) – Silver Triflate Polymer Electrolyte System,” *Mater. Sci. Appl.*, vol. 2, pp. 1639–1643, 2011.

[182] M. Sundar and S. Selladurai, “Effect of fillers on magnesium–poly(ethylene oxide) solid polymer electrolyte,” *Ionics (Kiel).*, vol. 12, no. 4–5, pp. 281–286, Oct. 2006.

[183] J. Joseph and E. D. Jemmis, “Red-, blue-, or no-shift in hydrogen bonds: a unified explanation.,” *J. Am. Chem. Soc.*, vol. 129, no. 15, pp. 4620–32, Apr. 2007.

[184] L. Jun, X. Shuping, and G. Shiyang, “FT-IR and Raman spectroscopic study of hydrated borates,” *Spectrochim. Acta Part A Mol. Biomol. Spectrosc.*, vol. 51, no. 4, pp. 519–532, Apr. 1995.

[185] S. Gadipelli, J. Ford, W. Zhou, H. Wu, T. J. Udovic, and T. Yildirim, "Nanoconfinement and Catalytic Dehydrogenation of Ammonia Borane by Magnesium-Metal–Organic-Framework-74," *Communication*, pp. 6043 – 6047, 2011.

[186] A. Kanturk, M. Sari, and S. Piskin, "Synthesis , crystal structure and dehydration kinetics of NaB (OH) 4 · 2H 2 O," vol. 25, no. 6, pp. 1331–1337, 2008.

[187] A. Y. Likhacheva, E. A. Paukshtis, Y. V. Seryotkin, and S. G. Shulgenko, "IR spectroscopic characterization of NH^4-analcime," *Phys. Chem. Miner.*, vol. 29, no. 9, pp. 617–623, Oct. 2002.

[188] R. C. Taylor and C. L. Cluff, "Vibrational Frequency associated with the Boron-Nitrogen Dative Bond in Amine Boranes," *Nature*, vol. 182, pp. 390–391, 1958.

[189] B. Kang and G. Ceder, "Battery materials for ultrafast charging and discharging.," *Nature*, vol. 458, no. 7235, pp. 190–3, Mar. 2009.

[190] D.-P. Kim, K.-T. Moon, J.-G. Kho, J. Economy, C. Gervais, and F. Babonneau, "Synthesis and characterization of poly(aminoborane) as a new boron nitride precursor," *Polym. Adv. Technol.*, vol. 10, no. 12, pp. 702–712, Dec. 1999.

[191] J. F. Kostka, R. Schellenberg, F. Baitalow, T. Smolinka, and F. Mertens, "Concentration-Dependent Dehydrogenation of Ammonia-Borane/Triglyme Mixtures," *Eur. J. Inorg. Chem.*, vol. 2012, no. 1, pp. 49–54, Jan. 2012.

[192] C. L. Casper, J. S. Stephens, N. G. Tassi, D. B. Chase, and J. F. Rabolt, "Controlling Surface Morphology of Electrospun Polystyrene Fibers: Effect of Humidity and Molecular Weight in the Electrospinning Process," *Macromolecules*, vol. 37, no. 2, pp. 573–578, Jan. 2004.

[193] S. Megelski, J. S. Stephens, D. B. Chase, and J. F. Rabolt, "Micro- and Nanostructured Surface Morphology on Electrospun Polymer Fibers," *Macromolecules*, vol. 35, no. 22, pp. 8456–8466, Oct. 2002.

[194] T. Jarusuwannapoom, W. Hongrojjanawiwat, S. Jitjaicham, L. Wannatong, M. Nithitanakul, C. Pattamaprom, P. Koombhongse, R. Rangkupan, and P. Supaphol, "Effect of solvents on electro-spinnability of polystyrene solutions and morphological appearance of resulting electrospun polystyrene fibers," *Eur. Polym. J.*, vol. 41, no. 3, pp. 409–421, Mar. 2005.

[195] G. C. Andrews and S. F. Neelamkavil, "Borane–Ammonia," *E-EROS Encyclopedia of Reagents for Organic Synthesis*, no. eq 5. pp. 1–2, 2008.

[196] G. Eda, J. Liu, and S. Shivkumar, "Solvent effects on jet evolution during electrospinning of semi-dilute polystyrene solutions," *Eur. Polym. J.*, vol. 43, no. 4, pp. 1154–1167, Apr. 2007.

[197] E. S. Medeiros, L. H. C. Mattoso, R. D. Offeman, D. F. Wood, and W. J. Orts, "Effect of relative humidity on the morphology of electrospun polymer fibers," *Can. J. Chem.*, vol. 86, no. 6, pp. 590–599, 2008.

[198] A. C. D. Newman, *Chemsitry of Clays and Clay Minerals*. Harlow, Essex: Longman Scientific and Technical, 1987.

[199] V. C. Farmer, M. J. Adams, A. R. Fraser, and F. Palmieri, “Synthetic imogolite: properties, synthesis, and possible applications,” *Clay Miner.*, vol. 18, pp. 459–472, 1983.

[200] K. Wada and N. Yoshinaga, “The structure of ‘imogolite,’” *Am. Mineral.*, vol. 54, pp. 50–71, 1969.

[201] C. Levard, A. Masion, J. Rose, E. Doelsch, D. Borschneck, C. Dominici, F. Ziarelli, and J.-Y. Bottero, “Synthesis of imogolite fibers from decimolar concentration at low temperature and ambient pressure: a promising route for inexpensive nanotubes.,” *J. Am. Chem. Soc.*, vol. 131, no. 47, pp. 17080–1, Dec. 2009.

[202] G. H. Koenderink, S. G. J. M. Kluijtmans, and A. P. Philipse, “On the synthesis of colloidal imogolite fibers,” *J. Colloid Interface Sci.*, vol. 216, pp. 429–431, 1999.

[203] D.-Y. Kang, J. Zang, E. R. Wright, A. L. McCanna, C. W. Jones, and S. Nair, “Dehydration, dehydroxylation, and rehydroxylation of single-walled aluminosilicate nanotubes.,” *ACS Nano*, vol. 4, no. 8, pp. 4897–907, Aug. 2010.

[204] B. Bonelli, I. Bottero, N. Ballarini, S. Passeri, F. Cavani, and E. Garrone, “IR spectroscopic and catalytic characterization of the acidity of imogolite-based systems,” *J. Catal.*, vol. 264, no. 1, pp. 15–30, May 2009.

[205] D. Cheddie, “Ammonia as a Hydrogen Source for Fuel Cells: A Review,” in *Hydrogen Energy - Challenges and Perspectives*, D. Minic, Ed. InTech, 2012.

[206] G. Srinivas, a Lovell, N. T. Skipper, S. M. Bennington, Z. Kurban, and R. I. Smith, “Ammonia absorption in calcium graphite intercalation compound: in situ neutron diffraction, Raman spectroscopy and magnetization.,” *Phys. Chem. Chem. Phys.*, vol. 12, no. 23, pp. 6253–9, Jun. 2010.

[207] M. Höhne, Y. X. Wang, and E. Stumpp, “New ternary alkaline earth metal-ammonia compounds,” *Synth. Met.*, vol. 34, pp. 41–46, 1989.

[208] H. A. Resing, B. R. York, S. A. Solin, and R. M. Fronko, “Preferred Orientation of Ammonia in KC24(NH3) Found by Proton NMR Spectroscopy,” *17th Bienn. Conf. Univ. Kentucky, Lexington, Kentucky*, vol. 24, pp. 4–5, 1985.

[209] G. Srinivas, A. Lovell, N. T. Skipper, S. M. Bennington, Z. Kurban, and R. I. Smith, “Ammonia absorption in calcium graphite intercalation compound: in situ neutron di raction, Raman spectroscopy and magnetization,” *Phys. Chem. Chem. Phys.*, vol. 12, pp. 6253–6259, 2010.

[210] C. J. Carlile, I. M. Jamie, G. Lockhart, and J. W. White, “Two dimensional caesium-ammonia solid sollution in $C2_{28}Cs(NH_3)_x$,” *Mol. Phys.*, vol. 76, no. 1, pp. 173–200, 1992.

[211] D. A. Neumann, H. Zabel, J. J. Rush, Y. B. Fan, and S. A. Solin, “Quasi-elastic neutron scattering study of rotations and diffusion in $KC_{24}(NH_3)_{4.3}$,” *J. Phys. Chem. C*, vol. 761, no. 20, pp. L761–L764, 1987.

[212] D. S. Kyser and J. C. Thompson, “Measurement of the Hall Effect in Metal—Ammonia Solutions,” *J. Chem. Phys.*, vol. 42, no. 11, p. 3910, 1965.